

Chemical Vapour Deposition Synthesis of Novel Nanostructured Materials

AZZULIANI SUPANGAT

MSc (Applied Physics)

Thesis submitted for the degree of Doctor of Philosophy

The University of Newcastle

March 2012

DECLARATION

This thesis contains no material which has been accepted for the award of any other degree or diploma in any university or other tertiary institution and, to the best of my knowledge and belief, contains no material previously published or written by another person, except where due reference has been made in the text. I give consent to this copy of my thesis, when deposited in the University Library, being made available for loan and photocopying subject to the provisions of the Copyright Act 1968.

(Signed):

Azzuliani Supangat

ACKNOWLEDGEMENTS

First and foremost, I would like to say Alhamdulillah, for giving me the strength and health during the completion of my studies. It is a pleasure to thank those who made this thesis possible. I am heartily thankful to my supervisors, Prof. Dr. Paul Dastoor, Dr. Warwick Belcher and Dr. Xiaojing Zhou whose encouragement, supervision and support from the preliminary to the concluding level enabled me to develop an understanding of the research. I would like to make a special reference to Dr. Glenn Bryant who helped me with the thesis writing. Without his co-operation I could not have completed my PhD. Lastly, I would like to offer my regards and blessings to my husband, Zulkhairi Zakaria, for supporting and encouraging me to pursue PhD. Without him, I would never have made it as far as I did. He has held me when I cried and cheered with me when I won, and I will love him forever.

APPENDIX: PUBLICATIONS ARISING FROM THIS THESIS

Part of the work presented in this thesis has been published to refereed journals. The following is lists of publications that have arisen as a result of work presented in this thesis.

- (1) **A. Supangat**, G. Bryant, W. J Belcher and P. C. Dastoor, “Synthesis of Indium Oxide Nanowires Encapsulated in Amorphous Carbon Nanostructures on Indium Tin Oxide Substrate”, *Materials Research Innovations*.
(DOI: 10.1179/1433075X11Y.0000000034)
- (2) **A. Supangat**, X. Zhou, W. J. Belcher and P. C. Dastoor, “Chemical vapour deposition of poly(p-phenylenevinylene) nanofilms for use in organic photovoltaics”, *Materials Research Innovations*, Vol 15, 2011. pp. 18-20
- (3) **A. Supangat**, G. Bryant, W. J. Belcher and P. C. Dastoor, “Templated Growth of Poly (p-phenylenevinylene) Nanostructures by Chemical Vapour Deposition”, *Materials Research Innovations*.
(DOI: 10.1179/1433075X11Y.0000000024)

LIST OF FIGURES

Figure 1-1: Current performance and price of different PV module technologies [23] ...	5
Figure 1-2: The graph of current-voltage curve with the illustration of FF, I_{sc} and V_{oc} ...	9
Figure 1-3: Thermal Chemical Vapor Deposition System [44]	11
Figure 1-4: Formation of Carbon Nanotube [62]	12
Figure 1-5: Diagram of reactor used for CVD of PPV [71]	15
Figure 2-1: Evaporator overview and dimensions	19
Figure 2-2: Fe layer thickness versus evaporation time plot	20
Figure 2-3: Schematic diagram of the Atomate CVD system	21
Figure 2-4: SEM image of alumina porous template	23
Figure 2-5: Schematic diagram of CVD polymerisation	25
Figure 2-6: (a) Photo of Philips XL30 SEM & (b) schematic diagram of SEM	26
Figure 2-7: (a) Photo of JEOL 1200 EXII TEM & (b) schematic diagram of TEM	27
Figure 2-8: Schematic of 4-point probe configuration [94]	28
Figure 2-9: Schematic of four-point probe setup for thin rectangular slice sample [94]	28
Figure 2-10: An optimal geometry of the ground state and excited state	32
Figure 2-11: Current density versus voltage characteristics ($J-V$) of an ideal solar cell [39]	35
Figure 3-1: (a) Influence of oxygen gas flow rate [108] and (b) annealing treatment [109]	37
Figure 3-2: Conductivity of ITO substrates at different annealing temperatures	41
Figure 3-3: AFM images of ITO annealed at different temperatures of	44
Figure 3-4: Plot of different surface roughness under different annealing temperatures	45
Figure 3-5: SEM image of ITO annealed at 700°C with the appearance of wrinkles and spikes	46
Figure 3-6: X-ray diffraction pattern of ITO substrate after annealing at (a) 700°C, (b) 600°C,	47

Figure 3-7: Graph of FWHM versus conductivity of (211), (222), (400), (440) & (622) planes.....	47
Figure 3-8: Peak intensity of (222) and (400) versus annealing temperature	48
Figure 3-9: Grain size of crystallites for (400) and (222) planes versus annealing temperature.....	49
Figure 3-10: UV-vis absorption spectra of ITO annealed at different temperature	51
Figure 3-11: EDS spectra of ITO substrate before (a) and after annealing at (b) 100°C, (c) 200°C, (d) 300°C, (e) 400°C, (f) 450°C, (g) 500°C, (h) 600°C & (i) 700°C.....	53
Figure 3-12: EDS spectra of indium peaks of ITO annealed at different temperature ...	53
Figure 3-13: Relative concentration (%) of indium and tin in the bulk composition	54
Figure 3-14: XPS spectra of ITO annealed at different temperatures: (a) wide scan & ..	56
Figure 3-15: Atomic relative concentration (%) of indium and tin at the surface	57
Figure 3-16: Ratio of In:O and Sn:O under different annealed temperatures.....	57
Figure 3-17: XPS spectra in the O1s region of ITO substrate before (a) and after annealing at	59
Figure 3-18: Atomic relative concentration (%) of O 1s chemical state versus	60
Figure 3-19: Atomic relative concentration of indium at the surface and in the bulk under different annealed temperature.....	61
Figure 4-1: SEM images of (a) carbon nanostructures grown on glass and ITO under similar growth conditions (b) carbon nanostructures grown on ITO & (c) cross sectional view of carbon nanostructures grown on ITO [8].....	66
Figure 4-2: TEM images of carbon nanostructures grown on ITO of (a) lower magnification &	66
Figure 4-3: SEM image of carbon nanocoils grown at 700°C [140].....	67
Figure 4-4: Schematic diagram of tin nanowire growth by the VLS mechanism [22] ...	68
Figure 4-5: Schematic depiction of silicon nanowire growth by the SLS mechanism [141].....	69
Figure 4-6: TEM image of tin nanowires encapsulated in amorphous carbon nanotube [22].....	70
Figure 4-7: EDX spectroscopic mapping image of indium (red) at the.....	71

Figure 4-8: SEM image (taken at 20000x magnification) of ITO (a) before and after (b) 10 min,	74
Figure 4-9: Schematic illustration of the observed ITO film fragmentation at different hydrogen reduction times	74
Figure 4-10: XPS spectra of ITO (a) before reduction and under the hydrogen reduction at 450°C of (b) 10 min, (c) 30 min and (d) 60 min	74
Figure 4-11: SEM image (taken at 20000x magnification) of 5 nm Fe (a) before and after (b) 10 min & (c) 60 min of hydrogen reduction at 450°C	76
Figure 4-12: Schematic illustration of the proposed Fe/ITO film fragmentation at different hydrogen reduction times	76
Figure 4-13: SEM images (taken at 20000x magnification) of nanostructures grown at 450°C for 10 min under the different system pressures of (a) 100 Torr (b) 200 Torr (c) 300 Torr & (d) 400 Torr	77
Figure 4-14: Illustration of interface layer and nanostructured layer within the carbon nanostructures	77
Figure 4-15: Interface layer thickness at different pressure	78
Figure 4-16: XPS spectrum of C peak at 284.5eV of carbon nanostructures	79
Figure 4-17: SEM images (taken at 20000x magnification) of (a) carbon nanostructures grown at 200 Torr after H ₂ plasma etching at different times of (b) 10 min (c) 30 min (d) 120 min (e) 240 min & (f) 360 min	82
Figure 4-18: Amorphous carbon film thickness at different etching time	85
Figure 4-19: FESEM images (cross-section and top view) and EDX data (line scan) of nanostructures grown at 400°C of 100 Torr for 1 min (a-c), 5 min (d-f) and 10 min (g-i)	86
Figure 4-20: 3D graph distribution of relative atomic concentration of O, C, In and Fe growth at 400°C and 100 Torr of different growth time	87
Figure 4-21: FESEM images (cross-section and top view) and EDX data (line scan) of nanostructures grown at 400°C of 200 Torr for 1 min (a-c), 5 min (d-f) and 10 min (g-i)	89
Figure 4-22: 3D graph distribution of relative atomic concentration of O, C, In and Fe growth at 400°C and 200 Torr of different growth time	91

Figure 4-23: FESEM images (cross-section and top view) and EDX data (line scan) of nanostructures grown at 400°C of 300 Torr for 1 min (a-c), 5 min (d-f) and 10 min (g-i)	92
Figure 4-24: FESEM images (cross-section and top view) and EDX data (line scan) of nanostructures grown at 400°C of 400 Torr for 1 min (a-c), 5 min (d-f) and 10 min (g-i)	94
Figure 4-25: 3D graph distribution of relative atomic concentration of O, C, In and Fe growth at 400°C and 400 Torr of different growth time.....	94
Figure 4-26: FESEM images of (a) cross-section & (b) top-view of nanostructures grown at 450°C of 100 Torr for 1 min	95
Figure 4-27: FESEM images (cross-section and top view) and EDX data (line scan) of nanostructures grown at 450°C of 100 Torr for 5 min (a-c) and 10 min (d-f).....	96
Figure 4-28: Graph distribution of relative atomic concentration of O, C, In and Fe growth at 450°C and 100 Torr of different growth time.....	96
Figure 4-29: High resolution TEM images of carbon nanostructures grown at 450°C ..	97
Figure 4-30: TEM image showing the (a) lattice image of carbon nanostructure & Fast Fourier transform of the image (inset) and (b) plot profile of lattice image	98
Figure 4-31: Schematic illustration of the MWCNT nucleation and growth processes	100
Figure 4-32: FESEM images (cross-section and top view) and EDX data (line scan) of nanostructures grown at 450°C of 200 Torr for 1 min (a-c), 5 min (d-f) and 10 min (g-i)	102
Figure 4-33: High resolution TEM image of carbon nanostructure grown at 450°C ...	103
Figure 4-34: High resolution TEM image of particle encapsulated.....	104
Figure 4-35: FESEM images (cross-section and top view) and EDX data (line scan) of nanostructures grown at 450°C of 300 Torr for 1 min (a-c), 5 min (d-f) and 10 min (g-i)	105
Figure 4-36: 3D graph distribution of relative atomic concentration of O, C, In and Fe growth at 450°C and 300 Torr of different growth time.....	106
Figure 4-37: High resolution TEM images (a & b) and the corresponding fast Fourier transform (c).....	107
Figure 4-38: XPS spectrum of carbon nanostructure grown at 450°C of 300 Torr for 10 min	108

Figure 4-39: FESEM images (cross-section and top view) and EDX data (line scan) .	110
Figure 4-40: (a) A high resolution TEM image of carbon nanostructure grown at 450°C of 400 Torr for 10 min (inset: SEM image). (b) An image magnified from the yellow box in (a). (c) An image magnified from the yellow box in (b) and its fast Fourier transform image (inset)	111
Figure 4-41: (a) SEM image (b-d) TEM images of indium oxide nanostructure encapsulated by carbon layer grown at 400 Torr and (e) Selected area diffraction pattern of image in (d).....	113
Figure 4-42: XPS spectrum of indium oxide nanostructure encapsulated by carbon layer	114
Figure 4-43: XPS spectrum of ITO substrate.....	114
Figure 4-44: Schematic illustration of the proposed growth mechanism of indium oxide nanostructures encapsulated by carbon layer at 400 Torr	117
Figure 4-45: Raman spectra of carbon nanostructures obtained at 450°C	119
Figure 4-46: Raman spectrum of indium oxide nanostructures	120
Figure 4-47: FESEM images (cross-section and top view) and EDX data (line scan) of nanostructures grown at 500°C of 100 Torr for 1 min (a-c), 5 min (d-f) and 10 min (g-i)	122
Figure 4-48: FESEM images (cross-section and top view) and EDX data (line scan) of nanostructures grown at 500°C of 200 Torr for 1 min (a-c), 5 min (d-f) and 10 min (g-i)	123
Figure 4-49: FESEM images of (a) cross-section & (b) top-view of nanostructures grown at 500°C of 300 Torr for 1 min	124
Figure 4-50: FESEM images (cross-section and top view) and EDX data (line scan) of nanostructures grown at 500°C of 300 Torr for 5 min (a-c) and 10 min (d-f).....	124
Figure 4-51: FESEM images (cross-section and top view) and EDX data (line scan) of nanostructures grown at 500°C of 400 Torr for 1 min (a-c), 5 min (d-f) and 10 min (g-i)	126
Figure 5-1: Images of thin polymeric films on silicon trenches deposited by (a) spin coating a polymer solution and (b) CVD[59]	131
Figure 5-2: SEM images of poly(3,4-ethylenedioxythiophene) coated poly(acrylonitrile) fiber mats prepared by (a) spin casting and (b) CVD[180].....	131

Figure 5-3: Preparation scheme of 1,9-dichloro [2,2] paracyclophane [72]	133
Figure 5-4: Preparation of PPV via the vapor deposition polymerisation of 1,9-dichloro [2,2] paracyclophane [72]	134
Figure 5-5: Absorbance of PPV precursor (solid line) and PPV(dashed line), and photoluminescence of PPV (dotted line) [71].....	135
Figure 5-6: IR spectra (transmittance vs wavenumber) of (a) precursor and (b) PPV [72]	136
Figure 5-7: Absorption spectra of the unirradiated and the irradiated PPV films [100]	138
Figure 5-8: Photodegradation mechanism of PPV in air [100].....	139
Figure 5-9: Absorption and photoluminescence spectra of oligomers with a) 1, b) 2, c) 3, d) 4,	139
Figure 5-10: PPV precursor synthesis via CVD polymerisation	140
Figure 5-11: PPV synthesis via thermal de-hydrohalogenation.....	141
Figure 5-12: Calibrated deposition zone positions	142
Figure 5-13: UV-Vis absorption spectra of pristine quartz and PPV precursor	143
Figure 5-14: UV-Vis absorption spectra of PPV precursor located at spots 1 to 7	143
Figure 5-15: Time versus surface temperature of spot 1 and 2 at 700°C pyrolysis temperature.....	145
Figure 5-16: Time versus surface temperature of spot 3 to 7 at 700°C pyrolysis temperature.....	145
Figure 5-17: Fourier Transform IR spectrum of chlorine PPV precursor.....	146
Figure 5-18: Fourier Transform IR spectrum of bromine PPV precursor	147
Figure 5-19: UV-Vis absorption spectra of chlorine precursor and PPV	150
Figure 5-20: Fourier Transform IR spectra of chlorine precursor and PPV	151
Figure 5-21: Photoluminescence spectrum of chlorinated PPV (excitation at 350 nm)	151
Figure 5-22: PL spectrum of PPV with six uninterrupted phenylenevinylene units [102]	152

Figure 5-23: Chemical structure of PPV containing six phenylenevinylene units	153
Figure 5-24: UV-Vis absorption spectra of bromine precursor and PPV	154
Figure 5-25: Fourier Transform IR spectra of bromine precursor and PPV	154
Figure 5-26: UV-Vis absorption spectra of chlorinated PPV and brominated PPV	157
Figure 5-27: Fourier Transform IR spectra of chlorinated PPV and brominated PPV	157
Figure 5-28: UV-Vis spectra of PPV converted at different time.....	158
Figure 5-29: Fourier Transform IR spectra of chlorine precursor and 2 hours heated to PPV	160
Figure 5-30: UV-Vis absorption spectrum of a quartz substrate	162
Figure 5-31: UV-Vis absorption spectra of Cl-PPV after being exposed to air for up to 6 months	163
Figure 5-32: UV-Vis absorption spectra of Br-PPV after being exposed to air for up to 6 months	164
Figure 5-33: The current voltage characteristics of an ITO/PPV/PCBM/Al in the dark and under illumination of AM-1.5	166
Figure 5-34: The current voltage characteristics of an ITO/PPV/C ₆₀ /Al in the dark and under illumination of AM-1.5	166
Figure 5-35: The current voltage characteristics of (a) ITO/PEDOT/PPV/PCBM/LiFAl and (b) ITO/PEDOT/PPV/C ₆₀ /LiFAl in the dark and under illumination of AM-1.5 ..	167
Figure 5-36: The current voltage characteristics of (a) ITO/PEDOT/PPV/PCBM/CaAl and (b) ITO/PEDOT/PPV/C ₆₀ /CaAl in the dark and under illumination of AM-1.5....	169
Figure 5-37: External Quantum Efficiency (EQE) spectrum of PPV/C ₆₀	169
Figure 5-38: The efficiencies of cells produced by different device architectures	170
Figure 6-1: SEM images of PPV (a) nanotubes prepared in alumina filter membrane & (b) nanorods prepared in polycarbonate filter membrane [70]	172
Figure 6-2: SEM images of PTV nanotubes prepared by alumina filter membrane [11]	173
Figure 6-3: Schematic diagram of template positioned at (a) horizontal (0°) (b) 30° (c) 45° (d) 60° & (e) vertical (90°) respect to the planar surface	174

Figure 6-4: Photoluminescence spectra (excitation at 350 nm) of PPV deposited on alumina template of different angles.....	176
Figure 6-5: Photoluminescence intensity ratio of peak 1 to peak 2 of different deposition angles.....	176
Figure 6-6: SEM image of PPV deposited on horizontal alumina template of (a) lower magnification & (b) higher magnification	178
Figure 6-7: SEM image (Top view) of PPV deposited on alumina porous template taken from the bottom surface	178
Figure 6-8: Cross-section SEM image of PPV deposited on horizontal alumina template	179
Figure 6-9: Photoluminescence spectra (excitation at 350 nm) of PPV thin film deposited on quartz and PPV nanostructure deposited on alumina template at 0°	180
Figure 6-10(a-d): SEM image of PPV deposited on horizontal alumina template after being isolated from template.....	182
Figure 6-11: Schematic diagram of proposed nanostructure of fibrous-like PPV	182
Figure 6-12: SEM image of PPV deposited at 30° of alumina template angle of (a) lower magnification & (b) higher magnification	183
Figure 6-13: Cross-section SEM image of PPV deposited at 30° of alumina template angle	183
Figure 6-14: SEM image of PPV (a-c) deposited at 30° of alumina template angle after being isolated from template.....	184
Figure 6-15: Schematic illustration of the proposed formation of PPV nanotubes synthesis at deposition template angle of 30°Angle at 45°	185
Figure 6-16: SEM image of PPV deposited at 45° of alumina template angle of (a) lower magnification & (b) higher magnification	185
Figure 6-17: Cross-section SEM image of PPV deposited at 45° of alumina template angle	185
Figure 6-18: Photoluminescence spectra (excitation at 350nm) of PPV thin film deposited on quartz and PPV deposited on alumina template at 45°	186
Figure 6-19: SEM image of PPV (a-c) deposited at 45° of alumina template angle after being isolated from template.....	187

Figure 6-20: SEM image of PPV deposited at 60° of alumina template angle of (a) lower magnification & (b) higher magnification	188
Figure 6-21: Cross-section SEM image of PPV deposited at 60° of alumina template angle	188
Figure 6-22: SEM image of PPV (a-c) deposited at 60° of alumina template angle after being isolated from template	189
Figure 6-23: Photoluminescence spectra (excitation at 350 nm) of PPV thin film deposited on quartz and PPV deposited on alumina template at 60°	189
Figure 6-24: SEM image of PPV deposited on vertical alumina	191
Figure 6-25: Cross-section SEM images of PPV deposited on vertical alumina template	191
Figure 6-26: SEM image of PPV (a-d) deposited at 90° of alumina template angle after being isolated from template	193
Figure 6-27: Schematic illustration of the proposed formation of PPV nanotubes synthesis at deposition template angle of 90°	193
Figure 6-28: Photoluminescence spectra (excitation at 350 nm) of PPV thin film deposited on quartz and PPV deposited at different alumina template angles	194

LIST OF TABLES

Table 2-1: Recipe used in synthesizing the carbon nanostructures.....	22
Table 3-1: Description on the terminology of surface roughness	45
Table 5-1: Peaks and corresponding assignments of bromine PPV precursor in infrared	148

Table of Contents

1	INTRODUCTION AND MOTIVATION.....	1
1.1	CHALLENGES AND ISSUES.....	1
1.2	RESEARCH OBJECTIVES.....	2
1.3	ORGANISATION OF THESIS	3
1.4	PHOTOVOLTAIC TECHNOLOGY	4
1.5	ORGANIC PHOTOVOLTAICS (OPVs)	5
1.6	THE IMPORTANCE OF NANOSTRUCTURE IN OPVs	9
1.7	CARBON NANOTUBES (CNTs).....	12
1.7.1	Fabrication Methods and Mechanisms	12
1.7.2	Use in OPVs.....	13
1.8	POLYMER NANOSTRUCTURES.....	14
1.8.1	Fabrication.....	14
1.8.2	Use in OPVs.....	16
2	EXPERIMENTAL.....	17
2.1	FABRICATION OF CARBON NANOTUBES	17
2.1.1	Catalyst Layer Deposition.....	17
2.1.2	Thermal Chemical Vapour Deposition	20
2.2	FABRICATION OF POLYMER NANOTUBES.....	22
2.2.1	Alumina Porous Template.....	22
2.2.2	Chemical Vapour Deposition Polymerisation.....	23
2.3	CHARACTERISATION.....	25
2.3.1	Scanning Electron Microscopy	25
2.3.2	Transmission Electron Microscopy	26
2.3.3	Conductivity.....	27
2.3.4	Optical Spectroscopy	30
2.3.5	Photoluminescence Spectroscopy	32
2.3.6	X-ray Photoelectron Spectroscopy.....	33
2.4	OPV DEVICE FABRICATION	33
2.5	OPV DEVICE CHARACTERISATION	34
3	EFFECT OF THERMAL TREATMENT ON INDIUM TIN OXIDE SUBSTRATES.....	36

3.1	INTRODUCTION.....	36
3.1.1	Properties of ITO.....	36
3.1.2	Thermal Processing of Organic Electronic Films and Structures	38
3.1.3	Thermal Processing of ITO	39
3.2	EXPERIMENTAL SETUP	40
3.3	RESULTS AND DISCUSSION	41
3.3.1	Conductivity.....	41
3.3.2	Surface Morphology.....	42
3.3.3	Crystallinity.....	46
3.3.4	Optical Properties.....	51
3.3.5	Chemical Composition.....	52
3.3.6	Bulk Measurements.....	52
3.3.7	Surface Measurements	54
3.3.7.1	Combining the Bulk and Surface Compositional Measurements	61
3.4	CONCLUSION	62
4	CHEMICAL VAPOUR DEPOSITION OF CARBON NANOSTRUCTURES ON INDIUM TIN OXIDE	64
4.1	INTRODUCTION.....	64
4.1.1	Overview	64
4.1.2	Carbon nanostructures on ITO.....	65
4.1.3	Semiconducting nanostructures	67
4.2	EXPERIMENTAL SETUP	71
4.3	RESULTS AND DISCUSSION	72
4.3.1	Effect of hydrogen reduction on ITO.....	72
4.3.2	Effect of hydrogen reduction on iron-coated ITO.....	75
4.3.3	The growth of carbon nanostructures.....	76
4.3.4	Characterisation of the interface layer	77
4.3.4.1	Formation of an amorphous carbon layer	77
4.3.4.2	Effect of H ₂ plasma on the interface layer	80
4.3.5	Characterisation of nanostructured layer	85
4.3.5.1	Nanostructure growth at 400°C (100 – 400 Torr).....	85
4.3.5.1.1	Nanostructure growth at 100 Torr	85

4.3.5.1.2	Nanostructure growth at 200 Torr	89
4.3.5.1.3	Nanostructure growth at 300 Torr	91
4.3.5.1.4	Nanostructure growth at 400 Torr	93
4.3.5.2	Nanostructure growth at 450°C (100 – 400 Torr).....	95
4.3.5.2.1	Nanostructure growth at 100 Torr	95
4.3.5.2.2	Nanostructure growth at 200 Torr	101
4.3.5.2.3	Nanostructure growth at 300 Torr	104
4.3.5.2.4	Nanostructure growth at 400 Torr	109
4.3.5.3	Raman spectra at 450°C.....	118
4.3.5.4	Nanostructure growth at 500°C (100 – 400 Torr)	121
4.3.5.4.1	Nanostructure growth at 100 Torr	121
4.3.5.4.2	Nanostructure growth at 200 Torr	122
4.3.5.4.3	Nanostructure growth at 300 Torr	124
4.3.5.4.4	Nanostructure growth at 400 Torr	125
4.3.5.5	Effect of pressure on nanostructure growth.....	126
4.4	CONCLUSIONS	129
5	CHEMICAL VAPOUR DEPOSITION OF PPV AND PPV OPV.....	130
5.1	INTRODUCTION.....	130
5.1.1	Motivation for Polymer Synthesis by CVD.....	130
5.1.2	CVD Approaches to PPV Thin Film Formation.....	132
5.1.3	OPV Devices Made from PPV Films.....	136
5.1.4	Degradation of PPV films	137
5.2	EXPERIMENTAL SETUP	140
5.3	RESULTS AND DISCUSSION	142
5.3.1	PPV Precursor Absorbance.....	142
5.3.2	PPV Absorbance	149
5.3.3	Influence of Monomer Selection on Optical Properties.....	155
5.3.4	PPV Absorbance with Thermal Conversion Time.....	158
5.3.5	Degradation of Processed PPV Film.....	162
5.3.6	Integration of CVD PPV into OPV devices.....	165
5.4	CONCLUSIONS	171

6	CHEMICAL VAPOUR DEPOSITION OF THE PPV NANOSTRUCTURES	172
6.1	INTRODUCTION.....	172
6.2	EXPERIMENTAL DETAILS.....	174
6.3	RESULTS AND DISCUSSION	175
6.3.1	Photoluminescence.....	175
6.3.2	Surface morphology of PPV as a function of deposition angle	177
6.3.2.1	Horizontal (0°).....	177
6.3.2.2	Angle at 30°	182
6.3.2.3	Angle of 45°	185
6.3.2.4	Angle at 60°	187
6.3.2.5	Vertical angle (90°).....	189
6.3.3	Effect of nanostructures on optical emission	194
6.4	CONCLUSIONS	196
7	SUMMARY AND FURTHER WORK.....	197
7.1	SUMMARY	197
7.2	FURTHER WORK.....	199

ABSTRACT

The growth of carbon and poly-*p*-phenylene vinylene (PPV) nanostructures via chemical vapour deposition (CVD) has been studied. Working temperatures of 400, 450 and 500°C and 270°C have been applied for the growth of carbon and PPV, respectively. In this work, indium tin oxide (ITO) modified by the CVD growth of carbon nanostructures has been used as an electrode in the fabrication of organic photovoltaic (OPV) devices. Therefore, the effect of thermal treatment on ITO conductivity, physical properties and chemical composition is studied.

The growth of carbon nanostructures on ITO is studied under a variety of CVD conditions, in particular, the effect of varying growth time, temperature and system pressure have been investigated. Pressures between 100 and 400 Torr were used during the growth of the carbon nanostructures. Two layers, comprising a dense amorphous interface layer and the nanostructured layer have been observed at all pressures in this range. However, an abrupt change at the interface and nanostructured layer was seen at 400 Torr. The thickness of the interface layer, which is composed of amorphous carbon, is directly proportional to the system pressure. H₂ plasma treatment has been applied to reduce the amorphous carbon layer thickness. Multiwalled carbon nanotubes (MWCNTs) have been successfully synthesised at pressures between 100 and 300 Torr. The diffusion of indium from the substrate into the nanostructured layer is observed to occur at 450°C and 400 Torr which initiates the growth of indium oxide nanowires encapsulated by a carbon layer.

Presented here for the first time is an OPV whose active layer has been fabricated via the CVD technique. A PPV nanofilm is synthesised by CVD onto ITO without the use of solvent or solution. Two different monomers, α,α' -dichloro-*p*-xylene and α,α' -dibromo-*p*-xylene, are used and the properties of the chloro-derived PPV and bromo-derived PPV is compared for the future fabrication. The chloro-derived PPV has an advantage over bromo-derived PPV in terms of the energy band gap and conjugation length. As a consequence, an OPV is wholly fabricated by the starting monomer of α,α' -dichloro-*p*-xylene.

To realise PPV nanostructures that could potentially be integrated into OPV devices, CVD based polymerisation of PPV in a porous alumina template has been investigated.

Five different angles of the template with respect to the gas flow were tested. A series of interesting PPV nanostructures such as fibre-like and nanotubes have been effectively synthesised via this method.

1 INTRODUCTION AND MOTIVATION

Nanostructured materials have attracted enormous interest due to the interesting physical and chemical properties arising from their nanoscale dimensions [1-9]. A nanostructured material is classified as a material constructed from a layer or cluster of atoms with size of the order of nanometres [10-12]. Nanostructured materials can be defined with length scales between 0.1 and 100 nm in one to three dimensions. For example, nanotextured surfaces have one dimension on the nanoscale with the thickness of the surface object being between 0.1 and 100 nm. Two dimensional nanotubes have a diameter between 0.1 and 100 nm, but with much greater lengths. Spherical nanoparticles have three dimensions on the nanoscale with particle size is between 0.1 and 100 nm in each dimension.

1.1 CHALLENGES AND ISSUES

The overall goal of this work was to assess the potential of the chemical vapour deposition (CVD) technique for the fabrication and characterisation of various novel nanostructured materials used for organic photovoltaic device applications. A small number of significant achievements in the field of novel nanostructured materials have been reported as part of on-going research by many groups across the world [13-22]. The fabrication of novel nanostructured materials produced via solely by CVD has revealed a number of technical limitations and fundamental challenges associated with the science and technology of nanostructures. In particular, some of the major challenges include:

- (1) Controllable growth of nanostructured materials with low working/substrate temperature.
- (2) General understanding of the growth mechanism of novel nanostructured materials.
- (3) Understanding the origin of the exceptional functional properties of novel nanostructured materials and utilising these in device application.

- (4) On the basis of points (1)–(3) the development of new design strategies and methodologies for the fabrication of novel nanostructured materials.

1.2 RESEARCH OBJECTIVES

The research objectives in this work are to demonstrate the synthesis of novel nanostructure growth, and to integrate these new materials into prototype devices.

The technical objectives included:

- (1) Investigation of thermal effect on indium tin oxide (ITO) substrate.

Indium tin oxide (ITO) substrate is selected in this work due to its interesting physical properties and applications as a transparent electrode. Since the CVD process involves thermal treatment, it is worthwhile to study the effects of annealing on ITO. The changes in properties such as electrical conductivity, surface morphology, optical properties and surface chemistry of ITO heated at different temperatures are reported. In addition, the study on the oxidation and diffusion of indium into other thin film layers due to thermal treatment is considered.

- (2) Understanding the growth mechanism of CVD grown carbon and metal oxide nanostructures on ITO substrate.

This work involves the growth of a number of different nanostructured materials (carbon and metal oxide) on ITO substrates. Nanostructured materials grown on ITO substrate will be characterised by various techniques (SEM, EDX, TEM and SAED) to (i) evaluate the influence of growth time, growth temperature and system pressure on morphology and (ii) to elucidate the influence of the ITO substrate on the composition, structure and morphology of nanostructured materials (Publication 1). The strategy utilised in this thesis is to understand the growth conditions of CVD process which allow understanding of the correlation between optimised growth conditions and nanostructures growth.

- (3) Controllable synthesis of CVD grown polymer nanostructures and the fabrication of prototype devices.

A CVD grown polymer, poly(*p*-phenylene vinylene) (PPV) has been chosen due to its favourable electrical, optical, electroluminescent and photovoltaic properties. For the synthesis of PPV, a CVD technique based on the pyrolysis of a monomer (α,α' -dichloro-*p*-xylene and α,α' -dibromo-*p*-xylene) is employed under controlled pyrolysis temperature, time and pressure conditions. This process is expected to have unique advantages, such as the synthesis of PPV nanofilms using a shorter thermal conversion time and thus lower degradation of PPV nanofilms upon atmospheric exposure. A series of new generation prototype OPV devices is fabricated from the bottom-up by implementing the CVD of PPV (Publication 2).

- (4) Elucidating the implementation of new design methodologies in producing novel polymer nanostructures.

To obtain a deeper insight into chemical precursor infiltration, a porous alumina template is held at a range of angles within the deposition zone of CVD reactor. The transformation of chemical precursor into PPV nanostructures is studied in this work, and the nanostructures arising from the changing angle of deposition are investigated (Publication 3).

1.3 ORGANISATION OF THESIS

This thesis is organised in the following manner. Chapter 1 provides the objectives, motivation of research focus and an overview of the current activities. Chapter 2 explains the techniques and equipment relevant to the overall work. These techniques and equipment are essential to the readers' full understanding of the method used to obtain experiment results in the remaining chapters. Chapter 3 presents the systematic studies of thermal treatment on ITO substrates. Chapter 4 contains the details of process parameters and results relevant to the fabrication of novel nanostructured materials (carbon and metal oxide) grown on ITO substrates and discuss the factors responsible for the growth behaviours. Chapter 5 presents the controllable synthesis of polymer and the integration into prototype devices. The fabrication of novel polymer nanostructures via the implementation of new design methodologies are provided in Chapter 6. Finally, Chapter 7 is the summary of the thesis work.

1.4 PHOTOVOLTAIC TECHNOLOGY

Current trends in energy supply and usage are obviously unsustainable in terms of the economy, environment and social opinion. Air pollution and global warming are two of the greatest threats to human and animal health caused by the lack of a viable renewable energy alternative. Energy security uncertainty and the rising prices of conventional energy sources are also major concerns to economic and political stability. By 2050, energy-related emissions of CO₂ will more than double if rapid energy resource management is not implemented [23]. With regard to this matter, the *International Energy Agency* (IEA) has developed a series of roadmaps for some of the most crucial technologies. These roadmaps offer a solid analytical footing that facilitates the international community to move forward on technologies related to renewable energy.

Solar energy is the most abundant energy resource on earth and considered by many to be the alternative energy source of choice. In principle, solar energy is an entirely clean and inexhaustible source of energy. The amount of energy consumed by all human activities in a year is equal to one hour of hitting the earth's surface [23]. The vast amount of solar energy available on earth can be converted directly to electricity via photovoltaic cells.

Photovoltaic (PV) technology has great potential as a renewable source for the conversion of sunlight to electricity. PV power is an exceptionally promising area for technological growth in future. Since 2000, global PV capacity has been increasing at an average annual growth rate of more than 40% and there is the prospect of long-term growth over the next decades [23]. The recent IEA PV Roadmap envisages that by 2050, approximately 11% of global electricity production will be produced by PV power which is equivalent to 4500 TWh per year. Besides contributing to substantial greenhouse gas emission reductions, this level of PV will provide significant benefits in terms of the security of energy supply and socio-economic development.

Wafer based crystalline silicon (c-Si) and thin films are two broad categories used as commercial PV modules. Crystalline silicon and thin film PV modules account for 85 - 90% and 10 - 15% of the global market, respectively. However, as shown in Figure 1-1, there are high manufacturing costs for both wafer based c-Si and thin film PV modules.

On the other hand, new solar cell devices fabricated from organic materials have shown the potential to be manufactured inexpensively.

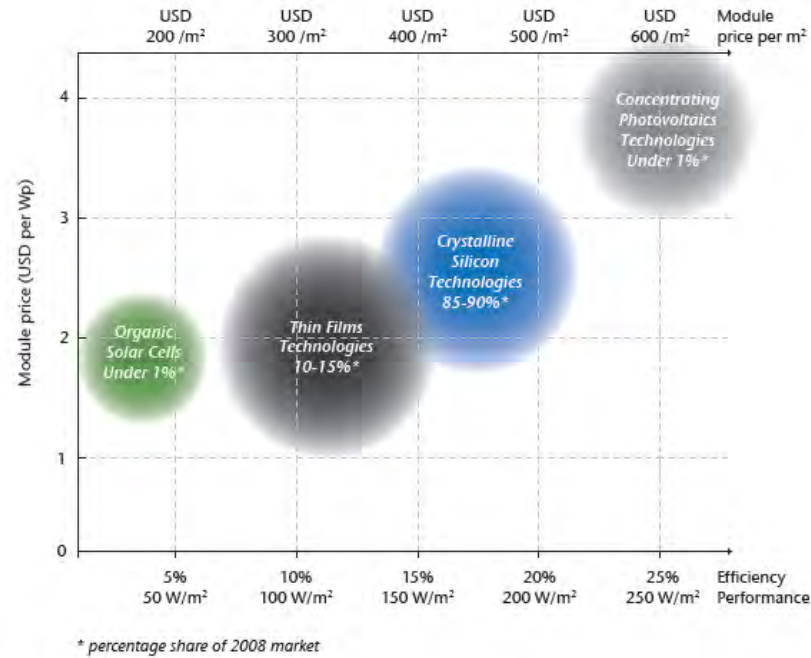


Figure 1-1: Current performance and price of different PV module technologies [23]

The fabrication of PV devices using polymeric and organic materials has received much attention in recent years. The term “organic materials” refers to chemical compounds that contain carbon, which may also contain elements such as hydrogen, nitrogen, oxygen and the halogens. PV devices based on silicon or other inorganic materials (such as CdTe) are either costly to fabricate or have limited abundance when compared with organic materials. However, despite continued efforts worldwide, organic photovoltaic (OPV) devices still lag behind their inorganic counterparts in the areas of solar energy conversion efficiency and stability.

1.5 ORGANIC PHOTOVOLTAICS (OPVs)

The PV effect was first observed by the French physicist Edmond Becquerel in 1839, but the first crystalline silicon photovoltaic device was not built until 1954 at Bell Laboratories [24]. A PV device or solar cell, converts absorbed photons directly into electrical charges that are subsequently extracted and used to energize an external

circuit. Inorganic semiconductor materials, such as crystalline Si have been used for fabricating standard conventional solar cells since the late 1950s [24]. Light absorption in a conventional solar cell creates electron-hole pairs that are immediately separated and accelerated to the appropriate electrode by the strong internal electric field that exists in these devices.

OPV cells comprise either small organic molecules or conducting organic polymer. Both the small organic molecules and conducting organic polymer utilised in PV have the general feature of a conjugated bonding system. A conjugated system is a system where the carbon atom backbone is covalently bound with alternating single and double bonds. Hydrocarbon electron p_z orbitals delocalize and form a delocalized bonding π orbital which is the highest occupied molecular orbital (HOMO) and a π^* antibonding orbital, the so-called lowest unoccupied molecular orbital (LUMO). The band gap of organic materials can be identified as the separation between HOMO and LUMO.

In 1959, the first OPV cells were developed based on single organic materials (or homojunctions), but unfortunately they exhibited very low power conversion efficiency due to the comparatively large resistance of the unexcited layer [25]. A single layer of small organic molecules is sandwiched between two electrodes, normally a high work function indium tin oxide (ITO) anode and a low work function Al or Ca metal cathode. In these single-layer cells, the built-in potential is created by the electrode work function differences or a Schottky-type potential barrier at metal/organic contacts. A large series resistance which correlates with the insulating behaviour of the organic layer is observed, and a poor fill factor (FF) is recorded from such a structure. Poor fill factors represents a low ratio of maximum obtainable power to the product of the open-circuit voltage and short-circuit current. The main drawback in the single layer OPV is insufficient electric field to dissociate the photogenerated excitons. The low dielectric function of these materials means that those electrons and holes tend to recombine with each other rather than transport to the appropriate electrode. To overcome this problem, the bilayer OPV, was introduced.

Bilayer-based OPVs were first reported in 1986 [26] when a power conversion efficiency of 1% was achieved by sandwiching an electron donor material layer and an electron acceptor material layer together in one cell. The first bilayer OPV cell was

fabricated from copper phthalocyanine (CuPc) and a perylene tetracarboxylic derivative (Pv). In this OPV structure, which is based on small organic molecules, the PV properties rely on the interface between the two organic materials rather than the interface between electrode and organic materials. Photogeneration of charges predominantly occurs in the interface region and this is thus crucial to PV performance. Despite the relatively low power conversion efficiency demonstrated by the bilayer OPV in 1986, continuous studies have been conducted to improve this kind of structure and have resulted in improved OPV efficiency of 3.5% [27]. The enhancement in bilayer OPV efficiency is a good starting point for the achievement of low cost solar cells.

Unlike inorganic materials, where incident light on the device produces free electrons and holes, organic materials irradiated with optical photons produce a mobile excited state consisting of a bound electron-hole pair known as an exciton [28]. Strong Coulombic forces, coupled with the low dielectric constant of polymer materials, tend to localize the exciton on the molecules [29]. As such, the exciton that is produced has to be dissociated in order to deliver separate charges (negative and positive) to the appropriate electrode with the possibility that this excited state may recombine before reaching its destination, resulting in reduced charge generation. This recombination is illustrated by the fact that excitons typically possess short diffusion lengths of the order of 14 nm [30]. Since, the thickness of the polymer layer needs to be at least 100 nm for efficient light absorption; it is impractical to achieve the same range as diffusion lengths. In order to deal with this problem, the bulk heterojunction (BHJ) OPV was proposed.

In the mid-1990s, the concept of BHJ organic solar cells was introduced - blending the donor and acceptor materials together. This structure forms a nanoscale interpenetrating network of donor-acceptor junctions throughout the device and a dramatic decrease in the number of excitons lost through recombination is achieved [31]. The mixture of donor and acceptor materials (eg: polymer-fullerene blend) is the active layer in BHJ solar cells. In the BHJ structure, the interface is spatially dispersed over the whole volume of the active layer. Absorption of light by the active layer leads to exciton generation. Electrons will be transferred from the conjugated polymer (donor) to the

highly efficient electron acceptor material fullerene. Electrons and holes are then transported to the appropriate electrode, with the electron travelling along the fullerene network while the hole moves within the conjugated polymer network.

The first fully organic BHJ device based on a mixture of soluble poly (*p*-phenylene vinylene) (PPV) derivative with a fullerene acceptor [32] was manufactured in 1995 by Yu and Heeger, and gave an efficiency of around 1%. Since then, the power conversion efficiency of BHJ-based cells has increased systematically. In 2001, devices consisting of a conjugated polymer poly (2-methoxy-5-(3',7'-dimethyloctyloxy)-*p*-phenylene vinylene) (MDMO-PPV) and [6,6] – phenyl (61-butyric acid methyl ester (PCBM) that mixed in a ratio of 1:4 wt% resulted in devices with 2.5% efficiency [33]. In 2005, efficiencies of more than 3% [34, 35] were recorded for polymer:fullerene BHJ solar cells based on polythiophene derivatives with optimised nanoscale morphology of the film. Moreover, BHJ solar cells using poly (3-hexylthiophene) (P3HT) and PCBM as electron donor and electron acceptor, respectively, record 5% power conversion efficiency [6]. Most recently, new polymers from the thieno [3,4-*b*] thiophenebenzodithiophene (PTB) family of PTB7 has exhibited power conversion efficiency up to 7.4% when blended with PC₇₁BM [36]. However, many other semi-conducting materials have been incorporated into OPV devices.

The performance of PV cells is generally rated in terms of their power conversion efficiency (PCE), external quantum efficiency (EQE), short circuit current (I_{sc}), open circuit voltage (V_{oc}) and fill factor (FF). These characteristics depend on a number of factors including: the relative position of HOMO/LUMO levels of the constituent materials, the solubility of the component materials, the solvent system, and the morphology of the active film. An optical band gap energy of around 2eV has been recorded for many of the poly (3-alkylthiophenes) P3ATs such as poly (3-hexylthiophene) P3HT, poly (3-octylthiophene) P3OT and poly (3-dodecylthiophene) P3DDT, which are commonly used as electron donors in polymer solar cells [37]. This relatively large band gap means that the absorption of these devices is poor in the red part of the solar spectrum and hence much work is currently underway to develop lower band gap materials [38]. Recently certified device efficiencies of 6.1% have been reported for lower band gap polycarbazole materials blended with PC₇₀BM [39].

The type of solvent used for polymer dissolution has an implication on OPV power conversion efficiency. BHJ organic solar cells based on P3HT processed from chlorobenzene solution have recorded a power conversion efficiency of 3.6% [40]. In order to investigate the role of solvent used in OPV fabrication, Kim et al 2005 [35] used two different solvents, chlorobenzene and 1,2-dichlorobenzene, and different power conversion efficiencies were recorded. Devices fabricated with the blend films (P3HT:PCBM = 1:1) dissolved in chlorobenzene and subjected to annealing treatment at 140°C for 15 min gave the best power conversion efficiency.

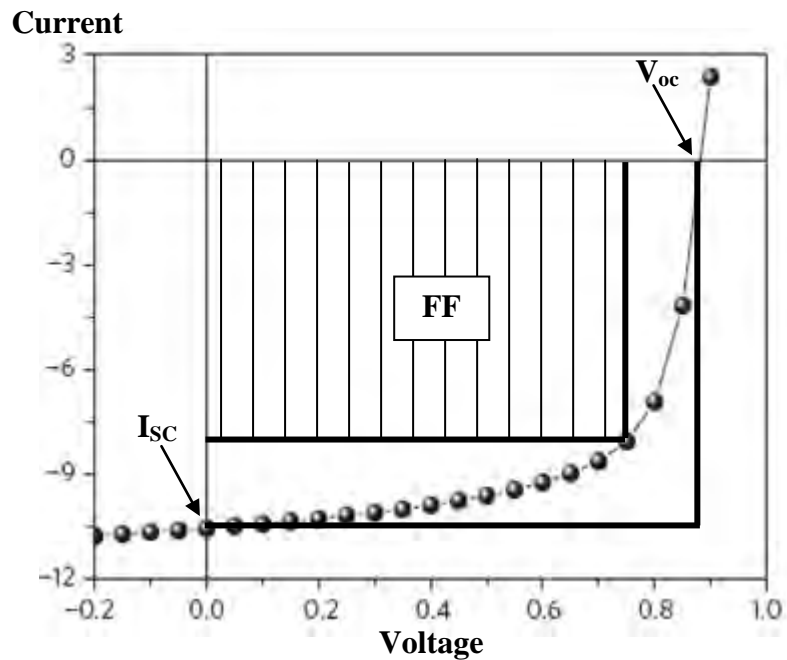


Figure 1-2: The graph of current-voltage curve with the illustration of FF, I_{sc} and V_{oc}

1.6 THE IMPORTANCE OF NANOSTRUCTURE IN OPVs

Despite the improvement of OPV cell efficiencies to more than 7% [39] (and in June 2011 a 10.1% device has been reported by Mitsubishi Chemical Corporation), a number of limitations to these devices remain. The main limitation of the OPV efficiency is the charge separation process at the donor and acceptor interfaces [41]. Inefficient separation of the charge carriers leads to problems with charge transport and mobility. Generally, the current state-of-art BHJ OPV devices are based on a mixture of donor and acceptor materials that produce an unstructured, phase segregated morphology in

the polymer blend. Existing fabrication methodologies such as spin coating, screen printing or spray coating are problematic since the phase segregation of the polymer mixture cannot be well controlled. In addition, as a result of low charge carrier mobilities, recombination is enhanced, resulting in charge losses. The performance of nanostructured OPV devices has been studied via a Monte Carlo model for charge carrier dissociation and recombination which considers all electrostatic interactions, energetic disorder and polaronic effects [42]. This model predicts that an interdigitated OPV nanostructure could achieve double the carrier collection efficiency of blend films.

The charge carrier transport properties of nanostructured OPV devices have also been investigated using a dynamical Monte Carlo model [43]. Six different heterojunction (HJ) morphologies were studied via this model and their structural characteristics as well as efficiency improvement and limiting factors were compared. The continuous layers of planar HJ with a flat interface have an advantage in charge collection efficiency. However, the exciton diffusion efficiency is limited by their short diffusion length which results in lower charge mobility and power conversion efficiency. The simple structure of mixed HJ, with and without annealing treatment shows an improvement in terms of the exciton dissociation efficiency and the charge collection efficiency. However, other factors limit this type of OPV structure, with the lack of continuous conductive pathways and trapped charge carriers both limiting carrier mobility. The proposed ‘chessboard’ structure of alternate donor and acceptor pillars sandwiched between donor and acceptor layers shows the ideal structure for high charge collection and exciton dissociation efficiency [43]. In principle, by using pillars of smaller diameter than the exciton diffusion length, optimal external quantum efficiency can be achieved. One approach to producing OPV devices with this sort of architecture is to fabricate nanotubes or nanorods of donor and/or acceptor materials.

The introduction of nanotubes and nanorods into the OPV structure could solve the morphology problem by forming an ideal ordered interdigitated OPV structure. Chemical vapour deposition (CVD) is a promising approach since nanotubes and nanorods can be fabricated directly onto desired substrates by CVD at low temperature [2]. The next generation of nanostructured OPVs could thus be directly fabricated from the bottom-up via CVD. CVD is frequently used in the semiconductor industry for

producing high-purity and high performance materials, particularly thin films. Moreover, conductive polymer deposition onto a range of substrates can be done via CVD [44]. There are a number of types of CVD that differ in the means by which the chemical reactions are initiated; plasma-enhanced CVD, metal-organic CVD, vapour phase (spray pyrolysis) CVD, distributed electronic cyclotron resonance CVD, initiated CVD, atmospheric pressure CVD, hot-wire CVD, catalytic CVD, floating-catalyst CVD, oxidative CVD and water-assisted CVD [18, 45-61].

One of the most favourable CVD techniques is so-called thermal chemical vapour deposition (TCVD) a schematic of which is shown in Figure 1-3. This technique offers advantages in production and allows choice of hydrocarbon sources, suitable for the synthesis of high quality materials and control of microscopic structure [44]. In this process, thermal production of radicals or initiators is separated from the film growth zone, allowing unimpeded bond configurations based on the chemical interface between the decomposition species. The substrate is rapidly heated by a heating coil in order to reduce the occurrence of unwanted gas phase reactions that lead to particle formation. Moreover, control of the precursor temperature, vapour flux and substrate temperature can be used to alter the molecular structure and composition to achieve film properties required for specific application.

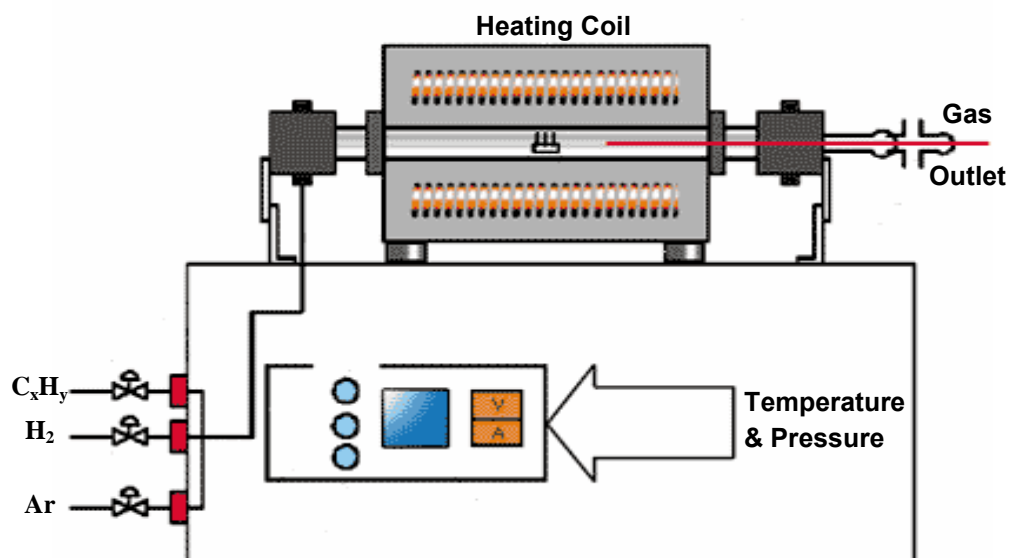


Figure 1-3: Thermal Chemical Vapor Deposition System [44]

1.7 CARBON NANOTUBES (CNTs)

1.7.1 Fabrication Methods and Mechanisms

Carbon nanotubes (CNTs) are unique nanostructures with astonishing electronic and mechanical properties, with applications in, for example, nanometre-sized electronics and composite materials. In essence a CNT is a hexagonal network of carbon atoms that has been rolled up to produce a seamless cylinder (Figure 1-4). The cylinder can be tens of microns long and each end is usually capped with half of a fullerene molecule. CNTs are 20-160 times stronger and 6 times lighter than steel [62]. In addition, they have a significant potential as transparent and conductive coatings due to their outstanding geometrical, mechanical and electrical properties [63].

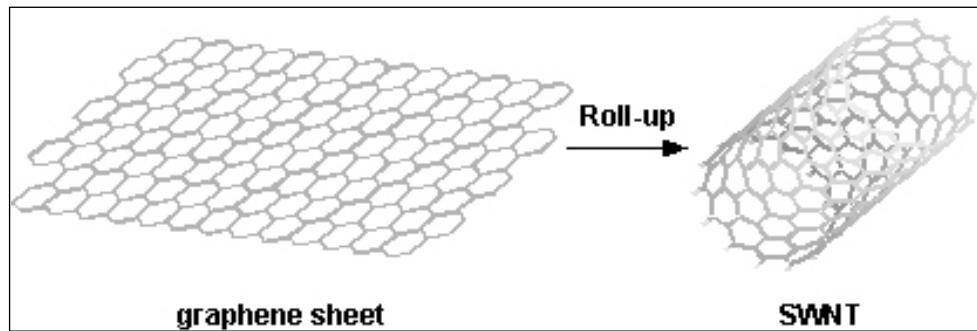


Figure 1-4: Formation of Carbon Nanotube [62]

Thermal CVD has been applied to the fabrication of CNTs and CNT based devices. Small hydrocarbon molecules such as CH_4 , C_2H_2 and C_2H_4 are used as the source of carbon atoms to produce CNTs at the relatively high temperature of 900°C . However, it is possible to grow CNTs and carbon nanorods (CNRs) at the relatively low temperature of 200°C [15] on a catalyst layer by forming hexagonal carbon clusters or one-dimensional carbon chain clusters from freshly produced C_2 . Direct growth of CNTs on substrates at low temperature acts as an important part in their application to the low cost production of solar cells. The characteristics of CNTs generated by the CVD method rely on parameters such as the temperature and pressure of operation, volume and concentration of hydrocarbon gas, size of metallic catalyst particles and the time of reaction.

1.7.2 Use in OPVs

The unique properties of CNTs are useful to organic solar cells, but current efficiencies of CNT based OPVs are at best 2.5% [64]. It has been suggested that the efficiency of CNT-based organic solar cells can be improved by eliminating carrier losses at the CNT/electrode interface [13].

According to Agrawal et al [65], charge transfer efficiency between CNTs and the cell electrode can be enhanced by directly growing them onto an indium tin oxide-layered (ITO) substrate. ITO films have a high crystallinity and excellent optical absorption properties [13]. Moreover, the high transparency ($\sim 80\%$) and low resistivity (1×10^{-4} ohm/cm) of ITO [66] has led it to be extensively used as an electrode in organic solar cells. ITO provides an ideal interface for carrier exchange because of its smooth surface [67]. As reported by Ulbricht et al [68], the photocurrent from an OPV can be doubled with the introduction of a CNT network to the planar ITO anode. This is due to the enhancement of hole collection and transportation to the ITO. A short circuit current (J_{sc}) of 11 mA/cm^2 , fill factor of 0.49 and an efficiency of 1.74% has been obtained with this hybrid anode, twice the short circuit photocurrent produced by OPVs with only ITO or CNT anodes.

Another reason for improved performance of solar cells fabricated from CNT has been proposed by Andre et al [1], who suggested that CNTs act as a nucleating agent that induces local order to the polymer chain. The addition of CNTs to the polymer allows charge separation of the photogenerated excitons and efficient electron transport to the electrode through the nanotubes. The work has demonstrated that the power conversion efficiency of solar cells can be increased by three orders of magnitude compared with the device without CNTs. This finding supports the work done by Valentini et al [14], who fabricated devices using an ITO/CNT/P3OT structure without an acceptor fullerene that showed photovoltaic behaviour. This behaviour could be attributed to the formation of internal polymer/CNT junctions, which act as an interface creating a continuous pathway for the electron to be efficiently transported to the cathode.

Another group using CNTs in solar cells is Wei et al [9]. This group claim that CNTs participate in both the photogeneration process and charge carrier transport. CNT films

with thicknesses of 35 nm or 50 nm show a transmission of >60% in the visible region of the spectrum. A CNT film with larger thicknesses of 200 nm has a transmission above 40% at a wavelength of 550 nm. Wei et al [9] also found that the sheet resistance of CNT film with thickness between 35 – 200 nm (0.5 - 5 Ω /sq) is lower than that of ITO (15 Ω /sq). The optimal thickness of CNT films was found to be 100 – 150 nm because thicker films are less transparent and prevent more incident light from reaching the active layer.

1.8 POLYMER NANOSTRUCTURES

1.8.1 Fabrication

Conducting polymer films can be deposited directly onto the CNT substrate with minimal bond defects if the process facilitates the polymerization reaction in accordance with the established thermodynamic considerations. Conducting polymer films formed by spin-casting or spin-coating techniques are not desirable due to low processing throughput, poor conformity, the inclusion of product impurities and the casting solvent, which is an environmental concern [69]. One example of a conducting polymer that has been effectively processed in thin film form is PPV. The degree of structural order and film morphology of the PPV can be controlled when prepared via the thermal conversion of a polymer precursor.

Thermal CVD has been widely used for surface modification and conducting polymer film formation. According to Kim et al [70], PPV nanofilms, nanotubes and nanorods can be easily prepared by performing CVD polymerization of α,α' -dichloro-*p*-xylene on the inner surface of pores of organic or inorganic membranes by using a reactor similar to that shown in Figure 1-5 [71]. Thin films of PPV prepared by the CVD method have been successfully obtained by Iwatsuki et al [72], Starring et al [73] and Shafer et al [74]. Low dangling bond densities were achieved by using thermal CVD in order to deposit fluorocarbon polymer films with a chemical resemblance to bulk polytetrafluoroethylene [75].

Researchers have been working with conducting polymer deposition via the CVD method for several years now. There are a number of conducting polymers that have

been successfully produced via the direct synthesis from the vapour phase. This method enables the in situ control of film morphology, molecular weight and cross linking. Ultra thin layers of insoluble polymers, for instance polytetrafluoroethylene (PTFE) and polyoxymethylene (POM) can be created in this way [53]. Poly (methyl methacrylate) (PMMA) films have been grown using the preheated monomer of methyl methacrylate and initiator vapors of *t*-butyl peroxide [76], while poly (dimethylaminomethylstyrene) (PDMAMS) and poly (diethylaminoethylacrylate) (PDEAEA) were formed using tert-amylperoxide as the initiator [54]. In addition, trivinyl-trimethyl cyclotrisiloxane monomer and terbutyl peroxide initiator were utilized to produce thin films of a novel organosilicon polymer [58].

The deposition rate and molecular weight are inversely proportional to the substrate temperature. As reported by Gupta et al [49], poly (glycidyl methacrylate) (PGMA) is deposited onto large stationary and moving substrates from the 2-hydroxyethyl methacrylate and perfluoroalkyl ethyl methacrylate monomers when these parameters are considered. Investigation of other parameters such as optical transmission and fundamental reflectivity spectra of polymer thin films have been conducted by Jarzabek et al [77], revealing that the absorption coefficient of polyazomethine (PPI) films prepared by CVD method give a significant broad band at 2.9 eV.

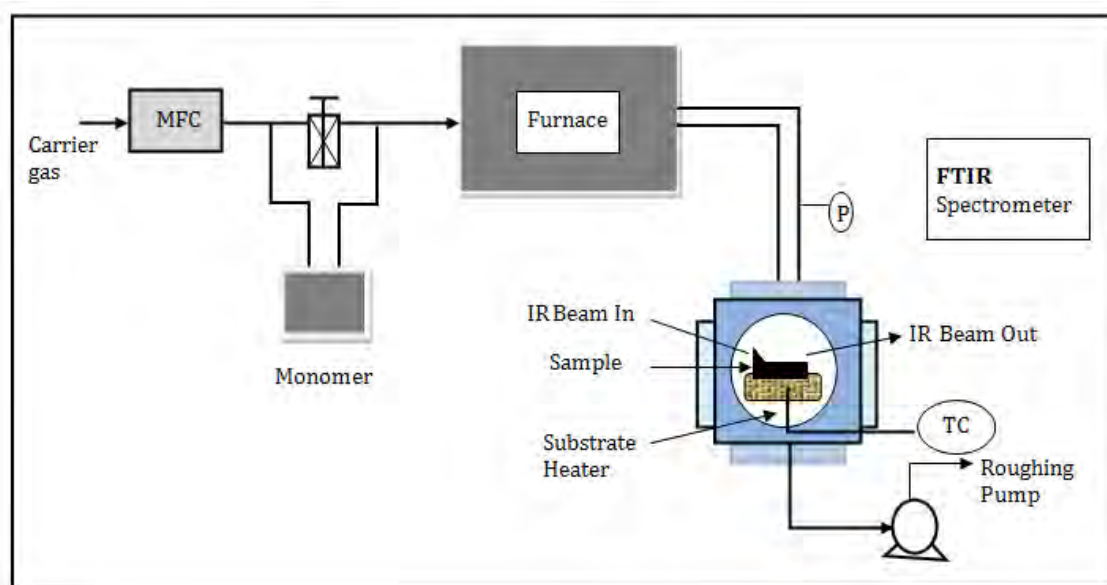


Figure 1-5: Diagram of reactor used for CVD of PPV [71]

1.8.2 Use in OPVs

Polymer based OPV devices can be constructed by employing PPV as the conjugated polymer material. According to Holt et al [78], PPV-based materials have a suitable UV-vis absorption spectrum. The electronic structure of PPV has a small exciton binding energy of 60 meV which has been found to be an important factor in most devices [79]. This small binding energy indicates that the charge carriers are well screened so that a band picture supplemented by the electron-phonon interaction and the electron-electron interaction is justified. The relatively high internal field in the OPV can assist with exciton dissociation and charge transport, as well as carrier extraction at the cell contacts.

Conducting polymers in nanostructure form can improve the optical and electronic properties of photovoltaic devices [80] and have been applied as the electron-donating and hole-transferring components in the photovoltaic materials. Conducting polymer of PPV can be fabricated to the desired shapes particularly at nano dimensions [70]. The photovoltaic effect has been well shown in the PPV/fullerene heterojunction fabricated via different polymerization techniques [81, 82]. However, to date there is no report on the fabrication of OPVs via CVD.

2 EXPERIMENTAL

This chapter describes the experimental techniques used in this work. The goal in providing this detail is to give the reader an understanding of the catalyst preparation, nanostructure growth and device characterisation. The methods presented include the CVD preparation of carbon and polymer nanostructures which form the basis of the work in Chapters 3 to 6.

2.1 FABRICATION OF CARBON NANOTUBES

Carbon nanostructures that comprise carbon nanotubes (CNTs), carbon nanofibres (CNFs) and carbon nanorods (CNRs) have been grown on ITO substrates via CVD. An ITO layer of 170 nm thickness is used as a substrate for carbon nanostructure growth. Due to the deformation of ITO-coated glass at 550°C, a low working temperature (400 – 500°C) is required. In this work, iron is evaporated to a thickness of 5 nm onto the ITO-coated glass by using electron beam evaporation and subsequently used as a catalyst for carbon nanostructure growth.

2.1.1 Catalyst Layer Deposition

Generally, the transition metals such as iron, nickel, cobalt and palladium are used as catalysts for carbon nanostructure growth, either alone or in combination. The ability of those transition metals to catalyse the formation of carbon nanostructures is mostly correlated to their catalytic activity for the decomposition of carbon compounds and the possibility for the carbon to diffuse through the metals. Additionally, the high melting point and low equilibrium-vapour pressure of these metals allow an extensive temperature window for the CVD of a wide choice of carbon precursors.

Iron is found to be more efficient than other transition metals for hydrocarbon decomposition [83]. Iron is more able to catalyse dissociation of a hydrocarbon molecule than other transition metals due to its electronic structure [84]. The hydrocarbon molecule is required to adsorb to the catalyst metal surface before the appropriate carbon nanostructure growth can take place. This interaction occurs via the transfer of electron density from hydrocarbon (donor-adsorbate) to catalyst metal

(acceptor). Generally, simultaneous back-donation will take place and this interaction leads to the dissociation of the molecule. Due to the degree of filling of the d-bands of iron, the catalytic activity and interaction with hydrocarbon is more intense than for most other transition metals.

Various methods of catalyst preparation have been used in growing carbon nanostructures for devices. Catalyst preparation involving the formation of the metal catalyst from solution has been widely used [85-89]. However, catalyst prepared from solution has several disadvantages including longer preparation time and the need for multiple preparation steps. Zielinski et al [85] have reported the use of magnetite (ferrofluid) in iron catalyst production. In this process, the ferrofluid needs to be vaporized and adhered to the specific substrate. However, control of the amount of metal particles deposited is difficult leading to problems in producing the desired structure of carbon.

An alternative method to solution based-catalyst preparation is to use iron pentacarbonyl as the metal particle precursor. However, due to the higher temperature needed for the thermal decomposition of the precursor to metallic iron, this method is not the most practical technique to be implemented.

The electron beam evaporation method has successfully been used to synthesise self-oriented regular arrays of CNTs [3]. It offers great flexibility as it allows the deposition of any metal, as well as some alloys and insulating compounds. Electron beam evaporation is a technique that uses electron bombardment to produce an intense localized heating of rods or a small crucible containing the material of interest (Figure 2-1). The rod is placed inside a ring filament while electrons from the incandescent filament are attracted towards it. The electron beam is used to heat the source materials and cause evaporation. Electrons are accelerated to up-to 2 kV at a current of up to 200 mA, making a total heating power of 400 W delivered into a very small area; temperatures of over 3500°C can be reached.

For this project ITO-coated glass with a surface resistivity of 8-12 Ω /square was purchased from Delta Technologies Limited and a sample area of 1 cm x 1 cm was used for all experiments. The ITO substrates were cleaned using a three stage ultrasonic

cleaning procedure: liquid detergent in water, deionised water and acetone for 15 min each. Dry nitrogen gas was used to blow dry all the ITO substrates at the end of the cleaning process in order to eliminate any retained moisture and small dust during the handling process. An iron layer with a thickness of 5 nm was then evaporated onto the cleaned ITO substrate using electron beam evaporation. The electron beam evaporator model EBE-1 was set at 15 mA and 1 kV for this process. Figure 2-2 shows the calibration of layer thickness and evaporation time data plot that was conducted on this evaporator in order to produce a calibration equation of the form $T = 1.258t - 0.373$.

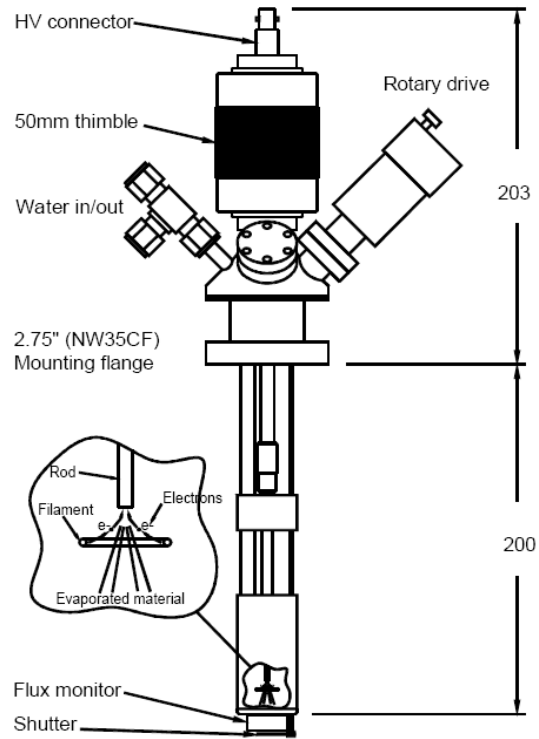


Figure 2-1: Evaporator overview and dimensions

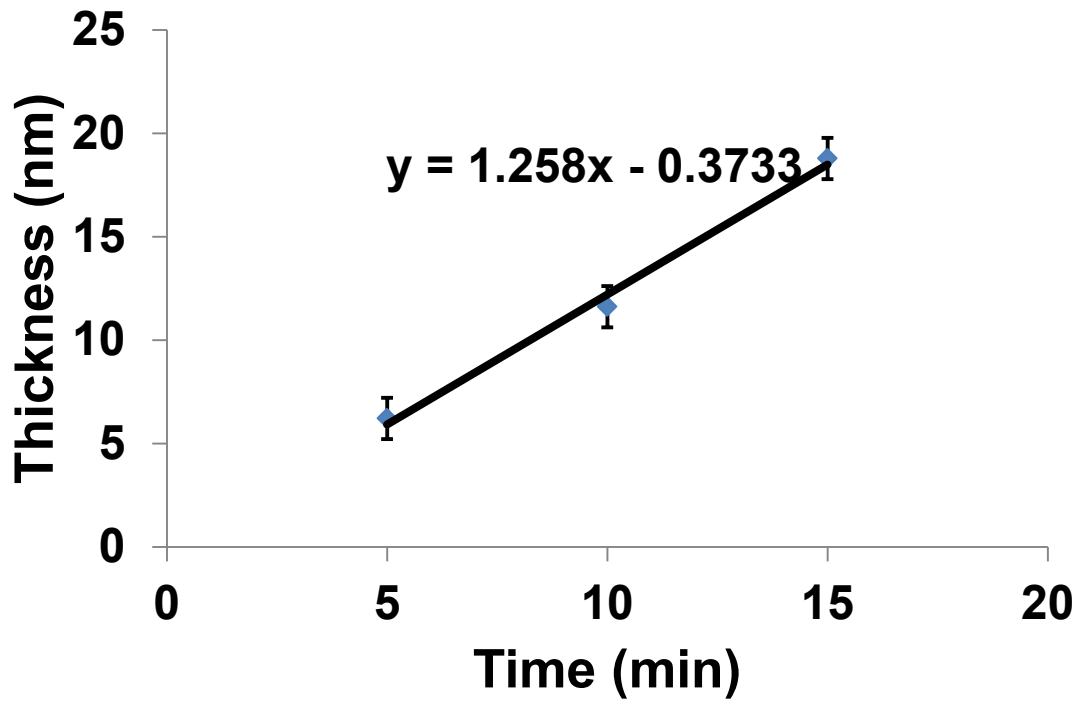


Figure 2-2: Fe layer thickness versus evaporation time plot

$$T = 1.258t - 0.373 \quad (2-1)$$

Where, T = thickness in nm

t = time in minute

Since 5 nm layer thicknesses are required in this project, an evaporation time of 4 min and 16 sec was used.

2.1.2 Thermal Chemical Vapour Deposition

Carbon nanostructures were synthesized using a CVD system from Atomate Corporation, shown in Figure 2-3. Three different growth temperatures of 400, 450 and 500 °C were introduced for the carbon nanostructure growth. The CVD system provides three heating zones using a standard coil heater element of NiCr. The maximum temperature the zones can reach is 1100°C. This system is equipped with a quartz tube with an inner diameter of 46 mm and a length of 1500 mm, into which the ITO substrates are loaded. Five steps are involved in the process of nanotube growth (Table 2-1). The first step is flowing argon and H₂ for 2 min and the second step is flowing

argon alone for another 2 min. The first two steps have been executed to reduce the partially oxidized iron particles to fully metallic ones and to activate the metallic iron. Once the system temperature reaches the desired growth temperature (400, 450 or 500°C) in the third step, argon with a flow rate of 500 sccm is added and maintained for duration of 10 min in order to reach a stable temperature. This allows the iron film to break into nanosized particles or islands before the fourth step in which acetylene is introduced as the carbon source [48]. A gas mixture composed of acetylene (25 sccm), H₂ (100 sccm) and argon (500 sccm) at the respective growth temperature is introduced for decomposition and carbon nanostructure growth over the catalyst nanoparticles. At the end of the process, a final cool down of 30 min under argon atmosphere is applied and the furnace cooled down to room temperature before the sample is removed. During this step, the chamber pressure is controlled by adjusting a butterfly valve connected to a vacuum pump. Samples were prepared at the same flow rate but a range of different chamber pressures.

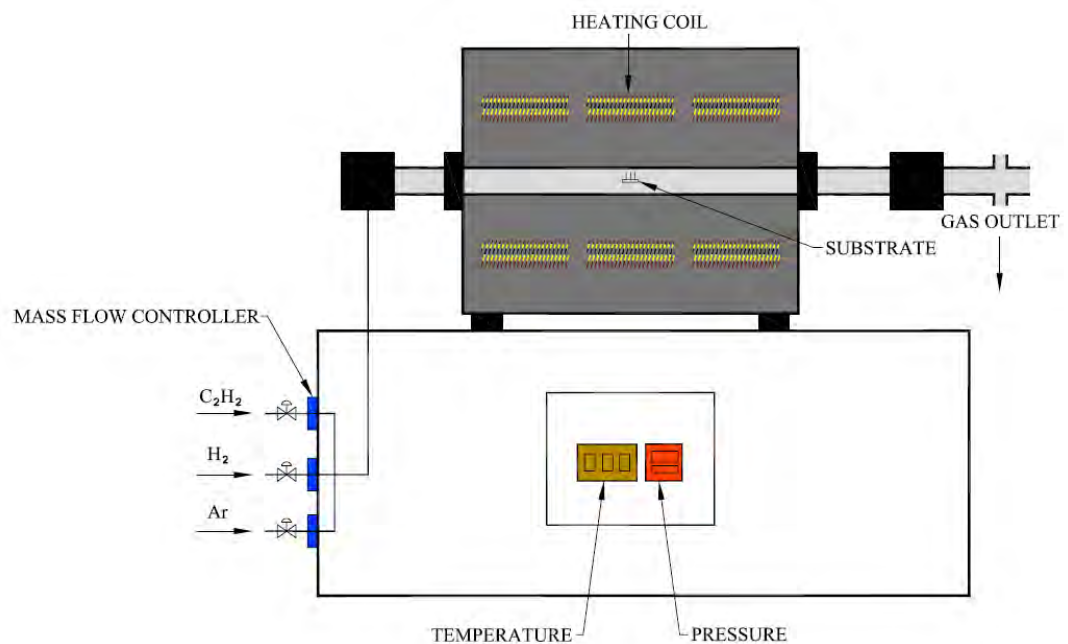


Figure 2-3: Schematic diagram of the Atomate CVD system

Duration (hh:mm:ss)	Ar (sccm)	C₂H₂ (sccm)	H₂ (sccm)	Temperature (°C)
00:02:00	500	-	100	-
00:02:00	500	-	-	-
00:10:00	500			450
00:10:00	500	25	100	450
00:30:00	500	-	-	-

Table 2-1: Recipe used in synthesizing the carbon nanostructures

2.2 FABRICATION OF POLYMER NANOTUBES

The growth of conducting polymer nanostructures for device applications is a new practice in nanoscience and nanotechnology. Novel methods have been used to manipulate the growth and consistency of “one-dimensional” polymer nanostructures (nanotubes, nanowires and nanorods). The use of hard templates for the fabrication of polymer nanostructures seems to be a reliable and expedient method. In this work, PPV nanostructures have been produced by deposition into a commercially available alumina porous template (Whatman) using CVD polymerization.

2.2.1 Alumina Porous Template

High aspect ratio alumina porous templates with diameter of 100 nm and 60 μm thickness were purchased from Whatman (Figure 2-4). These templates can withstand temperatures of 600°C. The templates are ultrasonicated with solvents such as water, acetone, ethanol and chloroform to remove contaminants and ensure the pores are open.

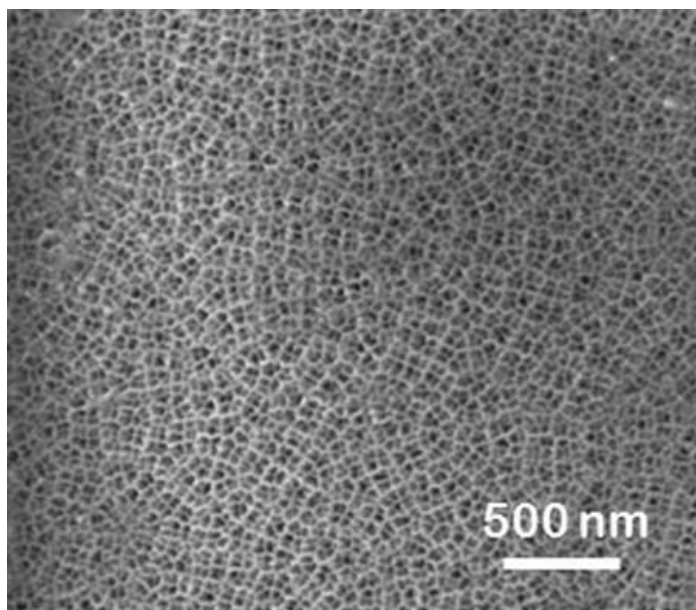


Figure 2-4: SEM image of alumina porous template

2.2.2 Chemical Vapour Deposition Polymerisation

The fabrication of polymer nanostructures from PPV is made difficult by its lack of solubility. Two well-known synthetic methods for synthesising PPV are the Wessling-Zimmerman method [90] and the Gilch polymerization [91]. Those methods utilise soluble precursors and have been used for several years. However, both methods use the water-soluble sulfonium salt precursor which involves a large amount of solvents and a high risk of producing contaminated polymer.

Because of this problem, CVD is considered to be one of the more promising tools for fabricating polymer nanostructures. The precursor polymers are thermally converted at an optimum temperature and duration. As shown in Figure 2-5, the quartz sample tube is divided into 3 different zones. The desired amount of α,α' -dichloro-p-xylene (monomer) is placed in an alumina boat in the vaporization zone. The monomer is vaporised at a temperature between 93°C to 95°C and carried to the pyrolysis zone by a 40 sccm flow of argon. Zone two (the middle) is heated to 700°C during the pyrolysis process. The activated monomer obtained after the pyrolysis, known as the precursor, is then deposited on the substrate which is placed in low temperature deposition zone. The

residence time of vaporised monomer within the 700°C pyrolysis zone has been calculated as 498 sec by using the expression [92]:

$$t = \frac{L}{V_m} \quad (2-2)$$

Where,

L = length of tube in cm

V_m = rate of gas flow in mL/cm²sec

$$V_m = \frac{D}{S}$$

D = total gas flow rate in mL/sec

S = cross sectional area of tube in cm²

Hence,

$$t = \frac{L}{V_m} = L \times \frac{S}{D} = 20\text{cm} \times \frac{\pi \times 2.3\text{cm} \times 2.3\text{cm}}{0.667\text{mL/sec}} = 498\text{sec} = 8.3\text{min}$$

During the deposition of the precursor, a system pressure of 400 mTorr is used for the total process time of 55 min. The precursor polymer is thermally converted to PPV by heating at 270°C for up to 14 hours. The system pressure is maintained at 400 mTorr by the 40 sccm steady stream of argon. During the precursor thermal conversion, the substrate is placed in the middle of the heating coil zone and all three heating zones are heated at 270°C.

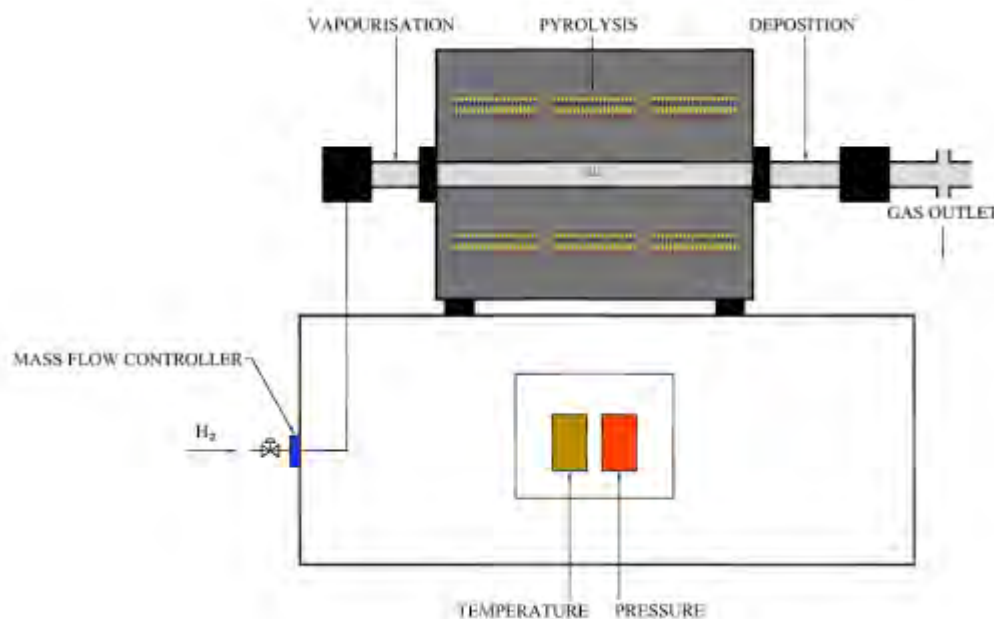


Figure 2-5: Schematic diagram of CVD polymerisation

2.3 CHARACTERISATION

The carbon and metal-based nanostructures have been characterised by scanning electron microscopy (SEM), transmission electron microscopy (TEM), four-point probe conductivity measurement, UV-vis spectroscopy, X-ray photoelectron spectroscopy (XPS), Raman spectroscopy and Fourier transform infra-red (FTIR) spectroscopy. Details on the each of these are provided in the following sections.

2.3.1 Scanning Electron Microscopy

Sample morphology has been characterised using a Philips XL30 SEM (Figure 2-6a). This conventional SEM is equipped with both a secondary electron and back-scattered electron detector. However, unless otherwise stated, all of the images collected here used secondary electrons. A high energy beam of electrons is used to scan the surface of sample before the image can be displayed. The electron gun located at the top of the microscope (Figure 2-6b) is responsible for the electron beam production which then follows a vertical path through the microscope directed by electromagnetic fields and focussed by lenses. The signal produced by the interaction between the electron beam

and atoms that made up the sample provides information on surface morphology, topography and composition.

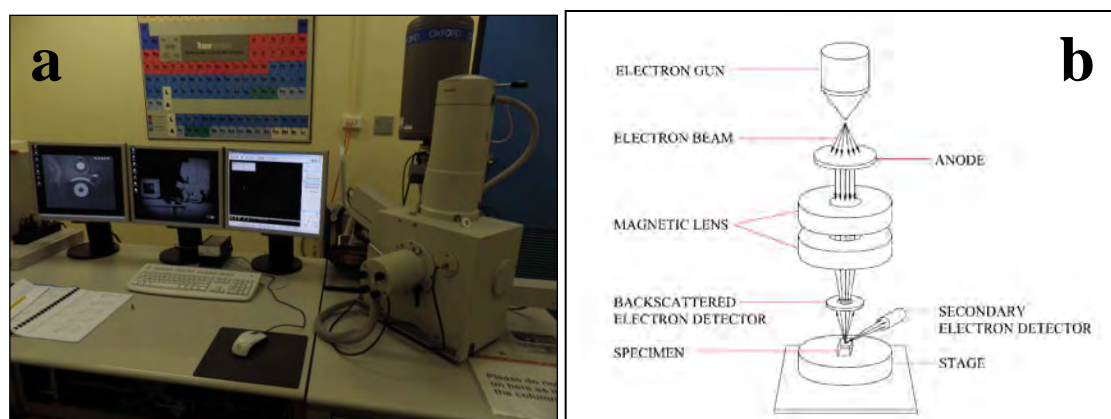


Figure 2-6: (a) Photo of Philips XL30 SEM & (b) schematic diagram of SEM

2.3.2 Transmission Electron Microscopy

Transmission electron microscopy (TEM) is a powerful tool in identifying and quantifying the chemical and electronic structure of individual nanoparticles [93]. Further characterization of surface nanostructure, particularly morphology and crystallographic information was performed using a JEOL 1200 EXII TEM with a beam voltage ranging from 80 to 120 kV (Figure 2-7a). Similar to SEM, an electron beam is emitted from the electron gun and travels through the microscope column (Figure 2-7b). TEM gives better resolution information than SEM on the size, shape and the arrangement of particles that make up the sample, with up to 100000 times magnification. Since it has been equipped with an electron diffraction pattern tool, crystallographic information such as arrangement of atoms and their degree of order can be obtained on the nanometer scale. TEM potentially reveals the finest details of internal structure due to the small wavelength of the electrons.

200 mesh copper grids (ProSciTech) were used as a substrate to hold a fragment of sample obtained by scratching it with a scalpel. 200 mesh is a standard name used for TEM grid. The mesh of the grid is defined by the number of hole within 1 inch. The diameter of grids is standard, as 3.05 mm, so 200 mesh grid has 20 holes along diameter direction. Careful handling of the fragment must be used during the transfer to the

copper grid. The scratching technique has been applied [60] to carbon nanocomposite characterization using a sharp tungsten tip and the collected material is then transferred to the copper grid.

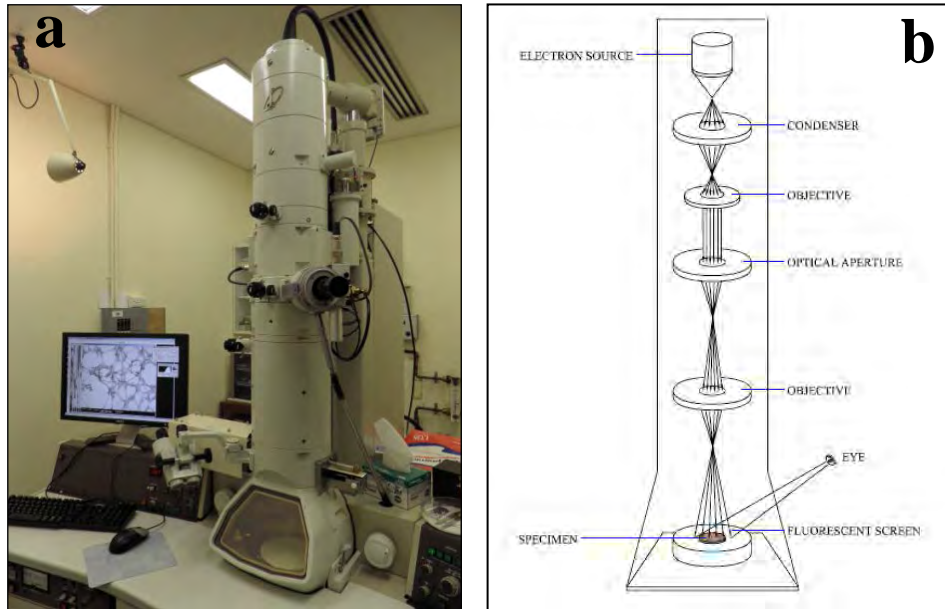


Figure 2-7: (a) Photo of JEOL 1200 EXII TEM & (b) schematic diagram of TEM

2.3.3 Conductivity

The conductivity of ITO-coated glass was measured using a four-point probe apparatus [94]. This technique can measure either bulk or thin film samples (for which a different mathematical expression needs to be used) [94]. A schematic of the four-point probe configuration is shown in Figure 2-8. It comprises four uniformly spaced tungsten tips with finite radius. The space between two metal tips is 2 mm. Each metal tip is held by springs so as to minimize sample destruction during probing. During the measurements, an auto-mechanical stage of the four metal tips travels up and down. The outer two probes are supplied with current from a high impedance current source, while the voltage is measured by voltmeter across the inner two probes.

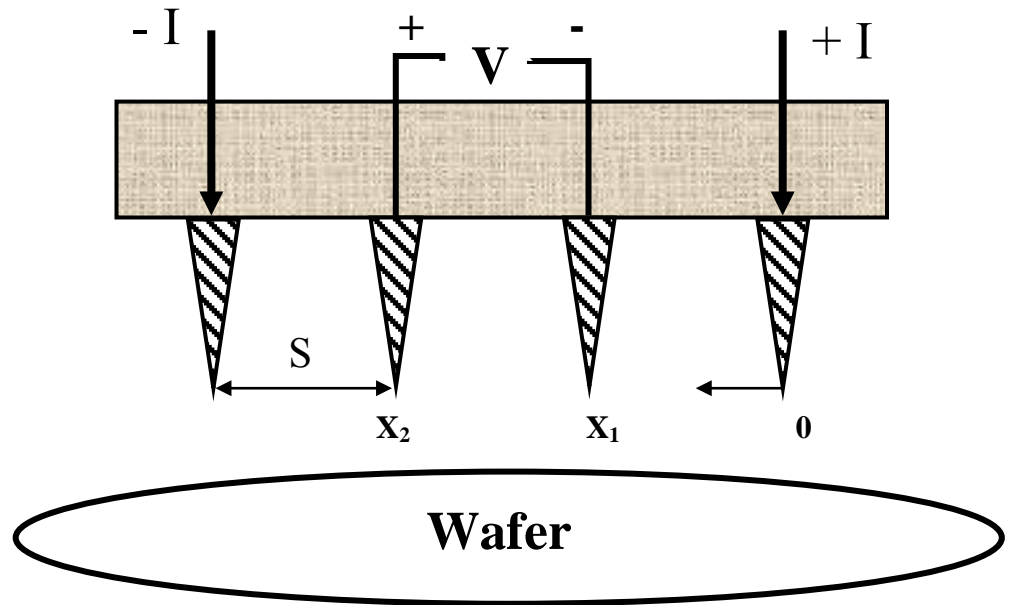


Figure 2-8: Schematic of 4-point probe configuration [94]

The electrical conductivity measurements performed in this study used the Haldor Topsoe formulae [94]. The dimension of the measured sample is 15 mm x 10 mm and the thickness is 170 nm, which is less than half the probe spacing. Due to the sample's dimension and thickness, the four-point probe setup configuration shown in Figure 2-9 was implemented.

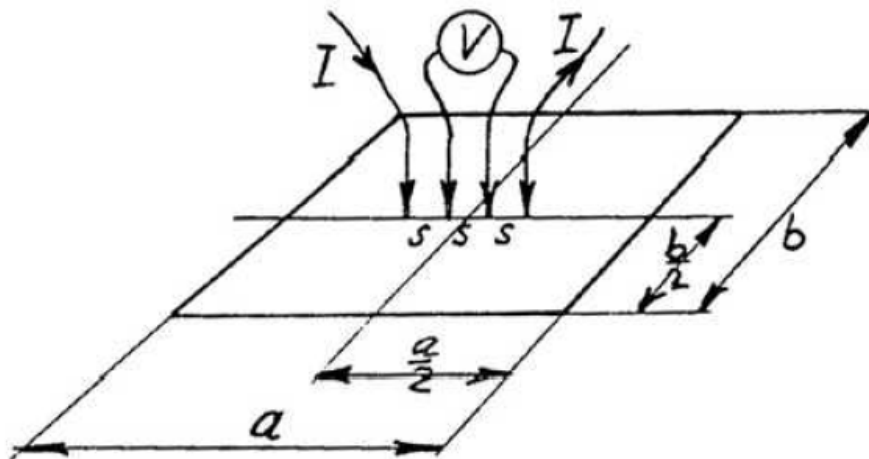


Figure 2-9: Schematic of four-point probe setup for thin rectangular slice sample [94]

For this configuration, the resistivity (ρ) is given by;

$$\rho = R_s \times t \quad (2-3)$$

$$R_s = R \times G \quad (2-4)$$

$$R = \frac{V}{I} \quad (2-5)$$

$$G = \frac{\pi}{\ln 2} \cdot t \cdot R_1 \left(\frac{b}{s} \cdot \frac{a}{b} \right) \quad (2-6)$$

Where,

$\frac{\pi}{\ln 2} \cdot t = 4.5324$. t is the geometric factor for an infinitely large slice of thickness $t < s$

$R_1 \left(\frac{b}{s} \cdot \frac{a}{b} \right)$ is the additional correction to apply because of the finite, rectangular shape.

Based on a , b and s values, G is tabulated in the Haldor-Topsoe tables [94] as 3.5749 (dimensionless).

R_s = sheet resistance (ohm/square)

R = resistance (ohm)

s = probe spacing (2 mm)

V = voltage (volt)

I = current (ampere)

t = thickness (1.7×10^{-5} mm)

a = 15 mm

b = 10 mm

2.3.4 Optical Spectroscopy

Optical spectroscopy is an important technique that has been widely used in investigating organic structures. Four optical analysis techniques used in this work are UV-vis absorption, photoluminescence, Raman and FTIR spectroscopy. These four techniques provide an insight into the chemical composition of organic materials.

A UV-vis absorption spectrometer determines the intensity of light passed through a sample (I) and compares it to the intensity of light before it passes through the sample (I_0). The ratio I/I_0 is described as transmittance, however, absorbance (A) is also used and is given by:

$$A = -\log\left(\frac{I}{I_0}\right) \quad (2-7)$$

The relative absorption of organic compounds that lie in the range of 190 nm to 900 nm can be measured via the UV-vis absorption spectrometer (Cary 6000i Varian UV-Vis-NIR). For a film sample the relative intensity of an absorption peak is proportional to the thickness of the material [95]. The absorption is due to an electronic transition of a valence electron (for example, between a lone-pair or bonding orbital to an anti-bonding orbital).

The transition of an electron from a HOMO to a LUMO determines the energy difference between the valence band and conduction band, which is called the band gap energy. Small band gap energy is favourable for OPV devices due to its importance in determining the amount of the solar spectrum that is absorbed. Thus, the band gap energy of polymer can be calculated from UV-vis absorption spectra [96] given by:

$$E = h \cdot \frac{c}{\lambda} \quad (2-8)$$

Where,

$$h = 6.626 \times 10^{-34} \text{Js},$$

$$c = 3 \times 10^8 \text{m/s and}$$

$$\lambda = \text{cut off wavelength}$$

Apart from the identification of the absorption peak, UV-vis absorption spectra can also provide information on polymer conjugation length [97]. Reduction in polymer conjugation length is visualised by a blue shift (or ‘hypsochromic’) in the absorption peak [98]. The degradation of polymer films can thus be inferred from this since a strong blue shifted implies degradation and shortening in conjugation length of the polymer. By contrast, a ‘bathochromic’[98] or red shift indicates highly conjugated systems.

The molecular structure and chemical bonding in the polymer can be revealed by FTIR spectroscopy [99]. Investigation of the molecular structure can provide information on the degradation process or contamination that might occur during synthesis. For instance, two peaks at 1695 cm^{-1} and 1278 cm^{-1} that are due to carbonyl bonds appear due to the photodegradation of PPV in air [100]. The FTIR used in this work was a Shimadzu model 8400S.

Carbon nanostructures are further characterised using the Raman technique based on the inelastic scattering of monochromatic light. An inVia Raman microscope equipped with 514 nm Argon ion laser was used in this study, which gives $\pm 1.25\text{ cm}^{-1}$ resolution. The Raman effect originates from photon absorption and reemission during which the photon frequency undergoes up or down shifting. Information about the vibrational, rotational and other low frequency transitions in molecules can be distinguished from the shifted frequency. Solid samples such as carbon nanostructures are ideal for Raman characterisation. For carbon structures, generally, two prominent peaks assigned as *D* and *G* peaks are visible and corresponded to disordered carbon and graphite-based transitions, respectively [101].

2.3.5 Photoluminescence Spectroscopy

Photoluminescence (PL) spectroscopy is well complimented with UV-vis absorption spectroscopy in providing information on organic compounds. A PL spectrometer probes electronic relaxations, whereas absorption spectroscopy is a characteristic of the electronic excitations. Figure 2-10 shows the vibronic transition from the ground state (S_0) to excited state (S_1). The vibrational levels correspond to C-C stretching modes and are related to the geometry relaxation in the excited state. The dashed curves show the vibrational wave function of the zeroth vibrational level (0), first vibrational level (1) and second vibrational level (2). All of the polymers are in the zeroth vibrational level of ground state. The PL spectrum of PPV exhibits 3 emission peaks which corresponding to 0 – 0, 0 – 1 and 0 – 2 transitions [102].

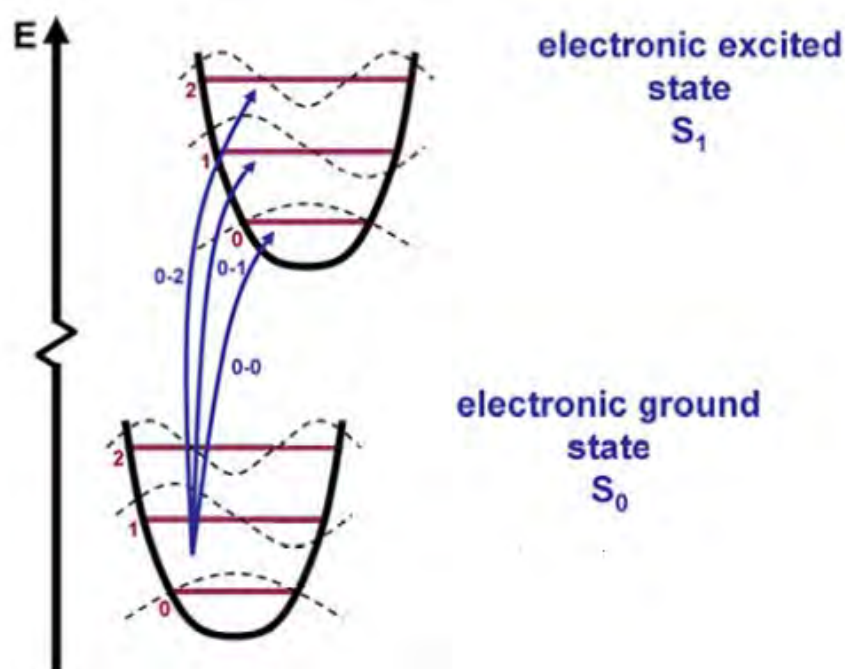


Figure 2-10: An optimal geometry of the ground state and excited state

2.3.6 X-ray Photoelectron Spectroscopy

The quantitative analysis of surface composition and identification of unknown elements is achieved by using X-ray photoelectron spectroscopy (XPS). In this study, a Physical Electronics XPS (PHI-550) spectrometer was used to examine the influence of metal elements such as indium, tin and iron on carbon nanostructure growth. In the present work, the hydrogen reduction of the iron-coated ITO substrate involves an annealing treatment at three different temperatures of 400, 450 and 500°C. Changing the annealing treatment from room temperature to elevated temperatures will manipulate the carbon nanostructures growth and alter the involvement of different materials in the substrate and catalyst layers [45]. The metal catalyst has a major impact on the synthesis of carbon nanostructures. However, the support substrate also contains metal elements and may result in unexpected metal inclusion in the final growth. In literature reported elsewhere [52], XPS characterisation has been shown to be capable of detecting major changes during the growth reaction caused by the support material. In addition, the support metal has been determined to be an important influence in boosting the activity of the metal catalyst. A better understanding of the formation mechanism of carbon nanostructures can be obtained via XPS particularly in growth that entails more than one type of metal element.

2.4 OPV DEVICE FABRICATION

In this study, the main fabrication technique used for depositing the electron donor is CVD polymerisation. Chemically vapour deposited PPV is coated onto patterned ITO-coated glass with and without the hole transport [103] or electron blocker conductive film of poly (3, 4-ethylenedioxythiophene)/poly (4-styrenesulfonate) (PEDOT/PSS). Thermal treatment applied to PEDOT:PSS thin films may decrease its conductivity and increase its surface roughness [104] and this therefore not appropriate for CVD growth. PEDOT: PSS is a hygroscopic material which competent in attracting and holding moisture from air. The conductivity of PEDOT:PSS may have been decreased over the thermal treatment temperature and time. O₂ molecules in air would have a negative effect on the conductivity of PEDOT:PSS film which degradation of the material may

have been occurred. In addition, the foremost role of PEDOT:PSS as intermediate layer (to planarise the rough ITO surface) between ITO and polymeric active layer, would not been fulfil due to the changes on its surface roughness. The greater surface roughness of PEDOT:PSS has been reported from the effect of higher thermal treatment temperature which leads to the increase of effective colloidal particle size [104]. However, the comparison between two different architectures (with and without PEDOT:PSS) is studied in order to verify the previous statement.

For the electron acceptor material, two types of deposition techniques were used namely solution-processed and evaporation. PCBM (solution-processed) was dissolved in chloroform with a concentration of 5 mg/ml. A thickness of 60 nm PCBM was spin-coated onto the chemically vapour deposited PPV by setting the spinning speed at 1000 rpm. C60 was deposited on top of PPV with a thickness of 60 nm via evaporation. PPV was deposited with the various thicknesses which were measured by surface profilometer (± 10 nm). No annealing treatment is applied either for the pre- or post-treatment. The final aluminium film was thermally evaporated onto the composite layer and acts as a cathode. For some architecture, lithium fluoride (LiF) or calcium (Ca) was used as an interfacial layer between the active layer and top electrode. These layers are known to improve device performance and act as hole blocking layers.

2.5 OPV DEVICE CHARACTERISATION

The current-voltage (I - V) curve is the significant characteristic of an OPV's photovoltaic performance, which can provide information on short-circuit current density (J_{sc}), open-circuit voltage (V_{oc}), fill factor (FF) and power conversion efficiency (η). The I - V curve is performed both in the dark and under the illumination of 100 mW/cm² of an AM 1.5 solar simulator.

The I - V curve is a graph presented as current versus voltage. This graph shows the short-circuit current (I_{sc}) and open-circuit voltage (V_{oc}), in which cell is operated at $V=0$ and $I=0$, respectively. However, in order to account for the dependence on device area, it is more conventional to take J_{sc} into account rather than I_{sc} . Figure 2-11 shows the J - V curve with the characteristics of an idealised OPV.

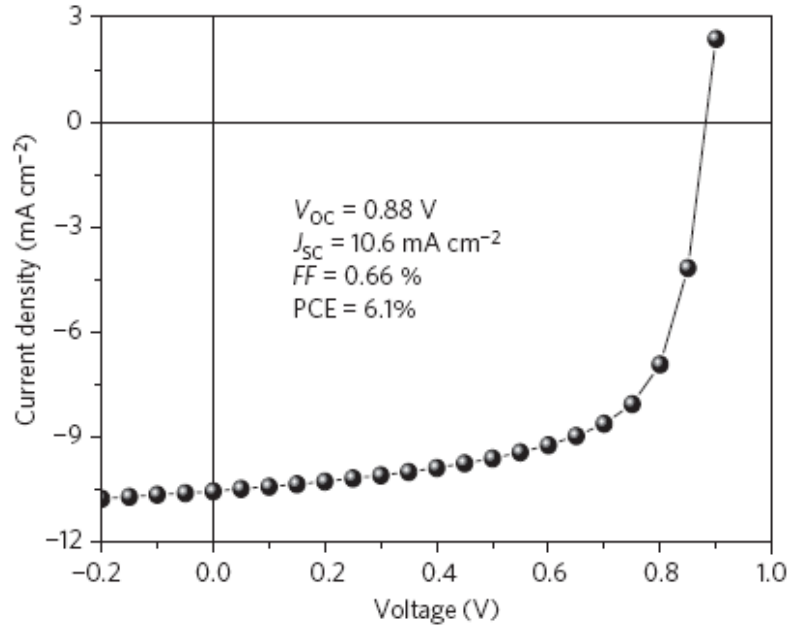


Figure 2-11: Current density versus voltage characteristics (J - V) of an ideal solar cell [39]

The FF of device which conveys the power delivery capability can be calculated as follows:

$$FF = \frac{V_m I_m}{I_{SC} V_{OC}} \quad (2-9)$$

Where, V_m = voltage and I_m = current in the maximum power point of I - V curve in the fourth quadrant.

By taking into account of all those parameters mentioned above, the device power conversion efficiency η can be evaluated as follows:

$$\eta = \frac{FF I_{SC} V_{OC}}{P_{in}} \quad (2-10)$$

Where the standard unit used is $I_{sc} = \text{A/cm}^2$, $V_{oc} = \text{volt}$ and $P_{in} = \text{W/cm}^2$.

3 EFFECT OF THERMAL TREATMENT ON INDIUM TIN OXIDE SUBSTRATES

3.1 INTRODUCTION

The performance of organic electronic devices is intimately tied to the physical and electrical properties of the indium tin oxide (ITO) substrate upon which they are fabricated. This chapter outlines a detailed study of the electrical conductivity, surface morphology, optical properties and surface chemistry of the ITO substrate as a function of thermal processing. The goal of this chapter is to provide insights into effect onto the ITO substrate of growing CVD nanostructures at elevated temperatures.

3.1.1 Properties of ITO

Generally, the conductivity (σ) of ITO relies on the carrier concentration (N) and the mobility of free carrier (μ). This is given by the following equation (where e is electron charge):

$$\sigma = N\mu e \quad (3-1)$$

Thus, in order to obtain an ITO film with high conductivity, the carrier concentration and mobility should be concurrently optimised. The majority charge carrier (electron) in ITO are created by the tin dopant and the presence of oxygen vacancies [105]. Many attempts have been made to enhance the conductivity of ITO by raising the number of free carriers via doping. However, excessive tin doping causes impurity scattering of electrons and leads to increased resistivity due to reduced electron mobility [106]. Therefore, optimising conductivity by doping is a balance between charge carrier concentration and electron mobility.

Oxygen vacancies in the ITO structure act as doubly ionized donors with two electrons supplied to the ITO's conduction band as shown in the equation:



Where,

O_O^x = an oxygen ion sitting on an oxygen lattice site, with neutral charge

V_O = oxygen-array vacancies

$2e'$ = two electrons

The oxygen vacancies form a shallow impurity donor band about 30 meV below the ITO conduction band, which then overlaps with E_c (bottom of conduction band) and forms an n-type degenerate semiconductor. However, the presence of oxygen vacancies results in ion impurity scattering which reduces charge carrier mobility via the existence of O^{2-} ions [107].

Thus, a deficiency in oxygen vacancies can also lead to low conductivity. Indeed, diffusion of oxygen atoms into the ITO structure (upon annealing ITO films at high temperature in an air atmosphere) has been reported to result in reduced oxygen vacancies [108, 109]. Figure 3-1 shows how the conductivity of ITO decreases with increasing oxygen flow rate and higher annealing temperature air atmosphere; demonstrating that incorporation of oxygen atoms into the ITO structure results in a reoccupation of oxygen vacancies sites and hence a reduction in conductivity.

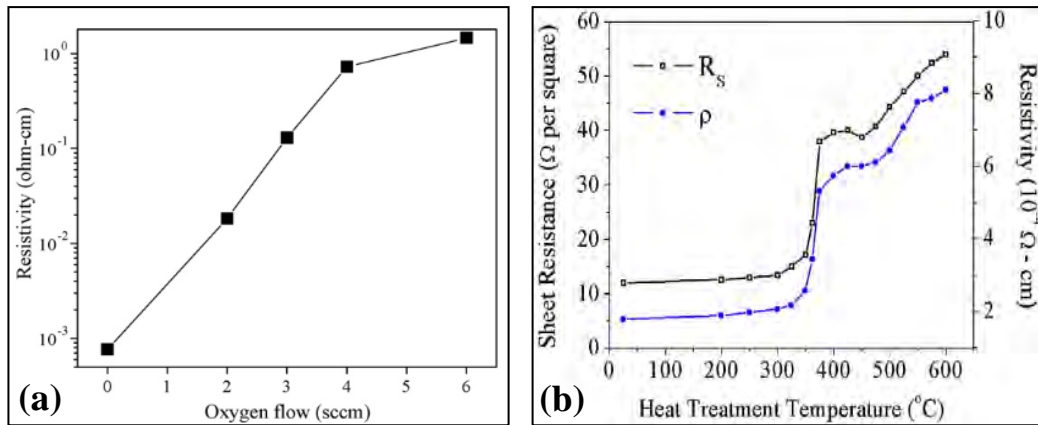


Figure 3-1: (a) Influence of oxygen gas flow rate [108] and (b) annealing treatment [109] to the resistivity of ITO films

Indium tin oxide (ITO) thin films are widely used as electrodes in various optoelectronic devices such as organic light emitting diodes (OLED) [110], organic photovoltaic cells [35] and flat panel displays [111], due to ITO's tunable conductivity and optical transparency. The fabrication of these optoelectronic devices can involve a

thermal treatment process such as the post-annealing process of OPV devices [35, 112] and the growth of carbon nanostructures on the electrode [8, 65].

3.1.2 Thermal Processing of Organic Electronic Films and Structures

For certain materials systems, such as P3HT:PCBM, bulk heterojunction OPV power conversion efficiency is improved upon thermal annealing [35]. Thermal annealing processes are known to improve the molecular packing and crystallite size of the donor and acceptor regions with a typical optimal device annealing temperature and duration of 140°C and 15 min, respectively [35]. However, these devices also show a significant reduction in both short-circuit current density and fill factor once the annealing temperature reaches 230°C. Kim et al found that when the annealing temperature is higher than the polymer melting point, reorientation of donor crystallites occurs due to heterogeneous nucleation at the substrate surface, which then degrades the performance of OPV. A deterioration in OPV device performance is also reported for devices that have been subjected to long annealing times, where upon a significant drop in efficiency, short circuit current density and fill factor were observed [112].

It has long been proposed that the fabrication of an ordered, nanostructured electrode will likely improve the efficiency of organic solar cells that are limited by the charge separation and transport processes of a bulk heterojunction architecture [41]. As such, the growth of carbon nanostructures onto ITO may serve to enhance the electrical transport properties of bulk heterojunction devices [65]. CVD is a common technique used for carbon nanostructure growth on ITO electrodes since it offers several potential advantages including; (1) an enhancement of the mechanical stability between the carbon nanostructures and the ITO electrode, (2) the formation of a continuous charge transport pathway from carbon nanostructures and ITO to the external circuit and (3) a reduction of electrical shorting by control of the dimensions of the carbon nanostructures.

The growth of carbon nanostructures directly onto ITO has been previously reported for integration in OPV devices [8]. This growth required a working temperature of 550°C for the CVD process. The authors compared OPV devices fabricated with the inclusion of CVD and those without the inclusion of the CVD process, and observed a

reduction in fill factor and power conversion efficiency. They suggested that the deterioration of device performance was due to a reduction in cell shunt resistance [8].

3.1.3 Thermal Processing of ITO

Thus, while the performance of OPV devices can be enhanced by annealing moderate temperatures ($\sim 150^{\circ}\text{C}$), a deterioration of device performance has been observed upon heating to temperatures above 200°C [35]. However, even higher temperatures (approaching 550°C) are typically used in the growth of carbon nanostructures by chemical vapour deposition (CVD) [8]. Given the range of heating temperatures that the device substrate might be exposed to, an understanding of how the ITO substrate responds to thermal processing is also required. For example, the stability and efficiency of organic electronic devices is highly dependent on the surface morphology of ITO [110] used as a bottom electrode. Moreover, it has been shown that increase in surface roughness of ITO correlate with higher annealing temperatures [113] and that high surface roughness results in high leakage current in OLED devices [110]. Thus, an even and smooth surface is just one ITO characteristics that is extremely important to device performance. Indeed, there are many properties of ITO, (such as electrical conductivity, surface morphology and optical properties) that have to be retained after thermal treatment in order to ensure optimal device performance.

Studies of thermal effects have been reported for the preparation of ITO thin films deposited by magnetron sputtering [113-116], sol-gel process [117], electron beam evaporation [118, 119], ion-assisted deposition [118] and chemical solution deposition [120]. These studies have shown that, a post-deposition annealing process is often required to produce the required ITO thin film properties. Indeed, significant differences in film properties may be exhibited between the commercial ITO used in our study and ITO prepared via various other techniques [113-120], due to fact that the commercial ITO deposited by magnetron sputtering (Delta Technologies) has already undergone a post-deposition annealing process during its preparation.

To date, there has only been one systematic study of annealing temperature on commercial ITO-coated glass at atmospheric pressure [109]. There was also a study of

annealing of a commercial ITO-coated glass in a hydrogen atmosphere [121]. These studies showed that there is a pronounced change in crystal structure, resistivity and transmittance of the ITO for annealing temperatures between 100 - 600°C. Higher temperatures result in the transformation of an amorphous ITO structure to a more crystalline structure [109, 121]. Additionally, indium has been reported to oxidize and diffuse into the other thin film layers if subjected to thermal treatment [122].

Given that the ultimate goal of the work presented in this thesis is the CVD growth of carbon and polymer nanostructures onto an ITO substrate at elevated temperatures, this chapter presents a detailed study of the physical and chemical changes that occur to the ITO substrate upon annealing. As we will see in later chapters, an ideal temperature of 270°C is used for the growth of polymer nanostructures and three different temperatures of 400, 450 and 500°C are used for the carbon nanostructures growth. As a preliminary step, this chapter investigates the changes in ITO properties that occur due to thermal treatment over this temperature range. In particular, the impact of thermal treatment on the electrical conductivity, surface morphology, optical properties and surface chemistry of ITO substrate is discussed with a view to the fact that these properties will in turn determine OPV device performance.

3.2 EXPERIMENTAL SETUP

In order to determine the range of temperature that an ITO substrate can be raised to without adversely affecting conductivity, physical structure and chemical composition, the sheet resistance of the substrate was measured (all at room temperature) using a four-point probe method after annealing the substrate to 100°C, 200°C, 300°C, 400°C, 450°C, 500°C, 600°C and 700°C for 20 minutes. Four ITO substrates were used for each annealing temperature, which provided a measure of experimental error. The annealing process was carried out using the CVD furnace shown in Figure 2-3. During the annealing process, no carrier gas was applied and the pressure of CVD was set to 3 Torr (air atmosphere). As noted in 2.3.3 the Haldor Topsoe technique [94] was used for the electrical conductivity measurement. Structural properties of the ITO were also examined via SEM, atomic force microscopy (AFM) and X-ray diffractometer (XRD). The transmission of the samples was determined using UV-vis absorption spectroscopy.

Characterisation of the chemical composition was completed via energy dispersive X-Ray spectroscopy (EDS) and X-ray photoelectron spectroscopy (XPS), providing information on the chemical compositions of the bulk and the top surface of the annealed ITO, respectively.

3.3 RESULTS AND DISCUSSION

3.3.1 Conductivity

Figure 3-2 shows the ITO conductivity change as a function of annealing temperature for temperatures ranging from room temperature (RT) to 700°C. The error bars are based on the standard deviation of the measurements. It can be seen that the conductivity of the ITO substrate decreases with increasing annealing temperature. ITO heated at 100°C results in less than 10% conductivity reduction. Further annealing to 400°C decreases the conductivity from 5700 ± 200 S/cm to 4300 ± 300 S/cm. However, the most significant conductivity reduction occurs between 500°C and 700°C, with the ITO substrate losing almost all of its conductivity if annealed at 700°C. However, the conductivity of ITO heated at 400 to 450°C remains the same. Thus, it is clear that 450°C is the maximum thermal processing temperature taking into consideration the ITO conductivity reduction.

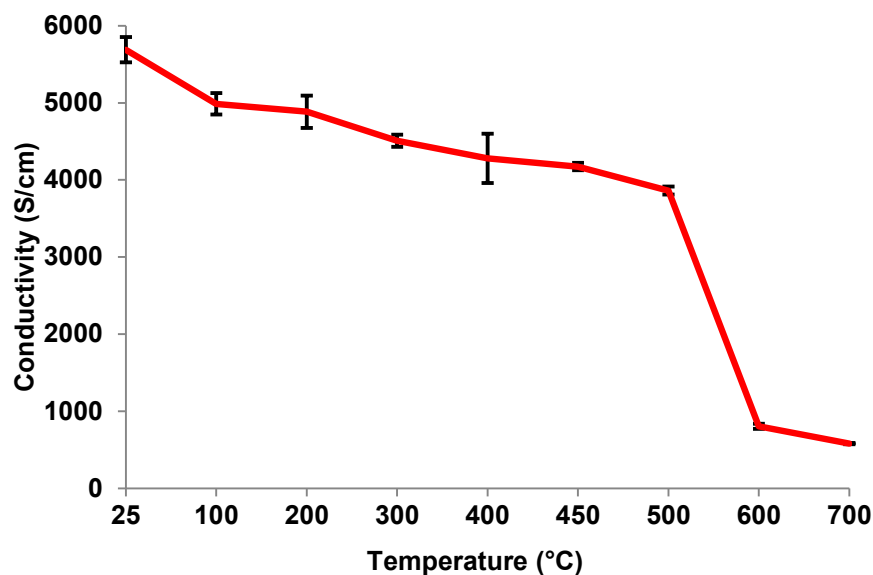


Figure 3-2: Conductivity of ITO substrates at different annealing temperatures

These observations are consistent with the work reported by Hsu et al [115]. They studied the effect of annealing sputtered ITO films on quartz with a thickness of 200 nm and found that once the annealing temperature exceeded 450°C, the degradation of electrical conductivity became severe, with an increase in sheet resistance to several hundred Ω /square. According to Agrawal et al, the sheet resistance of annealed ITO coated Si increased about 45% after being exposed to a temperature of 775°C [65]. The decrease in conductivity is suggested to be due to a decrease in oxygen content of the oxide during the reduction process. In addition, the work carried out by Bayliss [123], also indicated a reduction in ITO conductivity at an elevated temperature.

However, other reports indicate that although the conductivity of an ITO film annealed between 100°C to 200°C decreases, it is improved once the annealing temperature is elevated to 500°C [121]. In other literature, an ITO film annealed at 300°C was seen to have the lowest resistivity of $2.25 \times 10^{-4} \Omega\text{-cm}$ before the resistivity increased with further increases in annealing temperature [118]. These observations are not in agreement with the study done here, where a reduction in conductivity is observed for annealing temperatures as low as a 100°C. It is likely that the main reason for the disagreement between the present work and that reported in the literature [118, 121] might be due to the differences in the precise nature of the ITO used in the respective studies.

3.3.2 Surface Morphology

It is likely that the variations in conductivity that are observed are related to the microstructural morphologies of the indium and tin oxides. It is known that the conductivity of ITO can be enhanced by controlling the size and shape of the crystalline grains [120]. As the annealing temperature is increased, segregation of these grains becomes more significant and their size becomes larger [120].

In order to probe these microstructural changes, the surface morphology of annealed ITO films was investigated by AFM. The scanned area shown is $2 \times 2 \mu\text{m}$. The AFM images of the annealed ITO substrates reveal the nano-grain and heterogeneous topography. As shown in Figure 3-3, the surface grain size of ITO becomes larger and more uniform as the annealing temperature is increased up to 700°C in agreement with

work done by Kerkache et al [116], which showed that the effect of annealing on ITO thin films was to increase the electrical resistivity and grain size.

Since the surface roughness is crucial for the stability and efficiency of devices [110], three different measures of surface roughness were determined for these samples, which are summarized in Table 3-1. Root-mean-square (R_{rms}), average (R_a) and peak to valley (R_{pv}) roughness are used to characterize the annealed ITO and gauge their relation to other changes in properties such as conductivity, optical and composition. The overall changes in roughness illustrated by these three parameters are similar, with all of the roughness values tending to slightly vary with increasing temperature.

The trend of the different surface roughness parameters under the different annealing temperatures is shown in Figure 3-4. The un-annealed ITO substrate recorded the highest R_{rms} and R_a of 1.35 nm and 1.08 nm, respectively. By comparison, the ITO substrate subjected to 400°C exhibited the highest R_{pv} of 23.90 nm. However, there was not much variation in R_{rms} and R_a from un-annealed ITO to 700°C. R_{pv} is the only value that exhibited a significant variation under the different annealing temperatures. According to Tak et al [110], small wrinkles on the ITO surface result in a high value of R_a and R_{rms} , while spikes on the surface are reflected in a high value of R_{pv} . This hypothesis is supported by our observation of the high R_{pv} for ITO that has been annealed at 700°C. In this case, the wrinkles and spikes on the surface can be seen by the naked eye. The SEM image of these wrinkles and spikes are shown in Figure 3-5.

From the AFM analysis, preliminary smoothing of the ITO films starts at around 300°C, which may be due to the oxidation and sintering of irregular and sparsely-packed grains into regular and closer-packed grains. At 400°C, the film starts to roughen before it smoothen when further annealed up to 650°C is applied. However, the ITO is roughening again at 700°C due to the formation of a larger columnar grain structure.

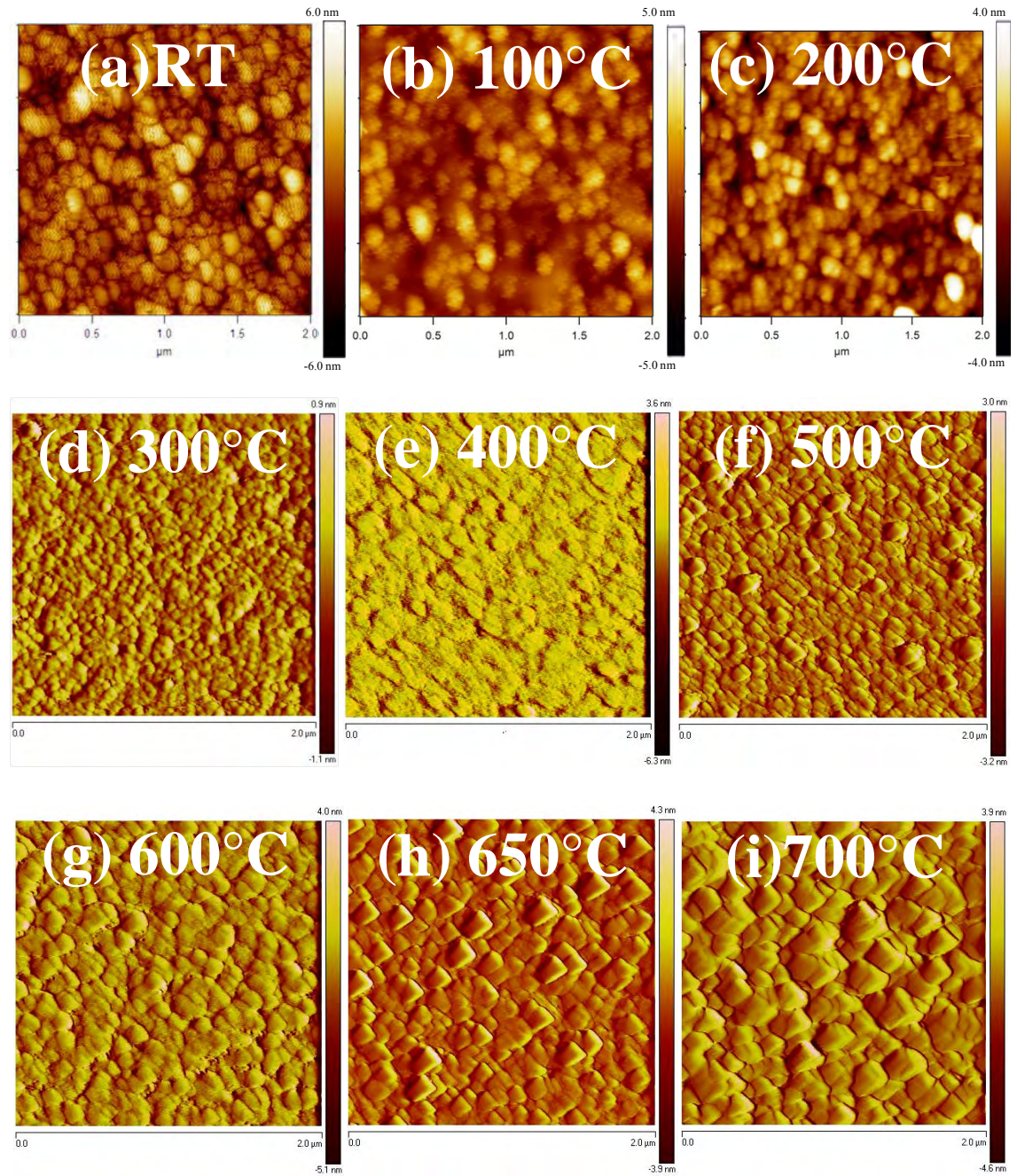


Figure 3-3: AFM images of ITO annealed at different temperatures of
(a) un-annealed ITO, (b) 100°C, (c) 200°C (d) 300°C, (e) 400°C,
(f) 500°C, (g) 600°C, (h) 650°C & (i) 700°C

Parameters	Description
Root mean square roughness (R_{rms})	Root mean square average of height deviations taken from the mean image data plane, expressed as: $\sqrt{\frac{\sum Z_i^2}{N}}$
Average roughness (R_a)	Arithmetic average of the absolute values of the surface height deviations measured from the mean plane. $\frac{1}{N} \sum_{j=1}^N Z_j$
Peak to valley roughness (R_{pv})	Maximum vertical distance between the highest and lowest data points in the image.

Table 3-1: Description on the terminology of surface roughness

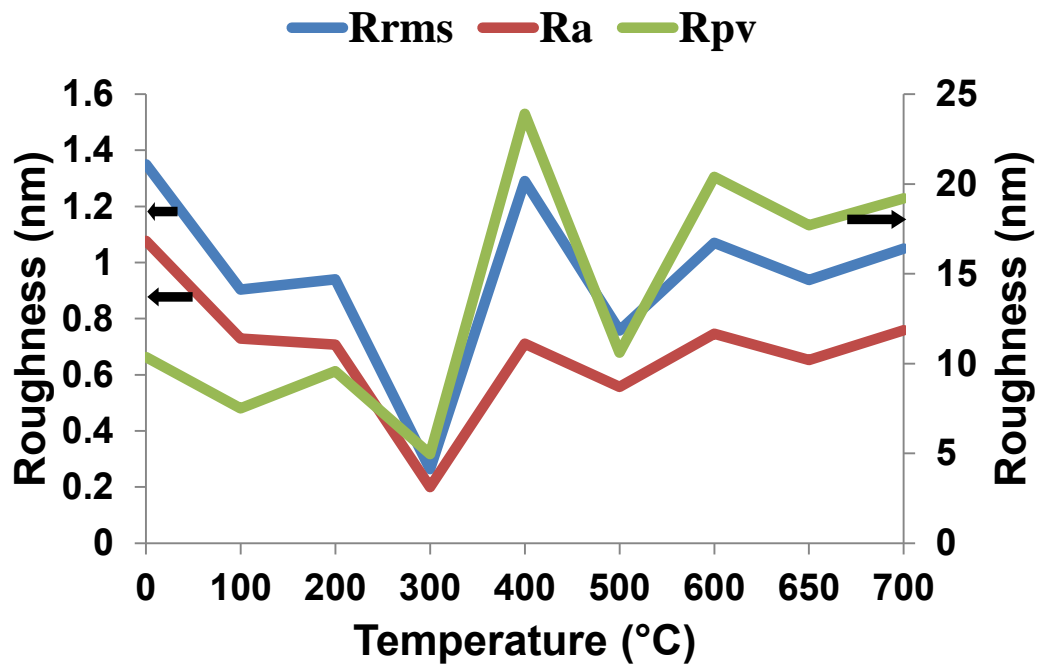


Figure 3-4: Plot of different surface roughness under different annealing temperatures

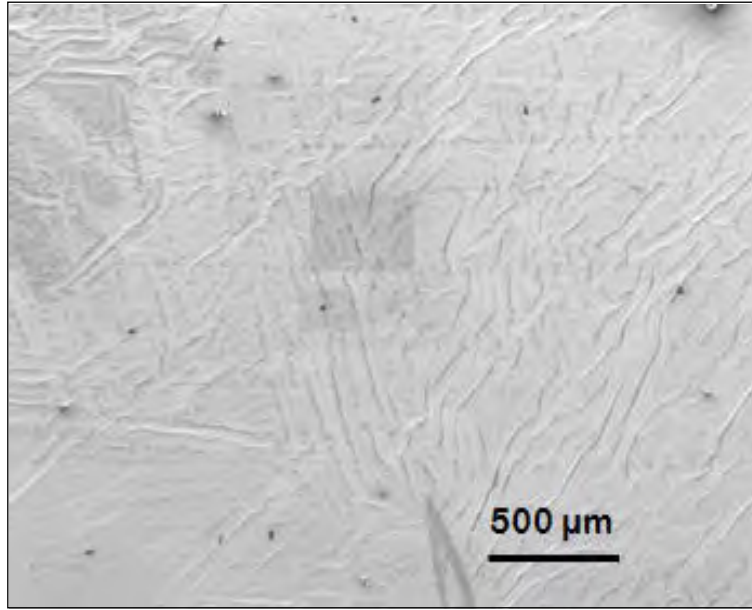


Figure 3-5: SEM image of ITO annealed at 700°C with the appearance of wrinkles and spikes

3.3.3 Crystallinity

The crystal structure and orientation of the ITO substrates are investigated using XRD. XRD patterns of the ITO substrates annealed at different temperature are presented in Figure 3-6. All the annealed ITO substrates have diffraction peaks at 21.5°, 30.5°, 35.4°, 50.9° and 60.6°, corresponding to the (211), (222), (400), (440) and (622) crystalline planes of the In_2O_3 cubic phase [122, 124]. The structure of ITO substrates annealed at 700°C are almost identical to those above 100°C exhibiting dominant (400) and (222) peaks. Sharper diffraction peaks are observed at the higher annealing temperatures which indicates a more regular crystalline structure [113]. A graph of full width half maximum (FWHM) versus conductivity of each plane is presented in Figure 3-7. For all reflections, ITO that was annealed at 700°C displayed the smallest FWHM, which correlates with the previously recorded the lowest conductivity.

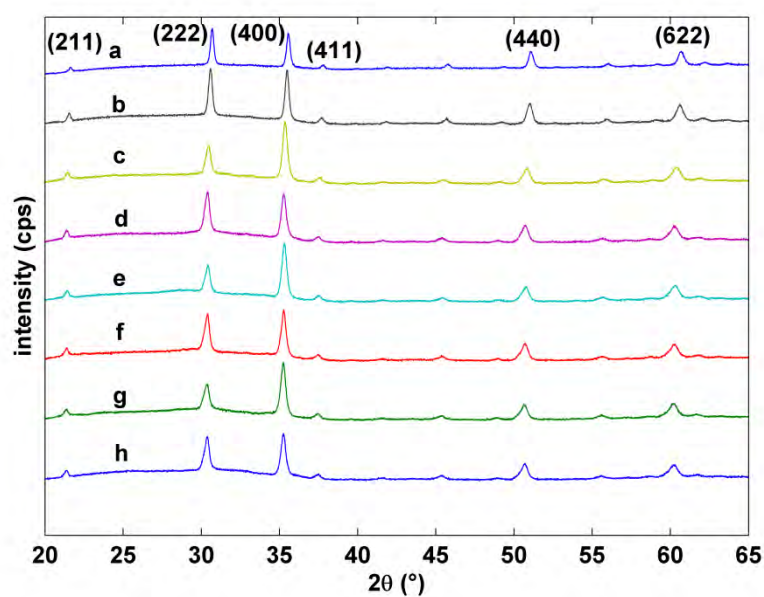


Figure 3-6: X-ray diffraction pattern of ITO substrate after annealing at (a) 700°C, (b) 600°C, (c) 500°C, (d) 450°C, (e) 400°C, (f) 300°C, (g) 200°C & (h) 100°C

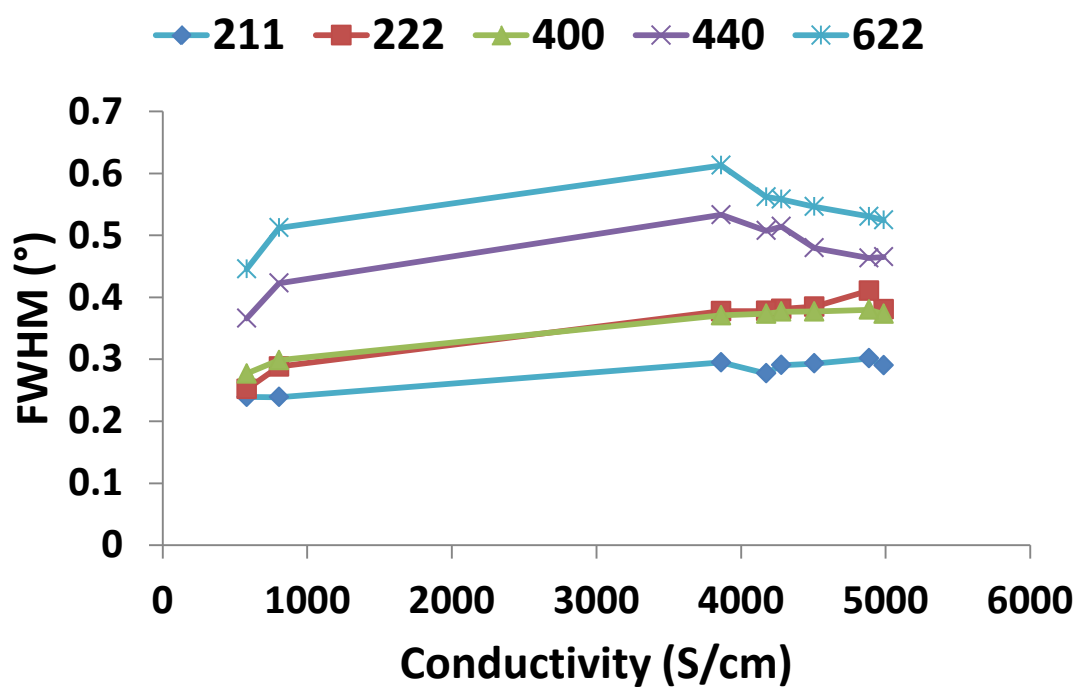


Figure 3-7: Graph of FWHM versus conductivity of (211), (222), (400), (440) & (622) planes

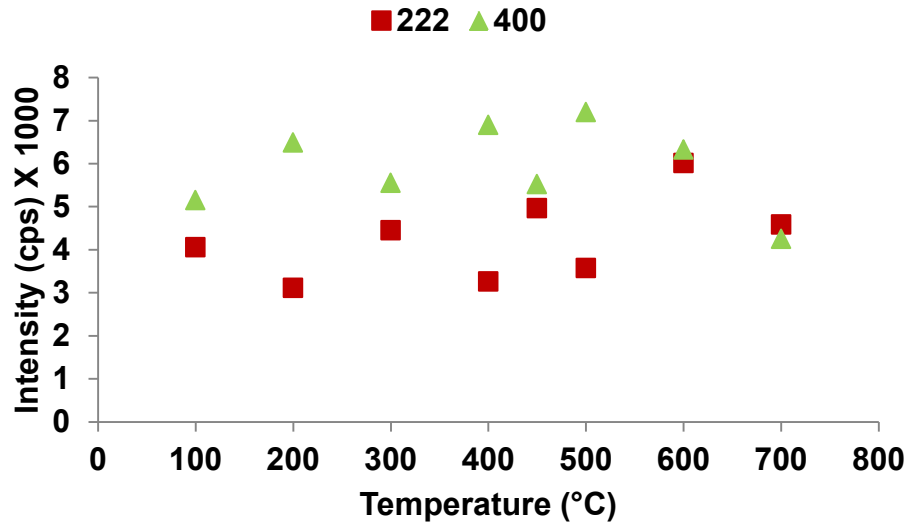


Figure 3-8: Peak intensity of (222) and (400) versus annealing temperature

As shown in Figure 3-8 the relatively stronger peak intensity at 35.4° is indicative of a preferential (400) orientation of non-annealed ITO and ITO annealed up to 600°C . In addition, the intensity of the (400) and (222) peaks increases with increasing annealing temperature, with the intensity of the (400) peak dropping for temperatures above 600°C .

One possible explanation for the observed and decrease in conductivity at high annealing temperatures is that arises from the absence of oxygen vacancies. A previous report on the incorporation of oxygen into ITO structure, which can decrease the number of oxygen vacancies and hence reduce conductivity, indicated a corresponding enlargement of grain size [109]. From Scherrer's formula, the crystallite grain size is calculated as:

$$D = \frac{0.9\lambda}{\beta \cos \theta} \quad (3-3)$$

Where,

D = grain size,

λ = wavelength of X-rays used (1.5405 \AA),

β = FWHM (in radians) and

θ = angle of diffraction

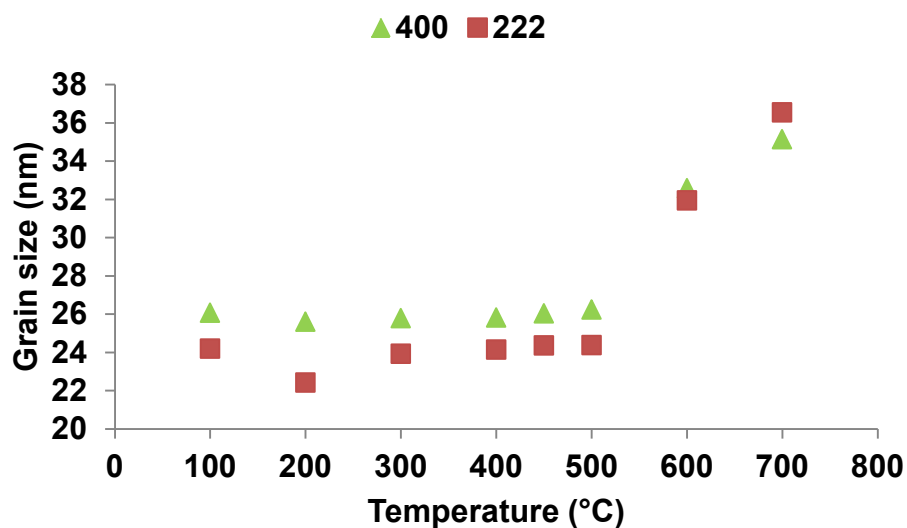


Figure 3-9: Grain size of crystallites for (400) and (222) planes versus annealing temperature

The variation of crystallite grain size with the annealing temperature calculated from the (400) and (222) reflections is shown in Figure 3-9. The grain size calculated from the both reflections are in relatively close agreement and show that ITO substrates with higher crystallinity (annealed at 700°C) recorded the larger grain size of 36.54 nm. The increase in grain size with the annealing temperature (indicated by the sharper diffraction peak at (222) orientation) is most likely due to increased thermal energy for crystallization, re-crystallization and grain growth. In addition, Figure 3-5 shows that wrinkles and cracks appeared on the film surface at 700°C; consistent with significant reorganisation of the ITO film at high temperatures.

The smaller grain size of 22.42 nm obtained for ITO annealed at 200°C is supported by the broader diffraction peak arising from the (222) plane at $2\theta = 30.33^\circ$. Interestingly, the grain sizes calculated by XRD are much higher than those observed by AFM. This difference may arise from the fact that XRD is able to probe the grain thickness normal to the substrates. On the other hand, AFM may be imaging a non-spherical or spherical grain structure that is smaller at the surface of the substrate.

Figure 3-8 also shows that the dominant crystallite orientation of annealed ITO substrate changes from the (400) plane to (222) plane with increasing annealing temperature. This observation further supports the assumption that higher annealing temperatures assist the ITO substrate to crystallize along the preferred (222) plane.

The decrease in conductivity that is observed during the change in crystallization from the (400) to (222) predominant planes indicates that the former structure has better conductivity. Previous studies have shown that, poor ITO crystallinity is usually associated with lower conductivity [125]. However, here we see that the conductivity of annealed ITO reduces at higher annealing temperature despite an increase in crystallinity and grain size as observed by XRD. One possible explanation is that the growth of larger ITO crystal grains could decrease the free electron charge density and increase the amount of electron-electron scattering [109]. Alternatively, it is well known that the charge carriers of ITO films are created by the substitution of In^{3+} by Sn^{4+} ions in In_2O_3 lattices and doubly charged oxygen vacancies [105, 113]. As such, the observed decrease in conductivity may arise from the decrease of electrically active tin dopant concentration and oxygen vacancies rather than the film crystallinity.

Another possible mechanism for the increase in resistivity could be due to enhanced diffusion of oxygen atoms into the ITO films [108]. The higher annealing temperature applied to ITO is likely to supply and incorporate more oxygen atoms which would most likely diminish the oxygen vacancy density since the thermal annealing is done in an air atmosphere. Additionally, the change of preferred crystal growth orientation is greatly affected by the diffusion of oxygen atoms during the higher heat treatment. This phenomenon can be further explained by the competition between the diffusion of oxygen atoms and increase in grain growth. As mentioned earlier, the smaller grain size obtained at lower annealing temperature has exhibited higher conductivity compared to the ITO with bigger grain size which recorded the lower conductivity. Taking into account only the increase in grain size effect, it is projected that conductivity of the ITO would increase since an enhanced grain size would lower grain boundary scattering [108]. However, due to the higher annealing temperature, oxygen atoms unavoidably diffuse into the ITO and have a greater influence on the reduction of carrier concentration (by occupying oxygen vacancies) than the observed increase in grain size.

3.3.4 Optical Properties

The optical absorption of annealed ITO in a wavelength range of 300 – 800 nm is shown in Figure 3-10. Compared to the spectrum of non-annealed ITO, spectra displayed by ITO annealed between 300 - 650°C exhibit little change in optical absorption and have the same absorption peak at 387 nm. Thus, ITO substrates preserve their high optical transmission even after annealing temperatures up to 650°C. However, pronounced changes in optical absorption can be seen at an annealing temperature of 700°C.

The optical absorption of ITO annealed at 700°C increases at longer wavelengths compared to lower temperatures. This observation arises from a drastic increase in absorption background. The rougher surface generates intense light scattering which brings about the increase in background absorption [126]. This hypothesis is supported by the significant differences in surface roughness values displayed in Figure 3-4 between ITO annealed at 300°C and ITO annealed at 700°C. Indeed, ITO that has been annealed at 700°C has an almost four-fold rougher surface than ITO that has been annealed at 300°C. In addition, ITO that has been annealed at 700°C also displays a lack of an absorption peak at 387 nm. Low conductivity can be determined from the low absorption in this visible region [127]. The UV-vis spectrum portrayed by ITO substrate annealed at 700°C is consistent with the lowest conductivity and larger grain size obtained in this study.

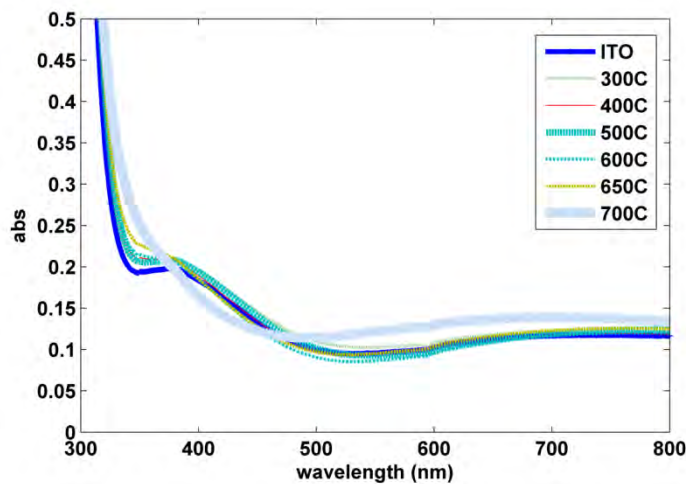


Figure 3-10: UV-vis absorption spectra of ITO annealed at different temperature

3.3.5 Chemical Composition

The conductivity is also related to the carrier concentration and its mobility. The charge carriers in ITO are created by the tin dopant and oxygen vacancies in the film. Each tin dopant generates one electron and another two electrons can be provided by an oxygen vacancy [105]. Annealing ITO can reduce the number of oxygen vacancies through reaction with oxygen from the air and so reduce the carrier concentration [113]. In order to probe the compositional changes that occur in the film upon annealing, EDS and XPS were used to characterise the surface and bulk concentration of the key components.

3.3.6 Bulk Measurements

The EDS spectra of annealed ITO substrates together with their corresponding elemental analyses are shown in Figure 3-11. EDS is less sensitive to surface chemistry changes than XPS due to the penetration depth (10 μm) of the incident electron beam and the lack of scattering of the ejected X-rays. It can provide qualitative and quantitative analysis of elements in the bulk substrate at up to 10 μm depth [128]. A gold thin film was used as a conductive coating in sample preparation. The same amount of gold coating was used for the further calibration of each sample by taking the gold intensity peak as reference.

As expected, the main components of the glass substrate, such as silicon, sodium, magnesium and aluminum, were detected in the EDS spectra. Although the thickness of the ITO coated on the glass is only approximately 170 nm, the EDS spectra exhibit clear peaks due to the presence of indium and tin. Although indium oxide is a semiconductor, it is not a highly conductive material. Thus, tin is added to indium oxide as a dopant and as electron donor. However, there is a limitation to the electron concentration that can be added to indium oxide. High electron concentration can lead to a reduction in electron mobility and low conductivity [129].

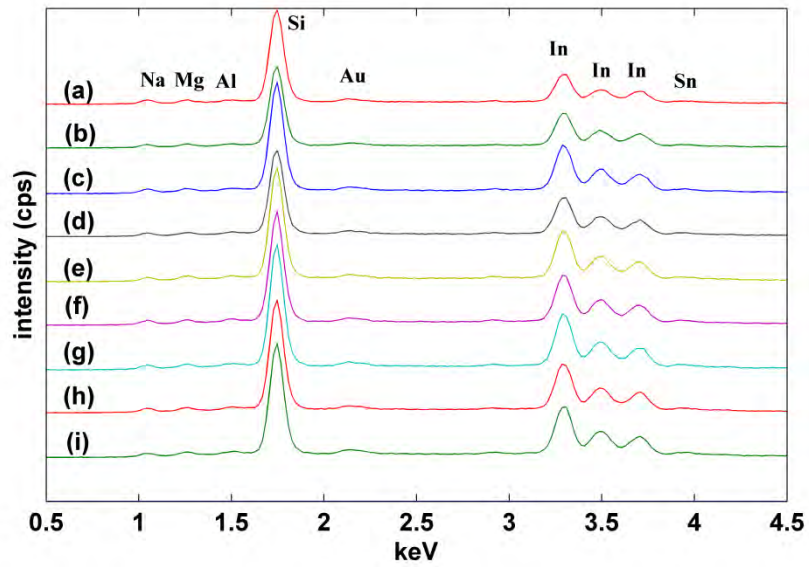


Figure 3-11: EDS spectra of ITO substrate before (a) and after annealing at (b) 100°C, (c) 200°C, (d) 300°C, (e) 400°C, (f) 450°C, (g) 500°C, (h) 600°C & (i) 700°C

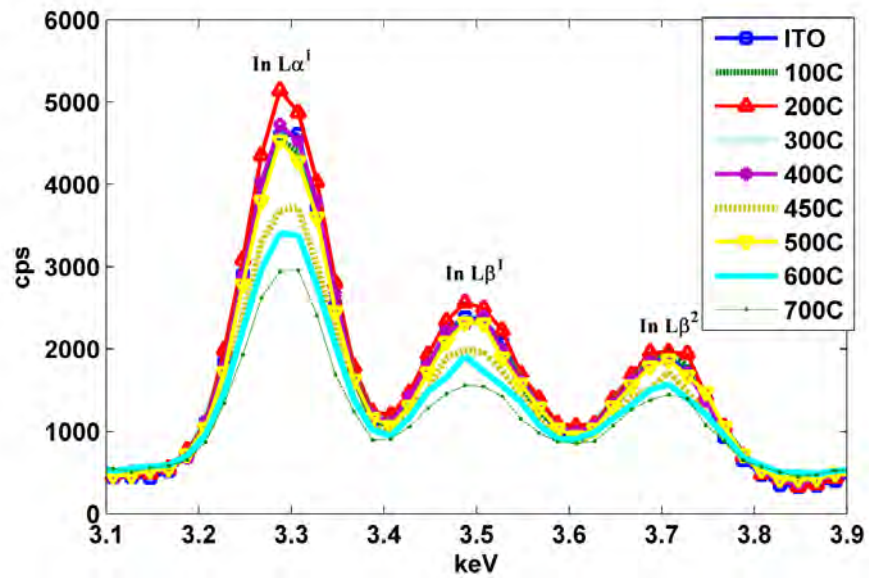


Figure 3-12: EDS spectra of indium peaks of ITO annealed at different temperature

High resolution EDS spectra at each annealing temperature (Figure 3-12) show the presence of indium $L\alpha^1$, $L\beta^1$ and $L\beta^2$ peaks at 3.3 keV, 3.5 keV and 3.7 keV, respectively. Given that the indium $L\alpha^1$ at peak 3.3 keV exhibited a much larger intensity compared with indium $L\beta^1$ and indium $L\beta^2$, only indium $L\alpha^1$ peak was

considered for further compositional analysis. Figure 3-12 reveals that the bulk composition of indium was substantially altered at the higher annealing temperatures.

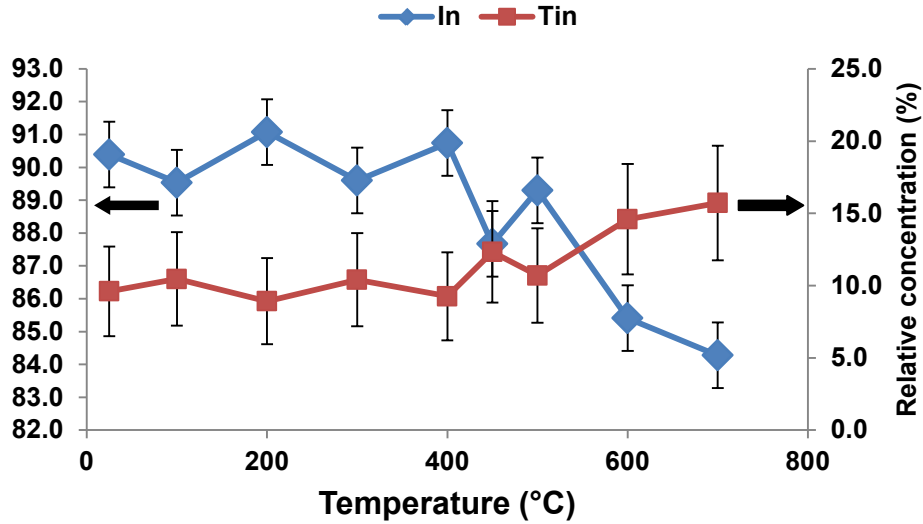


Figure 3-13: Relative concentration (%) of indium and tin in the bulk composition under different annealed temperature

The variation of indium and tin composition with annealing temperature is shown in Figure 3-13. Interestingly, the decrease in indium bulk composition observed for annealing temperatures between 500°C to 700°C follows the conductivity measurements. This decreasing indium signal indicates that the concentration of indium within the analyzed depth of 10 μm is reduced upon annealing to high temperatures and indicates that the indium is probably diffusing out from the bulk region to the top surface (10 nm) or deeper into the bulk of the glass (> 10 μm).

3.3.7 Surface Measurements

To determine the elements present on the surface of annealed substrates, XPS spectra were obtained. As shown in Figure 3-14a carbon, oxygen, indium and tin were observed in these spectra. The high-resolution XPS narrow scan indicates indium, tin and oxygen peaks are shown in Figure 3-14b. Indium, tin and oxygen are expected from the chemical surface composition of the ITO thin film coated onto glass. The carbon peak at 285 eV is seen in all spectra and is due to contamination on the sample surface from isopropanol during the cleaning treatment [130]. In addition, the carbon contamination

may also be due to a short exposure to air during the transportation and from a slight perpetual contamination in the preparation chamber of the XPS system [131].

In this analysis, emphasis is given to the elemental compositional changes that occur upon annealing, in particular, the composition of indium, tin and oxygen before and after annealing. The XPS spectrum obtained from an unannealed ITO substrate is used as a reference. Indium peaks are seen at approximately 444.5 eV ($\text{In}3d_{5/2}$) and 453.1 eV ($\text{In}3d_{3/2}$), while peaks at 486.5 eV ($\text{Sn}3d_{5/2}$) and 495.1 eV ($\text{Sn}3d_{3/2}$) are assigned to tin. The observed O1s peak at 530.3 eV can be assigned to the oxygen species in ITO. The atomic concentrations are determined from the area intensities of the $\text{In}3d_{5/2}$ (444.5 eV), $\text{Sn}3d_{5/2}$ (486.5 eV) and O1s (530.3 eV) peaks under the different annealed temperatures. The binding energy of $\text{In}3d_{5/2}$ (444.5 eV) and $\text{Sn}3d_{5/2}$ (486.5 eV) is attributed to the In^{3+} bonding state from In_2O_3 and to the Sn^{4+} bonding state from SnO_2 , respectively [117]. Therefore, the indium and tin atoms that are present in the chemical state of In^{3+} and Sn^{4+} , respectively, can be used as a reference to the existence of metallic particles.

The relative atomic concentration (%) of indium and tin as a function of annealing temperature are presented in Figure 3-15. The initially In-rich surface layer becomes steadily depleted of In with increasing annealing temperature, reaching a minimum at 600°C, before rising sharply again at 700°C. This observation is in contrast with the bulk compositional measurements (Figure 3-13), which showed the In concentration decreasing monotonically up to 700°C. As such, the compositional analysis reveals that whereas for temperatures up to 600°C indium is rapidly depleted from the surface, upon heating to 700°C it starts to accumulate back in the surface. This observation is in good agreement with the SEM image of ITO annealed at 700°C (Figure 3-5) which shows the appearance of small particles on the surface of the film.

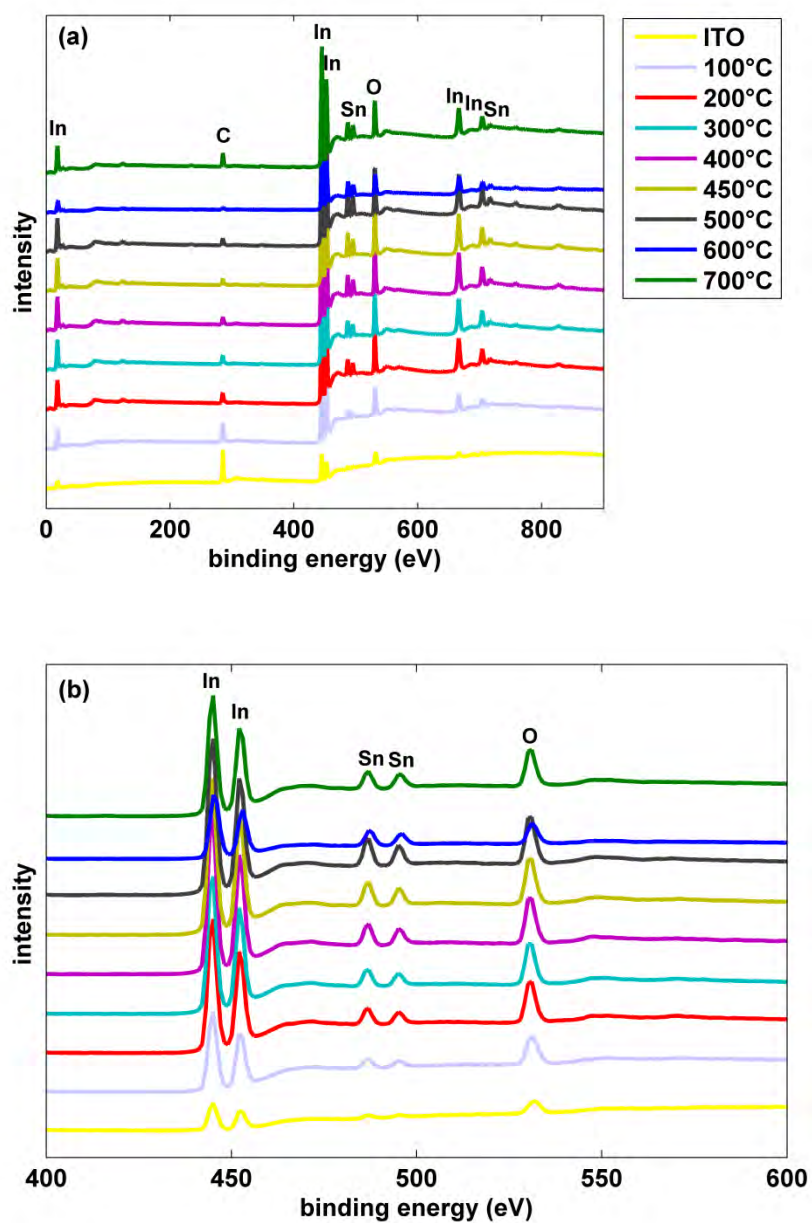


Figure 3-14: XPS spectra of ITO annealed at different temperatures: (a) wide scan & (b) narrow scan

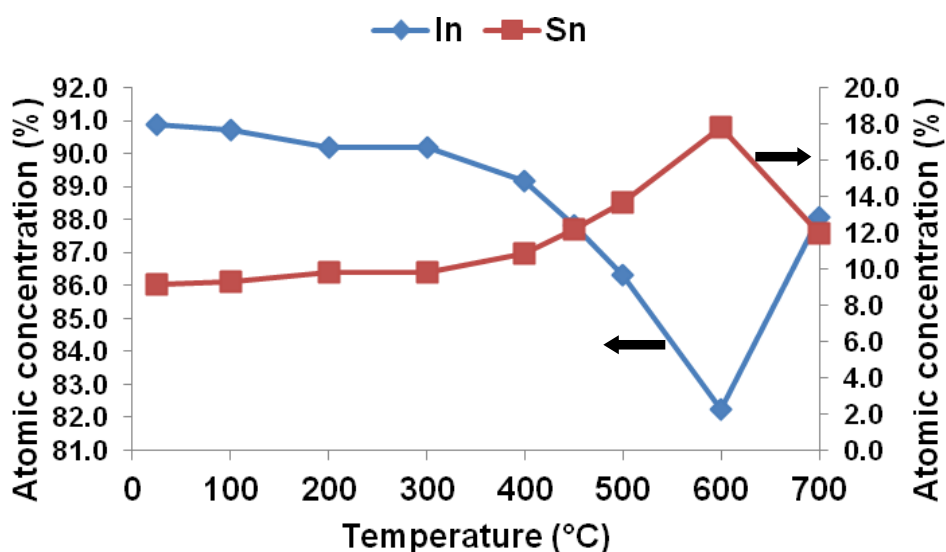


Figure 3-15: Atomic relative concentration (%) of indium and tin at the surface under different annealed temperature

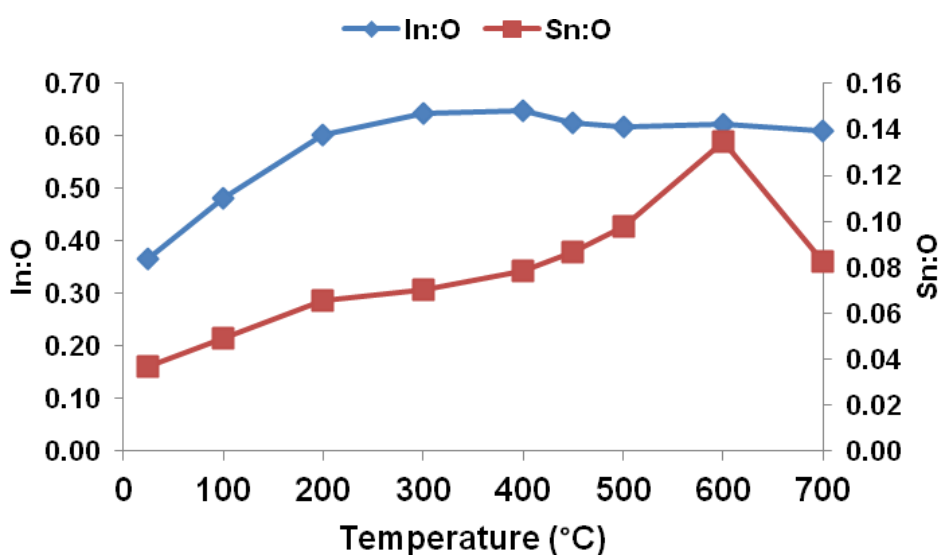


Figure 3-16: Ratio of In:O and Sn:O under different annealed temperatures

In order to further understand the origin of the changing electrical conductivity, both the In:O and Sn:O ratios were plotted as a function of annealing temperature. Figure 3-16 shows that both the In:O and Sn:O ratios increase with increasing annealing temperature with the Sn:O ratio dropping off rapidly at 700°C. It is unlikely that the increasing In:O and Sn:O ratios are associated with the depletion of oxygen from the film since this would result in an increase in oxygen vacancy. Rather, we propose that as the annealing

temperature increases, In and Sn diffuse to the surface of the film. Interestingly, the increase in Sn dopant concentration does not correlate with an increase in film conductivity and thus we conclude that the higher tin ion substitution into the lattice must contain electrically inactive tin dopant. Interestingly, the drastic decrease of tin dopant concentration from 600°C to 700°C is correlates well with the observed reduction of film conductivity and the change of preferred crystal growth plane orientation from (400) to (222).

As discussed previously, the conductivity of ITO is also dependent upon the oxygen concentration in the film and the nature of this oxygen content can be probed using the oxygen 1s peak in the XPS spectrum. It is well known that O 1s spectrum can be fitted using three peaks with a Gaussian-Lorentzian function as shown in Figure 3-17. These three peaks (O 1s A, O 1s B and O 1s C), are located at 530.3, 533.0 and 531.9 eV, respectively and a different chemical state is associated with each O 1s peak. Peak O 1s A is assigned to In_2O_3 lattice oxygen where the indium ions are fully bonded with the neighbouring O^{2-} ions, whereas peak O 1s B and O 1s C correspond to oxygen chemisorbed on the ITO surface and oxygen atoms bound to tin atoms, respectively [132].

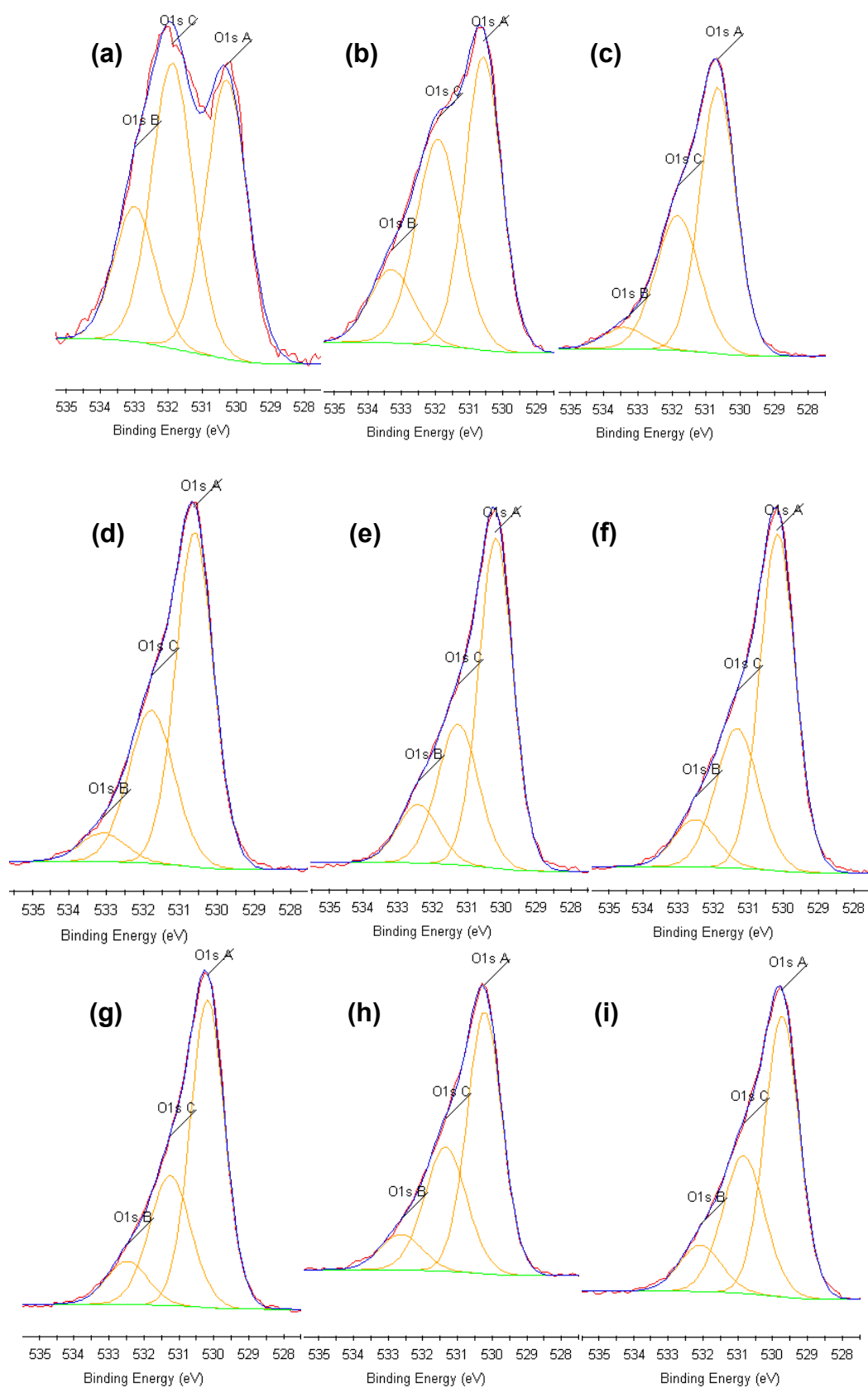


Figure 3-17: XPS spectra in the O1s region of ITO substrate before (a) and after annealing at (b) 100°C, (c) 200°C, (d) 300°C, (e) 400°C, (f) 450°C, (g) 500°C, (h) 600°C & (i) 700°

The relative concentration percentage of O 1s chemical state is summarised in Figure 3-18 with the highest intensity associated with O 1s A at 530.3 eV corresponding to lattice oxygen in the crystalline ITO. As the annealing temperature is increased, the number of indium ions that are fully bonded to the neighbouring O^{2-} ions increases, reaching a maximum at 450 – 500 °C before decreasing again slightly at annealing temperatures of 600°C and above. The corollary of the observed increase in the number of indium atoms fully bonded with oxygen is that the number of oxygen vacancies in the lattice must necessarily be decreased, resulting in a decrease in film conductivity. Figure 3-18 also shows that intensity of O 1s C at 531.9 eV (attributed to the presence of oxygen atoms bound to tin) as a function of temperature mirrors the intensity of O 1s A, reaching a minimum at 450 – 500 °C before increasing again slightly at annealing temperatures of 600°C and above. As such, it appears that the higher conductivity of the unannealed ITO occurs when there is an equal composition of both: (i) indium ions that are fully bonded with the neighbouring O^{2-} ions (In_2O_3 lattice oxygen) and (ii) oxygen atoms bound to tin atoms. The intensity of the (O 1s C):(O 1s A) ratio decreases with annealing temperature indicating a reduced delocalization of excess electron density across multiple oxygen atoms.

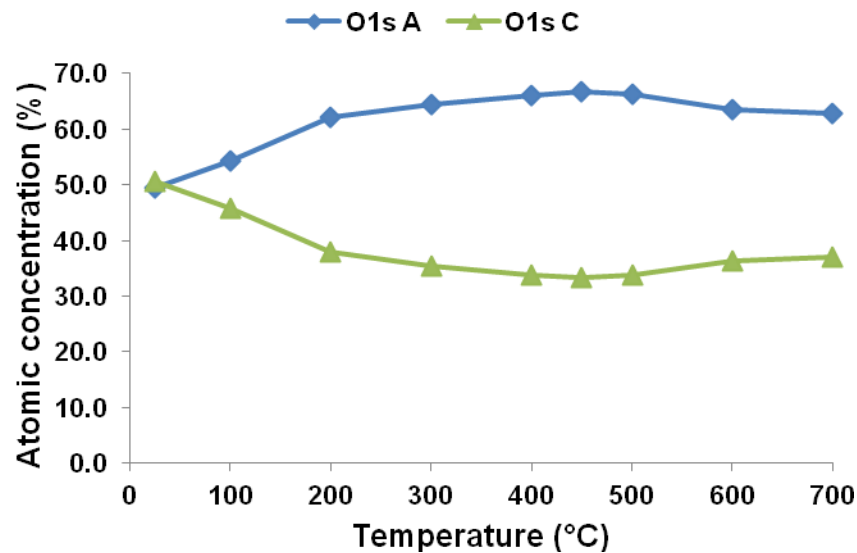


Figure 3-18: Atomic relative concentration (%) of O 1s chemical state versus annealing temperature

3.3.7.1 Combining the Bulk and Surface Compositional Measurements

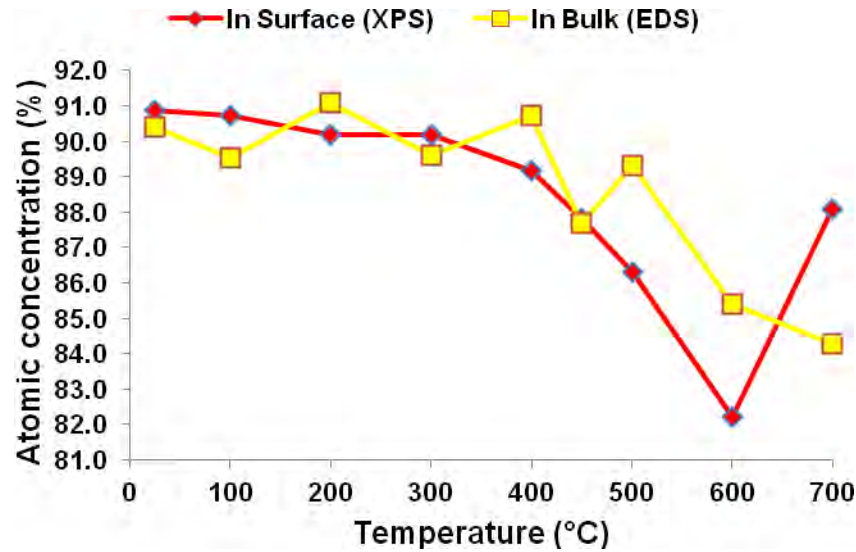


Figure 3-19: Atomic relative concentration of indium at the surface and in the bulk under different annealed temperature

Figure 3-19 shows the relative concentration percentage of indium both at the surface and in the bulk as the annealing temperature is increased. The atomic concentration of indium at the surface and in the bulk is quite similar, and both decrease systematically for annealing temperatures up to around 450 °C. At this point, while the bulk indium concentration continues to decrease monotonically, the surface indium composition decreases more rapidly up to 600 °C before increasing dramatically at 700 °C.

Interestingly, at an annealing temperature of 700°C, the indium composition in the bulk is reduced while more indium is obtained at the surface. Thus, when ITO is heated to 700°C, indium diffuses up to the top surface layer and dominates the top 10 nm layer thickness. The observation that indium (and tin) diffuse into the surface layer is consistent with previous work by Alet et al who showed that at 300°C, indium and tin from ITO substrate begin to diffuse out from the bulk into the surface layer [18].

The reduction of indium composition in the bulk also correlates well with the decrease of ITO conductivity as the annealing temperature is increased; consistent with conductivity being primarily a bulk phenomenon. In addition, the indium concentration indium is higher than tin for all of the substrates and, since oxygen is also observed,

In_2O_3 is assumed as the main component in ITO [133]. The indium bulk composition generally decreases over the annealing temperature as shown in Figure 3-19. As the annealing temperature is increased, indium moves to the surface of the layer.

We observe that the bulk concentration of indium remains essentially with the same as the surface concentration of indium until 500 °C. It is possible to speculate that the small fluctuations in indium composition (primarily in the bulk) that are observed in Figure 3-19 are related to the re-crystallization, diffusion and grain growth processes that occur during annealing. At 500 °C, the surface concentration of indium begins to fall before it rises at rapidly at 700 °C. At 700 °C we also see a rapid decrease in tin surface concentration. It is well known that indium and tin have a relatively low melting temperatures of 157 °C [12] and 232 °C [22], respectively. As such, Figure 3-19 is consistent with the decomposition and evaporation of indium and tin upon thermal annealing to high temperatures [119, 134]. Indeed, this high temperature behavior suggests a model which involves indium and tin evaporation from the ITO surface, with indium evaporation activated first (~ 500 °C) and then tin evaporation activated (~ 700 °C). At 700 °C, the bulk indium and tin species also becomes more surface mobile, resulting in the formation of metallic particles on the surface.

3.4 CONCLUSION

This chapter demonstrates that the behavior of ITO films upon annealing is complex and involves structural and chemical changes in both the surface and bulk of the film. Structurally, we observe that both the ITO grain size and the crystallinity of the grains change dramatically upon annealing; the grains increase in size and the dominant crystal plane changes from (400) to (222). The increased grain size and change in crystallinity is consistent with a decrease in oxygen vacancies in the ITO film, which would be expected to lead to a corresponding decrease in conductivity. This hypothesis is supported by EDS and XPS compositional analysis, which indicate that as the indium and tin diffuse to and evaporate from the film surface with increasing temperature, the oxygen vacancy density systematically decreases. Moreover, despite an increase in relative tin dopant concentration, the conductivity continues to decrease suggesting that the tin species is electrically inactive.

The measurement of ITO conductivity is particularly important for the carbon and polymer nanostructure growth and especially in relation to the fabrication of OPV devices from these materials. We observe that at higher temperatures the indium and tin become mobile in the bulk ITO and begin to form particles on the ITO surface. This corresponds to a significant change in the bulk ITO properties, resulting in an undesirable decrease in conductivity. As a result, this chapter informs our subsequent work on the CVD growth of nanostructures and indicates that, in order to maximize the conductivity of ITO films, low temperature growth is required. Consequently, temperatures of up to 500°C have been used for the CVD growth throughout the rest of this work. Apart of preserving the initial conductivity, the low temperature growth also minimizes the degradation of the physical and chemical substrate properties.

4 CHEMICAL VAPOUR DEPOSITION OF CARBON NANOSTRUCTURES ON INDIUM TIN OXIDE

4.1 INTRODUCTION

4.1.1 Overview

In this chapter we describe the synthesis of carbon and semiconducting-oxide nanostructures on an indium tin oxide (ITO) substrate. Due to the lack of literature on the growth of carbon nanostructures on ITO, and their potential benefits to OPV architecture, we have undertaken a study of the influence of certain experimental parameters, particularly growth temperature, growth time and growth pressure, upon carbon nanostructure growth. Taking consideration of the results presented in Chapter 3, a low growth temperature of between 400 and 500°C has been used for carbon nanostructures growth on iron-coated ITO, since no growth occurs below 400°C and the loss of ITO conductivity is kept to a minimum of ~ 33% with no significant physical deformation being observed.

A wide variety of carbon and metal oxide growths has been observed in this work, ranging from amorphous carbon to carbon nanotubes and metal oxide nanowires. The hydrogen plasma treatment which was applied to remove unwanted deposited amorphous carbon layer is described in Section 4.3.4.2. One significant observation in this work, presented in Section 4.3.5.2.4, is the observation of the growth of indium oxide nanowires encapsulated by a carbon layer which occurs within the parameter range studied. A growth mechanism is proposed for the indium oxide nanowire formation which explains the observed encapsulation by a structured carbon layer.

The effect of varying the conditions used in the CVD process has been widely studied for carbon nanostructure growth [135-140]. These variables include the flow rate, the ratios of hydrocarbon gases, catalyst preparation, catalyst selection, growth temperature, time and growth pressure. Different types of nanostructures have been grown by varying these parameters. This work represents an initial study of the growth morphology of carbon nanostructures and indium oxide nanostructures on iron-coated

ITO, examining the effects of the catalyst, growth time, growth temperature and system pressure upon the growth.

4.1.2 Carbon nanostructures on ITO

Due to their unique electronic properties, the integration of carbon nanostructures into optoelectronic applications has been of great interest in recent years [1-3, 8, 9, 64]. For example, a significant three-fold efficiency increase has been observed by integrating carbon nanostructures into organic solar cells [1]. This improvement is thought to be because the nanostructures enhance the charge separation of excitons created in the polymer matrix, and efficiently transport electrons to the cathode [1].

The creation of large area electrodes with carbon nanostructures grown directly onto the substrates is an opportunity offered by CVD. Indeed, the growth of carbon nanostructures directly onto substrates such as alumina, silicon dioxide, glass and ITO has already been carried out by chemical vapour deposition (CVD) [8, 55]. Moreover, the dimensions of carbon nanostructures grown directly onto a substrate can be better controlled compared with the method of simply mixing carbon nanostructures within the polymer matrix. The nature of the deposition substrate will allow control of the growth rate and morphology of these carbon nanostructures. For example, according to Miller et al [8], carbon nanostructures grown on ITO exhibit a slower growth rate than on a glass substrate. This difference offers control over the height of the nanostructures, which will be of benefit to their use in organic solar cells.

Figure 4-1 and Figure 4-2 show the SEM and TEM images of the carbon nanostructures grown on ITO as reported by Miller et al [8]. Nickel was used as a catalyst in this case with acetylene as the carbon source at a temperature of 550°C. A tip-growth mechanism is proposed due to the nickel particles observed sitting at the tip of the nanostructure. However, the authors claim contamination of the nickel catalyst by indium and tin that originated from the ITO substrate. The contamination of both indium and tin leads to a slower growth rate of the carbon nanostructures when compared with the growth rate of carbon nanostructures grown on the glass substrate. In addition, the formation of multiwall carbon nanostructures is identified from the TEM images. As reported by Pan et al [140], carbon nanocoils have been successfully grown on iron-coated indium tin

oxide. A high growth temperature of 700°C was used in this synthesis. Figure 4-3 shows the SEM image of the carbon nanocoils that were synthesised via CVD. The authors studied the roles of both iron and ITO as a catalyst and suggest that they are responsible for the formation of nanotubes and the helical growth of the nanotubule respectively.

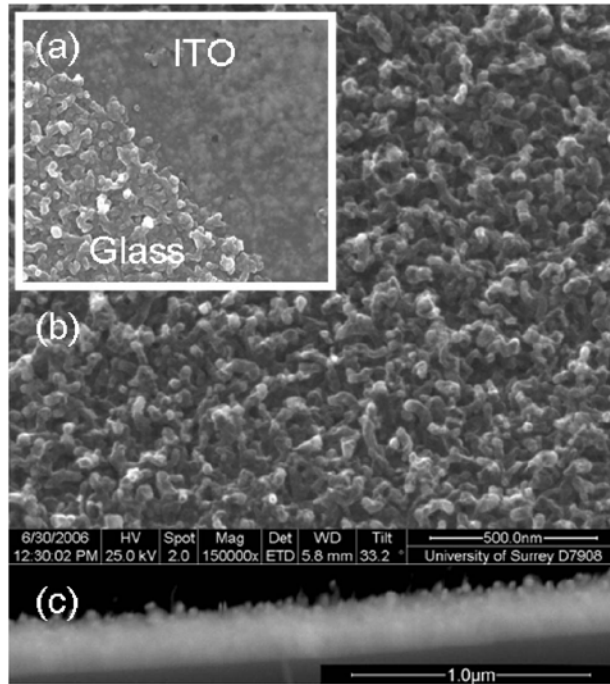


Figure 4-1: SEM images of (a) carbon nanostructures grown on glass and ITO under similar growth conditions (b) carbon nanostructures grown on ITO & (c) cross sectional view of carbon nanostructures grown on ITO [8]

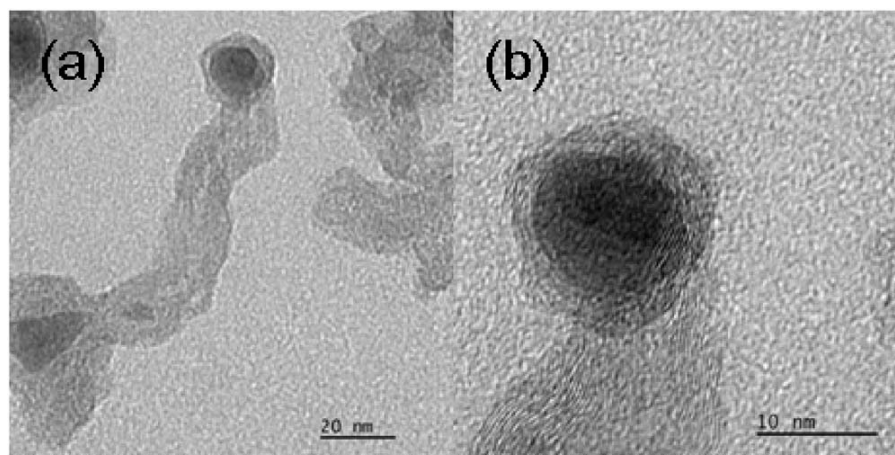


Figure 4-2: TEM images of carbon nanostructures grown on ITO of (a) lower magnification & (b) higher magnification clearly showing the catalyst at the tip of the structure [8]

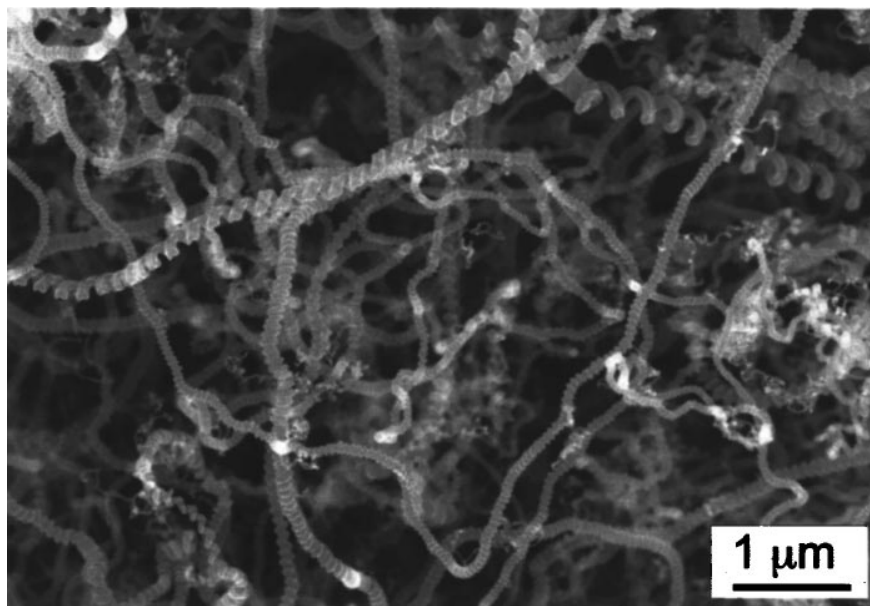


Figure 4-3: SEM image of carbon nanocoils grown at 700°C [140]

An issue for the potential use of these nanostructures in OPV devices is electrical shorting in these films due to bridging of the nanostructure across the entire active layer. This problem can be overcome since the length of carbon nanostructures grown via CVD is a dimension that can be readily controlled [55]. Apart from controlling carbon nanostructure dimensions, CVD of carbon nanostructures on ITO could also improve the contact between the substrate and the nanostructures. Carbon nanostructures that are grown via CVD on ITO substrate are directly bonded to the substrate and contact between them is likely to be enhanced [8]. This direct contact should provide a continuous pathway for charges to the external circuit [65].

4.1.3 Semiconducting nanostructures

Like their carbon counterparts, semiconducting nanostructures such as silicon nanowires [18, 141], zinc oxide nanowires [142], tin nanowires [22], indium oxide nanorods [143], indium germanate nanotubes [144], germanium nanowires [17] and indium tin oxide nanowires [5, 16] have been grown to examine their application in nano- and opto-electronics. These semiconducting nanomaterials were synthesised by various methods, and a range of different growth mechanisms have been proposed.

Most semiconducting nanostructures are thought to form via the vapour-liquid-solid (VLS) mechanism [16, 22, 142, 144]. In this mechanism, solid source material is heated to temperatures where vaporisation occurs. Figure 4-4 shows a schematic diagram of the proposed growth of tin nanowires encapsulated in amorphous carbon nanotubes by the VLS mechanism. Under this mechanism [22] tin powder is vaporised at 900°. Tin vapour can then be transported to the substrate where it undergoes condensation and formation of a liquid droplet [144]. Incoming tin vapour accumulates on the existing liquid droplet, resulting in an increase of the tin liquid droplet size. A liquid droplet can then act as a catalyst and becomes encapsulated within the carbon nanotubes thus formed. This growth involves the diffusion of carbon into the liquid droplet and then precipitation of carbon onto the catalyst surface.

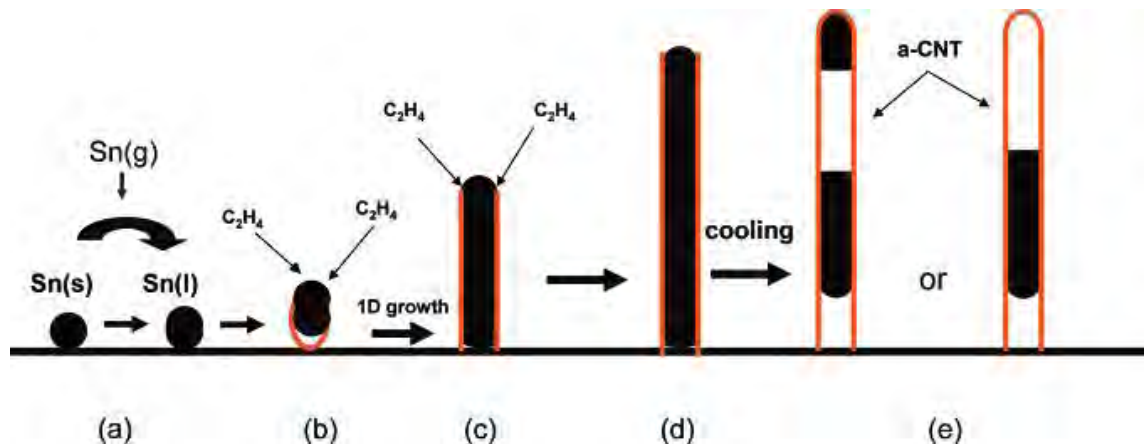


Figure 4-4: Schematic diagram of tin nanowire growth by the VLS mechanism [22]

A solid-liquid-solid (SLS) mechanism, which is directly comparable with the VLS mechanism, has been suggested in the growth of silicon nanowires [141]. In SLS, the silicon substrate is used as a source material which leads to the formation of silicon liquid droplets. The SLS mechanism does not require as high a growth temperature as VLS, since no vapour phase is involved. Figure 4-5 shows a schematic illustration of the proposed growth of silicon nanowire by the SLS mechanism.

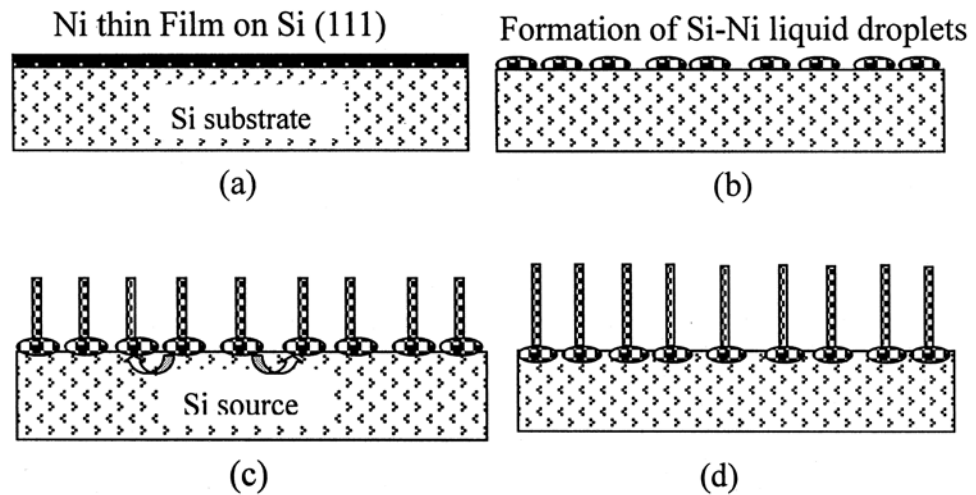


Figure 4-5: Schematic depiction of silicon nanowire growth by the SLS mechanism [141]

In this scheme [141] a thin film of nickel is evaporated onto the silicon substrate. At a certain temperature, liquid droplets composed of silicon and nickel is formed. Silicon from the bulk silicon substrate then moves into the droplet as wire growth proceeds. In order for a silicon nanowire to grow, silicon atoms need to diffuse into the droplets until saturation of silicon atoms occurs which leads to nanowire formation.

In situ generation of source materials as a catalyst can be achieved directly from the substrate for semiconducting nanostructure formation [18, 141, 143]. Alet et al [18] have reported on the growth of silicon nanowires from indium catalyst droplets which were generated from the ITO substrate. Plasma enhanced CVD was subsequently used to grow silicon nanowires at low temperature. Indium catalyst droplets were formed during the surface treatment using a hydrogen plasma at 250°C, and were seen sitting at the tip of the nanowires, indicating tip growth from indium catalyst particles.

The growth of semiconducting oxide nanostructures directly from the substrate was also observed by Lo et al [143]. Indium oxide nanorods have been successfully synthesised on an indium phosphide substrate with no other source of indium. Carbon that is formed from acetylene is suggested to act as a reducing agent for the formation of indium oxides, but no carbon atoms were observed to be incorporated into the semiconducting oxide nanorod. However, in other work reported on tin nanowire growth [22], amorphous carbon nanotubes grew simultaneously, and finally encapsulated the tin

nanowire. In that work, acetylene was used as the carbon source, which resulted in an amorphous carbon layer. Figure 4-6 shows the TEM images of tin nanowires that have been encapsulated in amorphous carbon nanotubes; more than one section tin nanowire is observed due to the splitting of one continuous tin nanowire upon cooling and solidification. In the figure, two non-identical regions are observed which comprise tin and carbon in the dark region and only carbon, with a very low level of tin, in the bright region. This then describes a production of hollow carbon nanostructure that allows the growth of another material (tin nanowire) within its core.

Indium from ITO has also been observed to diffuse into growing semiconducting oxide nanowires. According to Hsu et al [142], an ITO film deposited on a silicon substrate results in the diffusion of indium into zinc oxide nanowires when these are grown upon it. The ratio of indium to tin plays an important role in the diffusion, since, only indium atoms are detected at the bottom of the nanowire. The EDX spectroscopic mapping image of indium is presented in Figure 4-7.

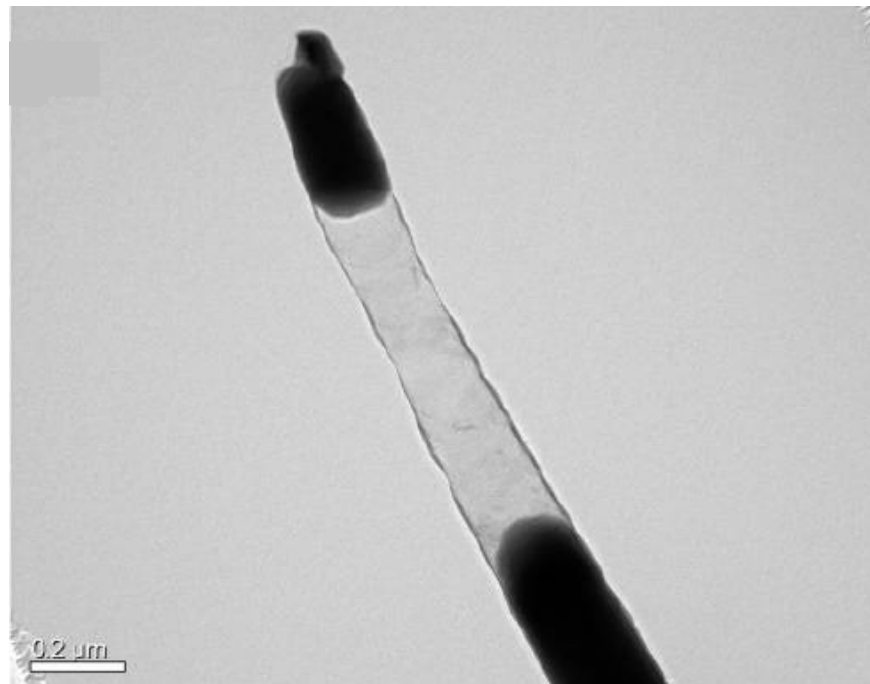


Figure 4-6: TEM image of tin nanowires encapsulated in amorphous carbon nanotube [22]

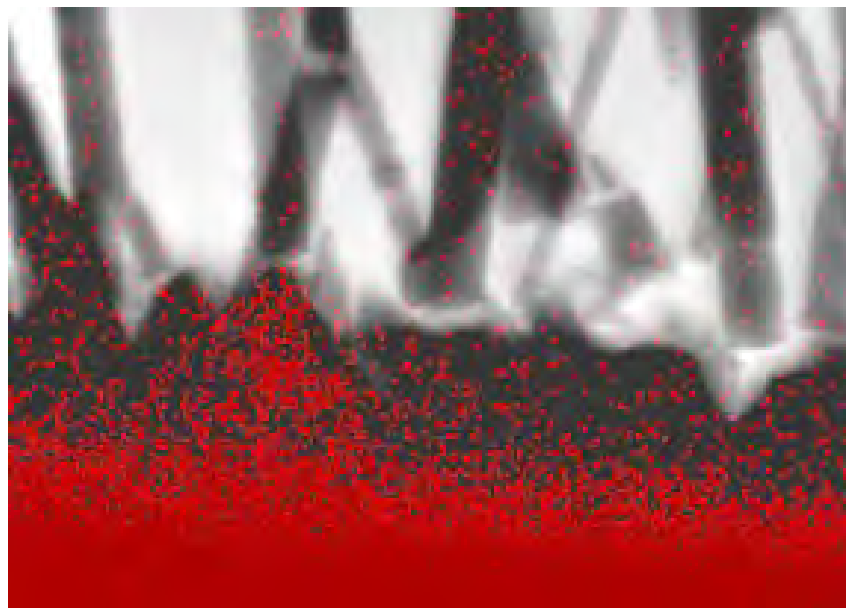


Figure 4-7: EDX spectroscopic mapping image of indium (red) at the bottom of zinc oxide nanowire [142]

The following study presents the growth of carbon and indium oxide nanostructures by CVD at low temperatures on ITO. A full study of the effect of temperature (within the imposed limitations of degradation of the ITO substrate as defined in the previous section), growth time and system pressure has been undertaken and the resulting semiconducting nanostructures characterised.

4.2 EXPERIMENTAL SETUP

The thermal CVD technique as described in chapter 2 and the recipe shown in Table 2-1 was applied to grown carbon and metal oxide nanostructures on an ITO substrate. A systematic study of growth parameters was undertaken by varying the growth temperature (400, 450 and 500°C), growth time (1, 5 and 10 min) and system pressure (100, 200, 300 and 400 Torr).

4.3 RESULTS AND DISCUSSION

4.3.1 Effect of hydrogen reduction on ITO

Reduction of the iron (Fe) film was conducted in the CVD by flowing 100 sccm of hydrogen over the substrate for 10 min at 450°C. This process is crucial for carbon nanostructure growth as it creates metal catalyst nanoparticles which allow the diffusion of carbon atoms to occur. Carbon atoms need to be absorbed into and then diffuse to the edge of catalyst particles [48] in order to further the growth of the carbon nanostructure, this is particularly important in CNT growth. The catalyst particle is always observed in the subsequent CNT structures, either sitting at the tip of the nanotube, which is defined as the tip growth mechanism, or attached to the substrate in the base growth mechanism [48].

In order to understand the carbon nanostructure growth mechanism in this work, a series of annealing experiments was carried out. Since a relatively low temperature of 450°C was chosen for the carbon nanostructure growth to avoid ITO deformation, this temperature was also applied in the reduction process. An ITO substrate without an evaporated Fe film was annealed at 450°C for three different reduction times of 10, 30 and 60 min. SEM images and XPS data were then used to observe differences in the catalyst particle formation and to quantify the particles formed under the different reduction times.

The appearance on the ITO film of indium and tin particles is shown in Figure 4-8(a-d). Figure 4-8b shows that indium and tin particles can be observed after 10 min of reduction. This image is similar to an atomic force microscopy (AFM) image obtained of an ITO film annealed at 400°C which showed hundreds of ~nm sized clusters [119]. The thickness of ITO supplied by Delta Technologies Limited is about 170 nm and particle diameter sizes ranging from 50 to 150 nm are observed after a 10 min reduction. However, increasing the reduction time to 30 and 60 min (Figure 4-8c & Figure 4-8d), apparently reduces the number of particles as well as the average particle size, possibly due to evaporation of the metals.

Annealing temperature and duration therefore clearly play an important role in the transformation of the ITO film structure. As the annealing temperature is elevated the ITO film structure becomes more crystalline [145]. As reported by Deng et al [114], thermal annealing of ITO films between 200 and 400°C results in the transformation of amorphous to crystalline films. However, this transformation was achieved using longer annealing times (between 1 and 5 h), whilst the SEM image obtained from 1 hour (Figure 4-8d) annealing time in this work does not reveal any information about a change in the crystalline structure.

A schematic illustration of proposed transformations of an annealed ITO film is shown in Figure 4-9. The thin film of ITO coated on glass undergoes a fragmentation process within 10 min of hydrogen reduction which create a diameter size of metallic particle suitable for catalysis of carbon growth. After 30 min of catalyst reduction, the number of particles is reduced, until near complete disappearance occurs after 60 min of reduction. The reduction in metal particles number can be also observed in the atomic concentration (%) data provided by the XPS spectra shown in Figure 4-10. From the indium and tin peak intensities displayed in XPS spectra, it can be confirmed that both indium and tin undergo a reduction in concentration at longer reduction times.

This observation is in agreement with previous work on annealed ITO-coated glass [117]. In that study, at 500°C indium/tin atoms increasingly move to the surface as the annealing time is increased. For the first 2 h annealing time, particles/clusters of a size of about 100 nm were seen growing on the surface. In addition, agglomeration of the indium/tin enriched particles occurred after the annealing time reached 3 h. This agglomeration seemed to disperse and the particles completely disappeared at longer annealing times.

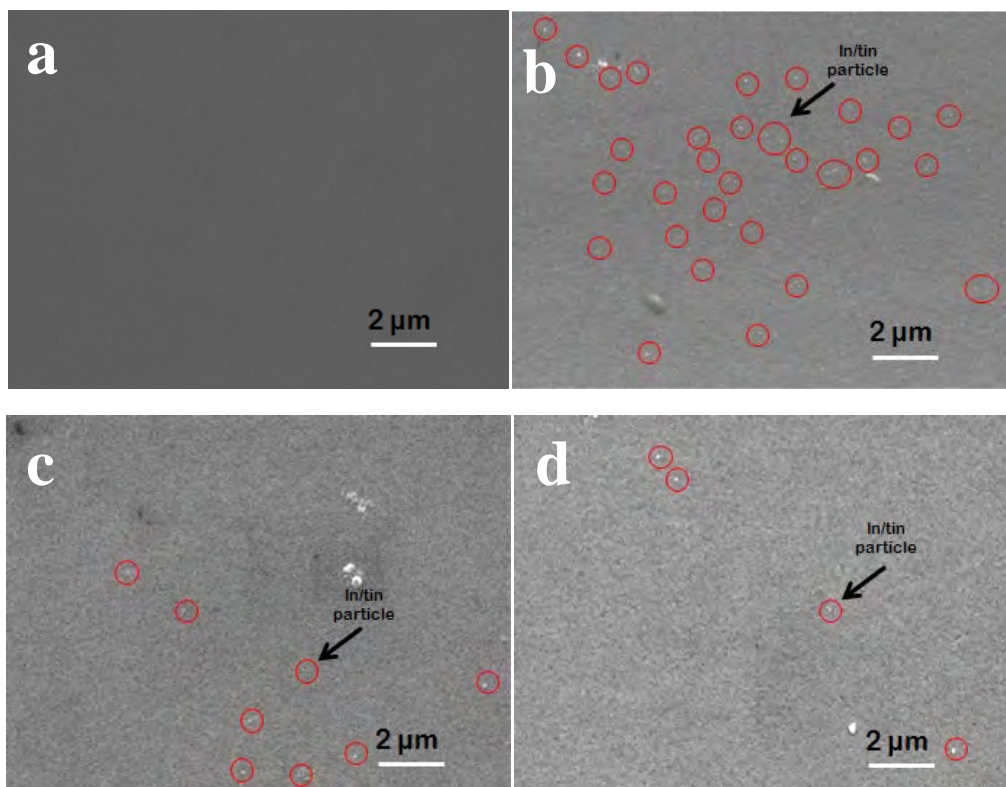


Figure 4-8: SEM image (taken at 20000x magnification) of ITO (a) before and after (b) 10 min, (c) 30 min & (d) 60 min of hydrogen reduction at 450°C

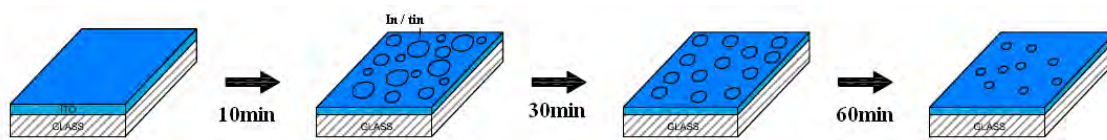


Figure 4-9: Schematic illustration of the observed ITO film fragmentation at different hydrogen reduction times

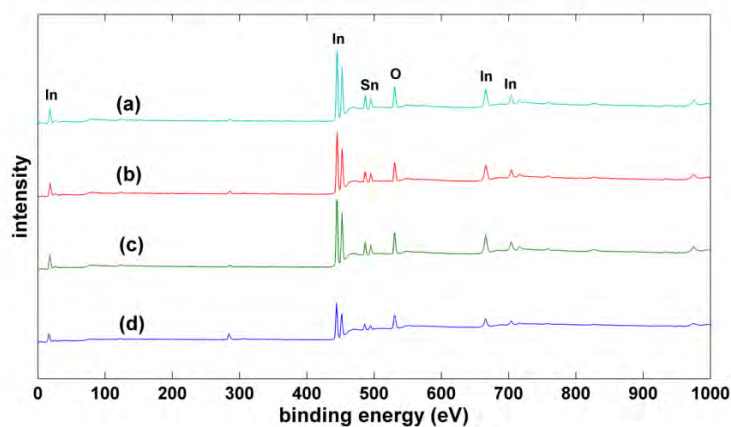


Figure 4-10: XPS spectra of ITO (a) before reduction and under the hydrogen reduction at 450°C of (b) 10 min, (c) 30 min and (d) 60 min

4.3.2 Effect of hydrogen reduction on iron-coated ITO

The identical experimental procedure as was used in section 4.3.1 was undertaken on an ITO-coated glass substrate onto which 5 nm of Fe had been evaporated. The SEM image of the 5 nm Fe layer taken before the hydrogen reduction (Figure 4-11a) shows a smooth Fe film with no particles apparent. However, during the 10 min reduction time, the film of Fe is completely converted to catalyst particles, as can clearly be seen in the SEM image (Figure 4-11b). A distinct difference can be observed between the 10 min reduction done on ITO with and without a Fe catalyst layer. The Fe layer forms into nanometre sized particles. The catalyst particle formation is uniform, the coverage is complete and a granular structure is formed. Due to limitations of the SEM imaging system at Newcastle, particles of diameter less than 10 nm are difficult to resolve, but it would appear that the catalyst particles formed are of this dimension.

As shown in Figure 4-11c, the Fe catalyst particles are reduced in size after 60 min of reduction time. This observation parallels the hydrogen reduction of ITO without any evaporated Fe catalyst, where the indium and tin particles also become smaller in size after 60 min of reduction. Carbon atoms produced from hydrocarbon gases in the CVD process diffuse into catalyst particles until they saturate the surface and start to form graphitic layers [48, 146]. Different size catalyst particles formed from the film reduction process can therefore radically influence the CNT growth mechanism [48]. Therefore, availability and control of catalyst particles is essential for the different growth modes of carbon nanostructures.

A schematic representation of the fragmentation process for an iron coated ITO film at different hydrogen reduction times is presented in Figure 4-12. After 10 min of reduction, ITO and the Fe film transform into indium/tin and Fe nanoparticles, respectively. The density of metal nanoparticles is high at 10 min of reduction when compared to that for 60 min. This phenomenon can be explained by work done by Zong et al [147] whose synthesised iron oxide nanostructures at different annealing temperatures and times. They proposed that the thickness of iron oxide is decreased due to the evaporation that occurs over the longer duration annealing. It was observed in our study that the film colour is different between 10 and 60 min hydrogen reduction - the

Fe film that was annealed for 60 min is lighter in colour and more transparent than the 10 min case. The colour difference is consistent with iron oxide evaporation [147] during annealing.

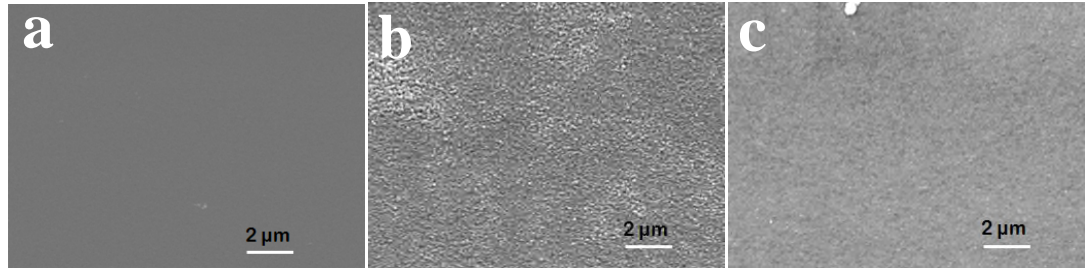


Figure 4-11: SEM image (taken at 20000x magnification) of 5 nm Fe (a) before and after (b) 10 min & (c) 60 min of hydrogen reduction at 450°C

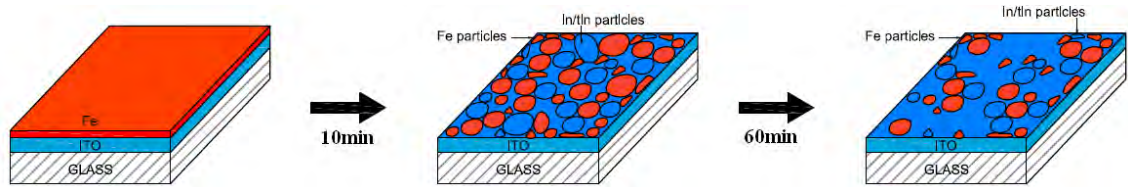


Figure 4-12: Schematic illustration of the proposed Fe/ITO film fragmentation at different hydrogen reduction times

4.3.3 The growth of carbon nanostructures

Four different CVD chamber pressures and three different growth temperatures and growth times were employed in this study. Shown in Figure 4-13, are the SEM images taken for nanostructures that have been grown at 450°C at each chamber pressure for 10 min growth time. As can be clearly seen, the morphology of the nanostructures is different in each case. These SEM images show two distinct layers. The carbon nanostructure growth is comprised of a dense unstructured interface layer and a nanostructured layer. The boundaries of these layers are further illustrated in Figure 4-14. The details of each layer will be elaborated upon in the following sections.

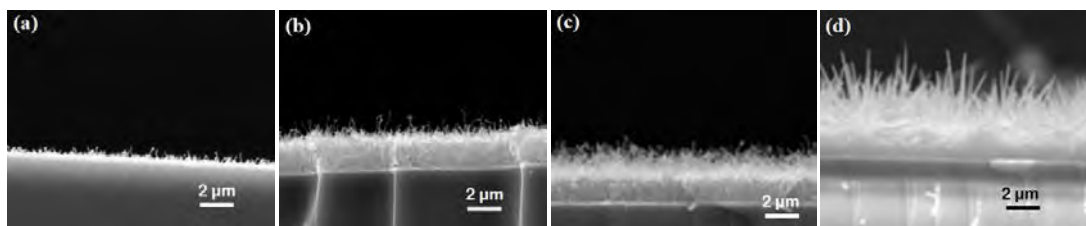


Figure 4-13: SEM images (taken at 20000x magnification) of nanostructures grown at 450°C for 10 min under the different system pressures of (a) 100 Torr (b) 200 Torr (c) 300 Torr & (d) 400 Torr



Figure 4-14: Illustration of interface layer and nanostructured layer within the carbon nanostructures

4.3.4 Characterisation of the interface layer

4.3.4.1 Formation of an amorphous carbon layer

As shown in Figure 4-13, four different SEM images were obtained from samples prepared under 100, 200, 300 and 400 Torr system pressures grown at 450°C for 10 min. Impurities such as amorphous carbon, multishell carbon nanocapsules and metal particles are known to occur during the synthesis of carbon nanostructures [15]. All carbon nanostructure films prepared in this work exhibit this unstructured interface layer with thicknesses of 208 ± 10 nm (100 Torr), 1278 ± 39 nm (200 Torr), 1465 ± 40 nm

(300 Torr) and 1980 ± 27 nm (400 Torr) respectively. A plot of interface layer thickness versus pressure is shown in Figure 4-15 and shows that a systematic increase in the thickness of this layer occurs with system pressure.

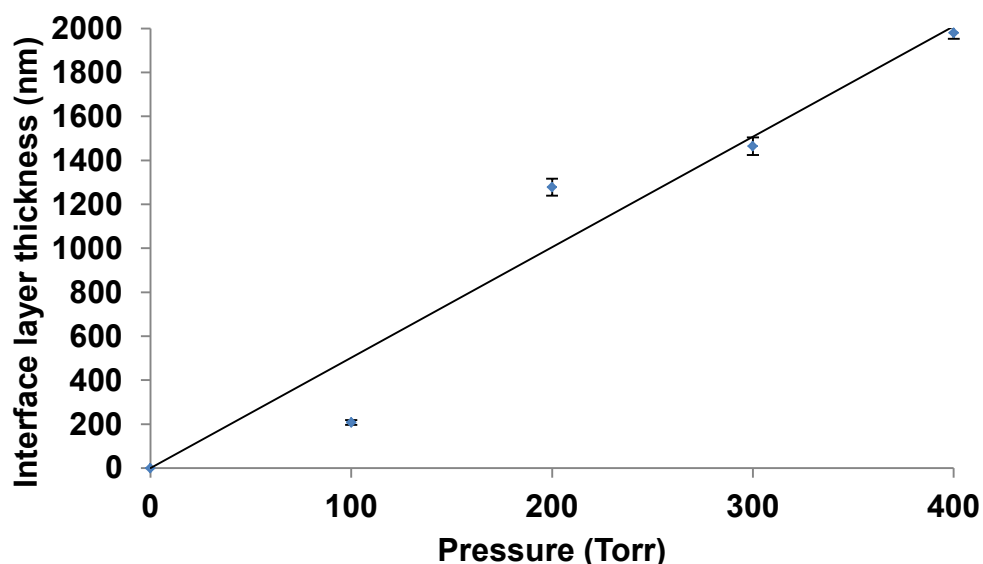


Figure 4-15: Interface layer thickness at different pressure

XPS was performed on the carbon nanostructures shown in Figure 4-13c. The image of the two different layers shown in Figure 4-14 highlights the porosity of the fibre structure. Due to the porosity of these carbon nanostructures, the penetration of XPS leads to measurement of the denser, partially exposed interface layer. Figure 4-16 shows the XPS spectrum which displays a strong carbon signal at 284.5 eV. The observation of a strong carbon signal at 284.5 eV is due to amorphous carbon structure as reported by Horikoshi et al [148]. These researchers reported the XPS spectrum of amorphous carbon film which showed a signal at 285 eV [148].

Inadequate availability of active catalyst particles could lead to the formation of amorphous carbon. In the initial stage of the CVD process, carbon atoms are produced from the decomposition of hydrocarbon gas before carbon atom diffusion process occurs on the catalyst particle. Carbon nanostructures start to grow until the concentration of carbon atoms reaches its solubility limit in the particle. Access to the

catalytically active surface is limited as carbon nanostructures grow over the catalyst particles. Amorphous carbon or other unwanted carbon materials would start to develop if the rate of gas phase carbon production exceeds the rate of nanostructure growth.

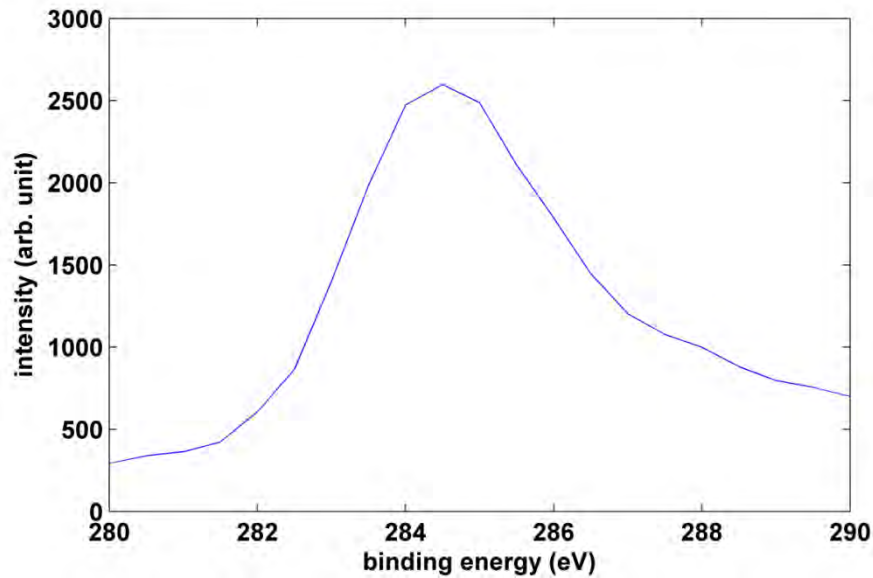


Figure 4-16: XPS spectrum of C peak at 284.5eV of carbon nanostructures

Escobar et al. [137] have investigated the effect of acetylene pressure and concentration on the structural and morphological properties of CNTs synthesized by CVD, with iron nanoparticles dispersed on a SiO₂ matrix as the catalyst. When the acetylene pressure is increased, the crystalline wall of the nanotubes is deposited within an amorphous carbon layer due to deactivation of the catalyst. Regular inner channels of CNTs can be synthesized at low acetylene pressure, which also results in reduced amorphous carbon formation.

The thickness of the amorphous carbon layer is proportional to the chamber pressure; with increases of 100 Torr give an increment of ~ half a micron in thickness. Therefore lowering the system pressure reduces the thickness of the unwanted amorphous carbon layer. We hypothesise that by decreasing pressure to 100 Torr, the reduced rate of carbon absorption by the particle means that the catalyst particle is more effectively used for carbon diffusion. According to Cuong et al [20], CNFs synthesised on graphite microfibers at 680°C are accompanied by relatively little amorphous carbon due to the obstruction of spontaneous pyrolysis of gaseous hydrocarbon. The required synthesis

temperature is very dependent on the nature of the gaseous carbon source; CNFs can be produced at lower temperatures if a more strongly dehydrogenated carbon source such as ethylene or acetylene is used instead of saturated hydrocarbons such as methane. However, amorphous carbon is easily formed together with the thicker CNFs in the more reactive hydrocarbon environment.

4.3.4.2 Effect of H₂ plasma on the interface layer

In the work undertaken here, the concomitant formation of amorphous carbon with CNTs growth apparently cannot be fully suppressed. Plasma etching is a technique which has been widely used to replace wet chemical processes for etching materials similar to the amorphous carbon layer observed [47, 149-162]. Furthermore, the plasma etching technique could improve the properties of any carbon nanostructures formed.

The field emission properties of MWCNTs films are enhanced after being treated by hydrogen plasma [153, 154]. The morphology of the treated nanotubes was changed from a smooth to a rough surface that was covered by carbon nanoparticle balls. The authors concluded that, due to the high energy ion bombardment from the plasma, the amorphous structure was produced from the MWCNTs. Thus plasma treatment can lead to defect formation-dangling bonds, interlayer cross-linkings and sp^3 defects. Sp^3 defects may have contributed to the bending and irregular graphitic structures obtained in this work. This finding is supported by Xie et al [161], where an amorphous carbon film treated by hydrogen plasma also showed changes in the surface morphology and conductivity even though the chemical effect was small. The graphitic structure of CNTs did not change when exposed to a shorter duration of hydrogen plasma treatment compared to a long exposure time of more than 5 h [158]. Application of hydrogen plasma for a short time is thus a promising candidate for optical material applications since longer exposure periods (5-10 hr) changed the bamboo-like structure of untreated CNTs into solid and helical structures. In addition, the parallel and complete graphitic layers became defective and disordered.

Hydrogen is not the only gas that has been used in the plasma etching treatment. Other gases such as argon, oxygen and nitrogen have been used to treat various materials. Argon plasma has been used to improve the photo-current density, the surface area

ratio, the optical and electrical reactive activity of TiO₂ films [155]. Argon plasma has also been used in combination with O₂ on CNTs. After the treatment, the CNT surface was much better orientated and its field emission properties were enhanced [154]. Differences in morphology and field emission properties of MWCNTs can also be observed by using either argon or nitrogen plasma etching [156]. Nanotubes become increasingly shorter with treatment duration, the density is decreased, and there is a formation of vertically aligned nanotube bundles where several nanotubes are joined at their tips. Argon plasma treatment has shown a greater etching rate than nitrogen, as it produces a lower density and shorter nanotubes compared with nanotubes treated by nitrogen plasma. Although a lower etching rate was produced by the nitrogen plasma treatment, nitrogen doping of the treated MWCNTs has been observed. This treatment could contribute to the observation that nanotubes have better field emission properties post nitrogen plasma treatment. Huang and Dai [152] have reported the application of H₂O plasma etching in removing the amorphous carbon layer that covers aligned CNT films. They found that, amorphous carbon could easily be removed by H₂O plasma etching, however prolonged plasma treatment could partially remove graphitic sheets from the CNTs structure. In light of these observed changes in carbon nanostructure properties, plasma etching was investigated as a post-film production processing step to improve film quality and remove amorphous carbon.

In order to understand how best to treat the amorphous carbon layer, samples of CNFs grown at 200 Torr were exposed to hydrogen plasma etching for times of 10, 30, 120, 240 and 360 min. Hydrogen plasma etching is done ex-situ with a RF power of 180 W used on each sample with a flow of 100 sccm of hydrogen at 3 Torr pressure. The main purpose of this experiment is to develop a means to reduce the amorphous carbon film layer deposited on the bottom of CNFs structure. All samples used were synthesised at the same time in order to avoid any difference in growth conditions arising from different batches. The surface morphology of each etched carbon film can be seen in the cross-sectional SEM images shown in Figure 4-17. Initially CNFs were generated in a tangled form together with the deposition of an amorphous carbon layer of ~1100 nm in thickness and is in reasonable agreement with the data presented in Figure 4-15. This thickness of amorphous carbon film would be expected to severely reduce the usefulness of these films for device applications.

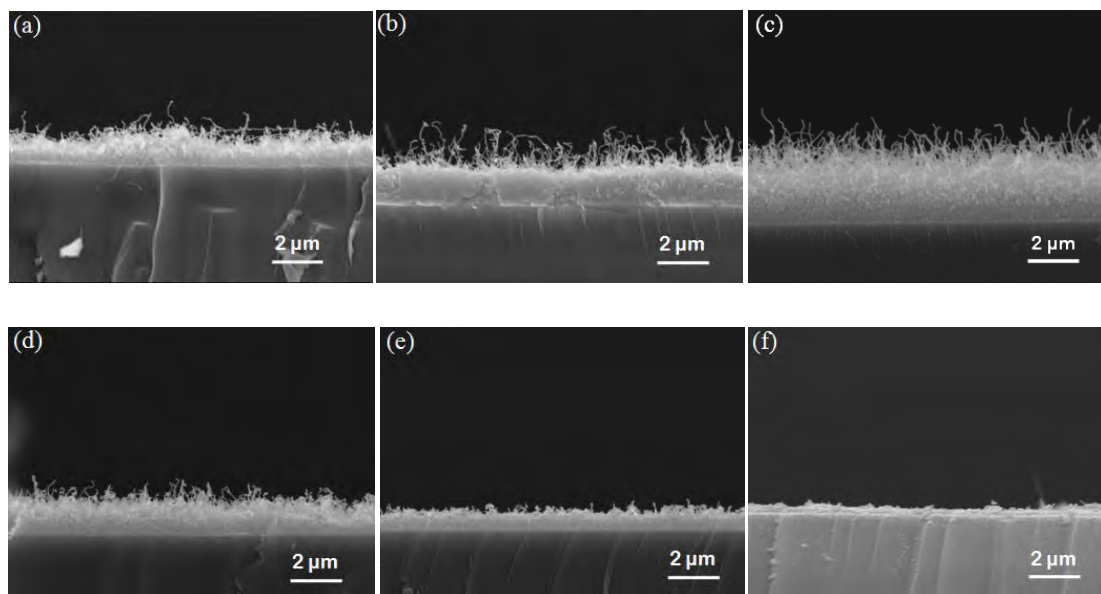


Figure 4-17: SEM images (taken at 20000x magnification) of carbon nanostructures grown at 200 Torr without H₂ plasma etching (a) and after H₂ plasma etching at different times of (b) 10 min (c) 30 min (d) 120 min (e) 240 min & (f) 360 min

Interestingly, after 10 min of hydrogen plasma treatment, the thickness of amorphous carbon layer increased from ~1100 nm to ~1600 nm. This increase is continuous up to 30 min of etching time is applied, where ~2300 nm of amorphous carbon is observed. Despite the increase in carbon film thickness, the morphology of CNFs improves with treatment time. The tangled nanofibres grown at 200 Torr are transformed to more aligned CNFs after 30 min of treatment with a more dense nanofibre distribution compared to the structure after 10 min of hydrogen plasma treatment. Mechanistically, hydrogen ions or atoms produced from the hydrogen plasma react with the carbon atoms forming C-H bonds. Due to the open structure between CNFs, these reactive hydrogen species easily reach the amorphous carbon film layer and react. The hydrogen plasma scavenges weak bonds and increases the hydrogen coverage on the growing film surface, resulting in the formation of a well-relaxed amorphous film network [152]. Investigation into hydrogenated amorphous carbon has been done by RF plasma with its degree of hardness showing a relationship to the etching gas pressure [150]. The etching rate of amorphous carbon films and hydrogen content also closely related to each other.

After 30 min of hydrogen plasma treatment, the carbon film layer is increased and aligned CNFs are obtained. We believe the observed carbon film layer thickness increase is due to the enhancement of hydrogen atoms on the carbon film surface which

leads to a more relaxed and less dense amorphous film network. Furthermore, the formation of C-H bonding may contribute to the phenomenon. Hydrogen ions impingement is higher on carbon film surfaces rather than on the tip of the CNFs because of the stronger graphitic bonding. Also the gaps between CNFs would allow more hydrogen ions or atoms to reach and bonded with carbon atoms at the surface.

A dramatic reduction in the amorphous carbon layer thickness is seen after 2 h of hydrogen plasma treatment. However, the surface morphology has changed from aligned CNFs to distorted ones. In addition, the CNFs seem have been significantly etched away together with the carbon film layer. As reported by Nakahara et al [151], the surface structure of carbon fibres vanishes after prolonged exposure to oxygen plasma. They also reported the disappearance of well-graphitized carbon layers in the pyrolytic graphite surface with oxygen plasma treatment. The effect of two different plasma gases, hydrogen and oxygen, is likely to be the same as the CNFs are destroyed after the longer exposure to plasma etching. According to Xu et al [162], by using hydrogen plasma annealing, the sp^2/sp^3 ratio is decreased. The weak carbon sites on the growing surface are chemically etched away and the growth of sp^2 clusters is also suppressed. This observation suggests that the sp^2 -related clusters can be significantly reduced.

After two hours of treatment the nanofibres reduce further in length and the tip joining is observed. Shrinkage in length must be due to the distortion or defects generated by hydrogen ion impingement. Both CNFs and amorphous carbon are removed by the prolonged exposure. Further exposure leads to the virtual disappearance of CNFs after 4 h, and their complete disappearance after 6 h of hydrogen plasma exposure.

CNFs cannot be seen after 6 h of treatment; however a carbon film layer of ~340 nm thickness still remains. Hydrogen plasma treatment favours etching of metallic single-wall CNTs over the semiconducting nanotubes [47]. Detachment of catalytic metallic particles might have occurred during the etching process which results to the opening of nanotube ends and the destruction of nanotube structures. Hydrogen plasma introduces specific defects on the metallic nanotube which propagate through the entire wall since the C-C bonds on metallic nanotubes are easier altered than in semiconducting nanotubes.

Katayama et al. have reported the erosion of a carbon deposition layer exposed to hydrogen plasma at an RF power of 250 W [158]. Before the application of this treatment, the carbon deposition layer consisted of a packed fibrous structure. However, after the plasma exposure, the authors found that the surface became mesh-like and the inside of the layer became more porous. The relatively high RF power of 250 W used in this study would probably be the cause of the erosion observed after 6 h of plasma exposure, in agreement with this study.

The plot of amorphous carbon film thickness versus etching time is shown in Figure 4-18 from which an etching rate of 2.1 nm/min can be obtained. For comparison, Kobayashi et al [150] found that the etching rate of hard amorphous carbon film is 6 nm/min when using the argon plasma at 0.05 Torr. These authors found that the etching rate of amorphous carbon films is directly proportional to the argon pressure. A much higher hydrogen pressure of 3 Torr was used in our study; but a lower etching rate of 2.1 nm/min was still obtained at 180 W. Hydrogen plasma etching on carbon films has been studied [149] and it was shown that the etch rate increases with hydrogen gas pressure and sample temperature. Hydrogen ions produced from plasma were able to etch amorphous carbon films at high etching rates [160]. As reported elsewhere, the hydrogen plasma etching rate can be very high when used on amorphous carbon film [161].

This study shows that hydrogen plasma etching can indeed be used to reduce or eliminate the amorphous carbon layer which accompanies carbon nanostructure growth. However, for short exposure periods this amorphous layer initially appears to actually grow in thickness and at longer exposure periods, where the amorphous layer is reduced, significant destruction of the carbon nanostructures is also observed. Therefore, if this technique is to be used to improve the films prepared in this project further work will need to be undertaken in order to optimise amorphous carbon etching whilst minimising carbon nanostructure destruction. None the less this preliminary study shows that such optimisation may be possible.

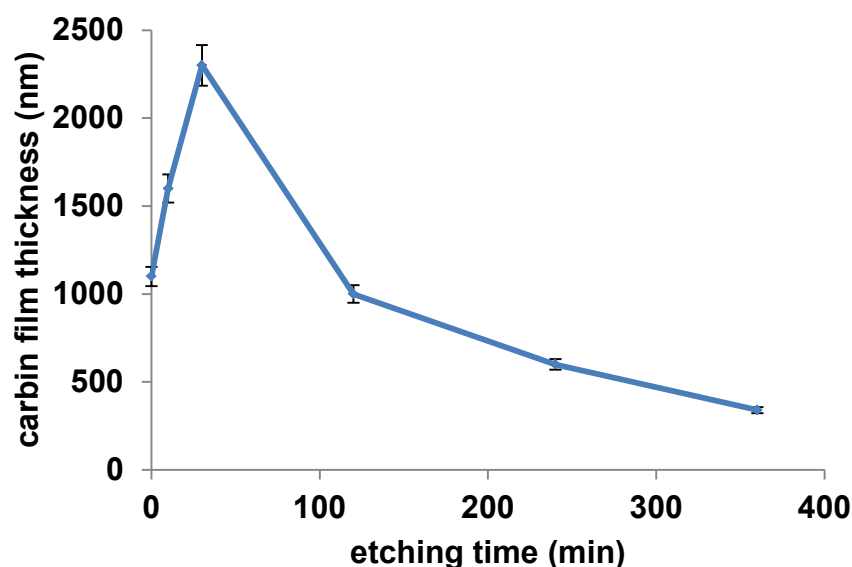


Figure 4-18: Amorphous carbon film thickness at different etching time

4.3.5 Characterisation of nanostructured layer

The following sub-sections detail the experimental results of systematically varying growth temperature, time and pressure. Two types of nanostructure are observed at the different system pressures. Between 100 and 300 Torr, the nanostructured layer comprised of fibres. In contrast, at 400 Torr, the nanostructured layer is dominated by needles.

4.3.5.1 Nanostructure growth at 400°C (100 – 400 Torr)

4.3.5.1.1 Nanostructure growth at 100 Torr

Carbon nanostructures in the form of carbon nanofibres (CNFs) are observed between 100 to 400 Torr at the growth temperature of 400°C. The structure transformation from catalyst to CNF can be seen between the initial growth time of 1 min to the final growth time of 10 min. Intermediate growth has been investigated by implementing a growth time of 5 min. The lowest growth temperature applied in this work is 400°. The predominant changes in structure, particularly from catalyst particle to carbon nanostructure can be seen in Figure 4-19. In Figure 4-19, high resolution SEM images are presented for both the cross-section and top view of substrates. In addition, the EDX

line scan of nanostructure has been taken from the top view. This elemental composition EDX measurement has a 5% error. In order to analyse the quantification of traced elements, a 3D graph distribution of carbon, oxygen, iron and indium is shown in Figure 4-20.

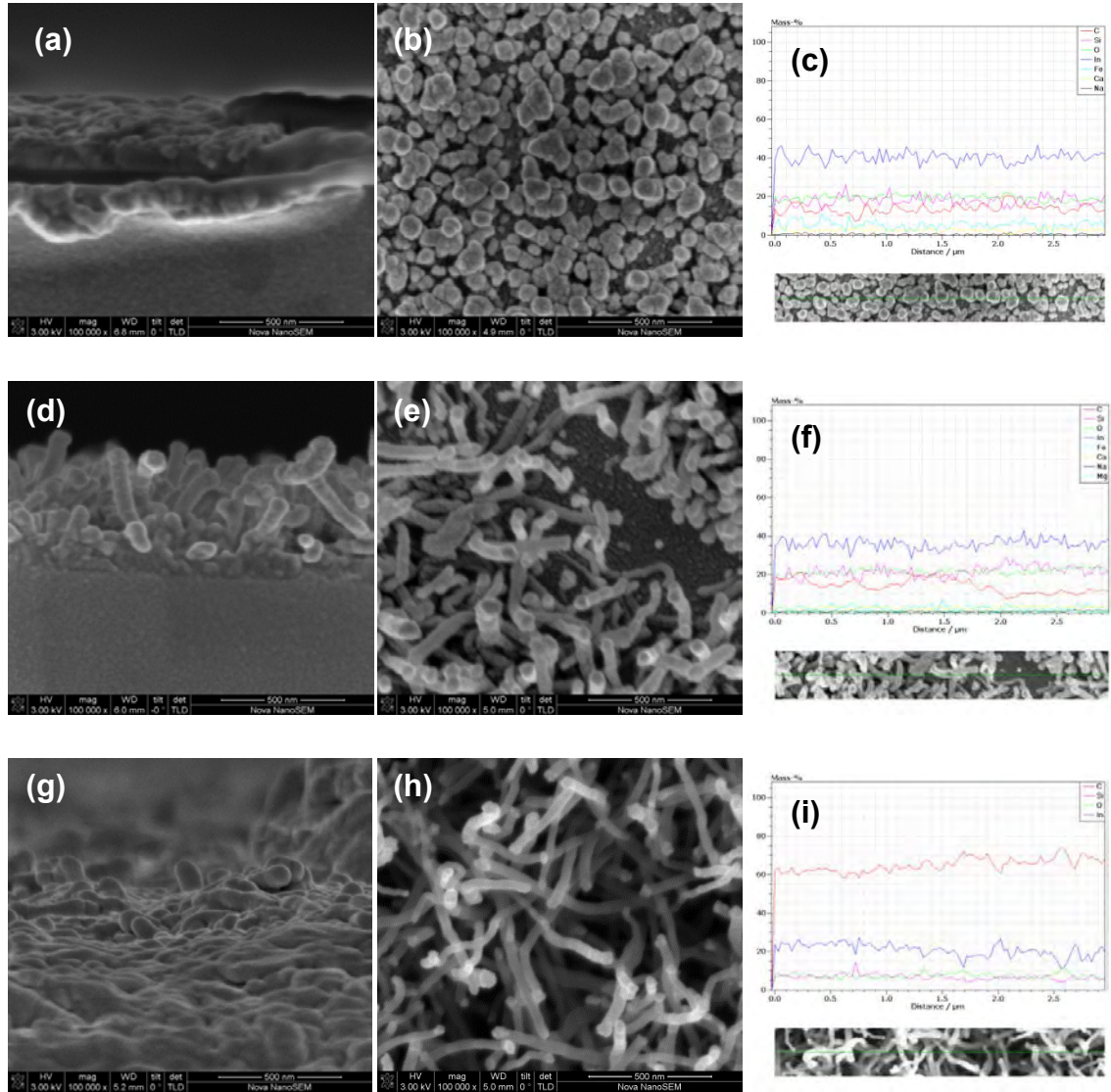


Figure 4-19: FESEM images (cross-section and top view) and EDX data (line scan) of nanostructures grown at 400°C of 100 Torr for 1 min (a-c), 5 min (d-f) and 10 min (g-i)

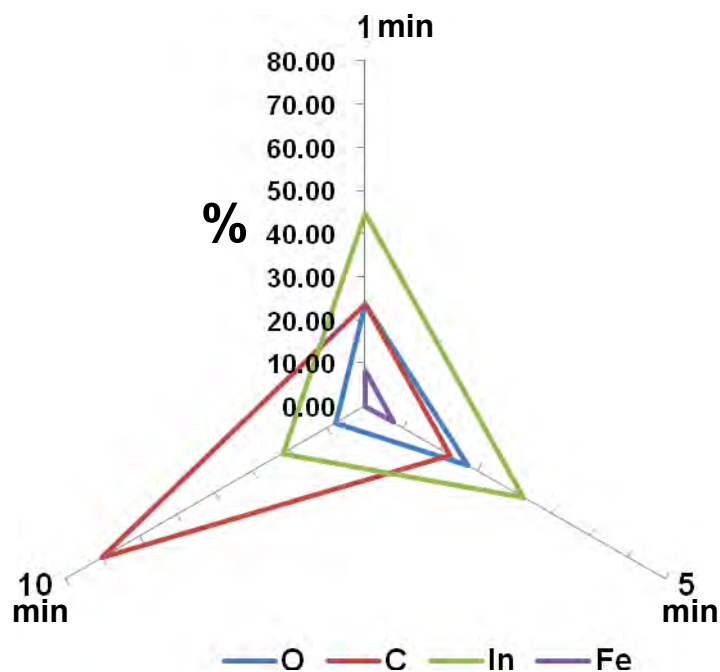


Figure 4-20: 3D graph distribution of relative atomic concentration of O, C, In and Fe growth at 400°C and 100 Torr of different growth time

At the lowest growth temperature (400°C) and growth pressure (100 Torr) implemented in this work, the indium signal is seen to dominate during the growth time of 1 and 5 min. However, smaller amounts of oxygen, carbon and iron were also observed. A low level of iron is detected during these growth times (1 and 5 min) before completely it completely disappears by 10 min. During the 1 min growth, surface particles with a variety of shapes develop (Figure 4-19a & b). The line scan of those particles shown in Figure 4-19c gives information for the mass percentage of the individual particles. By considering the changes in carbon, iron and indium concentrations conclusions as to the composition of the particles can be made. Interestingly, the graph of mass percentage for carbon and iron is largely invariant, with most of the peaks detected at the location of particles rather than in the gap between particles. By contrast, indium shows mass peaks in the gaps between the particles. We can therefore conclude that iron does indeed fulfill its role as the catalytic site for carbon growth.

During the 1 min growth at the lowest temperature, the thin film of iron catalyst transforms its initial film state into a distribution of individual particles. These iron particles then catalyzed the subsequent carbon growth. Whilst this growth occurs, the

ITO substrate remains largely unchanged. The detection of an indium maximum in the gap between particles would suggest that little diffusion of indium or tin occurs at this stage. This is supported by observation that the lowest levels of indium are detected at the particle whilst both iron and carbon show mass maxima. Catalysts such as nickel have been reported to become contaminated with indium and tin at growth temperatures of 550°C resulting in slower carbon nanostructure growth [8]. Since the melting point of indium is 157°C [12], possible contamination of the iron catalyst by indium and subsequent slowing of carbon nanostructure growth could occur here as well.

Increase in growth time leads to the continued growth of carbon nanostructures as evidenced by SEM and EDX measurements (Figure 4-19d-i). There is an apparent contradiction in the growth morphology between 1 and 5 min. The SEM cross-section image (Figure 4-19d), show that the thickness of the grown structure is approximately 500 nm. However, a variety of diameters and heights are observed for the nanostructures. There appears to be a systematic reduction of carbon nanostructure diameter from 1 min growth time to 10 min growth time. The diameter of a nanostructure is known to be highly dependent on the size of catalyst particle [48]. As such, it is possible that the larger catalyst particles grown undergo particle fragmentation to smaller sizes during longer growth times leading to nanostructures of smaller diameter. The EDX line scan image shown in Figure 4-19f shows that substrate surface is still dominated by both indium and iron, with low levels of carbon concentration seen in the areas of low nanostructure growth.

The nanostructure grown for 10 min (Figure 4-19g) shows a denser layer which now covers the entire growth area. The EDX line scan analysis shows that the mass percentage of carbon has correspondingly dramatically increased and that now no iron is detected. The complete absence of iron in the EDX spectra would appear to suggest that the nanostructure growth is not via a tip growth mechanism for these conditions.

Carbon nanostructures grown on ITO with the lower system pressure (0.68 Torr) have been reported [8]. A total thickness of the nanostructure of approximately 200 nm was achieved and this layer was successfully used as the hole-extracting electrode in a solar cell. The carbon nanostructures shown in Figure 4-19e and 4-19h are of the same

general dimensions and therefore show distinct promise for integration into organic solar cells.

4.3.5.1.2 Nanostructure growth at 200 Torr

Figure 4-21 shows the SEM images and EDX data (line scan) of nanostructures when the system pressure is increased to 200 Torr with the other growth parameters unchanged. This data shows that a similar nanostructure to that grown at 100 Torr is obtained. Unsurprisingly, no carbon nanostructures are grown during the 1 min growth time (Figure 4-21a & b), only a similar particle structure to that grown with the system pressure at 100 Torr is observed.

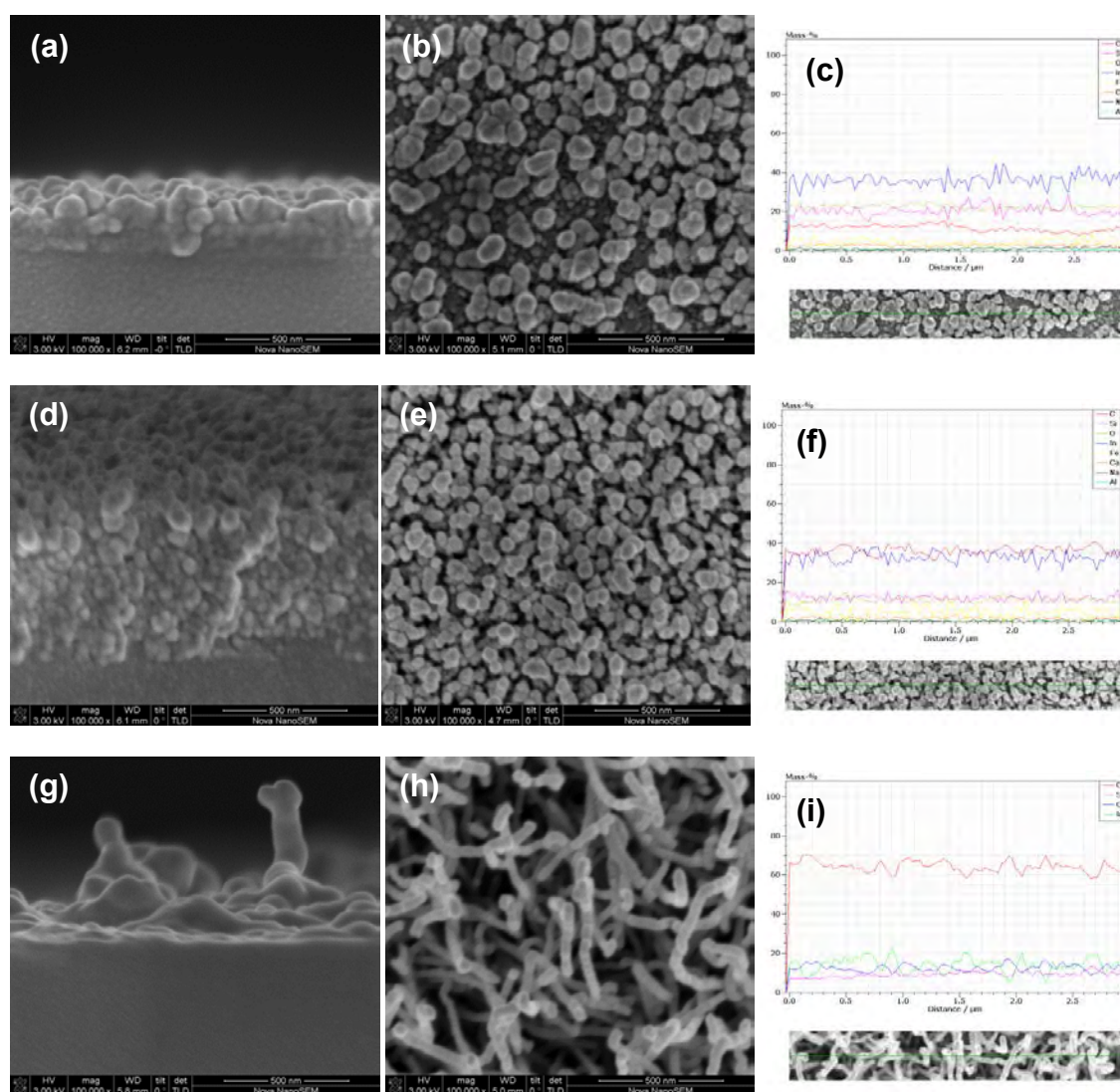


Figure 4-21: FESEM images (cross-section and top view) and EDX data (line scan) of nanostructures grown at 400°C of 200 Torr for 1 min (a-c), 5 min (d-f) and 10 min (g-i)

Again the mass concentration percentage of elements at the surface is dominated by indium. As shown in Figure 4-21c the peaks in the indium mass percentage correspond directly to some of the smaller particles on the surface but not to all of the particles. The melting point indium is 157°C. At the growth temperature of 400°C indium is known to melt and subsequently form indium droplets. Therefore at this growth temperature both iron and indium in the substrate could transform into surface particles. The detection in the SEM and EDX of particles with differing sizes and compositions seems to support this hypothesis. Therefore we believe a mixture of both indium and iron catalyst particles form under these conditions.

The morphology of the surface changes upon 5 min of growth time (Figure 4-21d & e), with a larger number of smaller diameter particles shown. A very different morphology of nanostructures is observed at 200 Torr as compared with the nanostructures grown at 100 Torr for 5 min. The nanostructures are more densely packed with each other with a greater increase in the mass concentration percentage of carbon recorded. At this stage, the mass percentage of carbon is level with the mass percentage of indium (Figure 4-21f). A higher system pressure at 200 Torr therefore appears to facilitate the growth of carbon nanostructure with a much denser morphology. Additionally, the thickness of this dense carbon layer has also been increased to nearly 1 μm .

The 10 min growth time sample (Figure 4-21g and 4-21h) appears very similar to that observed under the 100 Torr growth conditions. The nanostructures are again of substantially smaller diameter than the initial catalyst particles, suggesting division of these particles during the growth process. Again no iron is detected in the EDX line scan after 10 min growth (Figure 4-21i), though a small amount of iron is still observed at growth times less than 10 min. At the same time the mass concentration of indium is reduced to half of its initial value. This again suggests that a tip growth mechanism involving iron is not in operation.

The 3D graph distribution of relative atomic concentration of each element is presented in Figure 4-22. It shows a systematic growth of carbon and total loss of iron over the growth period. The indium percentage declines more slowly than the iron and the ratio of oxygen to indium initially decreases (5 min) suggesting the formation of elemental

indium on the surface and then increases (10 min) indicating the loss of this elemental indium – possibly by evaporation.

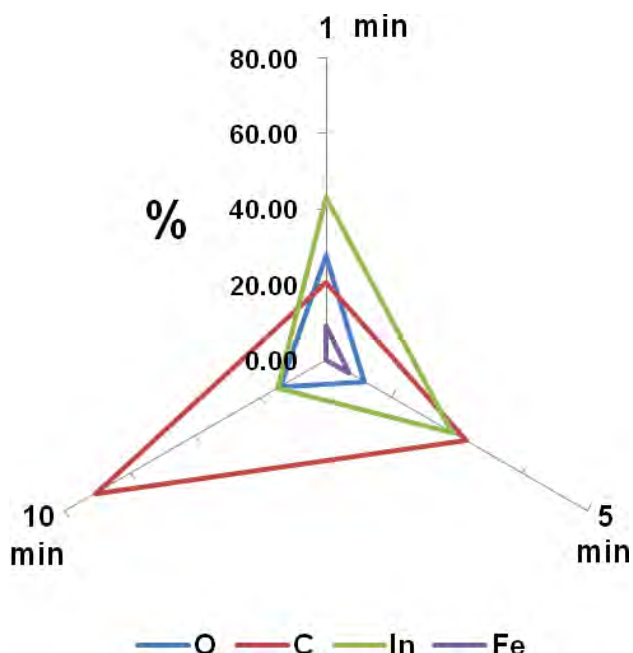


Figure 4-22: 3D graph distribution of relative atomic concentration of O, C, In and Fe growth at 400°C and 200 Torr of different growth time

4.3.5.1.3 Nanostructure growth at 300 Torr

Figure 4-23 shows that upon increasing the system pressure to 300 Torr a similar carbon nanostructure growth mechanism is preserved. There is very little change between the morphologies and elemental compositions observed in the SEM and EDX spectra for 200 Torr and 300 Torr growth. Interestingly the initial nanoparticle growth on the substrate surface is suppressed under the 300 Torr conditions. This may be due to the likely increased mobility that indium will have at the higher pressure, which may lead to suppression of iron nanoparticles. However, by 5 minutes of growth near identical results are obtained to those for 100 Torr. This similarity continues through to 10 min of growth where the only difference is a slight increase in the overall carbon coverage of the substrate by EDX (~ 75% carbon at 300 Torr vs ~ 65% carbon at 200 Torr).

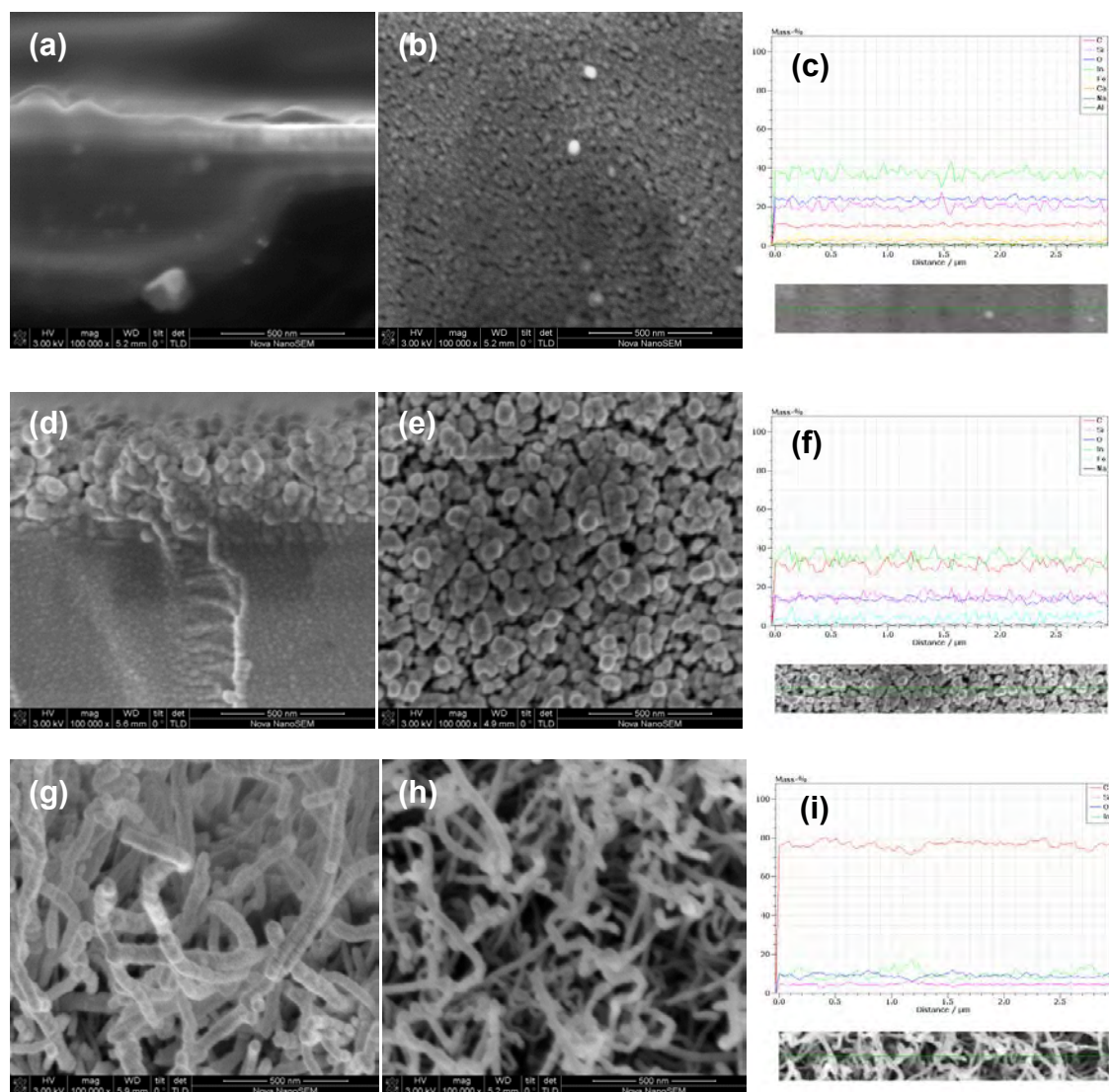


Figure 4-23: FESEM images (cross-section and top view) and EDX data (line scan) of nanostructures grown at 400°C of 300 Torr for 1 min (a-c), 5 min (d-f) and 10 min (g-i)

4.3.5.1.4 Nanostructure growth at 400 Torr

As the system pressure is increased to 400 Torr a significant change in film composition is observed as demonstrated in Figure 4-24. For all the applied system pressures (100 – 400 Torr), no carbon nanostructures are observed at the lowest growth time of 1 min. Generally, during the 1 min growth time, only transformation of the iron thin film into particles is observed. The morphology of these particles grown under different system pressure were different in terms of their distribution and size. As shown in Figure 4-24a-c the morphology of particles at 400 Torr is similar to those grown at 200 Torr. This is not consistent with the 300 Torr result but the formation of iron particles could be contaminated by indium and thus competition between the formation of iron and indium particles under the different pressures may lead to the observed results.

Under growth times of 5 and 10 minutes very similar nanostructure morphologies to those observed for 200 and 300 Torr are (Figure 4-24d-i). Iron again disappears from the elemental composition, whilst the carbon percentage of composition increases with growth time. Surprisingly at 400 Torr the indium composition percentage does not drop dramatically with growth time – this is a first hint that at higher pressures (and temperatures) indium may be come incorporated into the carbon nanostructure. This observation will be discussed in more detail in section 4.3.5.2.4.

The real picture of the elements distribution at the different growth times was is well shown as a 3D graph in Figure 4-25. Indium displays a relatively uniform percentage composition over the different growth times as the percentage composition of carbon increases suggesting that it is somehow included into the carbon growth. Iron is only observed during the 1 min growth before it vanishes upon longer growth times but may still be acting as a base catalyst for carbon growth.

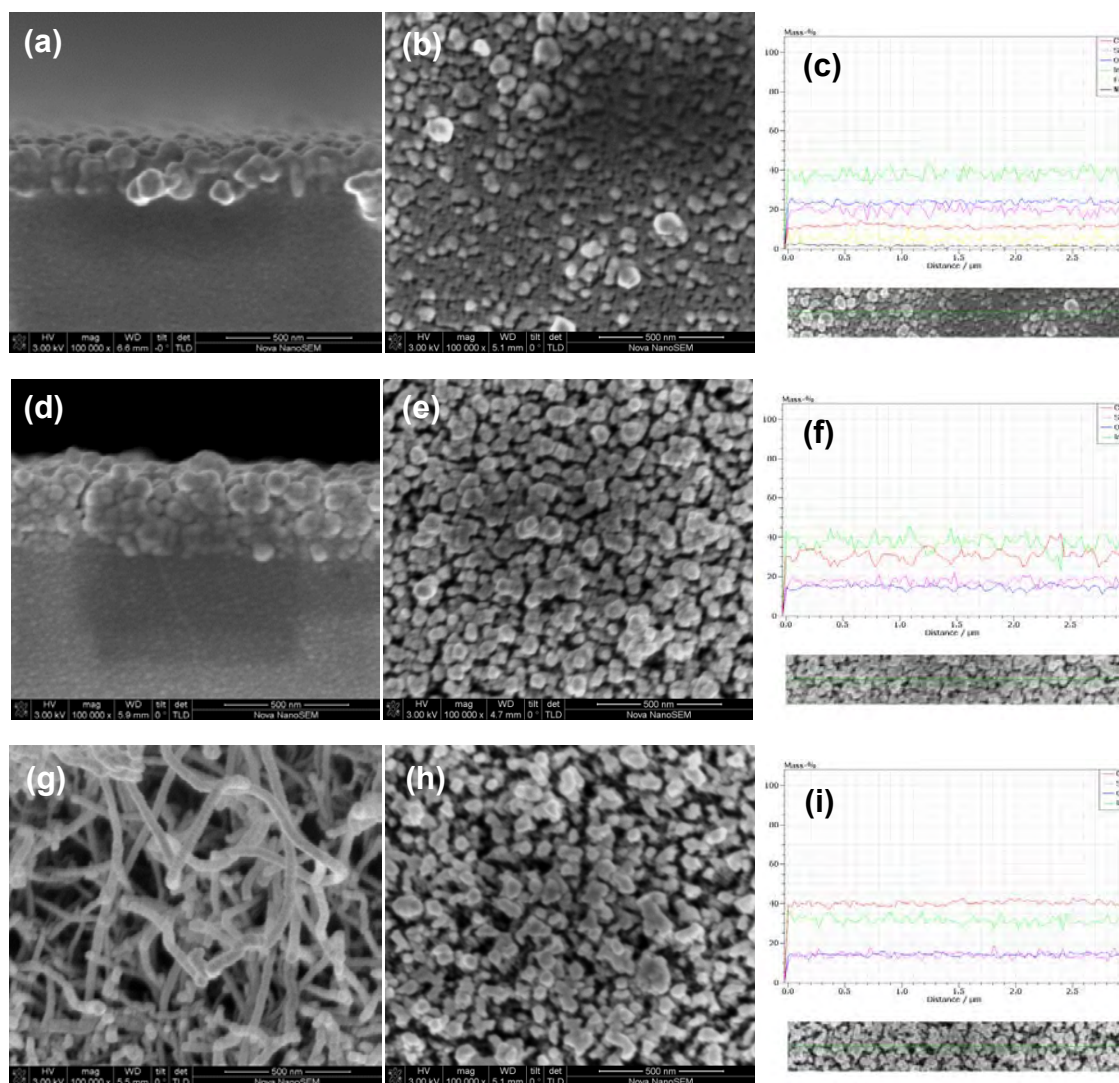


Figure 4-24: FESEM images (cross-section and top view) and EDX data (line scan) of nanostructures grown at 400°C of 400 Torr for 1 min (a-c), 5 min (d-f) and 10 min (g-i)

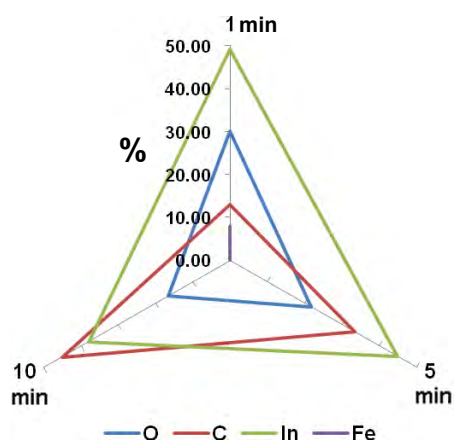


Figure 4-25: 3D graph distribution of relative atomic concentration of O, C, In and Fe growth at 400°C and 400 Torr of different growth time

4.3.5.2 Nanostructure growth at 450°C (100 – 400 Torr)

4.3.5.2.1 Nanostructure growth at 100 Torr

A significant change in the morphology of both the initial metal catalyst particles and also the subsequent carbon nanostructures is observed when the CVD system temperature is increased to 450°C. Figure 4-28 shows that a smaller diameter, more densely packed layer of particles is observed at 450°C than at 400°C after 1 min. The subsequent carbon nanostructure growth at 5 and 10 minutes leads to long nanotubes with overall much smaller diameters than observed at 400°C (Figure 4-28). From these observations it is apparent that the growth of catalyst particles on ITO is highly temperature dependent. As has been reported elsewhere [8], the growth rate and morphology of carbon nanostructures are heavily influenced by contamination of catalytic substrate. It is likely that the higher temperature would produce further contamination of the iron layer by indium which would slow down the transformation from thin film to particle and subsequently lead to very different nanotube morphology.

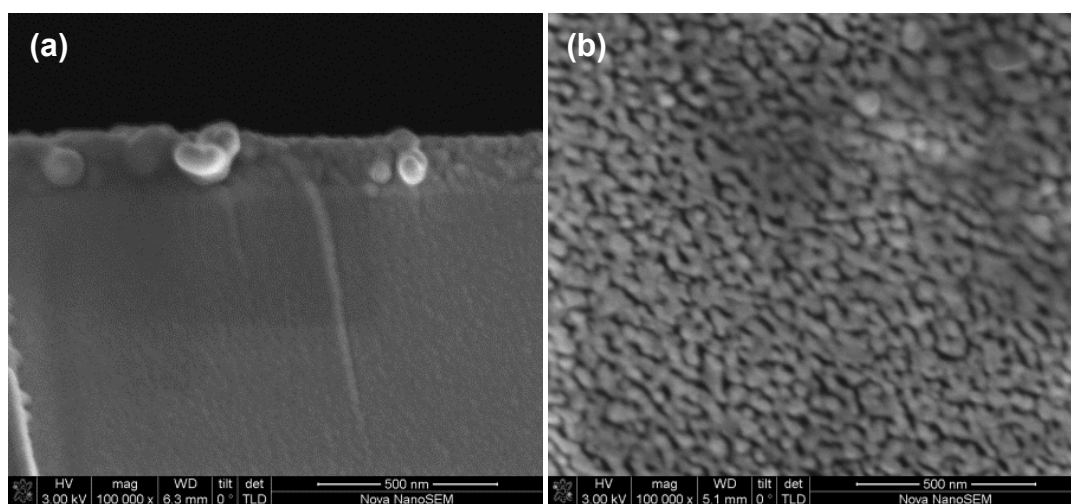


Figure 4-26: FESEM images of (a) cross-section & (b) top-view of nanostructures grown at 450°C of 100 Torr for 1 min

Although a slower growth rate of catalyst particles is observed, carbon nanostructures of longer length and smaller diameter compared to those grown at 400°C are obtained. These nanotubes are also less densely packed, with the substrate being clearly visible at 10 min growth time (both by SEM and EDX Figure 4-27e and Figure 4-28 respectively) and it appears that at the lower growth temperature a layer of amorphous carbon may be

incorporated into the carbon nanostructure. The formation of amorphous carbon is well known to dominate with deactivated catalyst particles where the rate diffusion of carbon atom into catalyst particle is higher than the formation of catalyst particle. Therefore it would appear that the larger catalyst particles obtained during the lower growth temperature of 400°C are deactivated compared to those obtained at 450°C.

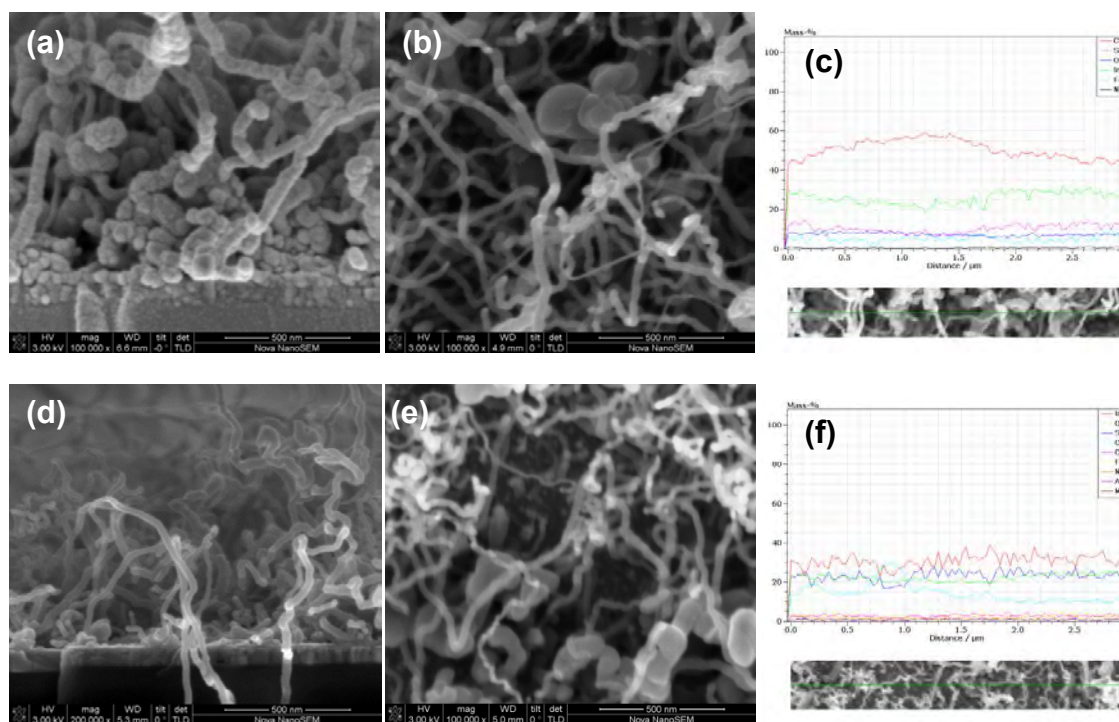


Figure 4-27: FESEM images (cross-section and top view) and EDX data (line scan) of nanostructures grown at 450°C of 100 Torr for 5 min (a-c) and 10 min (d-f)

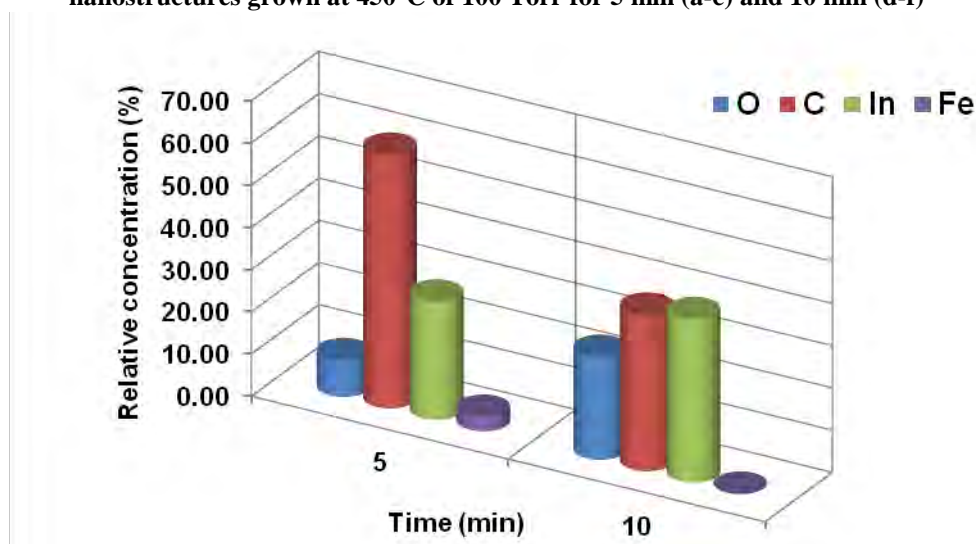


Figure 4-28: Graph distribution of relative atomic concentration of O, C, In and Fe growth at 450°C and 100 Torr of different growth time

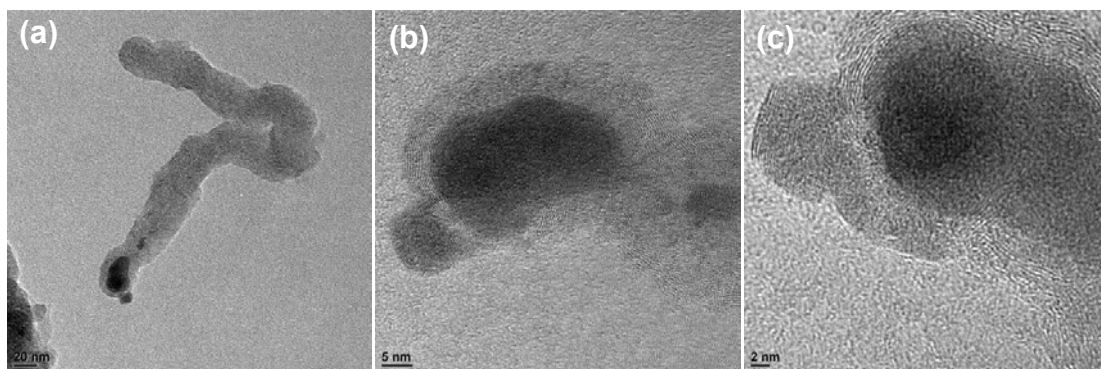


Figure 4-29: High resolution TEM images of carbon nanostructures grown at 450°C of 100 Torr for 10 min for the magnification of (a) 57 000X, (b) 300 000X and (c) 470 000X

Figure 4-29a-c show the high resolution TEM images of a carbon nanostructure grown at 450°C of 100 Torr for 10 min. The TEM images show an individual carbon nanostructure that is representative of the many other nanostructures obtained under these growth conditions.

From the TEM images, it is clear that the carbon nanostructure has grown with a particle sitting at the tip. The diameter of the particle is ~20 nm sitting within an approximately 40 nm (outer diameter) carbon nanostructure. The size of both the particle and nanostructure are in good agreement with particles and nanostructures observed in the SEM spectra (Figure 4-28b and Figure 4-28 respectively). The appearance of a metal particle within the carbon nanostructure is reflected also in the appearance, for the first time, of iron in the EDX spectra of both the 5 min and 10 min growth time samples, suggesting that the iron particles may now be participating in a tip-growth mechanism.

To aid identification of the carbon nanostructure a magnified region of Figure 4-29c has been reproduced in Figure 4-30a. From the magnifying image, a clear multiwalled structure is observed within the carbon nanostructure. The measured lattice spacing of the carbon nanostructure is 0.3577 nm (measured along the ‘yellow’ line (2.45 nm) and presented as a plot profile in Figure 4-30b). The 0.3577 nm spacing observed is in good agreement with reported *d*-spacing of multiwalled carbon nanotubes (MWCNT) [163]. It is well known that the CNT with the multiple walls structure may allow the incorporation of other materials within its hollow structure [46, 48, 61]. The high

resolution TEM image of the carbon nanostructure therefore clearly shows that it is a multiwalled carbon nanotube having more than ten layers of carbon wall.

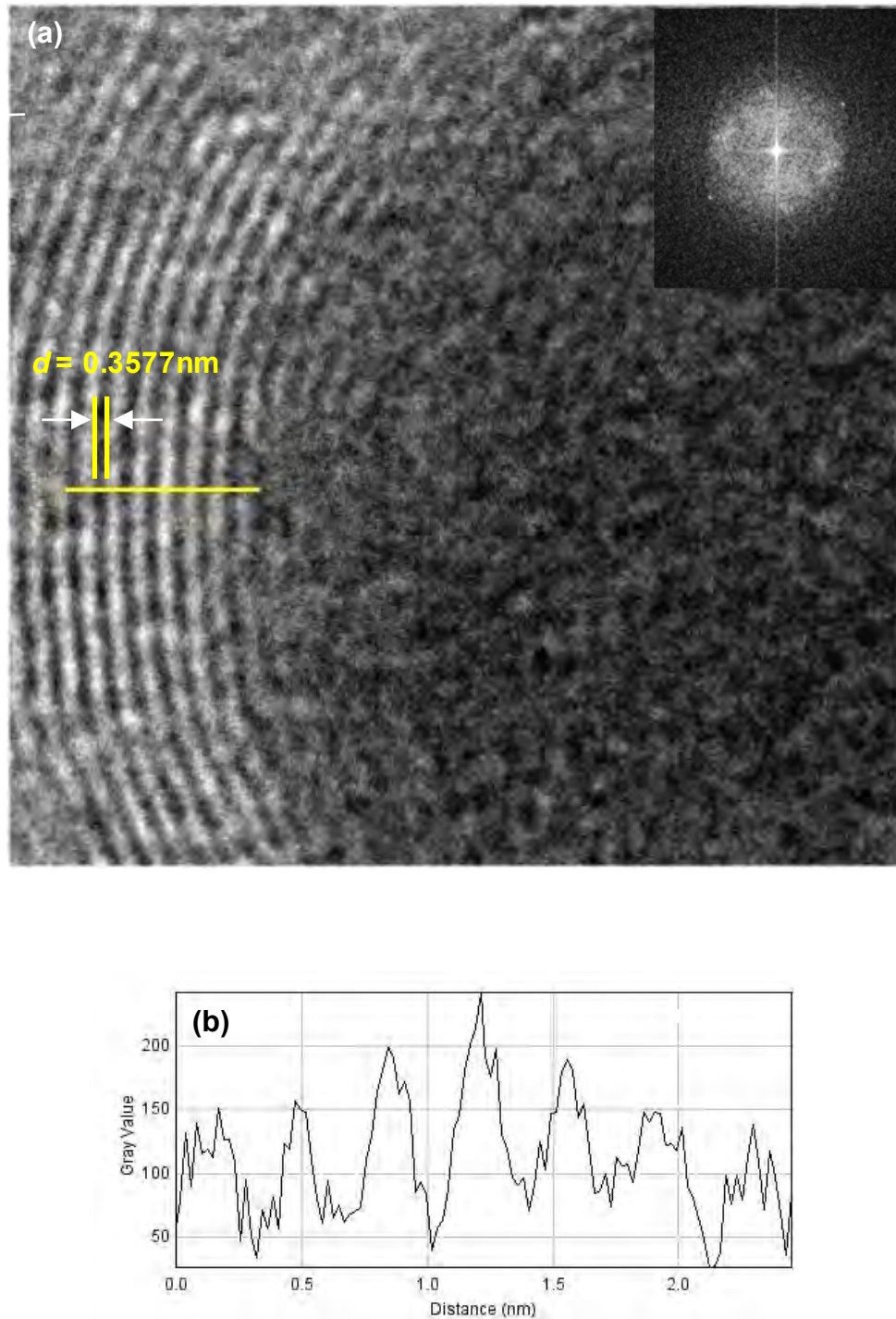


Figure 4-30: TEM image showing the (a) lattice image of carbon nanostructure & Fast Fourier transform of the image (inset) and (b) plot profile of lattice image

The diameter of the MWCNT is 40 nm in average and shows predominately tip growth mode. The exact length of deposited CNFs was hard to estimate because of the curled structure, but it is in range of several microns. The curled structure may be due to collisions between interfaces and with the low temperature applied in this experiment distortion of the graphitic layer during growth is expected to occur [2]. This entanglement was probably caused by the nucleation of the fibres occurring close to each other due to the closeness of the catalyst particles (Figure 4-11b). The densely packed iron catalyst particles could introduce competition and collision between two or more growing fibres during the carbon atom diffusion [4]. An example of such a circumstance is defects in graphitic layers caused by collisions between the two sides of the interface between the monocrystalline regions [164]. Carbon nanostructures that have been produced by Cuong et al [20] are similar in diameter and also highly entangled, indicating the existence of numerous topological defects inside the material due to the relatively low synthesis temperature.

As shown in Figure 4-29a, the tip-growth mechanism is observed, with catalyst particles of diameter 20 nm sitting at the tip of the fibre. A schematic illustration of the MWCNT tip-growth mechanism is illustrated in Figure 4-31. The tip-growth mechanism for CNT growth on silicon substrate with iron as catalyst has been observed by Yun et al [61]. Iron particles were found sitting at the tip of the nanotube due to the relatively weak adhesion between the substrate and catalyst film. In addition, Deck and Vecchio [46] reported the appearance of CNTs grown via thermal CVD that exhibited the tip growth mechanism with encapsulation of metal catalyst particles in each nanotube.

The MWCNTs grown under these conditions in our study follow the tip-growth mechanism reported in literature [46, 61]. A complete formation of catalyst particles has been achieved after the hydrogen reduction process (a). These formations allow the carbon atom to diffuse to the particle interface (b). During the dissociation of C_2H_2 into carbon atom, the top surface of the particle is exposed for further carbon absorption. Carbon atoms started to nucleate and form a graphitic structure which is usually a hexagonal network [165].

Due to the weak adhesion between catalyst and substrate [61], the catalyst particle tends to move towards the upper surface of open-fibre (c). As mentioned earlier, the growing

fibre experiences competition between the other fibres which led to the deformation of carbon nanostructure. The carbon nanostructure is not in a straight structure formation and curled fibre can be seen in Figure 4-29. As the growing fibre is exposed to carbon atoms, the absorption of carbon causes the simultaneous growth of a dense carbon nanostructure, which means intense growth competition occurs between fibres.

Finally, the catalyst particle sits at the tip of fibre after the completion of carbon supply (d). The supply of carbon atoms deteriorates over the growth time. Generally, the graphitic layer will form a cap-like structure to encapsulate the particle within the fibre. By terminating a carbon supply, the catalyst particle would be unable to move further to the upper fibre due to the more rapid formation of the cap-like graphitic layer than the movement of particle [48].

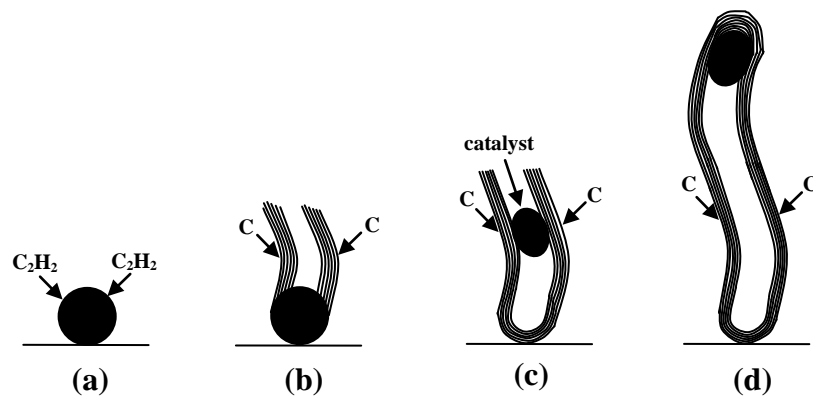


Figure 4-31: Schematic illustration of the MWCNT nucleation and growth processes

4.3.5.2.2 Nanostructure growth at 200 Torr

Figure 4-32 shows the SEM images and EDX line scan of nanostructures that have been grown at the system pressure and growth temperature of 200 Torr and 450°C, respectively. The growth was undertaken for the three different growth times of 1, 5 and 10 min. For the first time in this work, the appearance of carbon-based morphology was observed for the growth time of 1 min (Figure 4-32a & b). The morphology of the nanostructure grown under these conditions is similar to the morphology under the conditions of 100 Torr at 400°C for 5 min. Under the conditions used until now only the formation of catalyst particles (with very little growth of the carbon nanostructure) has been observed during the initial 1 min of growth. However, the EDX data (Figure 4-32c) clearly shows regions of significant carbon composition on the surface at 1 min of growth.

The carbon nanostructure that has grown by 5 and 10 min appear to be very similar in both morphology and composition (Figure 4-32d-i). It would therefore appear that at a system pressure of 200 Torr growth saturation occurs at around 5 min, with no enhancement in growth observed between the growth times of 5 to 10 min. For all three growth times, iron is detected in the EDX spectra. By contrast, iron was not detected at the growth temperature of 400°C between the system pressures of 100 to 400 Torr for 10 min growth time.

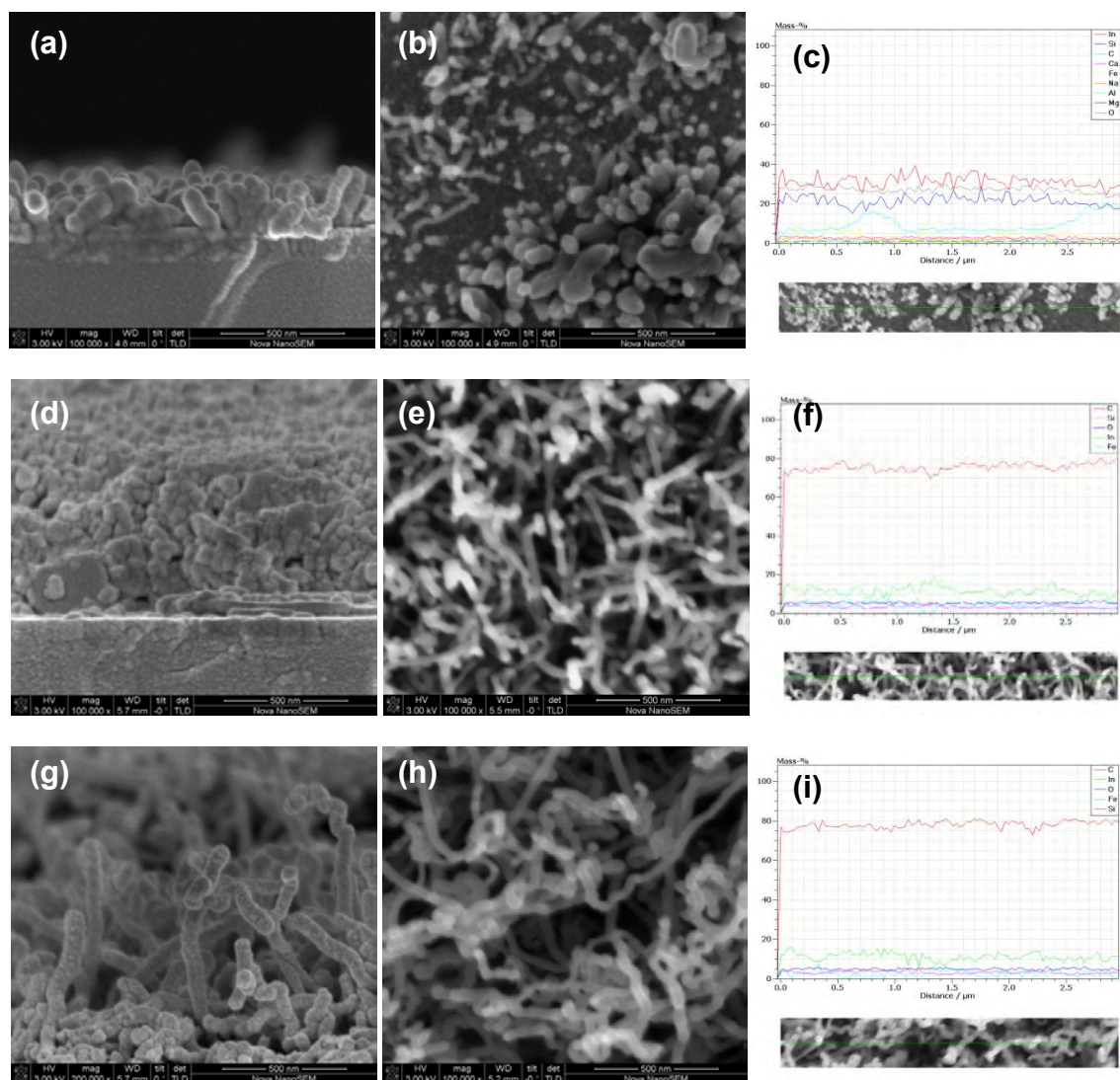


Figure 4-32: FESEM images (cross-section and top view) and EDX data (line scan) of nanostructures grown at 450°C of 200 Torr for 1 min (a-c), 5 min (d-f) and 10 min (g-i)

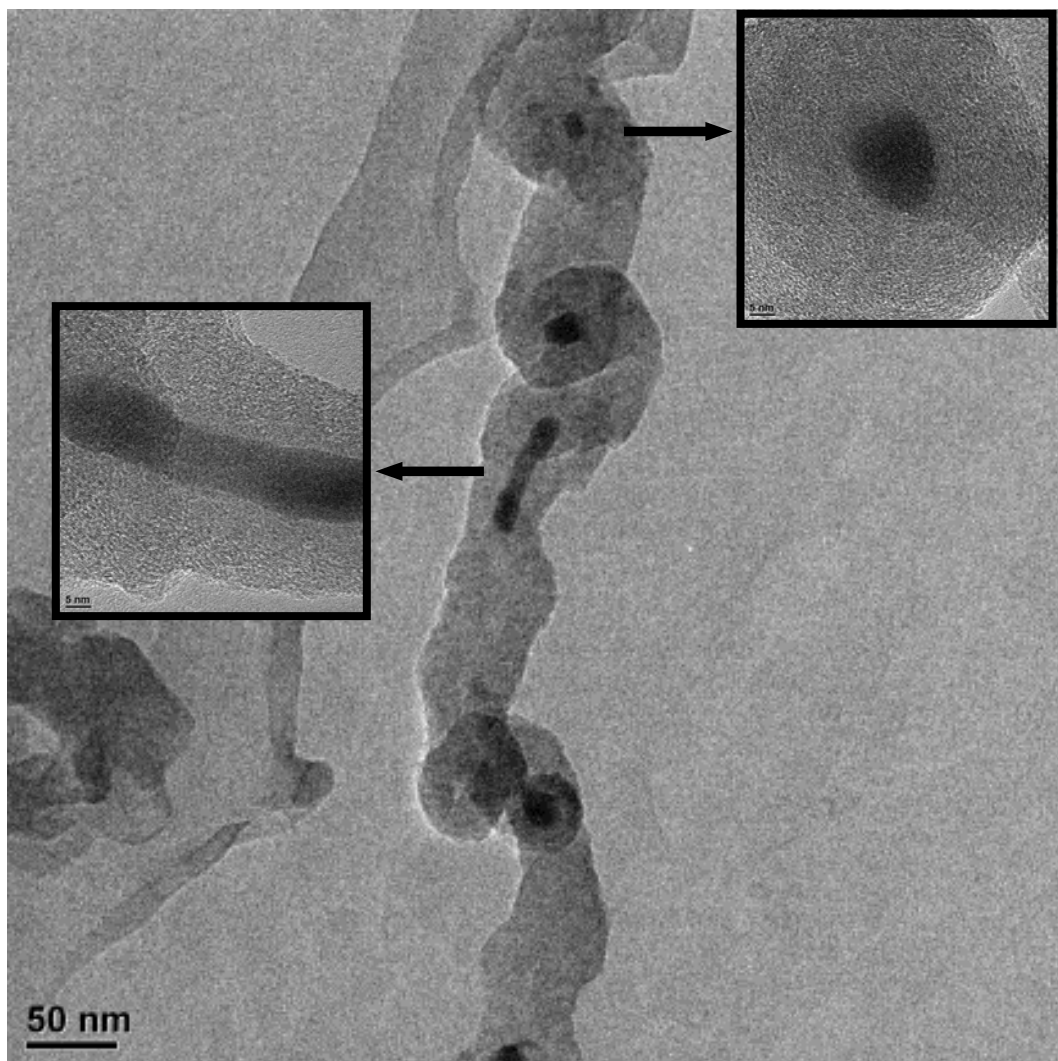


Figure 4-33: High resolution TEM image of carbon nanostructure grown at 450°C of 200 Torr for 10 min

A high resolution TEM image of one of the carbon nanostructures grown on iron coated-ITO under 200 Torr at 450°C for 10 min is presented in Figure 4-33. The image reveals a twisted nanocoil structure with a number of particles encapsulated within the coils. Two shapes of particles (spherical and rod shaped) have been magnified from within the nanofibre – these are encapsulated by the multiple layers of carbon. Many groups have reported the encapsulation of iron particles within the CNT [138, 166, 167], which could explain the observation in Figure 4-33. According to Pan et al [140], ITO generates helical growth of carbon nanotubule whereas iron is essential for carbon nanotubule formation. In other work reported by Okazaki et al [56], tin and indium used as a catalyst has resulted in the growth of carbon nanocoils.

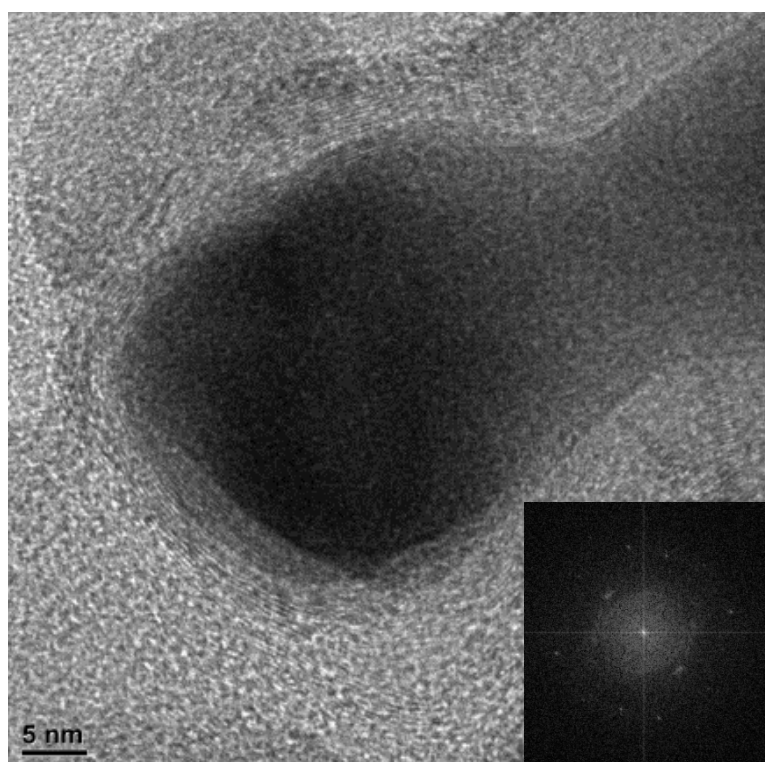


Figure 4-34: High resolution TEM image of particle encapsulated in multiwall carbon nanostructure

In order to identify the particles inside the cavity of the MWCNT, fast Fourier transform (FFT) on the corresponded particle was taken and is shown in Figure 4-34 (inset). The FFT image shows six spots that equidistant from the center which correspond to the (110) planes of iron [168]. It would thus appear that under these conditions iron particles are incorporated into the MWCNT during growth and that growth likely occurs via a tip-growth mechanism.

4.3.5.2.3 Nanostructure growth at 300 Torr

An increase in system pressure to 300 Torr again leads to a denser carbon nanostructure growth (Figure 4-35a-i). It is therefore reasonable to suggest that system pressure has an effect on the density of nanostructure growth, with higher system pressure leading to faster, denser growth.

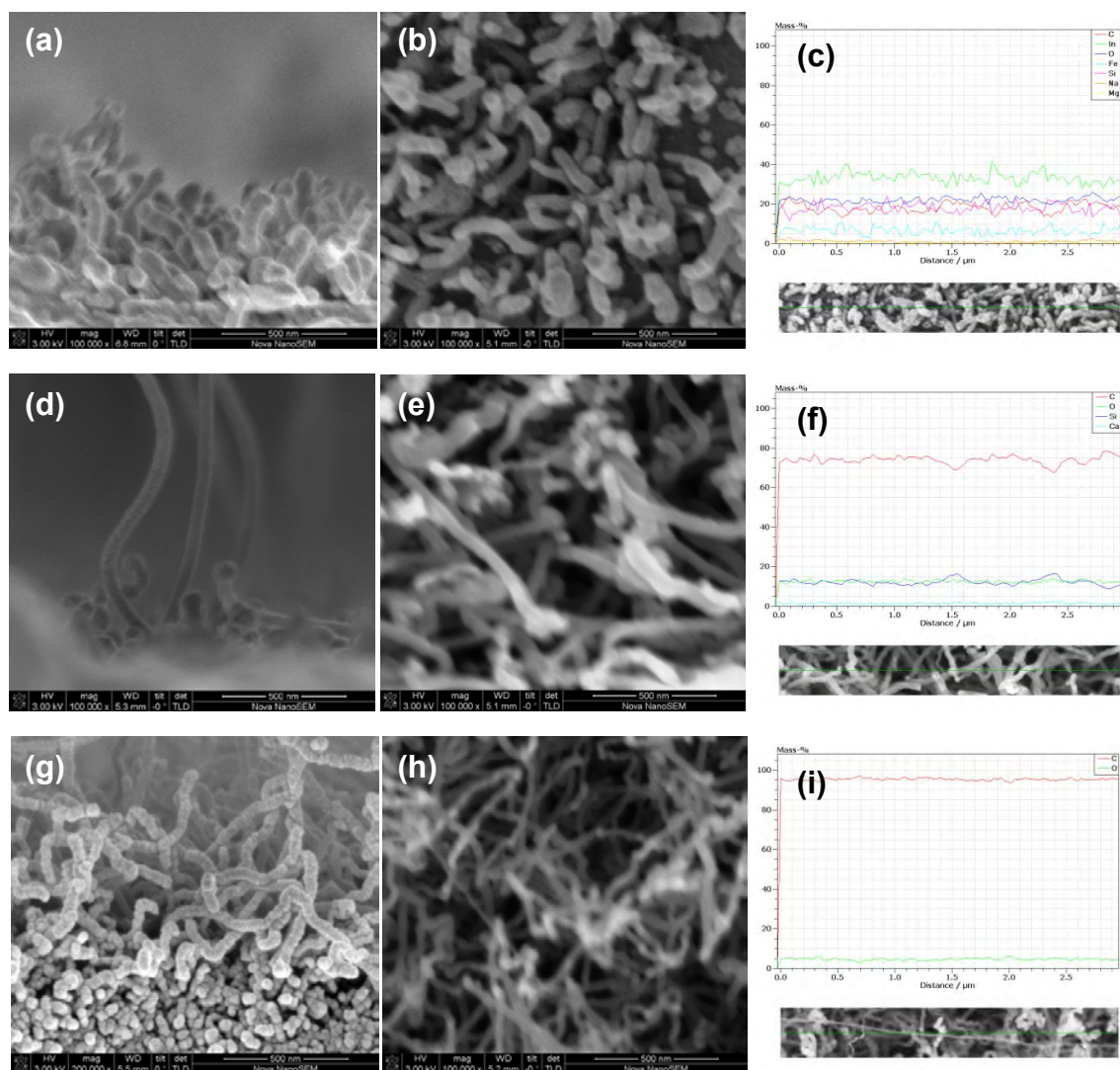


Figure 4-35: FESEM images (cross-section and top view) and EDX data (line scan) of nanostructures grown at 450°C of 300 Torr for 1 min (a-c), 5 min (d-f) and 10 min (g-i)

At higher system pressures both the amount of carbon available for nanostructure growth and its solubility and mobility within the metal catalyst will be higher. Both of these factors will lead to the more rapid carbon nanostructure growth observed. As a result, the growth and distribution of nanostructure after 1 min (300 Torr) is substantially greater compared to the other nanostructures that have been grown with the same growth time at lower system pressures and growth temperatures.

The percentage composition of carbon, indium and iron during the growth between 1 to 10 min is presented in Figure 4-36. At 5 and 10 min the concentration of carbon dominates over the other elements (indium and iron) and indium and iron both essentially disappear. This disappearance of both indium and iron suggests that the carbon nanostructure consist only of pure graphitic material without the incorporation of metal particles.

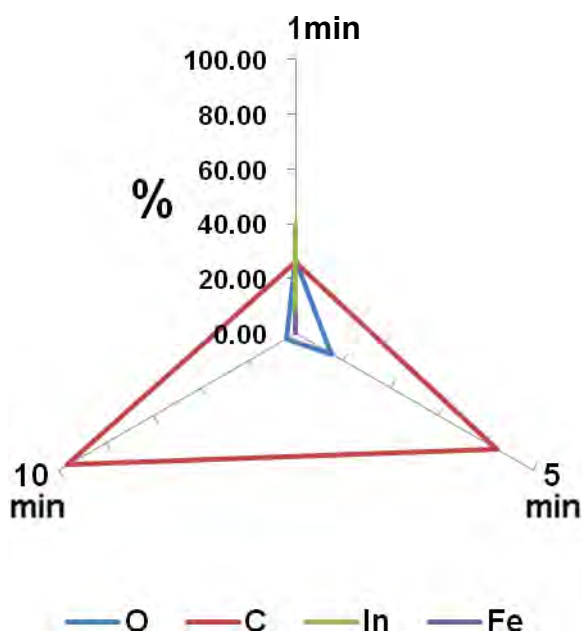


Figure 4-36: 3D graph distribution of relative atomic concentration of O, C, In and Fe growth at 450°C and 300 Torr of different growth time

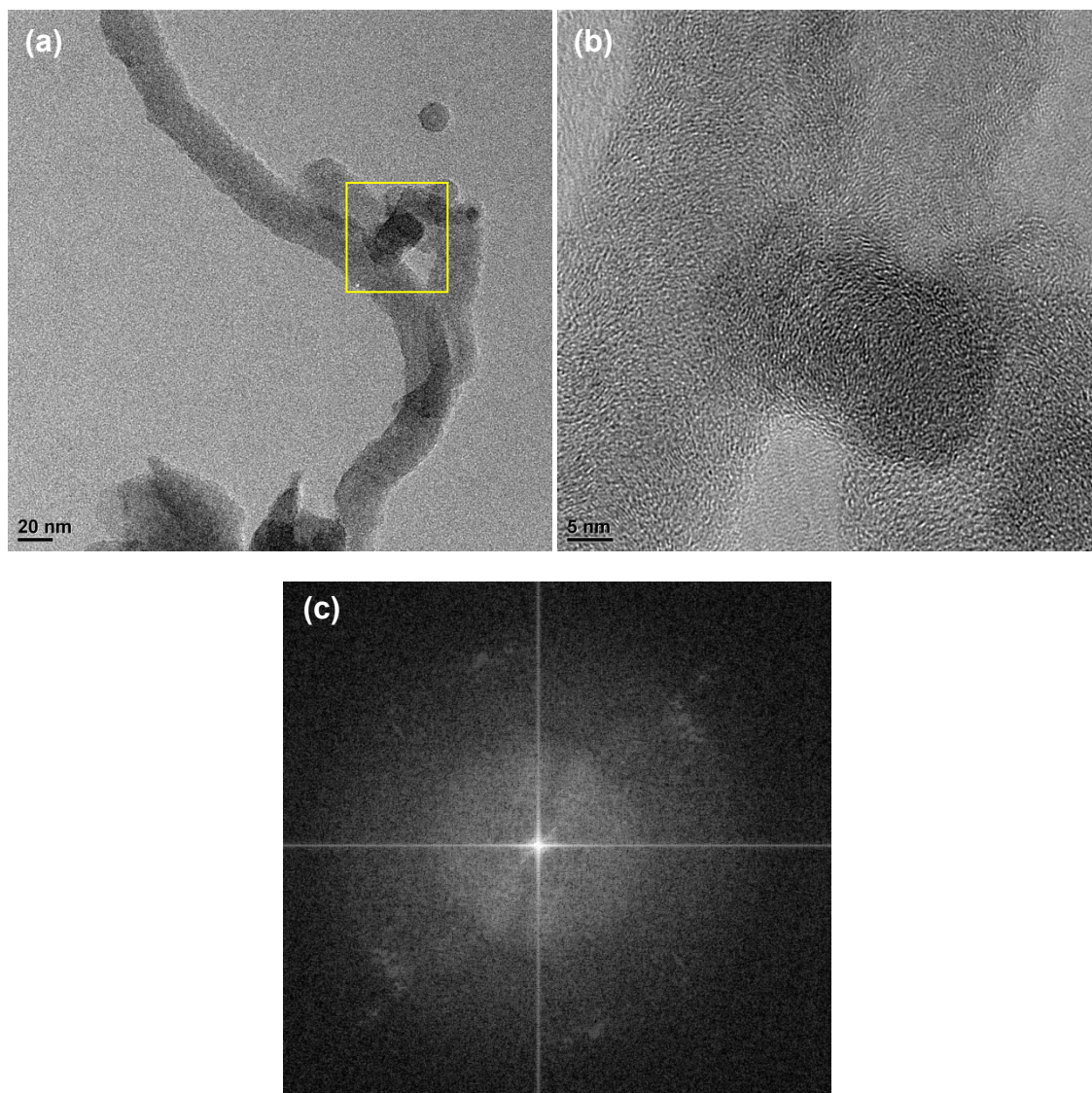


Figure 4-37: High resolution TEM images (a & b) and the corresponding fast Fourier transform (c) of carbon nanostructure grown at 450°C of 300 Torr for 10 min

The disappearance of iron (and indium) within the carbon nanostructure after the 10 min growth is explained by the high resolution TEM images shown in Figure 4-37a and Figure 4-37b. These figures show the TEM image of a representative individual carbon nanostructure taken in the low and high magnification. As can be seen the TEM images show a carbon nanotube free from the catalyst particles. This observation is further confirmed by the FFT image which indicates a poorly crystalline MWCNT from the diffuse spots with no metal present.

The FFT of an iron particle will always illustrate the six sharp spots with each of the spots equal distance from the centre [168]. The FFT image of the displayed nanotube shows only the blurred diffuse spots which indicate a poorly crystalline MWCNT with numerous imperfections [169]. The carbon nanostructure has been further characterised by XPS (Figure 4-38). Only carbon and oxygen were observed under the 300 Torr synthesis conditions. No iron (or indium) was detected in the XPS spectrum which in agreement with both the EDX spectrum and TEM image displayed in Figure 4-35i and Figure 4-37, respectively. This observation suggests to the reduction of any catalyst particles encapsulated within the MWCNT.

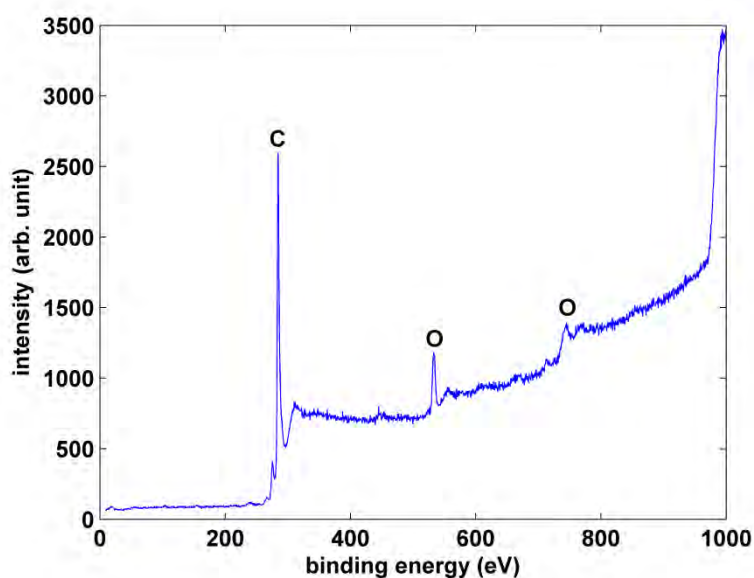


Figure 4-38: XPS spectrum of carbon nanostructure grown at 450°C of 300 Torr for 10 min

4.3.5.2.4 Nanostructure growth at 400 Torr

The morphology of carbon nanostructures synthesised with a system pressure of 400 Torr and temperature of 450°C are presented in Figure 4-39a-i for different growth times. When compared to the morphologies obtained for 100, 200 and 300 Torr under the same temperature and growth times this set of conditions best summarises the complexity of growing carbon nanostructures on ITO.

Remember that at 100 Torr MWCNTs were grown which have iron particles at their tips and thus suggest a tip-growth mechanism based on iron particles as the catalyst (section 4.3.5.2.1). At 200 Torr MWCNTs were grown which show increased defects and helicity with multiple iron particles of varying shapes located at these imperfections (section 4.3.5.2.2). At 300 Torr much straighter MWCNTs are observed which are now completely free of any encapsulated metal particles (section 4.3.5.2.3). Now at 400 Torr of system pressure initial growth shows a variety of metal particle sizes and shapes more reminiscent of those observed for 200 Torr at 400°C.

The growth of carbon nanostructures at 5 min leads to a dense film with a lot of sharp surface contrast in the SEM (Figure 4-39e). From the EDX line scan, the mass concentration of carbon is dramatically increased from its initial growth but not to the same extent as the mass concentration of carbon which grown at the lower system pressure of 300 Torr. Therefore, a slower growth rate of carbon nanostructures at 400 Torr could be assumed. Both indium and iron are visible in the EDX spectra during carbon nanostructure growth times of 1 and 5 min, before the iron completely vanishes at the longer growth time of 10 min. Interestingly indium is still visible at ~5% mass composition which was not observed at the system pressure of 300 Torr. The observed fluctuations in the appearance of indium and iron in the EDX spectra of these carbon nanostructure films is complex and has clouded the ultimate role both elements have during carbon nanostructure growth.

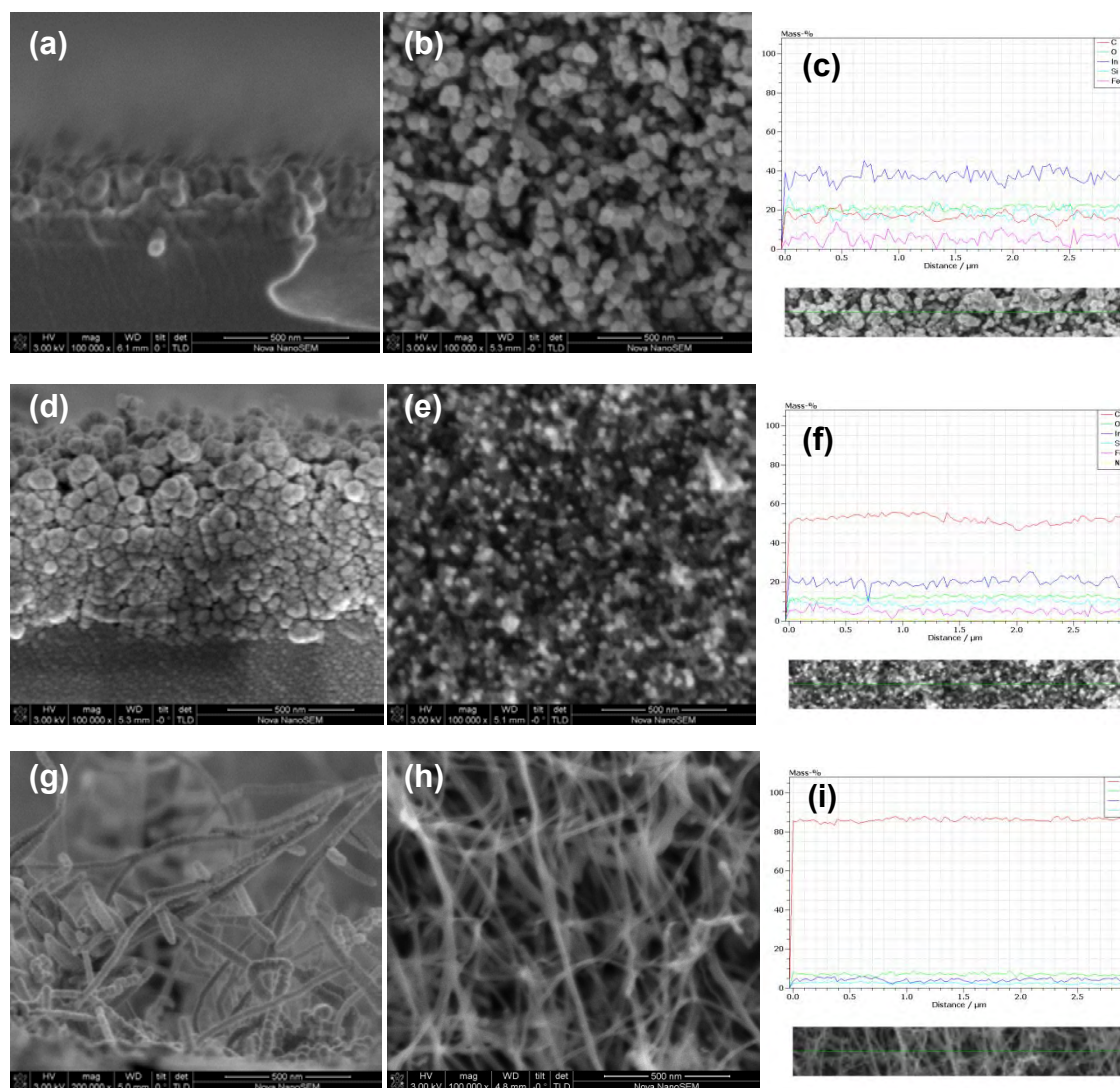


Figure 4-39: FESEM images (cross-section and top view) and EDX data (line scan) of nanostructures grown at 450°C of 400 Torr for 1 min (a-c), 5 min (d-f) and 10 min (g-i)

Unusual and extreme morphology is observed for the carbon nanostructure grown at 400 Torr (Figure 4-39g). Long, straight carbon nanostructures are grown at the higher pressure instead of the distorted, entangled forms observed throughout the rest of this work. High resolution TEM images were taken to further understand this morphological change.

Figure 4-40 shows the high resolution TEM images of a representative carbon nanostructure grown at 450°C and 400 Torr for 10 min. as well as a magnified image highlighting interplanar spacing of a particle within the structure (Figure 4-40b and c) and this images corresponding FFT image (Figure 4-40c). The image shows a straight,

needle-like carbon nanostructure with the attachment of few particles to the carbon nanostructure and budding nanostructures leading of the main needle. The SEM image of the carbon nanostructure on the TEM grid was taken confirming a needle-like carbon nanostructure morphology with branches on it (Figure 4-40a (inset)).

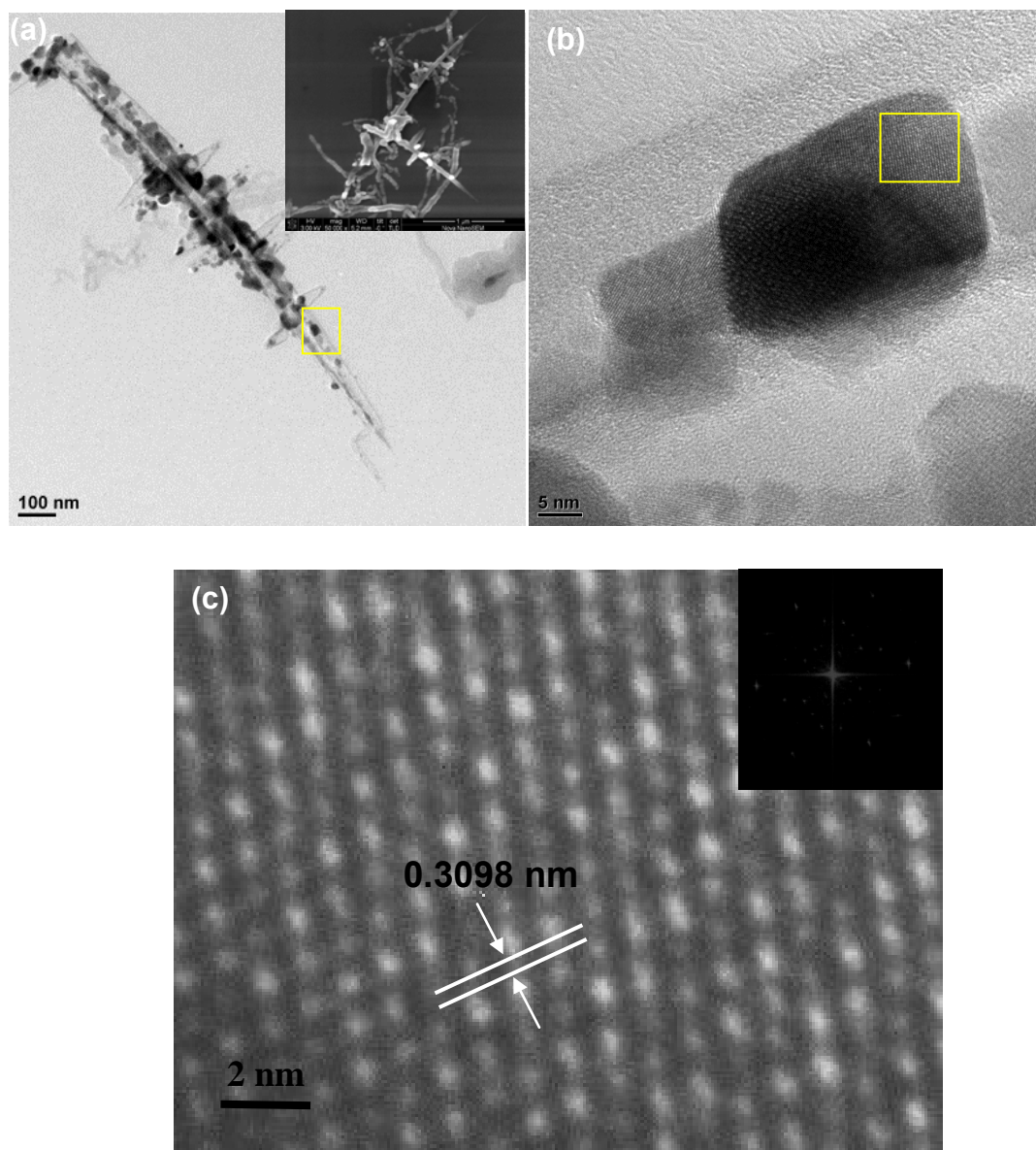


Figure 4-40: (a) A high resolution TEM image of carbon nanostructure grown at 450°C of 400 Torr for 10 min (inset: SEM image). (b) An image magnified from the yellow box in (a). (c) An image magnified from the yellow box in (b) and its fast Fourier transform image (inset)

The particles attached to the carbon nanostructure have been further identified by examining the interplanar spacing of a typical particle and its corresponding FFT image. From the higher magnification of TEM image in Figure 4-40b, a particle was seen sitting within the carbon nanostructure. An interplanar spacing of 0.3098 nm was obtained by the high magnification image Figure 4-40c, this value is close to the *d*-spacing value for the (222) lattice plane of crystalline indium oxide which is reported to be 0.293 nm [170]. Therefore, the particle that is encapsulated by the carbon nanostructure can be identified as indium oxide.

In addition to the TEM images displayed in Figure 4-40 which show what appear to be the initial growth of indium oxide structures incorporated within the carbon nanostructure, the SEM and TEM images shown in Figure 4-41a-d clearly show solid indium oxide nanostructures. The size of the solid nanostructures ranges from tens to a hundred nanometers in diameter and a few micrometers in length. The solid nanostructure tip is sharper than the base, which is flat or irregular in shape. A selected area electron diffraction pattern image shown in Figure 4-41e shows excellent agreement with the indium oxide lattice plane of (222) [170]. It is clear that the accumulation of indium oxide particles in carbon nanostructures (solid nanostructure) is driven by the high system pressure of 400 Torr.

The incorporation of indium oxide particles into the carbon multiwalled nanotube results in a tapered shape with a protruding tip of a smaller diameter of 20 nm. A tapered solid indium nanostructure can be caused by the diffusion and evaporation of indium at temperatures over 400°C [17]. In addition, the tapered cone-like nanostructure may be formed due to sidewall deposition. This kind of growth mechanism can be compared to the solid-liquid-solid mechanism which is activated by the formation of catalyst droplets. Further explanation of the growth mechanism will be provided in the following section.

The presence of indium within the nanostructures is confirmed by the XPS spectrum shown in Figure 4-42 where carbon, oxygen, indium and nitrogen are observed in the solid nanostructure. Oxygen is easily incorporated into the growth since the synthesis is implemented under only medium vacuum conditions [17]. Furthermore it would be expected to be observed as part of the indium oxide encapsulated within the

nanosstructure. Nitrogen is observed in the XPS spectrum due to sample preparation which used liquid nitrogen. As reported by Lo et al [143], carbon can act as a reducing agent for the further formation of indium sub-oxides. Indium oxide nanostructures encapsulated by carbon layer are believed to dominate in this synthesis due to the higher indium composition ratio of 90:10 to tin as evidenced in Figure 4-43. As reported elsewhere, indium oxide nanorods can be grown from catalyst droplets once the concentration of indium and oxygen atoms come to saturation [143].

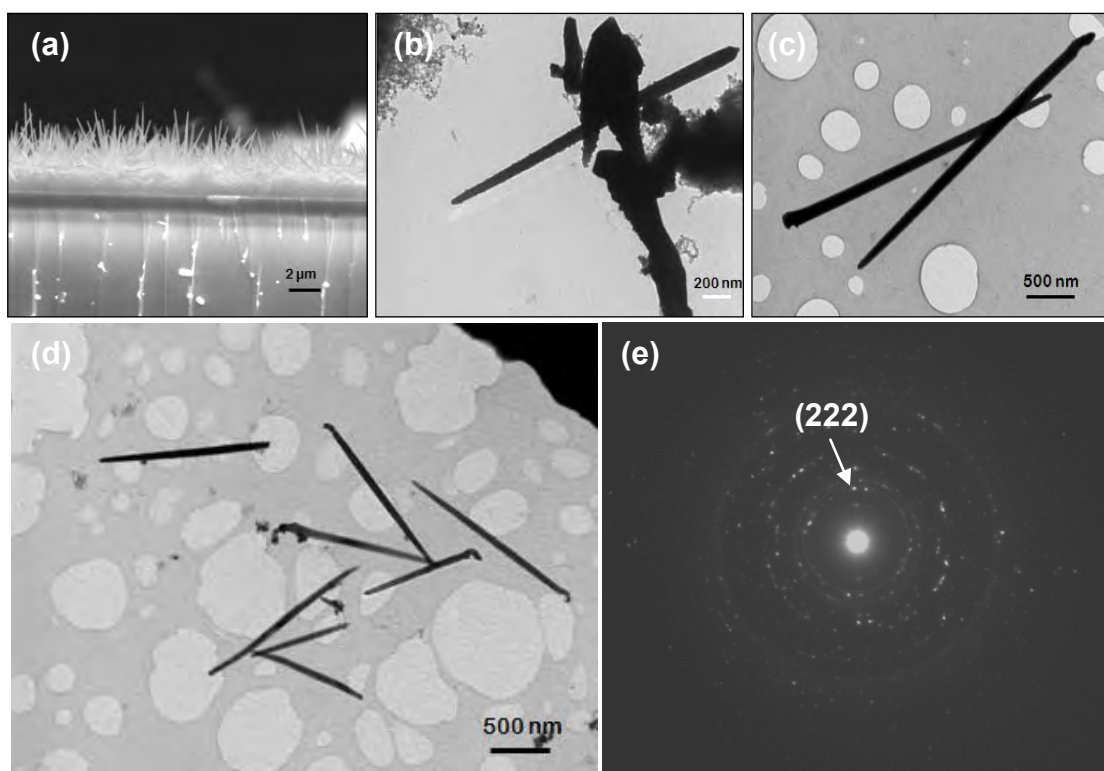


Figure 4-41: (a) SEM image (b-d) TEM images of indium oxide nanostructure encapsulated by carbon layer grown at 400 Torr and (e) Selected area diffraction pattern of image in (d)

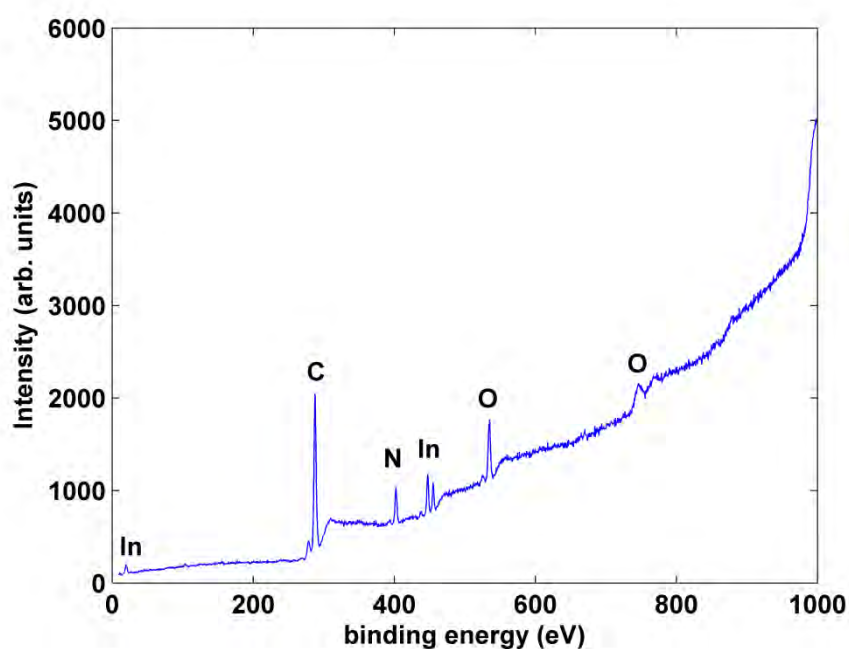


Figure 4-42: XPS spectrum of indium oxide nanostructure encapsulated by carbon layer

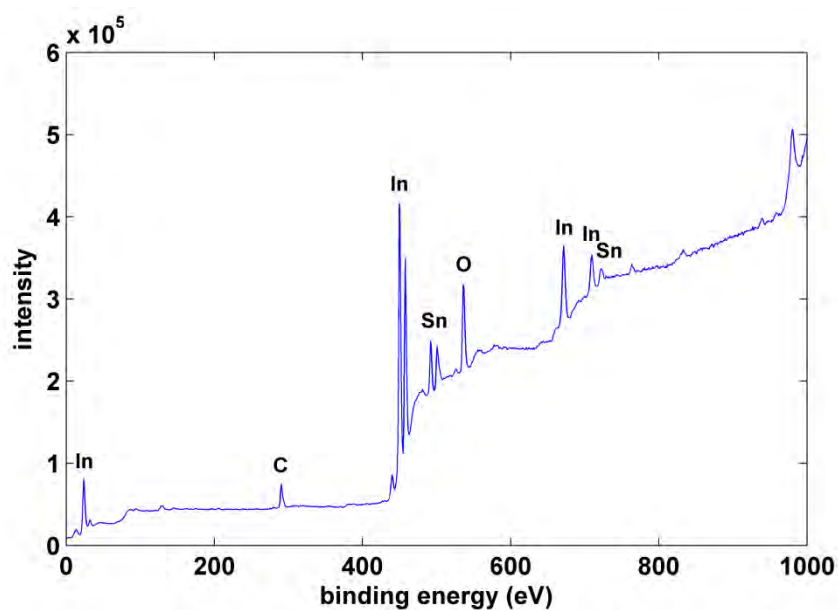


Figure 4-43: XPS spectrum of ITO substrate

Metals such as tin can be vaporised along with the introduction of hydrocarbon gas in order to produce tin nanowires encapsulated in amorphous carbon [22]. Thus, it is possible to grow an oriented nanotube array filled with other nanowires of different materials, so-called nano-heterostructures. Carbon is less soluble in metal catalysts such

as indium [12] or tin [22] compared with other well-known metal catalysts such as cobalt [48], iron [3, 45, 46, 48, 50, 86, 89, 137] or nickel [2, 8, 20, 46, 48]. Therefore typically in these systems formation of amorphous carbon is dominant over the growth of graphitic CNTs due to the low solubility between carbon and metal catalyst [22].

ITO-based nanostructures, a core-shell nanowire, can be prepared by CVD from ITO nanoparticles with the introduction of acetylene gas [16]. An amorphous carbon layer encapsulates the ITO nanoparticles via the VLS mechanism. This work [16] supports our observation on the growth of carbon layer as a sheath on the indium oxide nanostructure. In our study, the SLS mechanism [141] which is analogous to the VLS mechanism [22] is proposed to explain the formation of indium oxide nanostructures encapsulated by a carbon layer. Indium catalyst droplets can be generated *in situ* directly from a transparent conductive substrate of ITO [18]. At the synthesis temperature of 450°C, the ITO film changes its form to produce indium and tin liquids. Indeed, the ITO substrate can transform into indium and tin droplets at the growth temperatures as low as 250°C [18]. The indium and tin vapour phase is negligible at 450°C due to the exceptionally low specific surface/volume ratio of bulk ITO substrate compared with that of indium or tin. In addition, the ITO substrate was covered by a thin layer of iron which will help restrict the ITO components to the liquid form rather than the vapour phase [141]. The transformation from solid to liquid form is due to the relatively low melting points of indium and tin which occur at 157°C [12] and 232°C [22], respectively. Since, indium has a lower melting point than tin; indium liquid is formed prior to the formation of tin liquid. As reported elsewhere, indium has been observed to be a dominant metal traced after the reduction of ITO powder by acetylene gas [16].

The liquid phase of indium will become saturated and transform to the solid phase due to thermal and compositional fluctuations [141]. It is been proposed that the indium droplet dominates the transformation process allowing the incoming carbon atoms to diffuse over its droplet edge. *In situ* growth of an carbon layer is observed around the indium oxide nanostructure by the decomposition of acetylene which is in accordance with previous studies [16]. A carbon layer encapsulated indium oxide nanostructure is assumed to grow from the base since indium atoms can continue to diffuse from the

ITO film into the carbon hollow during the growth [142]. ITO nanowires synthesised from an indium catalyst can be formed via a self-assembly process in the absence of a carbon source via CVD [16]. According to Hsu et al [142], at synthesis temperatures of 550°C, an ITO film layer that was coated onto a silicon substrate started to diffuse at the bottom and filled the nanowire. Under the present conditions, however, temperatures as low as 450°C, is adequate for the diffusion of indium. The diffusion of tin atom is not observed during the growth which is in agreement with literature [142] and is likely, in part, due to the low ratio of Sn:In in the ITO.

From the SEM and TEM images, we proposed a possible growth mechanism of both the carbon layer and the indium oxide nanostructure encapsulated in the hollow carbon layer. A schematic illustration of the proposed growth mechanism is presented in Figure 4-44. The thin metal oxide film of iron and ITO deposited on the substrate tends to form catalyst particle islands and liquid droplets during the reduction step (b). Size and density of metal (indium or tin) droplets can be controlled by optimising the system pressure [18] consistent with the variations in growth observed during this work. Hydrocarbon gas is then introduced to supply carbon atoms for carbon nanostructure growth. If the reduction process has produced the desired uniform catalyst particle islands, carbon atoms can diffuse to each catalyst particle and grow as a carbon layer. The deposition of a thick carbon layer is observed as an interface layer due to the fast hydrocarbon gas decomposition rate which leads to a faster carbon deposition rate than carbon atom diffusion into the catalyst.

At higher pressure of 400 Torr fast deposition of the carbon atoms, which do not have sufficient time to completely diffuse into the catalyst particles occurs, thus an interface layer composed of amorphous carbon is formed (c). In addition, a low growth temperature likely fails to fully activate the catalytic activity of the iron particles [171]. The accumulation of the amorphous carbon indicates a large proportion of catalyst surface has been blocked, preventing carbon layer growth in the vertical direction.

In spite of this, straight solid nanostructures formed by indium oxide encapsulated in carbon layer are observed growing vertically on the top of, or through, the amorphous carbon layer with two or more solid nanostructures sometimes clumped together (d). The observed unidirectional growth is attributed to the cooling process occurring

between the carrier gas and spherical surface of indium droplets [141]. This indicates that some indium droplet sites are active and can initialize the growth of the solid nanostructure at 450°C. Indium has been widely used as a catalyst for nanotube [12, 144] and nanowire growth [16, 17]. As reported by Rao et al [12], indium maintains its liquid state at typical CVD growth temperatures and carbon nanostructures have been successfully synthesised from indium at the high temperature of 850° which indicates that during the growth, the indium is totally in its liquid state. Due to the poor wettability between indium droplets and the substrate, the spherical surface of the droplet can be maintained during the exposure to carbon atoms [12]. From Figure 4-45a it is clear that the carbon nanostructure is formed prior to the encapsulation of indium oxide rather than an indium oxide nanostructure templating subsequent carbon growth.

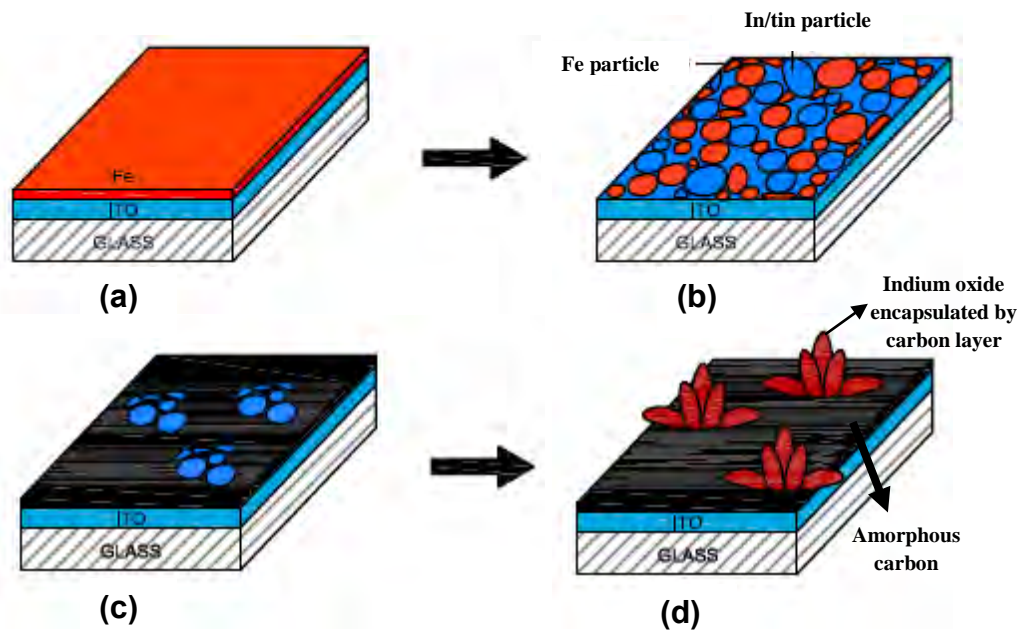


Figure 4-44: Schematic illustration of the proposed growth mechanism of indium oxide nanostructures encapsulated by carbon layer at 400 Torr

4.3.5.3 Raman spectra at 450°C

The Raman spectra of carbon nanostructures grown at 450°C for 10 min at the various system pressures are shown in Figure 4-45. Raman spectroscopy generates information on the purity, defects and tube alignment of carbon nanostructures, and assists in the identification of MWCNTs [172-174]. Raman spectra of pure CNTs show two characteristic bands at 1350 cm^{-1} (the *D*-band) and 1580 cm^{-1} (the *G*-band) [60]. Those two bands can be employed to examine the structural modification of carbon nanostructures synthesised at different system pressure since they contain structural information of the films. The *D* band is related to the presence of disorder in graphitic materials [175]. The origin of the *D* band in nanotubes is frequently considered as a measure of the ‘disorder’ of the tube. The *G* band is defined as graphitic in nature and is due to the sp^2 bonds in both rings and chains stretching [172]. It is also attributed to tangential vibrations of the graphitic carbon atoms. For the CNTs measured in Figure 4-45 the intensity ratio of the *D* to *G*-band is measured as 1.12 which corresponds to the degree of carbonaceous material structure disorder.

As shown in Figure 4-45 the two expected bands of MWCNT grown at 100 Torr are seen at 1346 cm^{-1} and 1580 cm^{-1} . The peak of *G* band at 1580 cm^{-1} supports the existence of pure CNTs even though the *D* band is shifted to a slightly lower wavenumber. A second-order harmonic of *G'* band of weak intensity is also observed at 2696 cm^{-1} . The *G'* band peak is caused by two-phonon scattering around the K point of the Brillouin zone with the intensity of this band relying strongly on the metallicity of the nanostructure [169]. CNTs with fewer than four-walls have shown a broad *G'* band that falls in 2630 cm^{-1} – 2700 cm^{-1} interval [174]. Due to this observation, carbon nanostructures obtained at 100 Torr appear to have multiple graphitic walls which clearly supported by the TEM image in Figure 4-30.

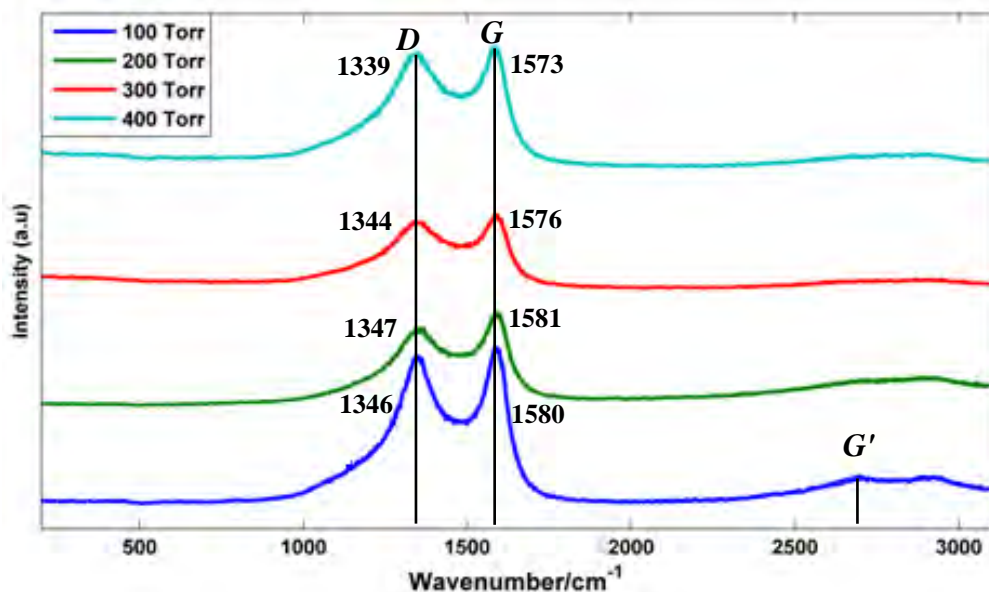


Figure 4-45: Raman spectra of carbon nanostructures obtained at 450°C

The significant difference between the Raman spectrum at 100 Torr and Raman spectra obtained between 200 Torr to 400 Torr is the appearance of a G' band. The G' band was only observed for the MWCNT grown at 100 Torr although the peak intensity is weak and the peak width broad. The I_D/I_G ratio of each Raman spectrum has been calculated from the normalized peak intensity and gives values of 1.2 (100 Torr), 1.24 (200 Torr), 1.31 (300 Torr) and 1.11 (400 Torr) respectively. The relative intensity of D to G bands is increased at 300 Torr indicating more defects of nanostructure. The TEM image of carbon nanostructure grown at 300 Torr supports this observation with multiple carbon layers being formed at this pressure.

The Raman spectra of the indium oxide nanostructure encapsulated by carbon layer synthesised at 400 Torr is presented in Figure 4-45 and Figure 4-46, which corresponded to the TEM images in Figure 4-40a and Figure 4-41d, respectively. As shown in Figure 4-46, two peaks were observed at 1312 cm^{-1} and 1590 cm^{-1} . The D band has experienced a shift (27 cm^{-1}) towards the shorter wavenumber compared to the Raman spectrum (400 Torr) displayed in Figure 4-45. An up-shift of 17 cm^{-1} is seen for the G band. The Raman spectrum for the solid nanostructures (Figure 4-41d) obtained at 400 Torr is much noisier compared that shown for indium oxide particles encapsulated by a hollow carbon layer (Figure 4-40a). Comparison of the two spectra shows that

upon incorporation of the indium the I_D/I_G changes from 1.11 to 1.33. This is indicative of increased graphitic disorder upon incorporation of the indium oxide. Changes in D -band can be related to a particular type of nanotube defect [174]. For example, integration of lithium into the disordered planes of nanorods has caused an increasing in intensity D -band [176]. This observation confirms that particle intercalation or incorporation occurs at the high system pressure of 400 Torr leading to a novel indium oxide nanostructure encapsulated by a carbon layer.

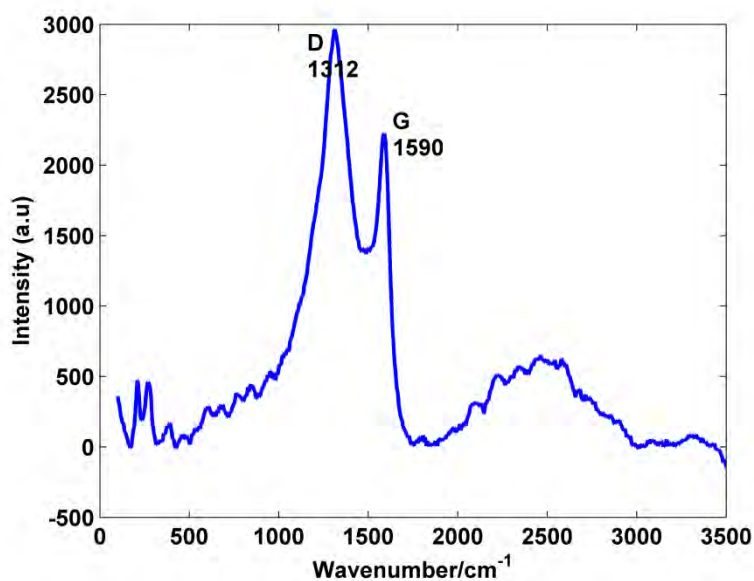


Figure 4-46: Raman spectrum of indium oxide nanostructures encapsulated by carbon layer obtained at 400 Torr

4.3.5.4 Nanostructure growth at 500°C (100 – 400 Torr)

4.3.5.4.1 Nanostructure growth at 100 Torr

The temperature dependence of carbon nanostructures growth at different system pressures and growth times was determined at the 500°C and shown in Figure 4-47a-i. Carbon nanostructure growth occurred after 5 min of growth time, with carbon nanostructure growth dominating after 10 min. For the growth between 5 and 10 min, twisted and entangled carbon nanostructures exist with a thicker, denser carbon nanostructure growth occurring after 10 min growth as shown by the EDX data (Figure 4-47i).

During the initial 1 min of growth fragmentation of catalyst thin film begins, however, but the complete transformation into catalyst particles, which has been previously evident at the lower growth temperatures (400 & 450°C). At the higher temperature, the increased thermal energy available to the catalyst thin film would be expected to enhance the transformation of thin film into particles. This is not observed, with a flat film of carbon forming over the substrate surface.

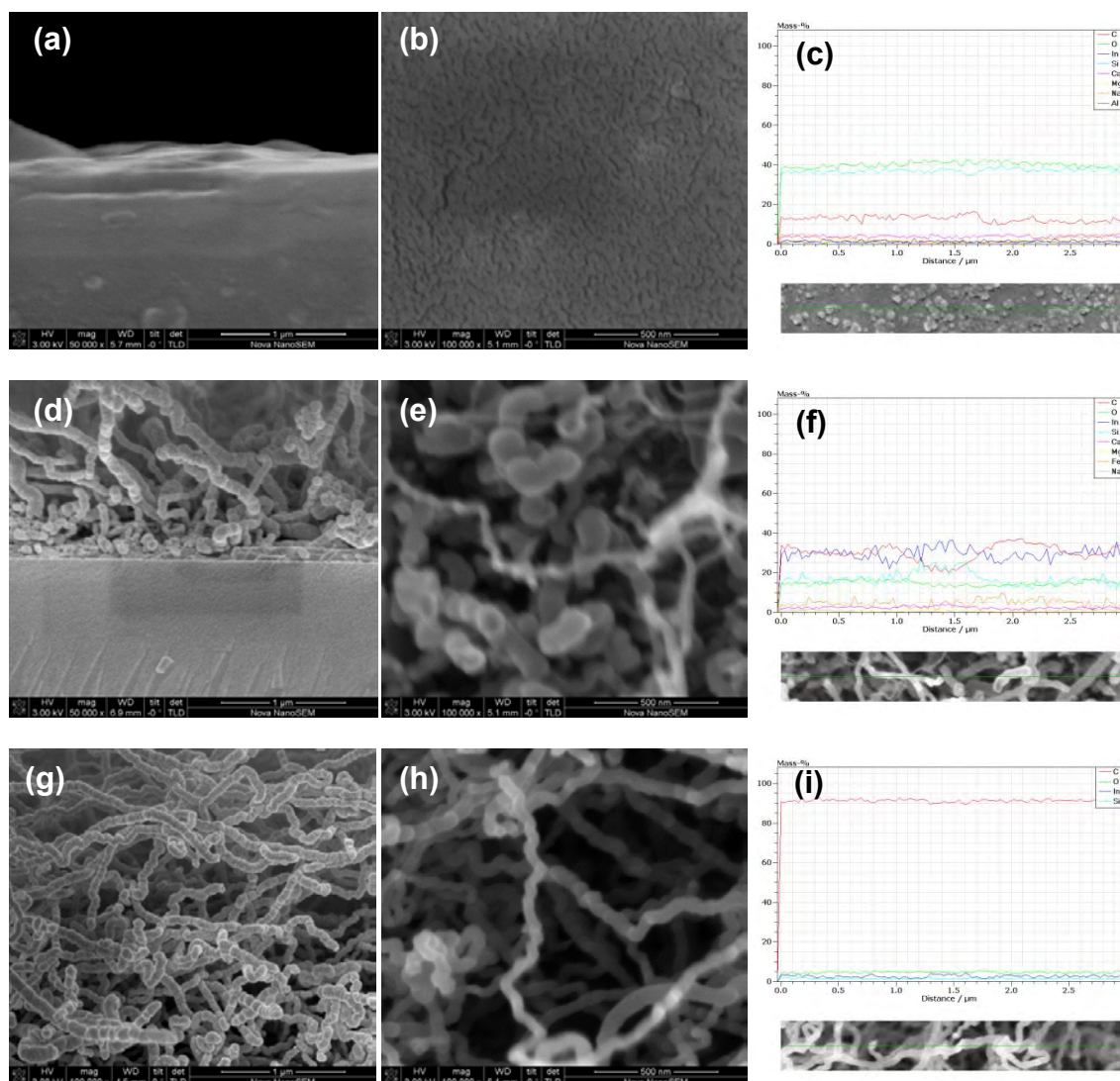


Figure 4-47: FESEM images (cross-section and top view) and EDX data (line scan) of nanostructures grown at 500°C of 100 Torr for 1 min (a-c), 5 min (d-f) and 10 min (g-i)

4.3.5.4.2 Nanostructure growth at 200 Torr

As the system pressure is increased carbon nanostructure growth is observed after only 1 min and this growth continues resulting in nanostructure films very similar to those for the 100 Torr system (Figure 4-48a-i). However in this case the carbon content peaks at ~75% of the 10 min growth compared to >95% for the same growth period at 100 Torr. Surprisingly the remainder consists of Si and O (suggesting that the glass substrate is partially exposed). The silicon EDX line scan for the 5 min sample, in particular, shows an excellent inverse correlation with the carbon composition suggesting that

silicon is exposed primarily in places where the carbon growth is not present. It may be that at this pressure and temperature melting and distortions of the ITO substrate combined with evaporation of indium and tin from the surface leads to exposure of the silicon-rich glass substrate. Certainly high levels of both silicon and oxygen are also seen for the 300 and 400 Torr samples which were synthesised at 500°C.

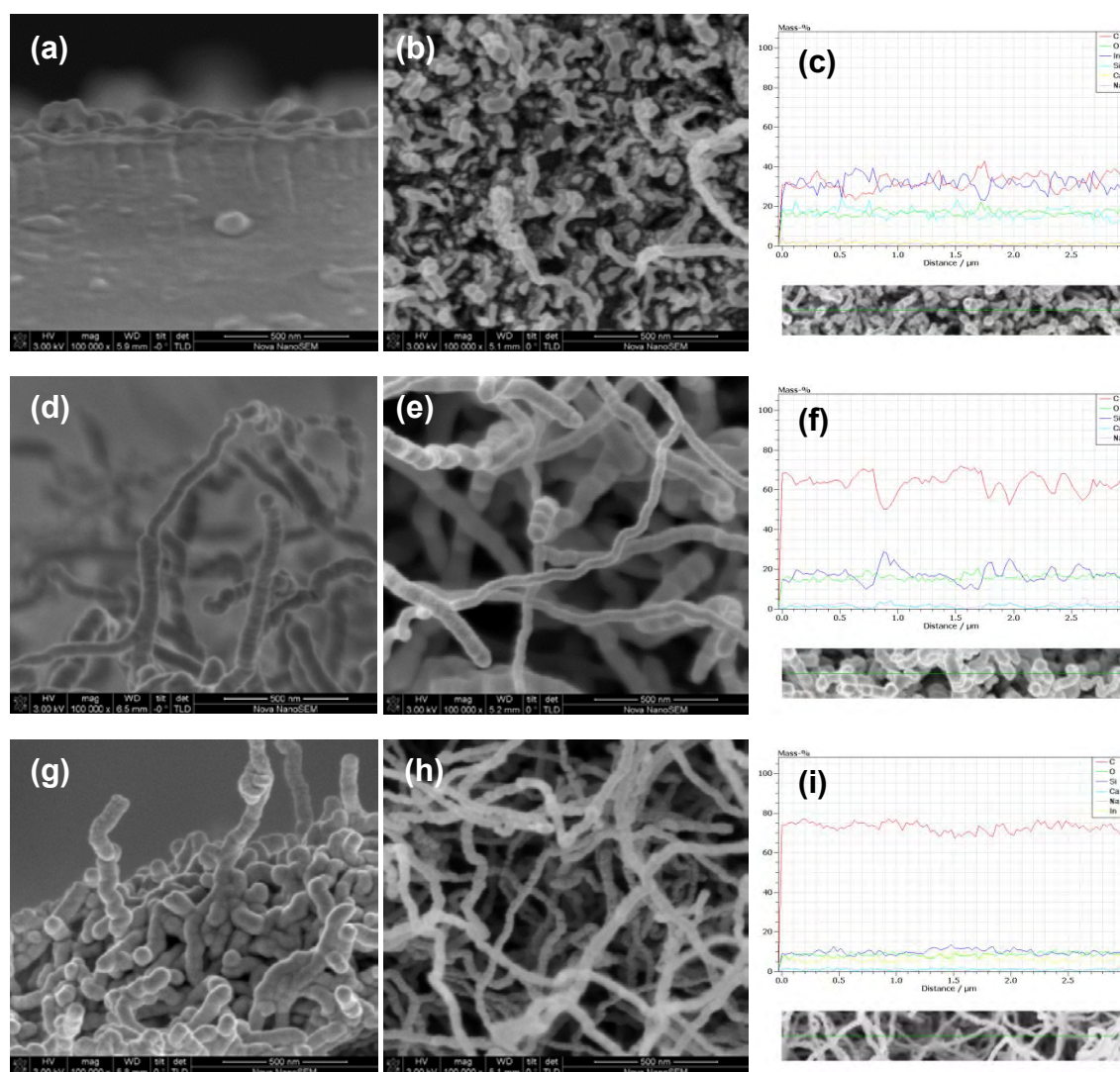


Figure 4-48: FESEM images (cross-section and top view) and EDX data (line scan) of nanostructures grown at 500°C of 200 Torr for 1 min (a-c), 5 min (d-f) and 10 min (g-i)

4.3.5.4.3 Nanostructure growth at 300 Torr

At 500°C and 300 Torr the growth of twisted, entangled carbon nanostructures no longer occurs. Initial growth leads to the appearance of nanostructures in patches with a much less dense distribution of growth (Figure 4-49a and Figure 4-49b).

Continued growth (Figure 4-50a-f) leads to long, very straight carbon nanostructures upon a crystalline substrate surface composed of particles of both silicon oxide and indium oxide.

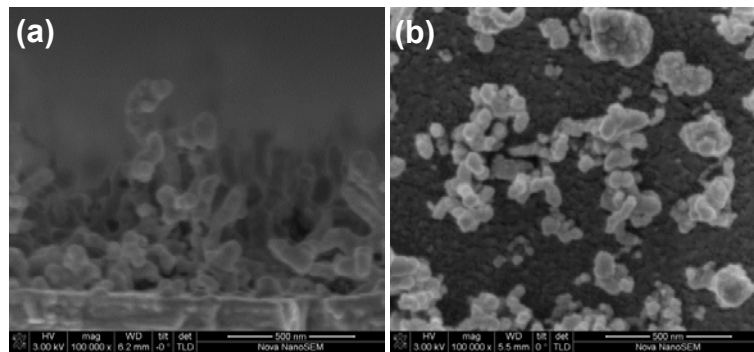


Figure 4-49: FESEM images of (a) cross-section & (b) top-view of nanostructures grown at 500°C of 300 Torr for 1 min

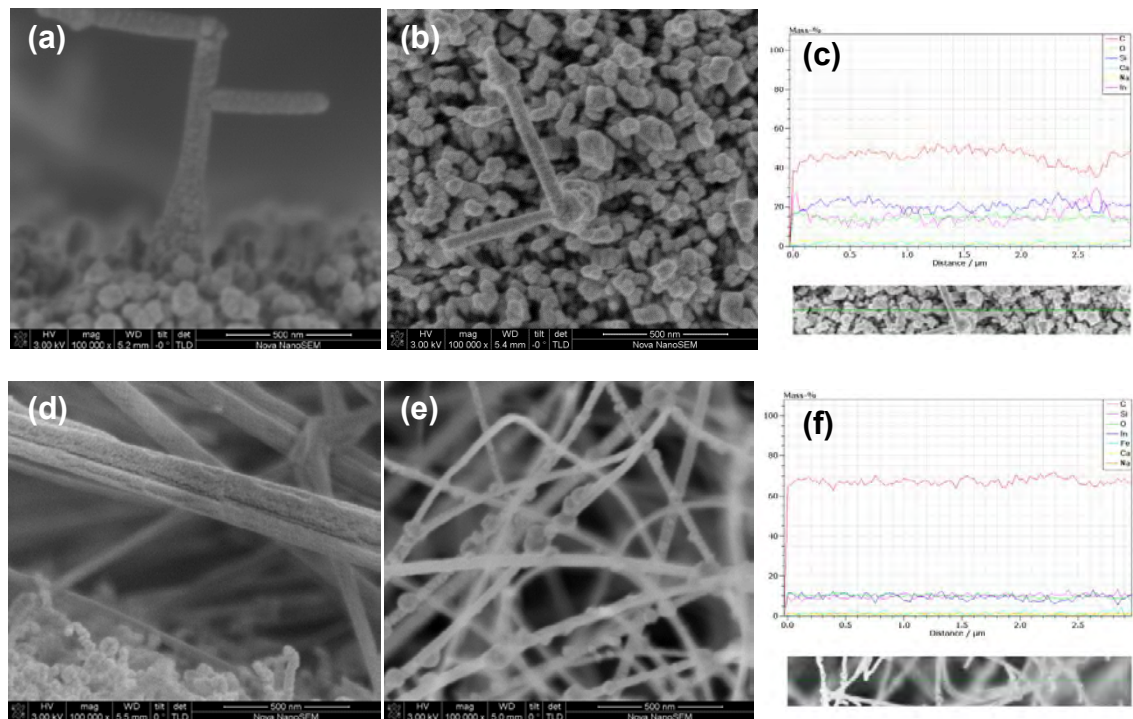


Figure 4-50: FESEM images (cross-section and top view) and EDX data (line scan) of nanostructures grown at 500°C of 300 Torr for 5 min (a-c) and 10 min (d-f)

4.3.5.4.4 Nanostructure growth at 400 Torr

Finally, the growth of carbon nanostructures onto the ITO substrate is completely suppressed at the highest system pressure and growth temperature. For growth between 1 to 10 min at 500°C and 400 Torr high compositions of iron, indium, silicon and oxygen are observed, with the only a minimal amount of carbon deposition (Figure 4-51a-i). Rather than carbon nanostructure growth it appears that under these conditions the major transformation is the continued formation of increasingly large metal oxide crystals. For all three growth times there is an inverse correlation in the appearance of indium and silicon in the EDX spectrum suggesting the growth of both indium oxide and silicon oxide carbon coated particles on the substrate surface. The silicon also shows an inverse correlation with the carbon composition, as was observed the 5 min, 500°C and 300 Torr sample. However, the indium composition is roughly correlated with the carbon composition, especially at 10 min growth time. This suggests that, as observed for the 450°C and 400 Torr sample, this sample may be composed of carbon coated indium oxide nanostructures.

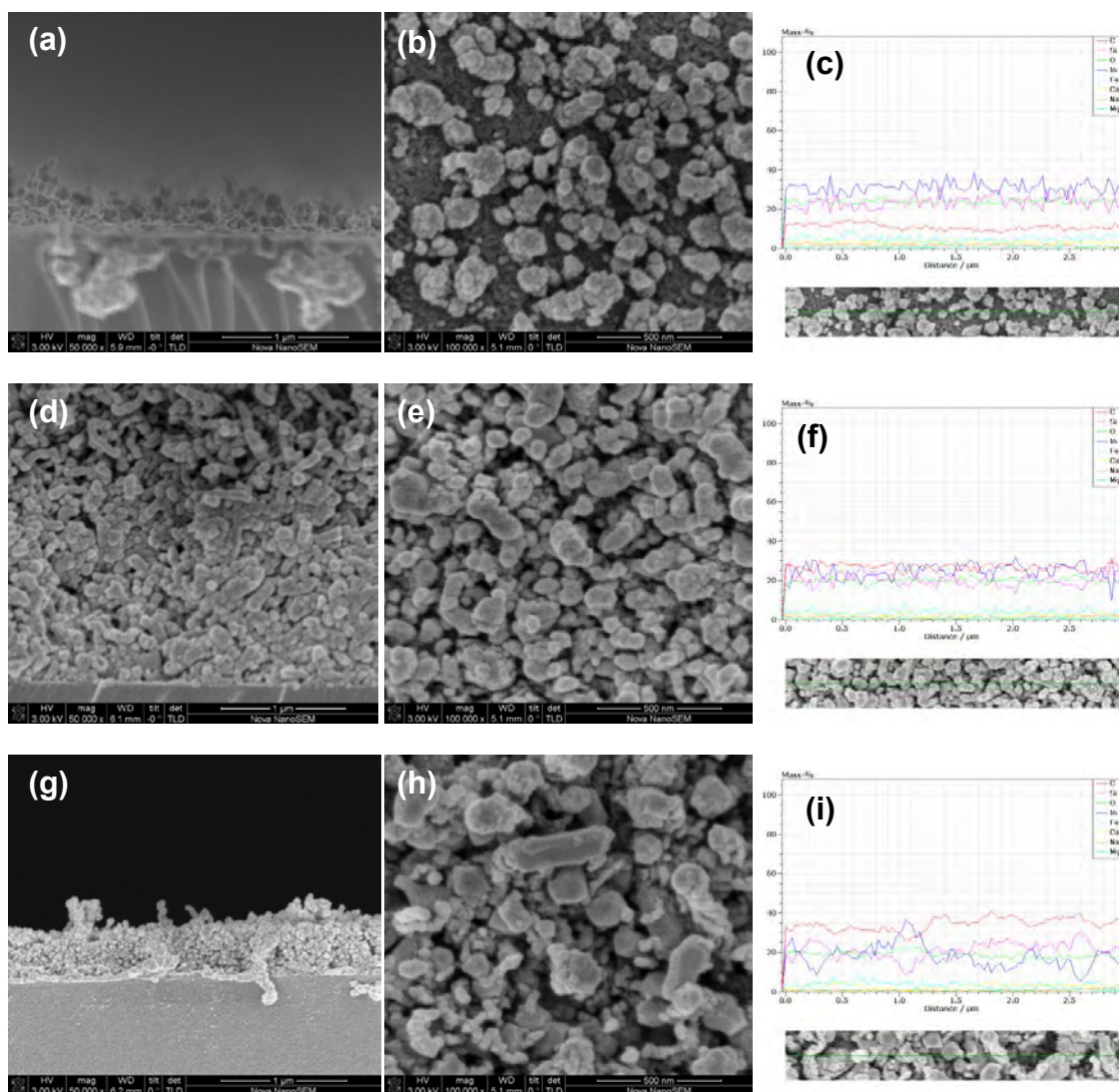


Figure 4-51: FESEM images (cross-section and top view) and EDX data (line scan) of nanostructures grown at 500°C of 400 Torr for 1 min (a-c), 5 min (d-f) and 10 min (g-i)

4.3.5.5 Effect of pressure on nanostructure growth

The effect of pressure on the deposition of carbonaceous materials using the laser ablation technique has been reported by Yudasaka et al. [177]. Synthesis of carbon nanostructures was carried out at pressures between 4 – 600 Torr. Only amorphous carbon was observed at 100 Torr and below, but increasing the pressure to 600 Torr resulted in the formation of carbon nanostructures as well as the amorphous carbon layer.

The dependence of the morphology of nanotubes on pressure was also examined by Alvarez et al [178]. The structures of the nanotubes could be changed over pressures between 90 – 450 Torr. However, in their study [177, 178] the common metal catalysts of cobalt and nickel were used without the presence of other metals such as indium or tin, so no diffusion or inclusion of other metals was observed.

In the present work, an abrupt change of structure from MWCNT to indium oxide nanostructure encapsulated by carbon layer has occurred through a change of pressure particularly at the growth temperature of 450°C. As explained in Section 4.3.5.2.1 and 4.3.5.2.4, the MWCNT was synthesised at pressures between 100 – 300 Torr, while metal oxide nanostructure growth was observed with increasing pressure at 400 Torr.

As reported by Hsu et al [142] the diffusion of indium into the bottom of zinc oxide nanowires was seen at the pressure as low as 10 Torr. However, the higher temperature of 550°C applied in their study would facilitate the diffusion of indium to the bottom of nanowire. The low pressure of 10 Torr may contribute to the observed behavior, whereby indium only diffuses into the bottom of the nanowire. This suggestion is supported by Miller et al [8], who showed that a pressure of 0.68 Torr used for the growth of carbon nanostructures on ITO substrate at 550°C does not lead to the diffusion and therefore inclusion of indium. In contrast, for our study, indium has diffused into the entire structure of hollow carbon layer to form a metal oxide nanostructure at a lower temperature of 450°C but much higher pressure of 400 Torr.

The higher pressure leads to a concentration gradient and supersaturation [141] of indium droplets which, in turn, leads to a continuous diffusion of indium atoms from the ITO substrate, through the substrate-liquid interface into the liquid droplets, and then from the liquid droplets into the solid nanostructure until it is fully formed as an indium oxide nanostructure that encapsulated by carbon layer. A cooling process occurring at the surface of indium droplets caused by the carrier gas (Ar or H₂) [22, 141], also contributes to the phenomenon of melting, solidifying and the movement of metal within the tubes.

The diffusion of indium into nanostructures is supported by the hydrogen reduction on ITO and Fe/ITO. As explained in Section 4.3.1 and 4.3.2 the ITO and Fe film is transformed into metal particles at 450°C which suggests that the indium is being more reactive and mobile at the higher pressure. At the higher pressure, the Fe particles are not been fully utilised as a catalyst due to the faster deposition of the carbon atoms. Most of the Fe particles become covered by a layer of carbon and only the mobile liquid indium droplets are exposed to the carbon atoms for further growth. Consequently, at the higher pressure, the growth of MWCNT is disrupted and the diffusion of indium is enhanced.

As indicated by previous studies [8, 142], pressure has a significant impact on the diffusion of indium into the nanostructure. In this thesis, this impact has been more pronounced with the use of an ITO film as the substrate. Interestingly, the suppression of MWCNT growth was induced at the higher pressure which then introduced the diffusion of indium oxide. Indium oxide was seen to dominate the entire nanostructure which was encapsulated by a carbon layer.

4.4 CONCLUSIONS

In conclusion, MWCNTs and indium oxide nanostructures encapsulated by carbon layers have been grown directly on an ITO substrate. A considerable amount of amorphous carbon was seen to be deposited along with the nanostructure growth in all cases. Investigations into the use of hydrogen plasma to remove this layer show that this can successfully be achieved – however substantial degradation of the carbon nanostructures is also observed. Both types of nanostructure were synthesised at surprisingly low temperatures in the CVD system. In general, carbon nanostructures have been successfully grown at 10 min growth time for system pressures and growth temperatures between 100 to 400 Torr and 400 to 450°C, respectively. At the higher growth temperature of 500°C and lower system pressures (100 & 200 Torr) MWCNTs are also obtained. However, as the system pressure is increased (to 300 and 400 Torr) carbon coated metal oxide particles become the favoured product and silicon from the underlying glass substrate becomes increasingly exposed to the surface.

At the temperature of 450°C MWCNTs can be synthesised at pressures between 100 - 200 Torr with iron catalyst incorporated into the nanostructure. At 300 Torr MWCNTs are observed with no incorporated metal particles. Further increasing the system pressure (to 400 Torr) leads to the diffusion of indium oxide into the carbon nanostructure. During the synthesis of nanostructures at higher pressures, indium oxide nanostructures encapsulated within the carbon nanostructure are formed with the MWCNTs becoming increasingly disrupted. Therefore, it appears that in this system iron catalysed CNTs act as a template for the growth of an indium oxide nanostructure. It is worth noting that our present work on the dependence of pressure on the control of nanostructure is reported for the first time. The alteration of nanostructure from CNF to metal oxide nanowire can be demonstrated by simply (and subtly) changing the pressure of the CVD system.

5 CHEMICAL VAPOUR DEPOSITION OF PPV AND PPV OPV

5.1 INTRODUCTION

Chemically vapour deposited PPV can be used as an alternative to the more traditional solution processing methods of fabricating OPVs. In the following chapter the fabrication of OPVs with the integration of a PPV layer fabricated via CVD is described. A prototype OPV device is fabricated with and without a thin layer of PEDOT:PSS. None of the previous work on PPV synthesised by CVD has attempted to fabricate an OPV using this structure.

5.1.1 Motivation for Polymer Synthesis by CVD

Deposition of polymer thin films and nanostructures via chemical vapour deposition (CVD) has become an extremely popular technique in the fabrication of sensing devices [70, 71, 179]. CVD can be effectively used to deposit polymers with greater control of film conformation [59] and also allows for the elimination of solvent effects [73]. CVD polymerisation typically involves the transport of vapour-phase monomers that are polymerised *in-situ* to produce chemically well-defined conjugated polymer films precisely on the surface of a substrate. Since the CVD polymers are grown by transporting vapour-phase monomers to a surface, this technique of thin solid film polymerisation and formation is a single step all-dry process. Unlike solution-based methods utilised for polymer formation, which can suffer from non-wetting and surface-tension effects that lead to poor film quality, CVD polymerisation offers potentially improved conformal film coverage [59, 180].

As an example, Figure 5-1(a) and Figure 5-1(b) show the conformal nature of thin polymeric film on silicon trenches prepared by spin coating a polymer solution and CVD, respectively [59]. Differences in step coverage can be seen on the top surface, trench side walls and trench bottom of the silicon wafer. Polymeric thin films prepared by CVD provide a considerably more uniform coverage. Polymer prepared from

solution leads to a poor coverage by the polymer thin film, which may be due to the effect of solution surface tension [181].

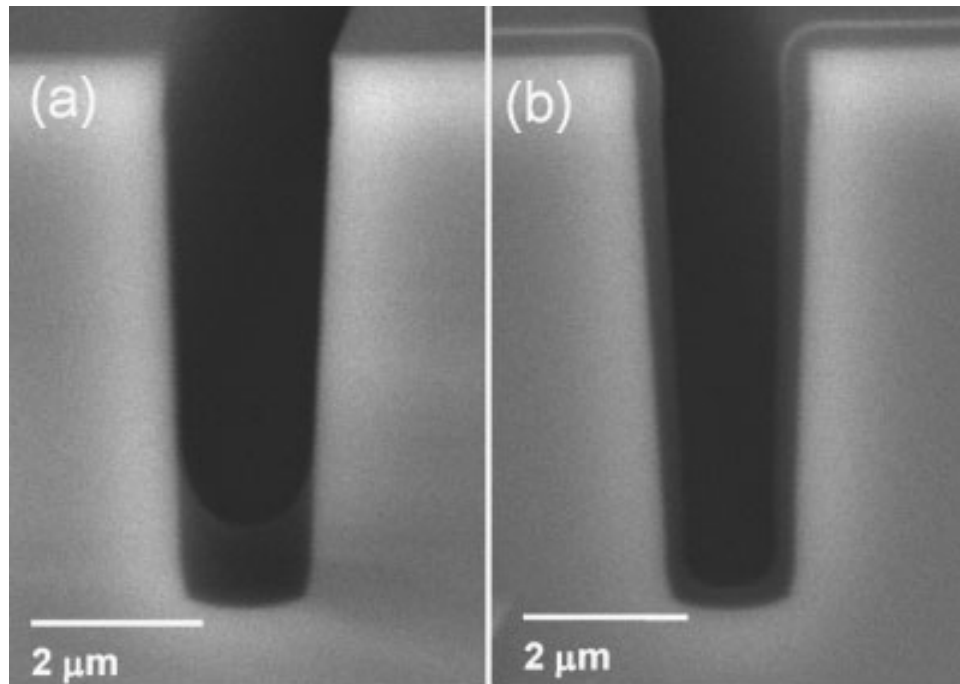


Figure 5-1: Images of thin polymeric films on silicon trenches deposited by (a) spin coating a polymer solution and (b) CVD[59]

The ability of CVD to produce good conformal film coating is further evidenced by Figure 5-2(a) and Figure 5-2(b). According to Vaddiraju et al [180] the conformal coating of poly(3,4-ethylenedioxythiophene) (PEDOT) has been obtained on a poly(acrylonitrile) fiber mat via CVD. In contrast, spin casting PEDOT results in irregular fiber morphology and aggregation due to non-wetting effects [180].

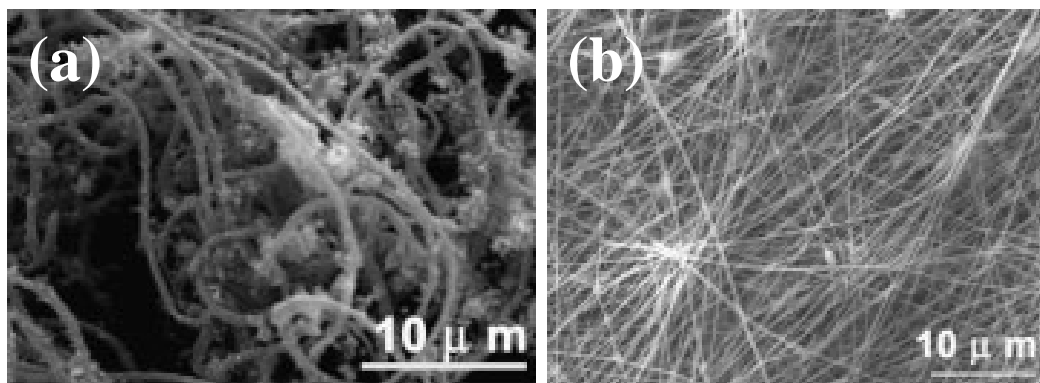


Figure 5-2: SEM images of poly(3,4-ethylenedioxythiophene) coated poly(acrylonitrile) fiber mats prepared by (a) spin casting and (b) CVD[180]

Apart from providing conformal polymer film coverage, CVD offers a pathway to solution free OPV fabrication. Typically, two different solvents have to be used in bilayer OPV fabrication, because the right selection of solvent is crucial for a sharp and well-defined interface between the two layers (fullerene and polymer) [27]. However, the use of ‘orthogonal’ solvents for fullerene and polymer may still cause changes in the surface morphology of the polymer underlayer.

The use of solvents in bilayer organic photovoltaic (OPV) fabrication has a considerable impact on device performance [27]. Ayzner et al [27] argued that all-solution-processed P3HT/PCBM bilayer OPVs required solvents such as dichloromethane and *o*-dichlorobenzene, which should serve as an excellent pair of orthogonal solvents [182]. The proper choice of solvent for fullerene dissolution was expected to avoid the redissolution of polymer which would lead to the interdiffusion of fullerene into the polymer underlayer [27]. However, it is challenging to find good orthogonal solvents for P3HT/PCBM bilayer OPVs as they are originally designed and synthesised to have an identical solution behaviour [182]. Issues related to the selection of solvent can be overcome by implementing the CVD of polymer film since no solvent is required in this technique. Due to the limited ranges of compatible solvents, polymer synthesis by CVD is considered a reliable method for producing the solvent-free materials.

5.1.2 CVD Approaches to PPV Thin Film Formation

Good film forming properties makes CVD-deposited polymers extremely attractive for surface modification applications. CVD polymers are well matched to the geometry of the underlying substrate, resulting in more uniform film thickness compared with conventional solution coating methods [59]. This method has been used widely in producing hole free polymer films by applying a thermal treatment as the final step [70-74, 179]. The thermal treatment applied to the polymer precursor can be varied in terms of temperature and duration [71].

Poly(*p*-phenylene vinylene) (PPV) has attracted considerable interest due to its favourable electrical, optical, electroluminescent and photovoltaic properties. Its potential as an electron donor for light emitting diodes and solar cell applications has made it a promising organic conducting polymer [179]. The performance of solution-

processed PPV-based OPV devices is highly dependent on the processing steps used to prepare the polymer. In particular, the poor processability of this polymer requires either *in situ* polymerisation, or the use of functionalised PPV (such as poly[2-methoxy-5-(3',7'-dimethyloctyloxy)-1,4-phenylene vinylene] (MDMO-PPV) with improved solubility [33].

PPV was first synthesised as a powder via the Witting reaction of p-xylylene bis(triphenylphosphonium chloride) with terephthalaldehyde [183]. However, due to its nonfusibility and insolubility in any solvents, this synthesis was difficult. In 1968, a precursor route was introduced by Wessling and Zimmerman [90] for PPV film preparation. In this method, water-soluble poly(p-xylylene α -diethylsulfonium bromide) was prepared via the reaction of p-xylylene diethylsulfonium bromide with a base in water prior to conversion to PPV film under thermal desulfonium reaction.

Previous studies have shown that CVD can be applied to the direct synthesis of PPV [70-74]. The PPV precursor is synthesised prior to the thermal conversion step of HCl or HBr elimination. There has been substantial attention paid to manipulating the properties of the PPV precursor synthesised via CVD [71, 73, 74]. To date, PPV CVD polymerisation has used a number of different reagent monomers [73, 74]. The synthesis of a PPV precursor via CVD was first carried out in 1991 [72] by vapour deposition polymerisation of 1,9-dichloro [2,2] paracyclophane. Iwatsuki et al [72] have used 1,9-dichloro [2,2] paracyclophane **1** as a starting material. However, this material needs a further purification which can be achieved via a non-wetting method of 1,9-dihydroxy [2,2] paracyclophane **3** and 1,9 dimesyloxy [2,2] paracyclophane **4** (Figure 5-3).

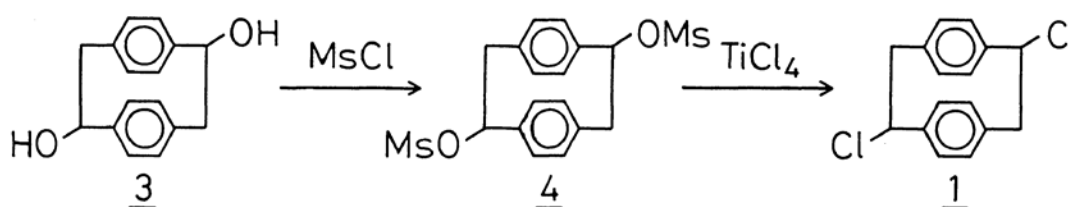


Figure 5-3: Preparation scheme of 1,9-dichloro [2,2] paracyclophane [72]

As shown in Figure 5-4, following the purification of 1,9-dichloro [2,2] paracyclophane, a sublimation process is used under a pressure of 75 mTorr and 120°C. The vaporised monomer is transported in a vacuum pyrolysis step at 580°C. The pyrolysed gas 2 is condensed on a surface at 20°C to give a tough, transparent and colorless PPV precursor film, before it is converted into PPV via thermal dehydrochlorination at 300°C for 1 hour in a nitrogen environment. The PPV precursor produced via this route was insoluble in acetone, chloroform, THF, DMSO and *m*-cresol, but soluble in ethyl benzoate if heated at 150°C. The method proposed by Iwatsuki et al [72] has been modified by Staring et al [73] and Schafer et al [74], who eliminated the difficult synthesis of the starting material (1,9-dichloro [2,2] paracyclophane) by instead using a starting material with a higher vapour pressure.

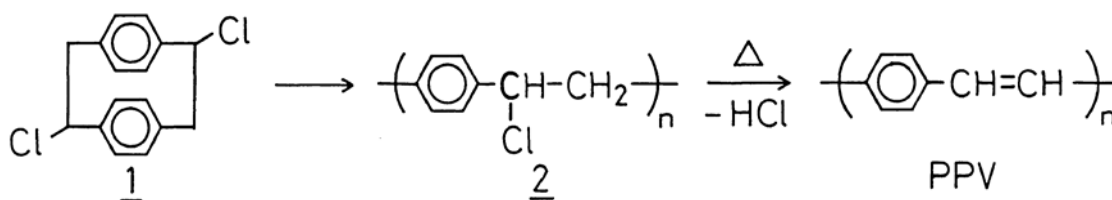


Figure 5-4: Preparation of PPV via the vapor deposition polymerisation of 1,9-dichloro [2,2] paracyclophane [72]

Further improvement of the starting material used for CVD polymerisation was achieved when additional purification of starting material was no longer needed [70, 71]. As reported by Vaeth et al [71], a commercially available compound, α - α' -dichloro-p-xylene, can be used as the starting material. This monomer is heated to 60°C before being pyrolysed at 625°C and transported to the furnace by 8 sccm of argon at low pressure of 100 mTorr. The same pressure of 100 mTorr was used in the thermal conversion of the precursor to PPV at temperatures between 95°C and 300°C.

Although there are advantages in eliminating the incorporation of carbonyl defects [71] due to residual oxygen during the conversion process [184], in our work we increased the system pressure from high vacuum [71-74] to medium vacuum. A medium vacuum of 400 mTorr was used both in the pyrolysis and thermal conversion process. The quality of PPV films synthesised under moderate vacuum was then compared with those synthesised at 100 mTorr and below. In addition, the optimisation of the thermal conversion temperature and duration was explored.

The optical properties of CVD PPV film have been widely reported [71-74]. The UV-vis absorption spectra of PPV precursor and PPV prepared via CVD polymerisation [71] are shown in Figure 5-5, along with the fluorescence of a PPV thin film excited at 235 nm. The absorption peak of PPV [71] is located near 400 nm. The strong absorbance in the visible region makes PPV a promising material for the fabrication of organic solar cells [185].

Infra-red spectroscopy has also been applied to determine the chemical structure and confirm the synthesis of PPV. The first IR spectra were obtained in 1991 [72] with vapour deposition of 1,9-dichloro [2,2] paracyclophane as a starting material. Figure 5-6a shows an absorption peak at 720 cm^{-1} which is assigned to C-Cl. Absorption peaks corresponded to C-Cl (630 & 696 cm^{-1}) and CH_2 stretching (2854 & 2921 cm^{-1}) were diminished after the thermal treatment at 300°C (Figure 5-6b). A reduced intensity was also observed for peaks between 1514 to 1430 cm^{-1} , which corresponded to C=C stretches.

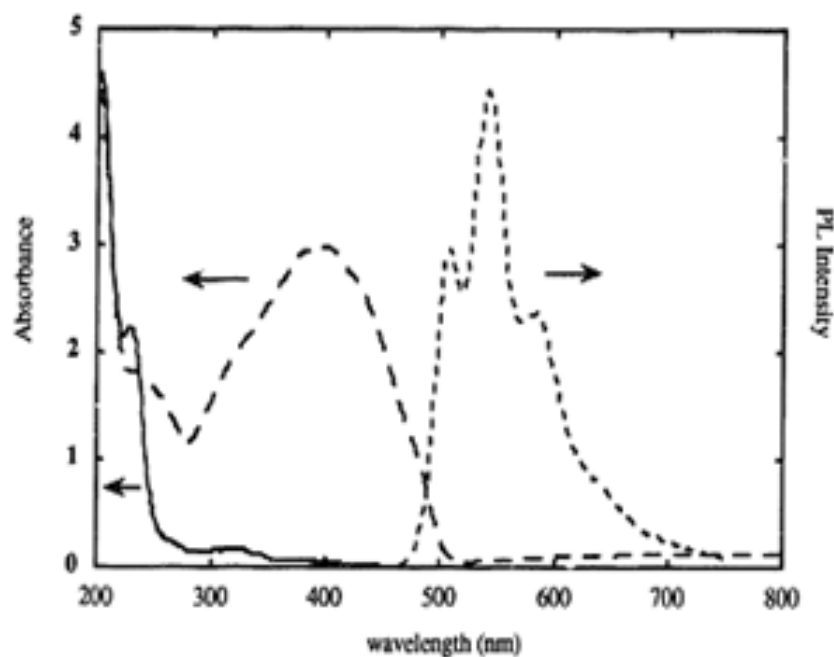


Figure 5-5: Absorbance of PPV precursor (solid line) and PPV(dashed line), and photoluminescence of PPV (dotted line) [71]

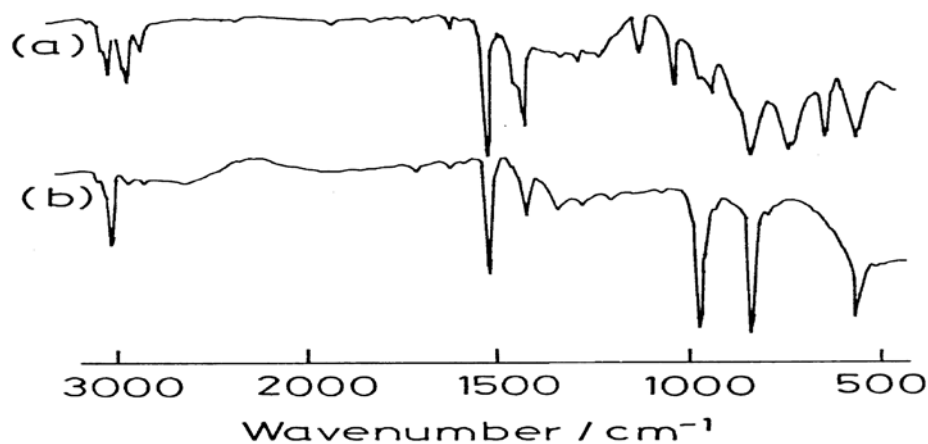


Figure 5-6: IR spectra (transmittance vs wavenumber) of (a) precursor and (b) PPV [72]

5.1.3 OPV Devices Made from PPV Films

Although organic solar cells are less efficient than silicon cells, properties such as low cost, flexibility and large area processability make them an exciting potential contributor to energy generation. The first polymer solar cell based on hole conducting conjugated polymers of polyacetylene exhibited low power conversion efficiency [186]. A major breakthrough to higher efficiency was realised by exploiting new conjugated polymers such as polythiophene (PT), PPV and their derivatives [82, 187, 188]. These conjugated polymers were used in conjunction with suitable electron acceptors by mixing them together.

The photovoltaic response in PPV thin film devices was first reported by Marks et al [189]. In these devices, a PPV thin film was sandwiched between two electrodes without the incorporation of an electron acceptor. The open circuit voltage of these devices was reported to be higher than its work function which suggested the occurrence of a chemical reaction between the electrodes (Al) and the PPV. Further research on the integration of PPV films into devices was carried out by Halls et al [81, 190]. A PPV thin film synthesised via the sulfonium salt precursor was spin coated onto ITO prior to thermal conversion. After heating the precursor PPV for 12 hours at 200°C in vacuum, the resulting PPV thin film was then coated with C₆₀ (electron acceptor) in order to create the device heterojunctions. The power conversion efficiency of these devices was not reported, however, an open circuit voltage of 0.9 V was obtained [190].

OPV devices made using a different approach from PPV are reported by Brabec et al [82]. Homogeneous blends of PCBM and PPV were synthesised using a novel non-ionic precursor route [82]. The thermal conversion of the polymer precursor to PPV was suggested to be completed even in the presence of PCBM. Power conversion efficiencies of devices made from these blends were as high as 0.25% [82]. A thin layer of PEDOT:PSS as a electron blocker was used in these devices [82]; being deposited onto ITO prior to the spin-coating of precursor PPV/PCBM blend. Although promising device efficiencies can be achieved with solution-based methods, there are still some concerns regarding the conductivity of the electron blocker layer used in these devices due to thermal treatment [104]. The thermal treatment applied for the conversion of precursor PPV is thought to reduce the conductivity of PEDOT:PSS [104]. Therefore, the application of PEDOT:PSS in OPV fabrication that involve thermal treatment may not be appropriate.

The best power conversion efficiency for functionalised PPV has been recorded at 2.5% with the blend of poly[2-methoxy-5-(3',7'-dimethyloctyloxy)-1,4-phenylene vinylene] (MDMO-PPV) and PCBM [33]. However, this efficiency was achieved only after optimising the selection of solvents. Even though the efficiency is promising from solution-processed PPV [33] compared to thermally converted PPV [82], it does not provide conformal film coverage [59, 180]. Since the ultimate objective of our present work is to minimise the reliance on solvent, improvements to thermally converted PPV are required.

5.1.4 Degradation of PPV films

Optical and electrical properties of devices can be affected if the conjugated polymer exhibits degradation. Conjugated polymers can degrade due to photo aging [100, 191], environmental aging [192] or thermal aging [191]. This degradation is directly related to the long-term stability of devices made from these polymers. Zyung et al [100] have reported on the photodegradation of PPV polymer by irradiating the film with laser light at different wavelengths. As shown in Figure 5-7, UV-vis spectra of PPV irradiated with laser light at both wavelengths (458 nm & 514 nm) in air has demonstrated a strong reduction in the UV-vis absorption peak. Before the irradiation, a broad absorption

located at 440 nm is observed and attributed to the polymer conjugated structure. Decline in intensity of absorption peak accompanies by a blue shift indicates the loss of vinylene-type functions. Loss of visible absorption also suggests the photo-bleaching of the PPV and shorter conjugation length [191]. The chemical structure of PPV has changed during the irradiation in atmospheric oxygen and to an extent that will affect the performance of any electronic device.

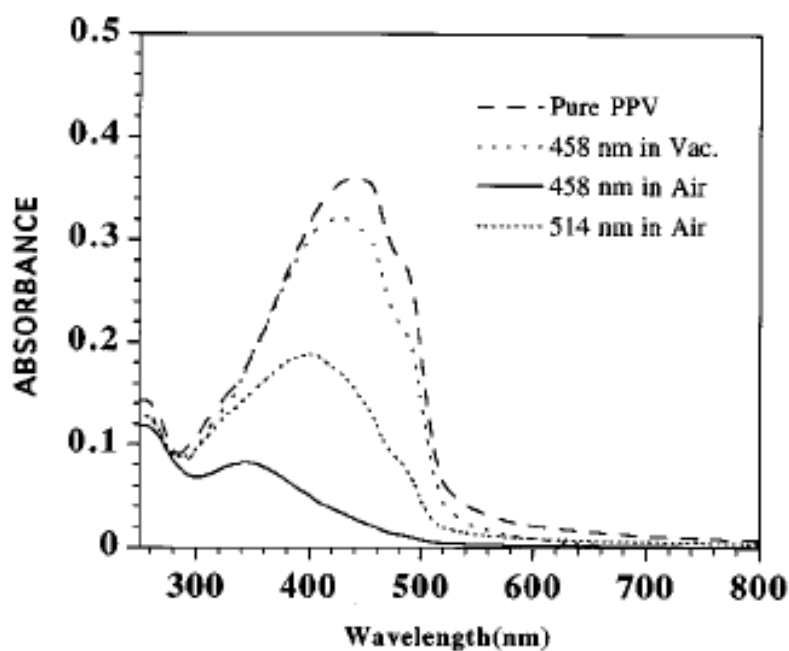


Figure 5-7: Absorption spectra of the unirradiated and the irradiated PPV films [100]

The photodegradation mechanism of PPV in air is shown in Figure 5-8. A chain scission reaction occurs during photodegradation. However, the *p*-phenylene group remains in the reaction products after the photodegradation process.

It is possible to synthesise phenylene vinylene monomers and oligomers even though PPV is commonly known as a long chain polymer. As shown in Figure 5-9, peak absorption at 500 nm experiences a blue shift as the chain length decreases [193]. Damage to the PPV polymer backbone can shorten its conjugation length and should display a similar change in absorbance and photoluminescence spectra as that seen in Figure 5-9.

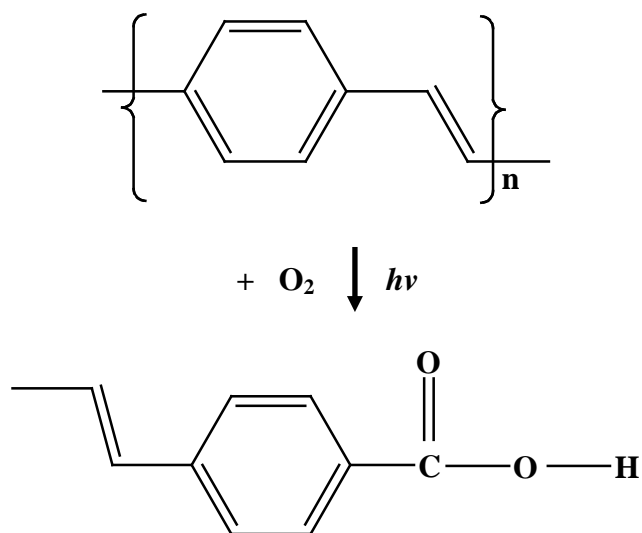


Figure 5-8: Photodegradation mechanism of PPV in air [100]

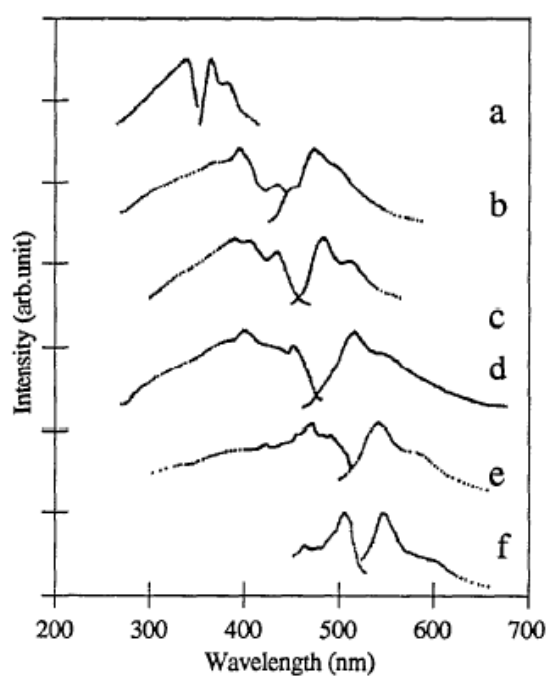


Figure 5-9: Absorption and photoluminescence spectra of oligomers with a) 1, b) 2, c) 3, d) 4, e) 6 phenylene vinylene units and of f) PPV [193]

5.2 EXPERIMENTAL SETUP

PPV CVD polymerisation was carried out as described in Section 2.2.2. In addition to using α,α' -dichloro-p-xylene as a starting material, α,α' -dibromo-p-xylene was also trialed. However, throughout this work α,α' -dichloro-p-xylene was predominantly used, including for the final OPV fabrication. The method used for PPV precursor synthesis is a modification of that presented by Vaeth et al [71]. Figure 5-10 shows the synthesis of PPV precursor with α,α' -dichloro-p-xylene **1** as a starting material. The starting monomer is vaporised at 60°C prior to transportation to the pyrolysis zone by 8 sccm of argon. Pyrolysis is done at 700°C for 15 min at 400 mTorr in order to produce chlorinated xylylene **2**. The chlorine PPV precursor **3** is obtained after condensation and polymerisation process occurs on a surface at temperatures between 85°C and 95°C. In our present study, precursor PPV and PPV were synthesised in a moderate vacuum of 400 mTorr, unlike the previous work reported [71-74] in which a higher vacuum was implemented (30 mTorr).

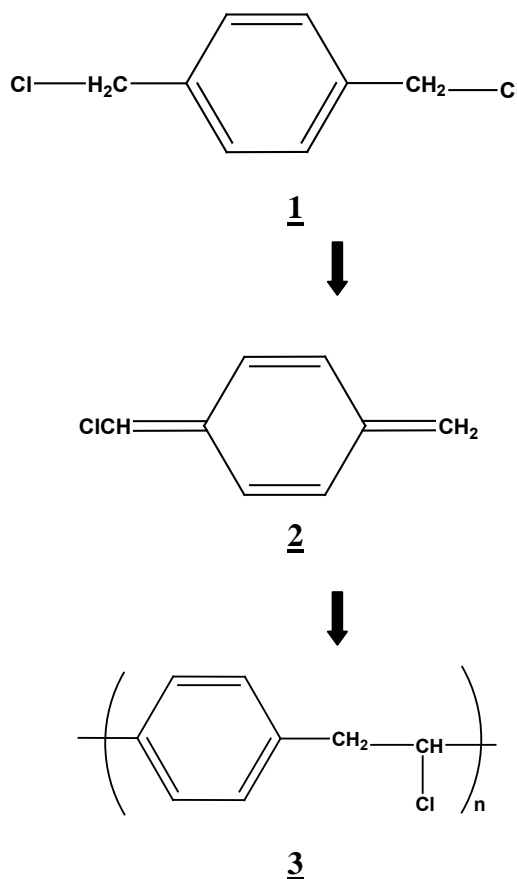


Figure 5-10: PPV precursor synthesis via CVD polymerisation

The reaction scheme in Figure 5-11 shows PPV synthesis via thermal treatment. The chlorine polymer precursor **3** was heated at 270°C for several hours (2 to 14). During the thermal treatment, the system pressure was 400 mTorr. Modification of method parameters such as lower thermal treatment temperature, higher system pressure and thermal treatment duration have been examined in this work.

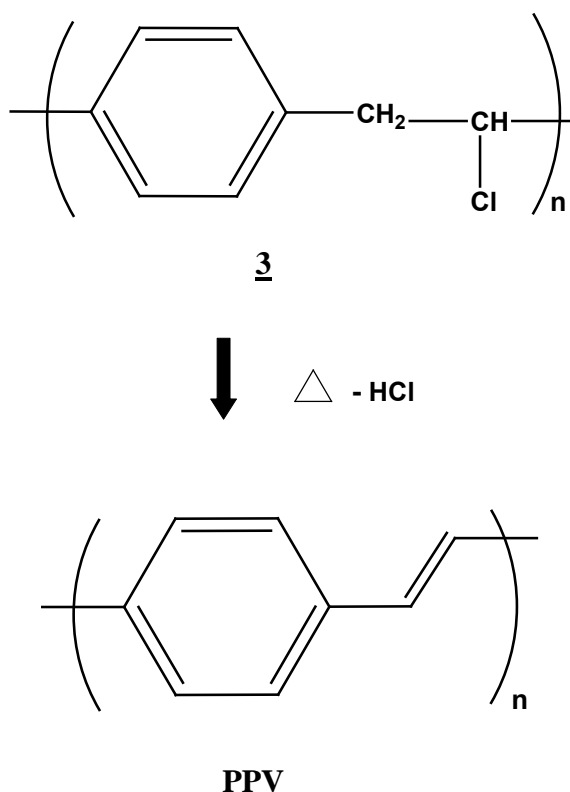


Figure 5-11: PPV synthesis via thermal de-hydrohalogenation

Calibration of the deposition zone locations was done by dividing the 14 cm section of quartz tube outside the furnace into seven spots (Figure 5-12). The purpose of this calibration was to identify the optimum substrate position. 1 x 1 cm quartz substrates were used. PPV films were characterised by Fourier transforms infrared (FTIR), UV-vis and photoluminescence spectroscopy. OPVs were fabricated on patterned indium tin oxide (ITO) substrates (Kintec) that were first cleaned by successive sonications in detergent solution, deionized water and acetone. For the fabrication of devices that utilised the electron blocker layer, PEDOT:PSS was spin coating onto an ITO to yield a layer of approximately 50 nm. PCBM (Solenne) was dissolved in chloroform at a concentration of 5 mg/ml. This solution was deposited on top of the PPV film by spin

coating at 2000 rpm for 1 min. C60 thin layer was evaporated on top of the PPV film as an another technique for the deposition of acceptor layer. Finally, an 80 nm thick aluminium cathode was thermally deposited on top of the PCBM layer; with some of devices have the incorporation of interface layer such as lithium fluorine (LiF) or calcium (Ca). Photovoltaic performance was determined under AM-1.5 illumination (Newport).

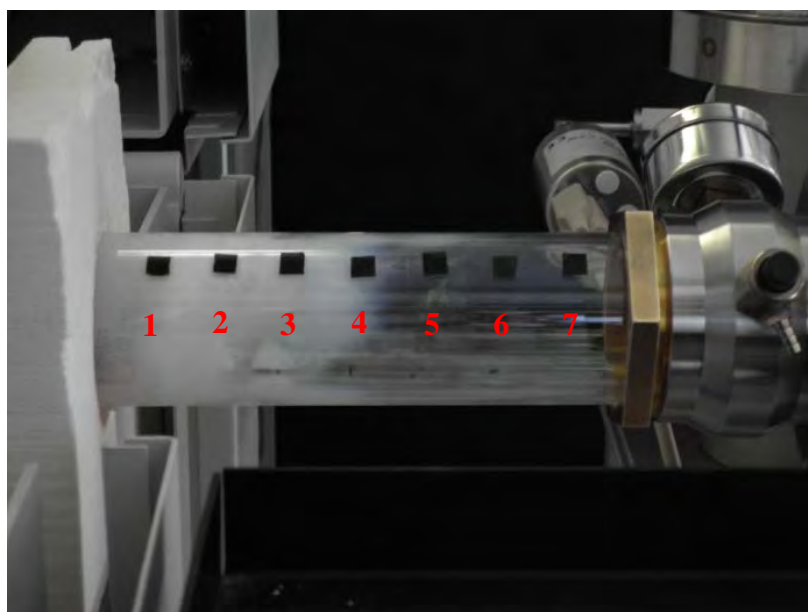


Figure 5-12: Calibrated deposition zone positions

5.3 RESULTS AND DISCUSSION

5.3.1 PPV Precursor Absorbance

Figure 5-13 shows the UV-vis absorption spectra of quartz and PPV precursor deposited onto quartz. The as-deposited PPV precursor is relatively transparent, and the π - π^* transition is located at a λ_{max} of 231 nm. The UV-vis spectra of the PPV precursor obtained in this study is in agreement with Vaeth et al [71] (Figure 5-5), where their PPV precursor's absorption peak is at around 230 nm. Thus, we can be confident that the CVD process has lead to the deposition of the PPV precursor onto the substrate surface.

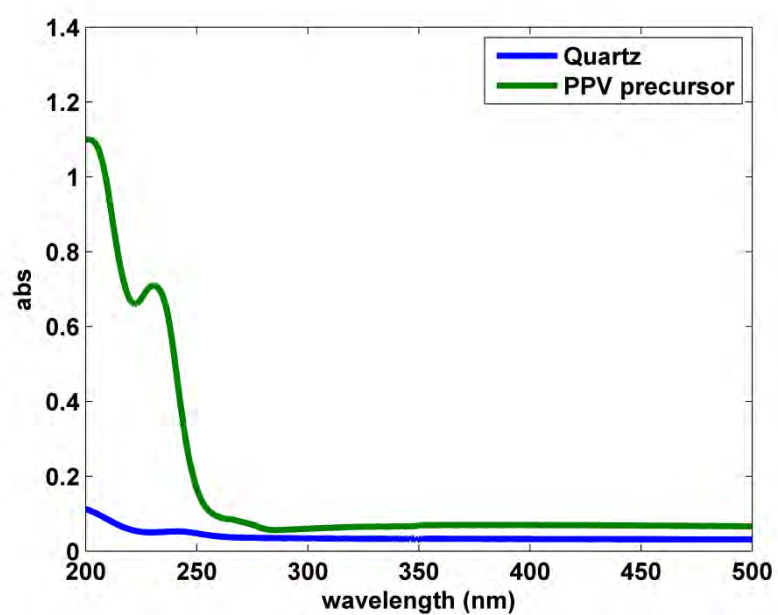


Figure 5-13: UV-Vis absorption spectra of pristine quartz and PPV precursor

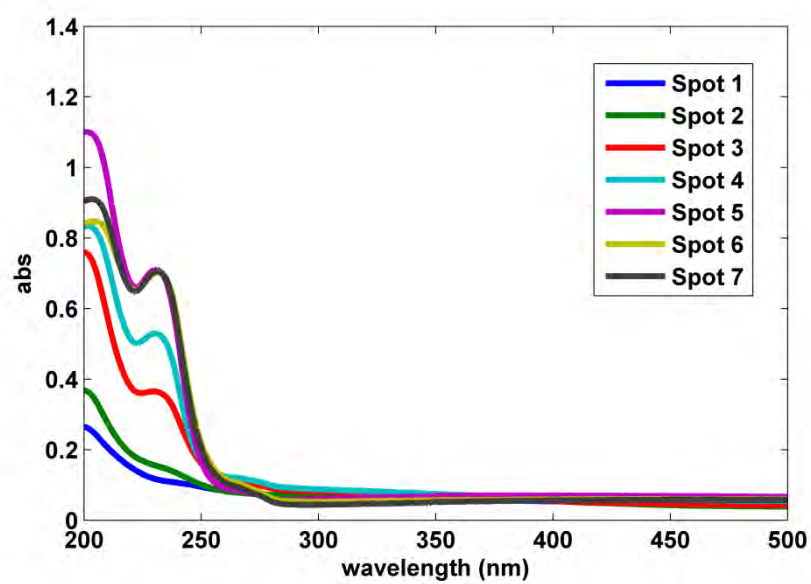


Figure 5-14: UV-Vis absorption spectra of PPV precursor located at spots 1 to 7

Calibration of precursor deposition at spot 1 to 7 is shown in Figure 5-14. These spots were all tested at the same time. The UV-vis absorption spectra of PPV precursor deposited at spot 1 and 2 is similar to that of the quartz substrate, indicating that no PPV precursor has been successfully deposited at spot 1 and 2 (with 200 mg of starting material). The occurrence of unsuccessful deposition at spot 1 and 2 is probably due to the high substrate temperature, since spot 1 and 2 was the nearest spot to the boundary of pyrolysis zone and deposition zone. The ideal deposition zone temperature is between 85 to 95°C, condensation polymerisation of chlorinated xylylene monomer will not occur if surface temperature is out of this range [71].

The surface temperature at spots 1 & 2 was measured using a thermocouple. The measurements were taken for 30 min after the pyrolysis temperature reached 700°C. As shown in Figure 5-15, after 15 min of pyrolysis at 700°C, the surface temperature at spot 1 and spot 2 was 134°C and 107°C, respectively. As reported elsewhere [71], the chlorine polymer precursor was unable to be grown above 95°C.

The remaining spots 3, 4, 5, 6 and 7 show successful precursor deposition, with differences in the amount of deposited. The amount of precursor collected at spots 5, 6 and 7 are essentially the same. The surface temperature at those spots may be identical since they located farthest from the boundary of pyrolysis zone and deposition zone. The chlorinated xylylene monomer started to nucleate when it reached spot 3. As this pyrolysed monomer flowed further to spot 4, larger amount of precursor were deposited before it is saturated at spot 5.

As shown in Figure 5-16 the condensation polymerisation of chlorinated xylylene monomer between 85°C to 95°C suggested by Vaeth et al [71] is supported by our present work. After 15 min of pyrolysis at 700°C, substrate temperature of spot 3, 4, 5, 6 and 7 were measured between 87.5°C to 94.3°C. The substrate temperature at spot 7 was lowest at 87.5°C after 15 min of pyrolysis.

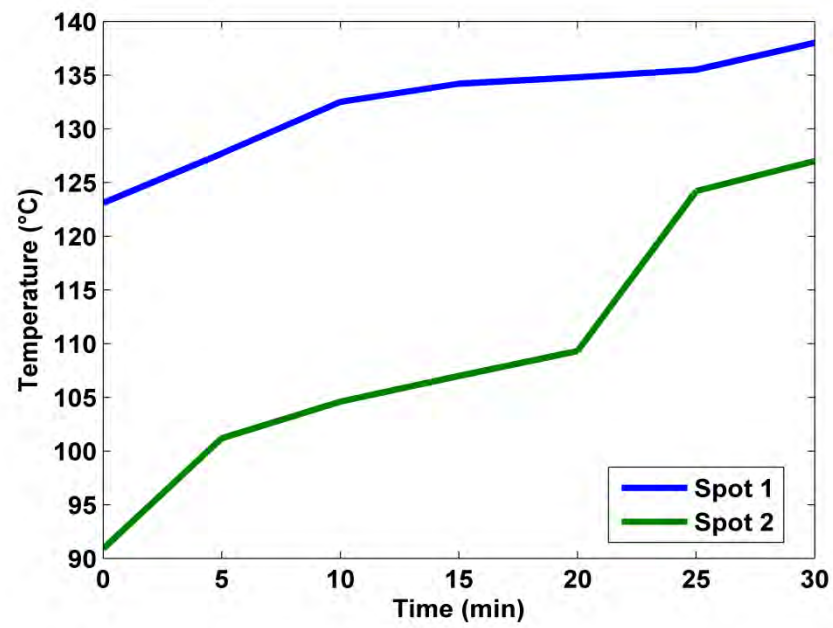


Figure 5-15: Time versus surface temperature of spot 1 and 2 at 700°C pyrolysis temperature

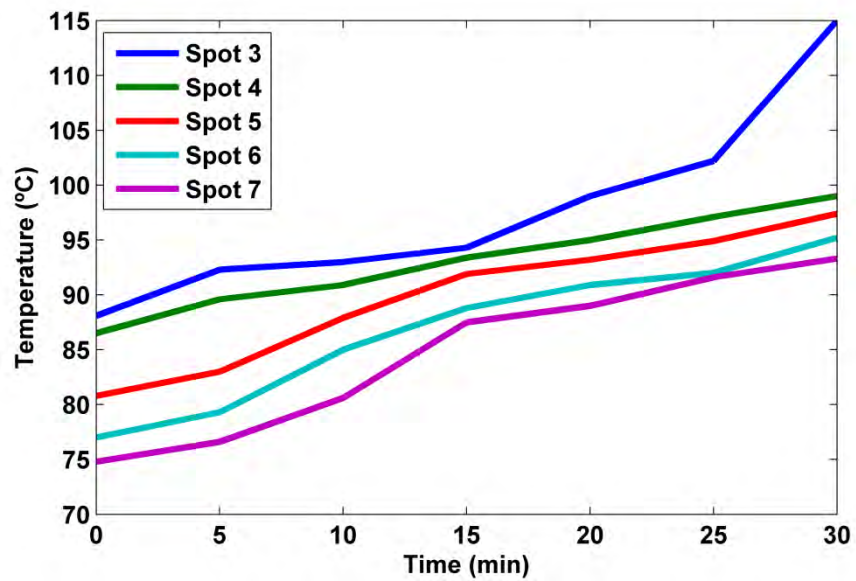


Figure 5-16: Time versus surface temperature of spot 3 to 7 at 700°C pyrolysis temperature

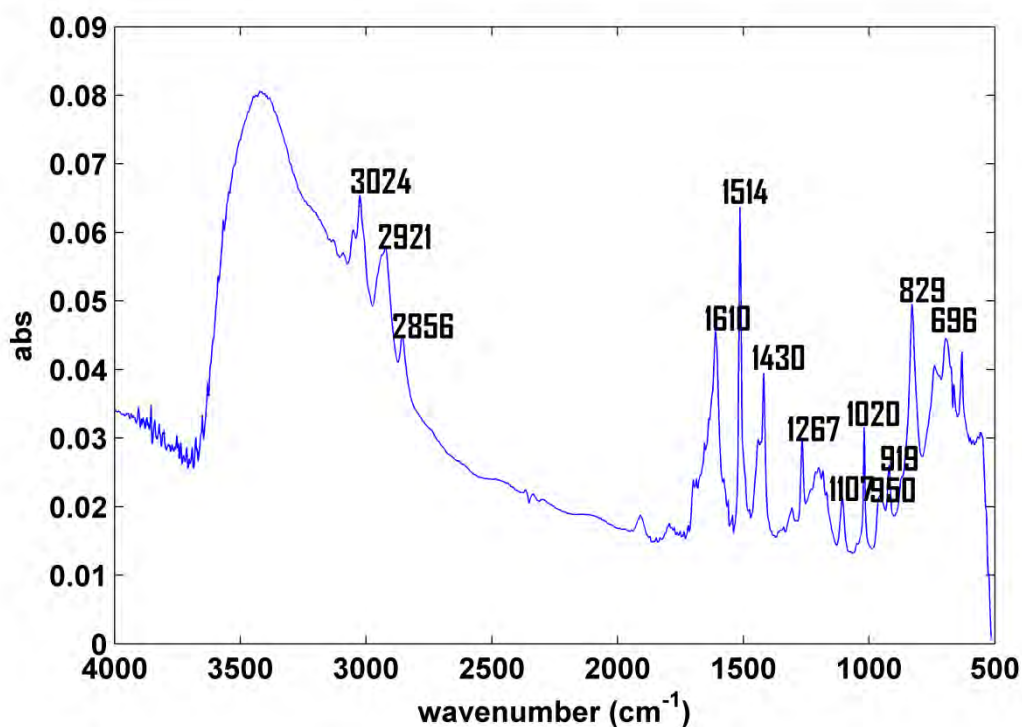


Figure 5-17: Fourier Transform IR spectrum of chlorine PPV precursor

The two different starting materials (α,α' -dichloro-p-xylene and α,α' -dibromo-p-xylene) were measured by FTIR spectroscopy. From the FTIR spectroscopy of the chlorine PPV precursor prepared by α,α' -dichloro-p-xylene (Figure 5-17), C-Cl stretching bands at 630 cm^{-1} [194] and 696 cm^{-1} were detected. The detection of C-Cl stretching modes at those frequencies indicates that the condensation and polymerisation of vaporised monomer has occurred without the complete elimination of chlorine.

Identification of several significant absorption peaks in FTIR spectrum supports the notion that the chlorine precursor has been synthesised by CVD. The FTIR spectrum of the chlorine precursor exhibits an absorption peak characteristic of phenylene C-H bending mode at 829 cm^{-1} [179]. The spectrum presents a weak absorption at 919 cm^{-1} and 950 cm^{-1} which assigned to the trans-vinylene =C-H out-of-plane bending mode [11, 195]. This observation implies the formation of small vinylene units in the chlorine precursor and indicates the premature removal of hydrogen chloride.

Two absorption peaks assigned to the in-plane C-H bending mode were revealed at 1020 cm^{-1} and 1267 cm^{-1} . In addition, the characteristic of in-plane phenyl C=C stretching mode were observed at 1107 cm^{-1} and 1514 cm^{-1} , with the latter absorption peak showing the intense absorption. Both absorption peaks were observed by Lefrant et al [196] where the weakest absorption peak was also detected at 1108 cm^{-1} rather than at 1518 cm^{-1} . Other absorption peaks revealed in the FTIR spectrum of the chlorine precursor were attributed to the C-C stretching and C-H stretching modes.

FTIR spectrum of bromine PPV precursor (Figure 5-18) shows slightly different absorption bands in comparison to that in Figure 5-17. Some of the absorption bands observed in the chlorine precursor are not observed in bromine precursor or vice-versa. The absorption intensity for the C-Br stretching mode is observed at 611 cm^{-1} which is in agreement with that found at around 615 cm^{-1} by Lee et al [197].

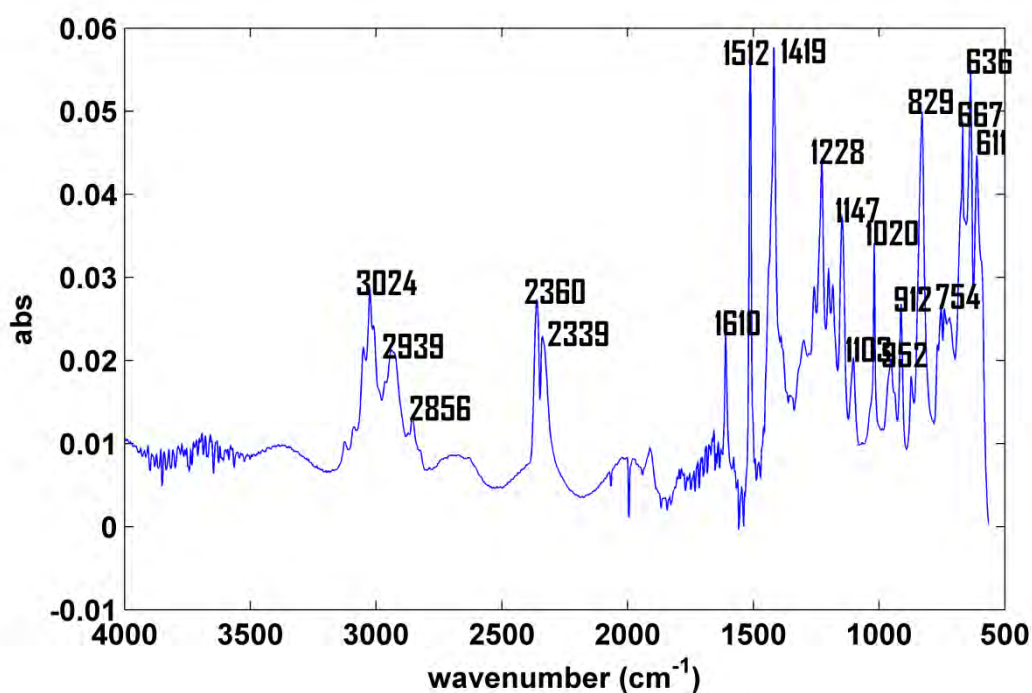


Figure 5-18: Fourier Transform IR spectrum of bromine PPV precursor

Wavenumber (cm ⁻¹)	Assignment
636	C-Br stretch
667	CH out-of-plane deformation
754	CH out-of-plane bending
1147	CH in-plane bending
1228	
1419	CH ₃ deformation
1610	Phenyl C=C stretch
2856	C-H stretch
2939	
3024	

Table 5-1: Peaks and corresponding assignments of bromine PPV precursor in infrared

As seen in the chlorine precursor spectrum, an absorption band at 829 cm⁻¹ [179] attributed to the phenylene C-H bending mode was identified in FTIR spectrum of bromine precursor. Both bands at 912 cm⁻¹ and 952 cm⁻¹, assigned to the trans-vinylene =C-H out-of-plane bending mode [11, 195], are also observed. The strong absorption observed at those bands indicates that the formation of vinylene units in the brominated PPV precursor has occurred. Other peaks due to the bromine PPV precursor that were not present in the FTIR spectrum of the chlorine PPV precursor are assigned in Table 5-1.

5.3.2 PPV Absorbance

PPV precursor of chlorinated xylylene and brominated xylylene were heated at 270°C for 14 hours in order to convert them into PPV thin films. The experimental conditions were chosen based on the work done by Kim and Jin [70] in which the PPV precursor was converted into PPV nanotubes and nanorods. As shown in Figure 5-19, UV-vis spectra of the chlorine precursor and PPV films reveal changes in their electronic structure. There is a red shift to longer wavelength after the thermal treatment of chlorine precursor, which indicates that hydrogen chloride attached to the vinylene moiety has been eliminated and a highly conjugated PPV chain is formed [71]. A broad absorption band from 300 to 500 nm corresponds to the π - π^* transition of the PPV backbone. The absorption peak obtained at 400 nm is also observed by others [179, 197].

The absorption edge of non-conjugated chlorine precursor at 212 nm, which is equivalent to band gap energy of 5.86 eV, was significantly red-shifted to 512 nm after 14 hours of thermal treatment. Elimination of hydrogen chloride has converted the precursor into PPV and reduced the band gap energy to 2.42 eV. This hypothesis is in agreement with the band gap energy of the absorption edge reported by Tung and Nghia [179] for the CVD polymerization of PPV. The fully conjugated PPV synthesized via CVD has reported to have a broad continuous absorption band with the maximum absorption peak at 410 nm [179].

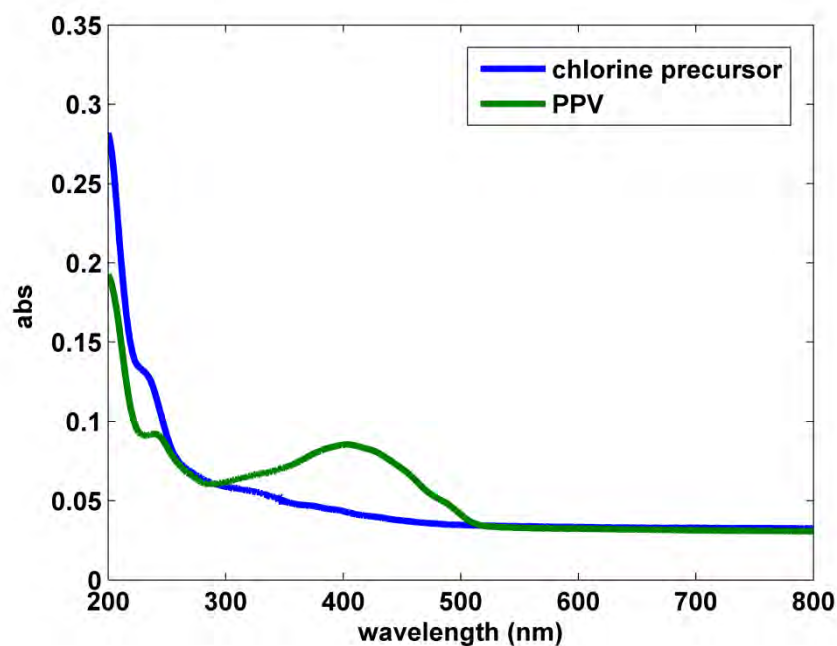


Figure 5-19: UV-Vis absorption spectra of chlorine precursor and PPV

The changes in the UV-vis spectra of PPV film can be correlated with the FTIR spectra shown in Figure 5-20. Absorption bands near 630 cm^{-1} and 696 cm^{-1} are seen in the precursor spectrum, but are absent in PPV spectrum. This observation is consistent with the formation of a carbon double bond via the elimination of HCl, causing a loss of the C-Cl stretching peak that is complete after the thermal treatment of 14 hours. The absorption peak at 1020 cm^{-1} , which is attributed to the in-plane C-H bending mode, has also diminished. A peak at 924 cm^{-1} , possibly associated with the CH_2CHCl group [71], also disappears after thermal treatment. In addition, no carbonyl band is detected at 1690 cm^{-1} , which shows that there is no oxidative degradation during the polymerisation process [71]. A significant reduction in intensity is observed at 1514 cm^{-1} , 1604 cm^{-1} , 2854 cm^{-1} , 2921 cm^{-1} and 3022 cm^{-1} . These bands are associated with the in plane phenyl C=C stretching mode and C-H stretching mode. In addition, the absence of bands at 740 , 1382 , 1463 , 2872 & 2960 cm^{-1} associated with the CH_3 asymmetric bending, CH_3 symmetric bending, CH_2 rocking, CH_2 symmetric & CH_3 asymmetric deformation [198] is observed.

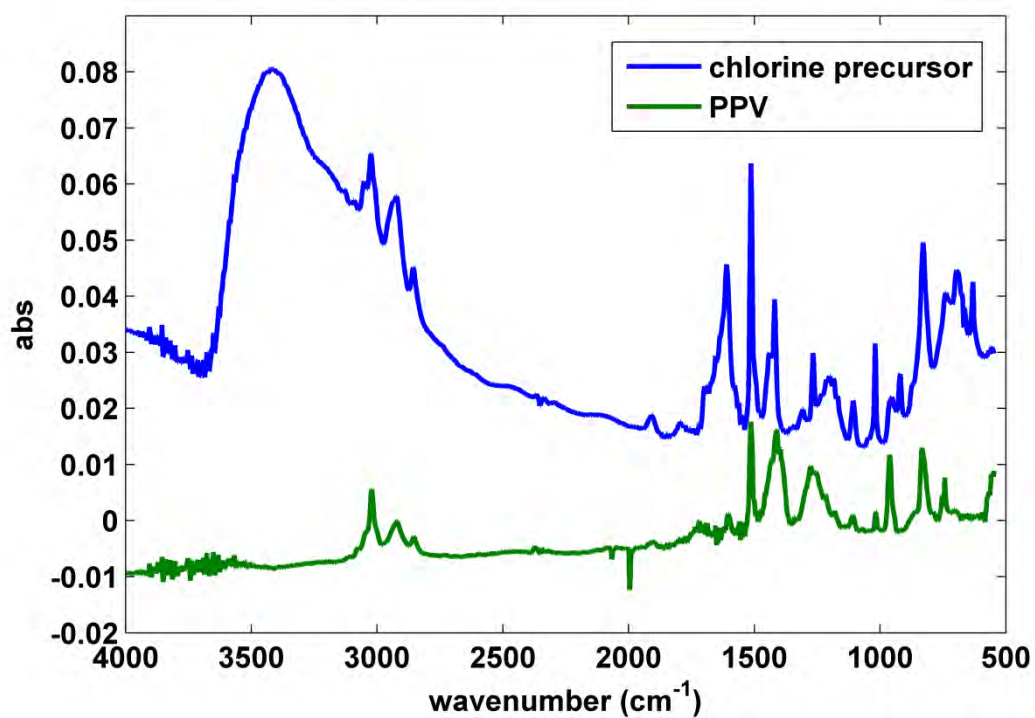


Figure 5-20: Fourier Transform IR spectra of chlorine precursor and PPV

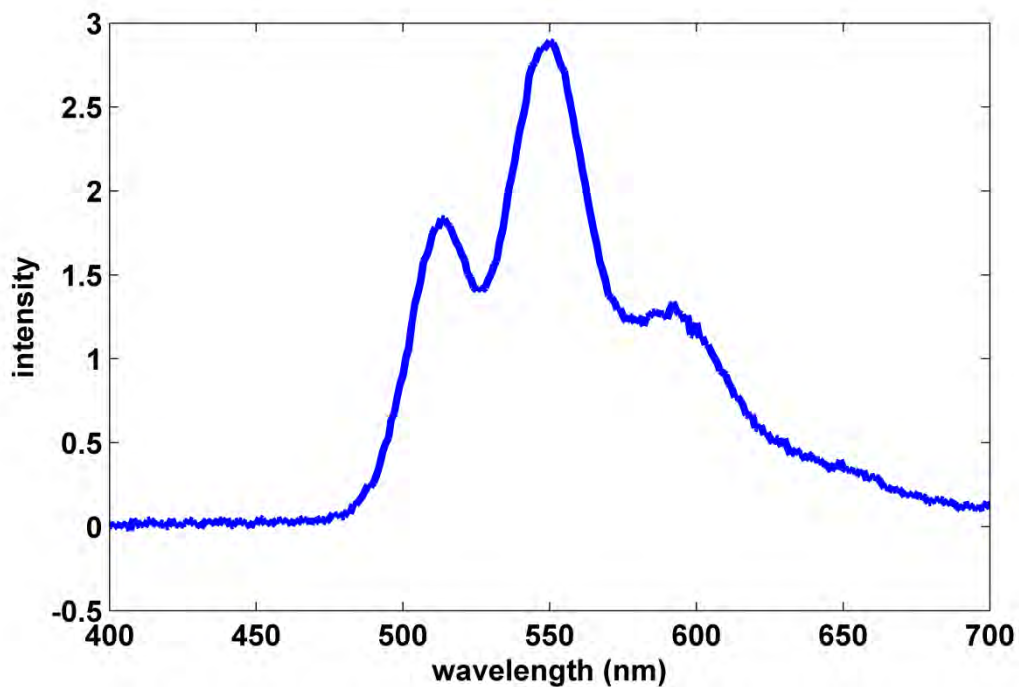


Figure 5-21: Photoluminescence spectrum of chlorinated PPV (excitation at 350 nm)

The photoluminescence (PL) spectrum of PPV from a chlorinated starting material deposited onto quartz is shown in Figure 5-21. This spectrum has similar peak characteristics to that reported by Vaeth et al [71] in Figure 5-5. Three peaks can be seen located at 513 nm (peak 1), 550 nm (peak 2) and 592 nm (peak 3). Peak 1, 2 and 3 corresponding to the 0→0 vibronic transition, 0→1 transition and 0→2 transition, respectively [7]. This vibrational structure is attributed to the backbone stretching modes of PPV [199]. The three emissions shown in Figure 5-21 represents at least six uninterrupted phenylenevinylene units of conjugation segments as assumed by comparison to that reported by Rothberg et al [102] (Figure 5-22). The chemical structure of PPV synthesised via CVD that comprises of six phenylenevinylene units is illustrated in Figure 5-23.

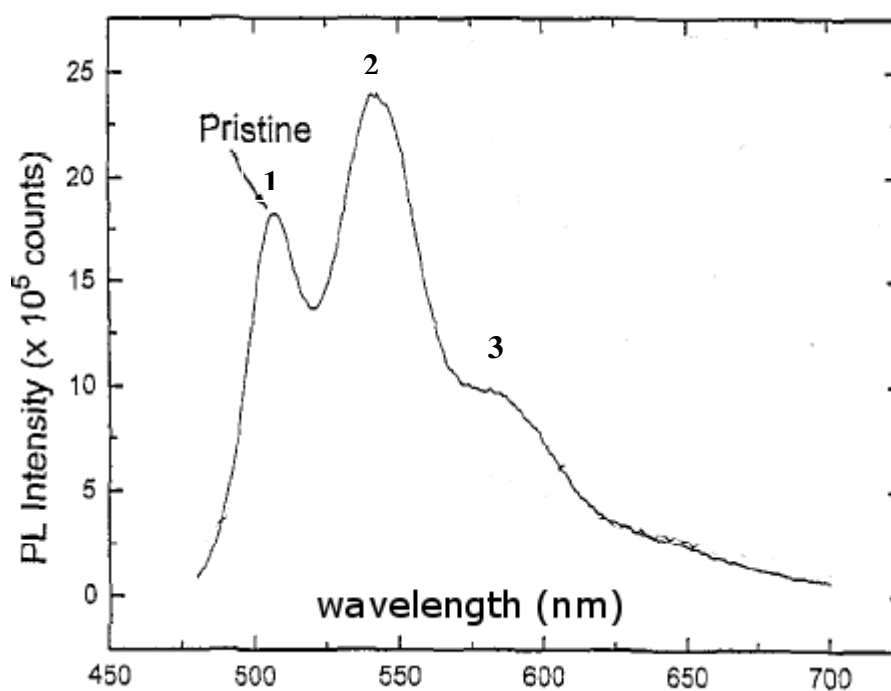


Figure 5-22: PL spectrum of PPV with six uninterrupted phenylenevinylene units [102]

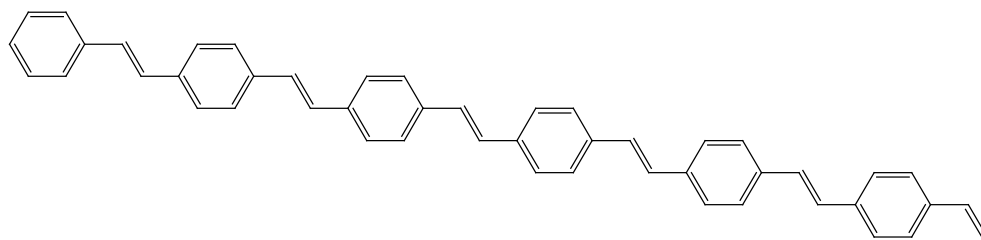


Figure 5-23: Chemical structure of PPV containing six phenylenevinylene units

Figure 5-24 shows the UV-vis absorption spectra of brominated PPV precursor before and after thermal conversion for 14 hours. A strong broad absorption peak appeared at 380 nm for the PPV synthesised by α,α' -dibromo-p-xylene. The blue shift to shorter wavelength and larger optical band gap compared to the chlorinated monomer indicates a shorter conjugation length results in this case. Interestingly, the absorption edge recorded by bromine precursor has a smaller optical band gap (3.9 eV) than the chlorine precursor (5.86 eV).

To further investigate the effect of monomer choices on the PPV optical absorption properties, FTIR spectra of the bromine precursor and PPV prepared by α,α' -dibromo-p-xylene are shown in Figure 5-25. The disappearance of the peaks at 611 cm^{-1} and 636 cm^{-1} , corresponding to the C-Br stretching mode, is an obvious difference between the two spectra. Dehydrobromination was thus achieved by heating the bromine precursor for 14 hours. There were, however, two unknown peaks at 667 cm^{-1} and 742 cm^{-1} which did not change in intensity.

The intensity of most peaks increased after thermal treatment. This increase is most obvious for peaks at 960 cm^{-1} , 2856 cm^{-1} , 2921 cm^{-1} and 3020 cm^{-1} . Those bands are assigned to the trans-vinylene =C-H out of plane bending mode and C-H stretching mode. The increase in intensity observed at 2856 cm^{-1} , 2921 cm^{-1} and 3020 cm^{-1} is due to the enhancement of aliphatic hydrocarbon incorporation into the polymer backbone [200] after the thermal treatment. This enhancement is consistent with the blue shifted peaks seen in the UV-vis absorption spectrum.

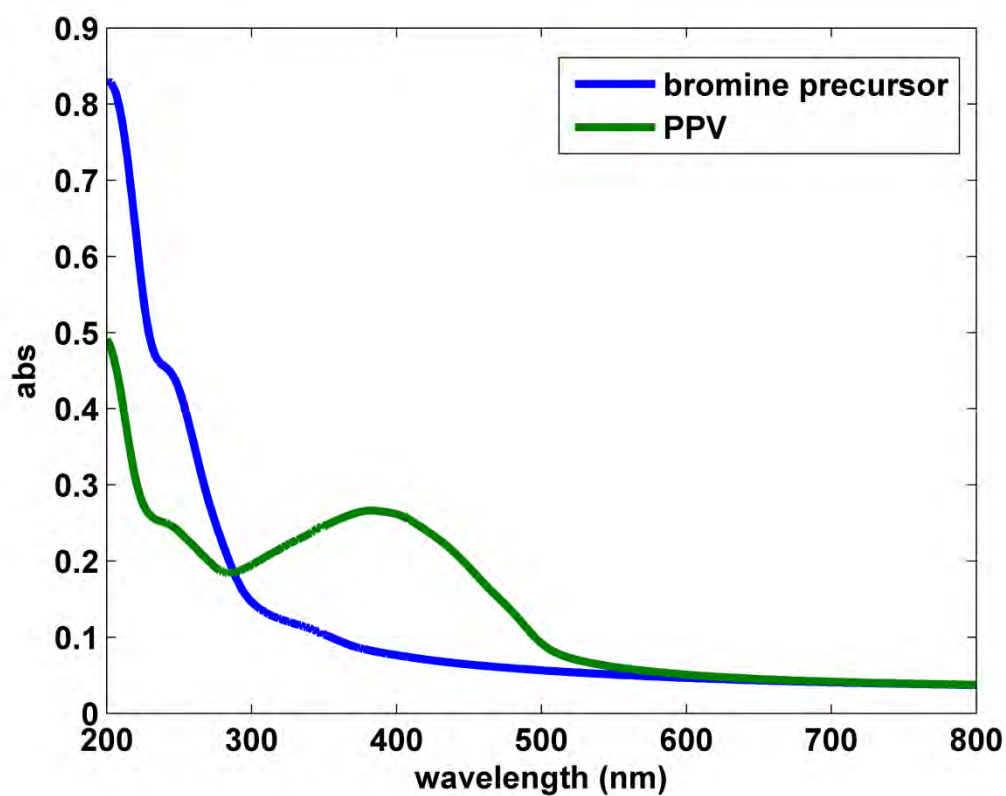


Figure 5-24: UV-Vis absorption spectra of bromine precursor and PPV

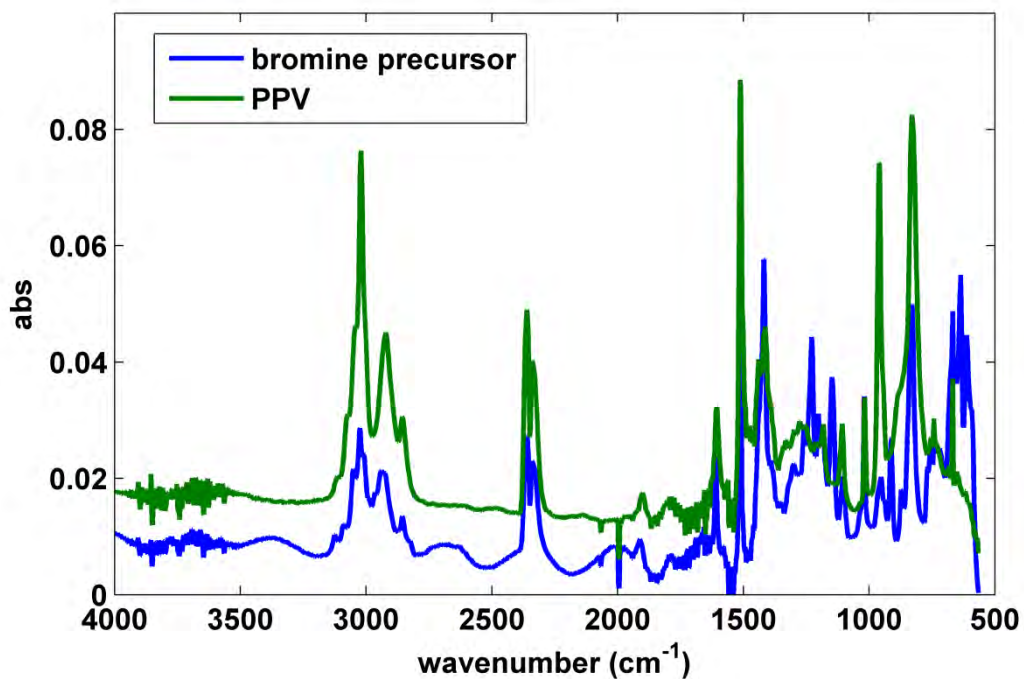


Figure 5-25: Fourier Transform IR spectra of bromine precursor and PPV

5.3.3 Influence of Monomer Selection on Optical Properties

The choice of commercially available α,α' -dihalo-*p*-xylene as CVD monomer can have an effect on the optical properties of the deposited polymer. Previously, Vaeth and Jensen [200] systematically studied the influence of monomer selection and reaction conditions on PPV film composition and luminescence properties. However, the UV-vis absorption spectra of PPV synthesised from different monomers were not reported. As mentioned earlier, α,α' -dichloro-*p*-xylene and α,α' -dibromo-*p*-xylene were used as a starting monomer for the CVD polymerisation. The selection of these monomers is due solely to their availability in commercial stock. Thus, it is worthwhile to investigate the effect of different monomers on optical properties that are important to electronic applications.

As shown in Figure 5-26, clear differences in the absorption peak position and shape were observed for the PPV films synthesised by the different monomers. The difference was also noticed in the FTIR (Figure 5-27) spectra obtained from two different monomers. PPV film synthesised using α,α' -dibromo-*p*-xylene is prone to disruption of the π -bonded electron structure. The larger band gap energy and absorption peak shifted to the shorter wavelength observed in this work is consistent with work reported by Vaeth and Jensen [200]. Shortening of the conjugation length is probably the reason for the differences in optical absorption spectra between two monomers.

Less pronounced incorporation of aliphatic hydrocarbon into the polymer backbone was seen with α,α' -dichloro-*p*-xylene than with α,α' -dibromo-*p*-xylene as evidenced by the higher intensity observed at 2856 cm^{-1} , 2921 cm^{-1} and 3020 cm^{-1} from FTIR spectrum of PPV synthesised with α,α' -dibromo-*p*-xylene. Experimental conditions such as the pyrolysis step and deposition temperature remained the same for the two different monomers. However, a considerable amount of carbonaceous residue was observed with bromine precursor compared to chlorine precursor. According to Staring et al. [73] a substantial amount of carbonaceous residue can be seen in the pyrolysis zone with bromine precursor at pyrolysis temperatures between 500°C to 600°C , compared to the chlorine precursor pyrolysed at higher temperature of 700°C .

Significant amounts of carbonaceous residue would therefore be expected at pyrolysis temperatures of 700°C with α,α' -dibromo-*p*-xylene. The amount of these residues was correlated with pyrolysis temperature, as reported for α,α' -dichloro-*p*-xylene [200]. It is likely that imperfect fragmentation of α,α' -dibromo-*p*-xylene during pyrolysis [200] has caused the production of carbonaceous residue, which would also explain the enhancement in residual aliphatic hydrocarbon into the polymer backbone and shortening in conjugation length.

An intense hydrocarbon incorporation observed in the FTIR spectrum of PPV derived from the brominated precursor is suggested by the additional peak at 2361 cm⁻¹. This peak is attributed to the –CH stretching of the aliphatic chains and aromatic rings [201]. The delocalized structure of π -bonded electrons would be regularly interrupted by the additional aliphatic segments which can lead to a shorter conjugation length. The significant amount of soot deposited on the furnace tube after the pyrolysis process indicates that the pyrolysis temperature at 700°C used in our study is perhaps too high. α,α' -dibromo-*p*-xylene is therefore an unfavourable PPV precursor due to its poor optical properties.

On the other hand, α,α' -dichloro-*p*-xylene is a promising monomer for PPV synthesis. As shown by the UV-vis absorption spectra, a longer conjugation length of PPV can be obtained from the chlorinated precursor than the brominated one. A maximum absorption peak at 410 nm has been reported for PPV synthesis via CVD [179]. Reports of a longer PPV conjugation length in literature [179] compared to that obtained in our study suggests that the polymerisation conditions used here may not be optimal, and further work may be required to generate a longer conjugation length and smaller band gap.

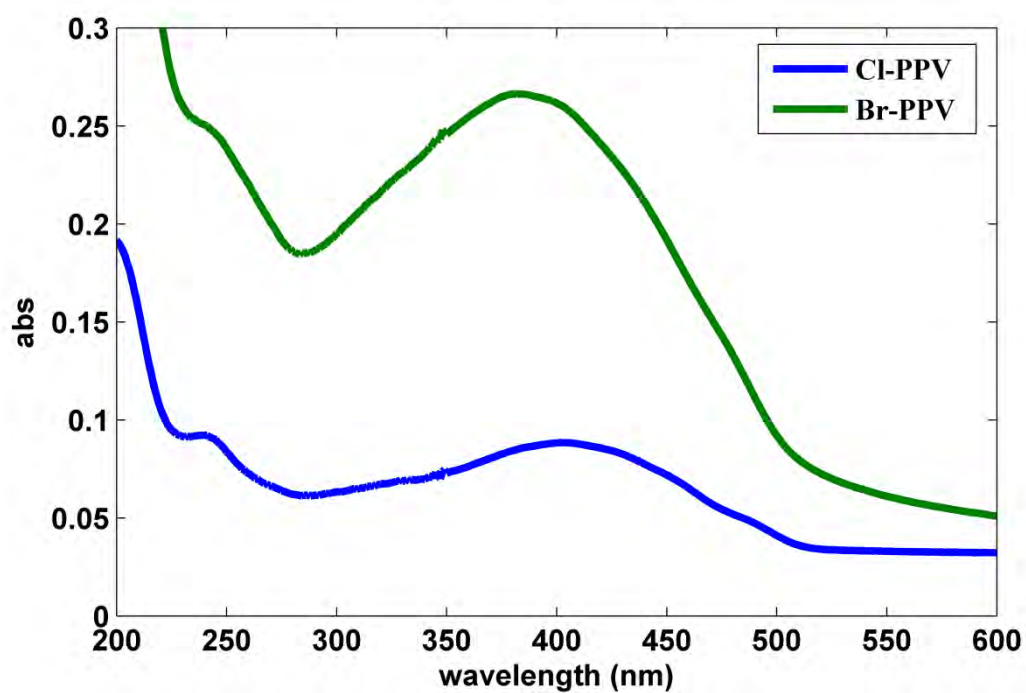


Figure 5-26: UV-Vis absorption spectra of chlorinated PPV and brominated PPV

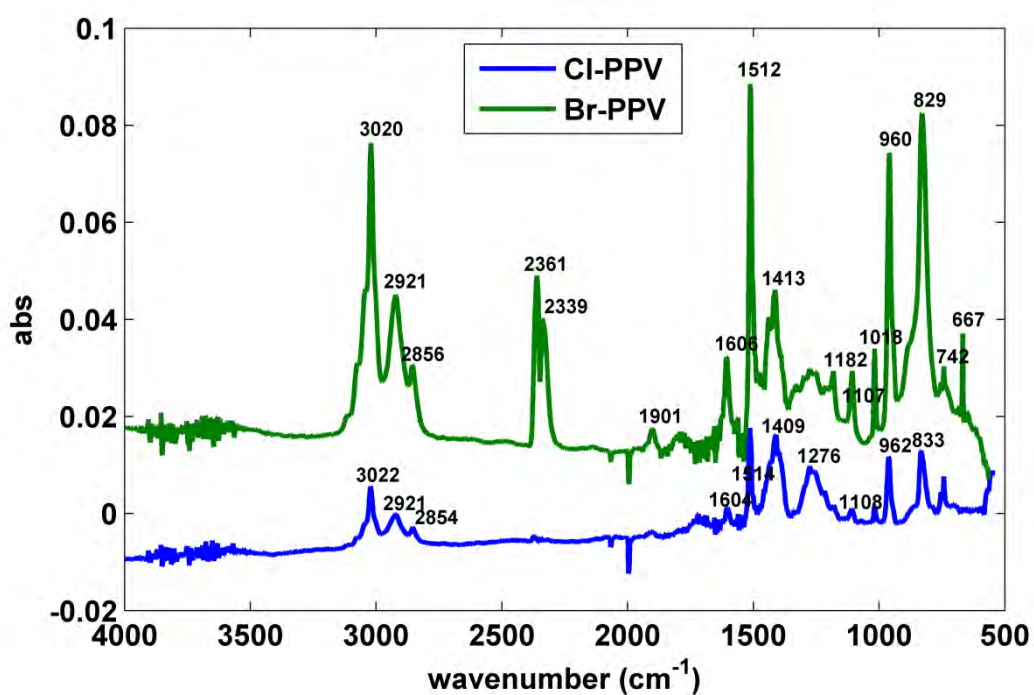


Figure 5-27: Fourier Transform IR spectra of chlorinated PPV and brominated PPV

5.3.4 PPV Absorbance with Thermal Conversion Time

A series of different thermal conversion times was applied to the chlorinated PPV precursor. As previously shown in Figure 5-19, the chlorinated PPV precursor has effectively been converted to a PPV thin film under 400 mTorr pressures after 14 hours of thermal treatment at 270°C. The maximum absorption in the UV-vis absorption spectra was recorded at 400 nm. Figure 5-28 displayed the UV-vis absorption spectra of six different thermal conversion times: 30 min, 1, 2, 3, 4, and 5 hours. A line at 400 nm provides a reference to the different thermal conversion time's absorbance maxima.

The UV-vis absorption spectrum of PPV film converted for only 30 min exhibits a broad spectrum with poorly defined maximum. For this reason PPV obtained after 30 min of thermal treatment can be considered as incompletely dehydrochlorinated. The chlorine groups may not been eliminated through dehydrohalogenation during the thermal treatment. The polymer thin film has been produced with only partial production of the double bonds and conjugated system of π - π^* electron transition characteristics.

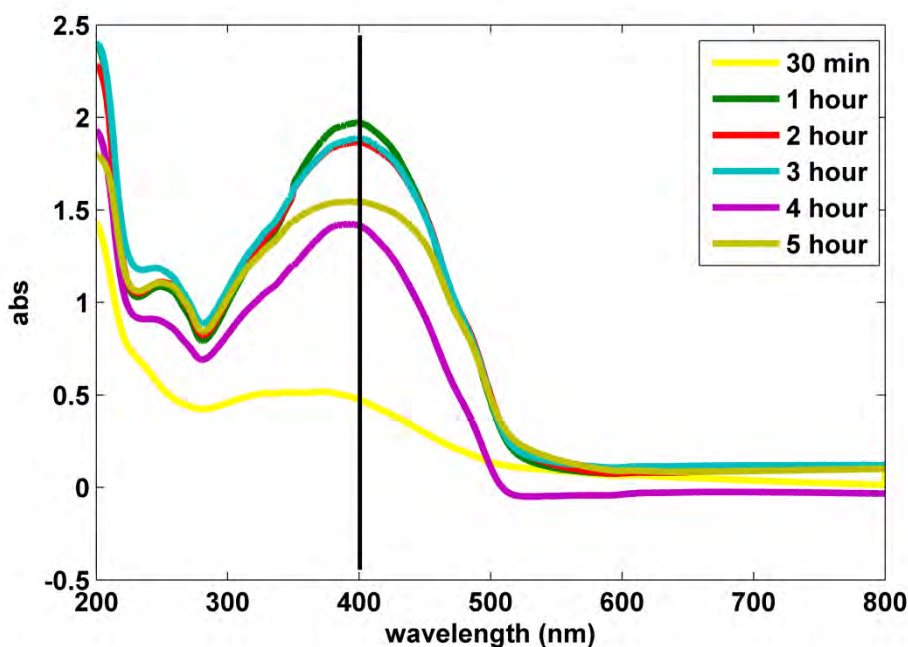


Figure 5-28: UV-Vis spectra of PPV converted at different time

The expected UV-Vis absorption spectrum was observed after 1 hour of thermal treatment, with maximum peak absorption located at 400 nm. This peak indicates that elimination of chlorine group is closer to completion after increasing treatment time and the non conjugated, soluble chlorinated polyxylene (precursor) has been converted to the conjugated insoluble PPV polymer after a treatment time of 1 hour. Given that the maximum absorption peak of UV-vis spectrum is one of the characteristics of complete dehydrohalogenation; 1 hour of thermal treatment can be suggested as an optimum conversion time.

This process was taken closer to completion after a process time of 2 hours. This observation is supported by the FTIR spectra shown in Figure 5-29. The halide peaks at 630 cm^{-1} and 696 cm^{-1} were diminished as soon as PPV precursor is heated for 2 hours. The remaining peaks followed the behaviour of the spectrum measured after 14 hours of thermal treatment (Figure 5-20). Detection of aliphatic hydrocarbon residuals at 2854 cm^{-1} , 2921 cm^{-1} and 3022 cm^{-1} after 2 and 14 hours of thermal treatment indicate that longer treatment times [200] do not necessarily result in purer PPV.

The crystallinity of PPV film depends on the relative amounts of *cis* and *trans* linkages. A mixture of *cis*- and *trans*-PPV cannot result in a highly crystalline film. The *cis* linkage disrupts the conjugation length and thus, packing in PPV [202]. On other hand, domination of *trans* in PPV film may perhaps increase its crystallinity. Amorphous PPV has been synthesized via a soluble precursor route [202]. Infra-red spectrum of amorphous PPV reveals an absorption peak at 868 cm^{-1} , assigned to the formation of *cis*-PPV [202].

As illustrated in Figure 5-29, no peak has been observed around 868 cm^{-1} both before and after thermal conversion of the PPV precursor film. On the contrary, an out-of-plane bending mode of the *trans* vinylene group was detected for both spectra at 960 cm^{-1} . The crystallinity of PPV film synthesized via CVD polymerization is in qualitative conformity with the absence of *cis* linkages.

The similarity of the UV-Vis absorption spectra peak intensity between PPV films treated for 2 and 3 hours indicates a similar film thickness [95]. The PPV precursor treated for 3 hours also exhibits a clear π - π^* transition of PPV since it has an indistinguishable UV-vis absorption spectrum to that of the film treated for 2 hours. The removal of chlorine and hydrogen atom from adjacent carbons was entirely completed after 3 hours of thermal treatment as the UV-vis absorption spectrum shows a peak at 400 nm which is the characteristic peak of PPV.

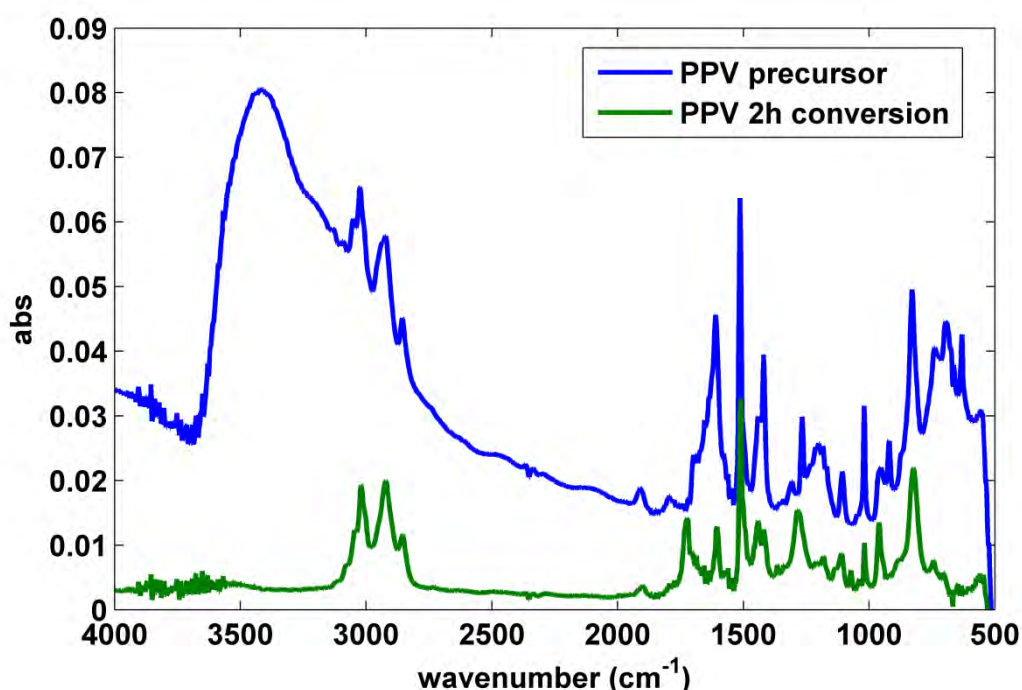


Figure 5-29: Fourier Transform IR spectra of chlorine precursor and 2 hours heated to PPV

In terms of the absorption band shape and intensity, the UV-vis absorption spectrum after 4 hours was different to those for a PPV precursor heated for 2 and 3 hours. Differences in peak intensity can be attributed to differences in film thickness [95]. Despite having maximum absorption peak near 400 nm, the overall peak structure is blue shifted. This peak shift to the shorter wavelength is, however, very small (~ 5 nm). The polymer intra-chain π -conjugation length is related to the shift of wavelength with longer polymer conjugation lengths resulting in red shifted peaks [203]. In contrast, the peak shifts to shorter wavelength observed in the UV-vis absorption spectra most likely arise from a shortening in conjugation length of the polymer backbone.

Further increase in thermal conversion time to 5 hours brings an absorption band peak at 400 nm. However, a broad symmetric absorption band was observed which was not observed in other UV-vis absorption spectra. This observation suggests the conversion of residual precursor segments to phenylenevinylene sequences. Most probably, the absorption spectrum shift to short wavelength after 4 hours of thermal conversion did not involve the crystallinity or degradation of film. Conversely, a decrease in π -conjugation length and intermolecular π - π stacking may have occurred.

In those PPV precursor films heated at 270°C for 1, 2, 3 and 5 hours, the energetically lowest π - π^* transition consists of a reasonably broad absorption band with its maximum at 3.1 eV or 400 nm. The absorption band edge is positioned at around 521 nm which equivalent to a band gap of about 2.38 eV. A notable variation between those absorption spectra and absorption spectrum after 4 hours thermal conversion time was observed. After 4 hours of thermal treatment, PPV precursor film exhibited less absorption band edge and higher band gap energy. However, those absorption edges were identical in which they appear to be spread out consistently.

Figure 5-30 shows the UV-vis absorption spectrum of a quartz substrate. Peak absorption at ~240 nm is seen, and accounts for the additional peak in Figure 5-28, since the PPV was deposited on the quartz substrate. Therefore, an additional peak observed at ~240 nm is not related to the properties of polymer. The strong scattering effects on the surface and polymer can impinge on the qualitative appearance of absorption edge [204]. Film quality is often reflected in the appearance of vibrational progressions in the absorption spectra. As observed in the absorption spectra shown in Figure 5-28, the vibrational progression was absent. It is reasonable to speculate that the quality of PPV film synthesised via CVD is good.

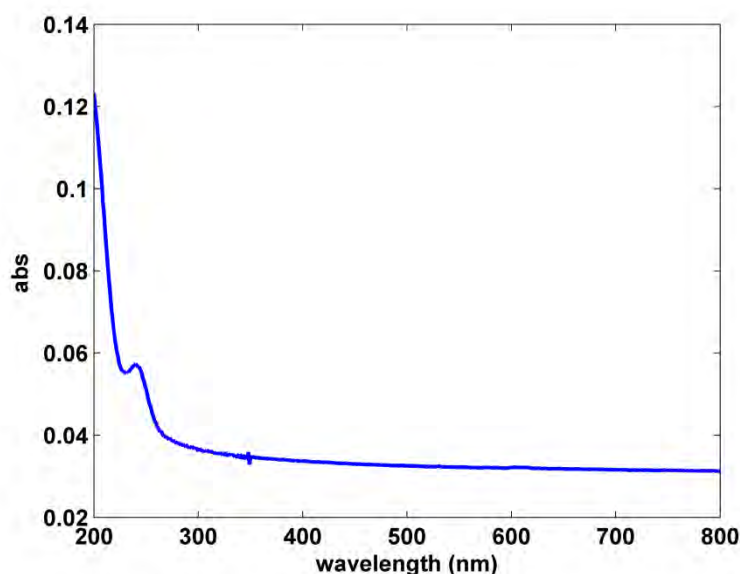


Figure 5-30: UV-Vis absorption spectrum of a quartz substrate

5.3.5 Degradation of Processed PPV Film

Degradation of CVD PPV films synthesised using two different monomers were characterised by UV-vis absorption spectroscopy. Both PPV films were exposed to air for up to six months. Degradation of conjugated polymers typically involves photo-oxidation of the polymer species [100, 205-207] from oxygen and light exposure. UV-vis absorption spectra were taken for each month in order to elucidate the environmental stability of PPV film grown by CVD polymerisation. In our study, the stability of PPV film is only being measured by exposing them into the air, without any irradiation as reported in previous works [100, 191, 192, 205-208].

Film stability or degradation is typically characterised by a shift in the peak absorption of the PPV film, indicating a change in polymer chain conjugation length [100, 191]. Figure 5-31 shows the absence of any blue shift to shorter wavelengths upon air-exposure suggesting that there has been no modification to the overall conjugation length. However, a small systematic reduction in total absorption of the main absorption peak at 400 nm is observed. The change in peak intensity is greatest after the first month of air exposure and then reaches a limiting value over the next 5 months.

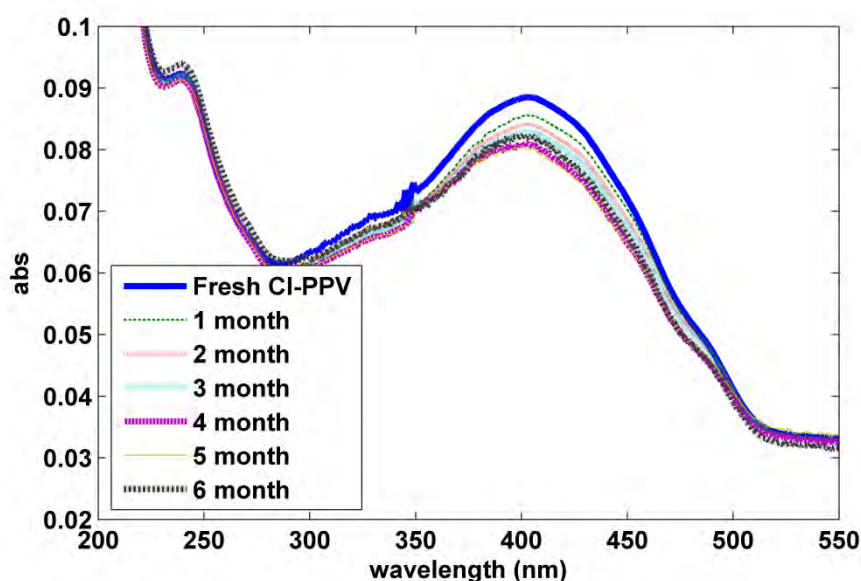


Figure 5-31: UV-Vis absorption spectra of CI-PPV after being exposed to air for up to 6 months

The absorbance of a material depends upon the thickness and concentration of the absorbing species. Given that the aged films started with the same initial film, the reduction in absorption intensity shown in Figure 5-31 is most likely due to changes in polymer film thickness [95]. PPV is a conjugated polymer with a characteristic π - π^* bonding system. As such, air exposure leads to oxidation of the polymer chain with oxygen incorporation interrupting some of the π - π^* bonds which then consequently leads to a decrease of the π - π^* absorption peak. In addition, the longer exposure time might be expected to result in a loss in thickness as the amount of oxygen increases with the exposure time. However, given that the original main peak absorption intensity of 0.09 was only slightly decreased to 0.08 suggests that there is a minimal reduction of PPV film thickness even after 6 months of air exposure. This small decrease in UV-vis absorption intensity supports the assumption that there is an insignificant change in thickness for PPV films synthesised by CVD polymerisation even after long periods of air exposure.

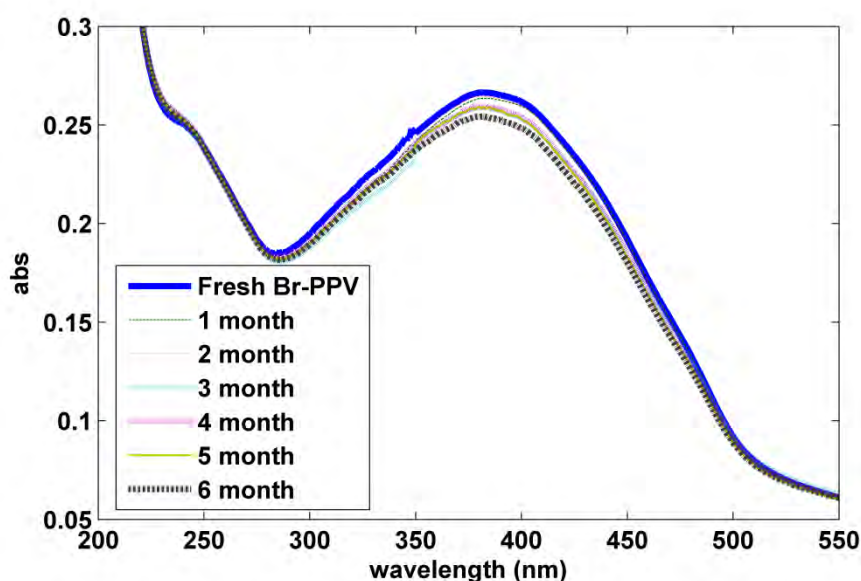


Figure 5-32: UV-Vis absorption spectra of Br-PPV after being exposed to air for up to 6 months

As shown in Figure 5-32, the same observation is made for PPV films synthesised via α,α' -dibromo-p-xylene. No conjugation length distortion was observed after 6 months of air exposure. Additionally, the intensity of absorption peak was degraded minimally for all exposure times. Previous work has shown that changes in the colour of the initial polymer film can be related to the photo-degradation pathways of the conjugated polymer [209]. For example, bleaching can induce the transparency of the pristine polymer films which leads to a loss of visible-light absorption of the polymer. Alternatively, changes in polymer film colour from yellow to brown are indicative of changes in PPV chemical structure [100]. In contrast, both PPV films that have been synthesised here using two different monomers show an opaque yellowish-coloured film that is maintained even after 6 months of air exposure.

Photo-degradation of pure films has been shown to result in a severe decline in the UV-vis absorption peak [100, 191, 192, 208, 210] and a drastic increase in film thickness due to chemical structural changes [207]. It has also been suggested that linewidth narrowing [208] in the UV-vis absorption spectra is also initiated by film degradation. A shift of the absorption peak to shorter wavelengths is an indication of a reduction of polymer conjugation length. As reported by Zyung and Kim [100], UV-Vis absorption spectra of irradiated PPV films shows a blue-shifted absorption peak. Moreover, this

shift was accompanied by a decrease in peak intensity which was attributed to the presence of oxygen facilitating the degradation of polymer films through the formation of carbonyl units on the PPV polymer chains [100, 209, 210].

In contrast, the PPV films synthesised via CVD polymerisation are capable in absorbing light even after long periods of air exposure and exhibit an insignificant loss of visible-light absorption shown in Figure 5-31 and Figure 5-32. The absence of any blue-shift in the absorption spectra indicates that the average conjugation length of PPV films is preserved from the chain scission reaction [100] of the carbonyl group. The absence of any shortening of PPV conjugation length indicates that CVD grown films exhibit semiconducting properties [209] that are stable even after months of air exposure. This stability suggests that CVD grown PPV polymer films offer the prospect of reliable electron donor materials for OPV devices.

5.3.6 Integration of CVD PPV into OPV devices

Two bilayer OPV devices have been fabricated using CVD PPV as the electron donor material and solution-processed PCBM or thermally evaporated C₆₀ as electron acceptor materials, respectively. The overall device architecture is glass/ITO/PPV/PCBM (or C₆₀)/Al. The active layer thickness for the two devices are PPV (159 nm)/PCBM (60 nm) and PPV (43 nm)/C₆₀ (60 nm). The device current-voltage characteristics in the dark and under illumination are shown in Figure 5-33 and Figure 5-34.

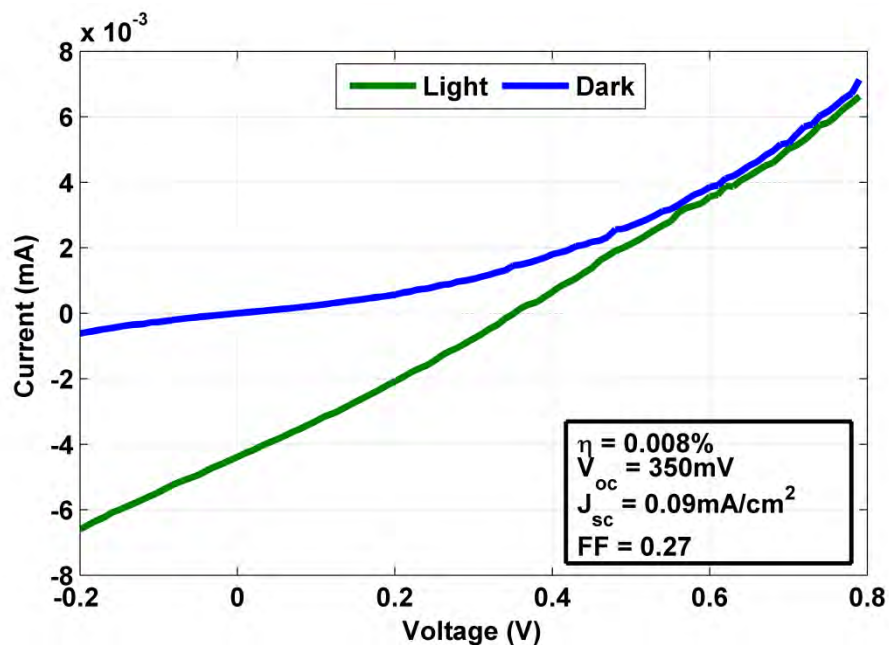


Figure 5-33: The current voltage characteristics of an ITO/PPV/PCBM/Al in the dark and under illumination of AM-1.5

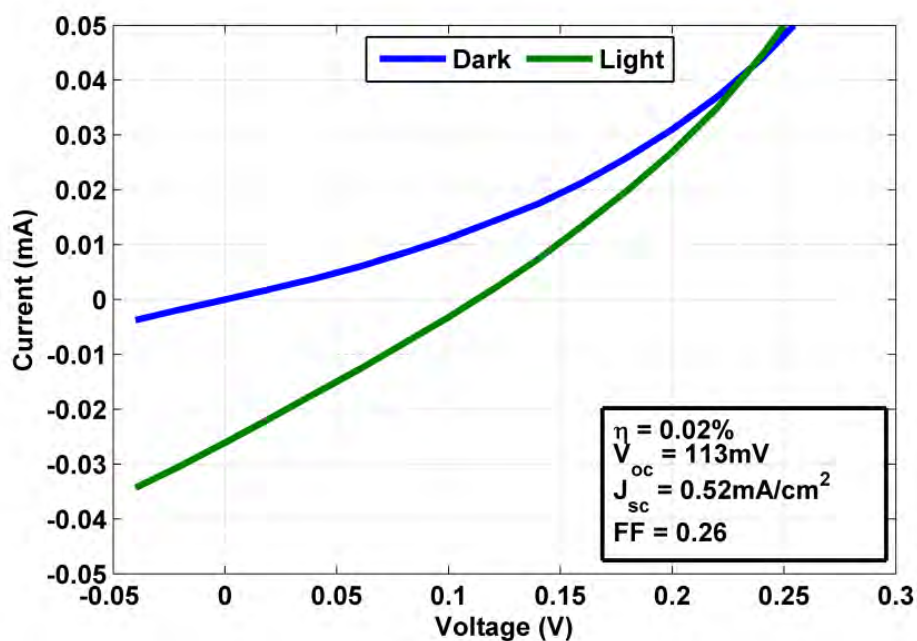


Figure 5-34: The current voltage characteristics of an ITO/PPV/C₆₀/Al in the dark and under illumination of AM-1.5

Both devices are rectifying in the dark under forward bias. The illuminated devices exhibit photovoltaic properties with an open circuit voltage (V_{oc}) at 350 mV and 113 mV. Both devices show very poor power conversion efficiency (PCE). In particular, both devices have very low V_{oc} , which are much lower than that reported by Brabec [82]. The low V_{oc} are highly likely due to pinholes in the active layer, therefore leading to a short-circuit pathway in the devices [211]. Low J_{sc} of 0.09 mA/cm² and 0.52 mA/cm² are obtained from these devices. The low fill factor (FF) of 0.27 and 0.26 and shape of the IV curve suggest the presence of a high series resistance in the cell [212]. Series resistance (R_s) and shunt resistance (R_{sh}) were modelled from the IV data and values of $5.06 \times 10^4 \Omega\text{cm}^2$ and $8.87 \times 10^4 \Omega\text{cm}^2$ were obtained for PPV/PCBM device. These values are much higher than it would be expected for a standard PPV/PCBM bilayer device, would be in part due to the absence of a PEDOT:PSS interfacial layer in the ITO interface. The device using C₆₀ as the electron donor material shows a slightly higher PCE than that for PCBM due to a higher I_{sc} , which indicates a better compatibility using evaporated C₆₀ than spin coated PCBM. An increase in short circuit current density demonstrates an improved electron donor/acceptor interface and therefore more efficient charge separation for PPV/C₆₀ structure. In the PPV/PCBM structure, being exposed to solvents such as chloroform most likely leads to PPV re-arranging during spin coating process and the creation of an ill-defined interface.

To eliminate the shorting and reduce the series resistance, a layer of PEDOT:PSS was been incorporated to coat on ITO before preparing PPV layer. Furthermore, a layer of LiF is also deposited as a buffer layer before Al cathode deposition.

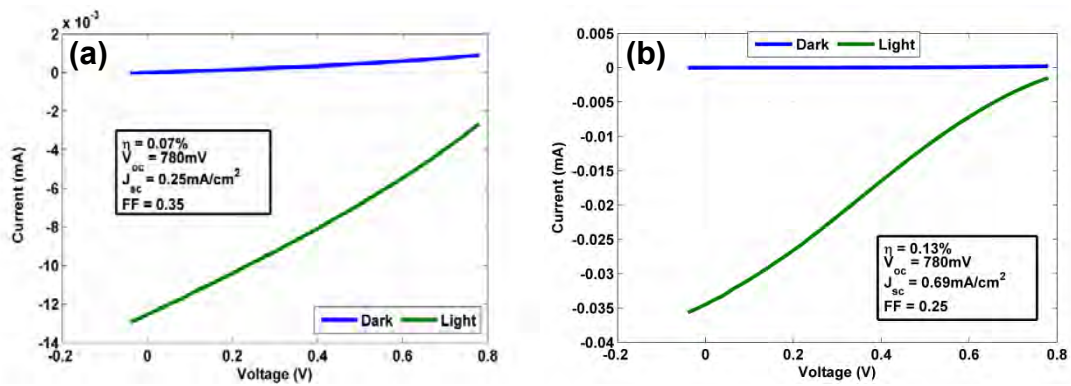


Figure 5-35: The current voltage characteristics of (a) ITO/PEDOT/PPV/PCBM/LiFAl and (b) ITO/PEDOT/PPV/C₆₀/LiFAl in the dark and under illumination of AM-1.5

The incorporation of PEDOT:PSS layer has largely improved the device efficiency with PCEs of 0.07% and 0.13% shown in Figure 5-35a and Figure 5-35b, a 9 fold increase for the PPV/PCBM device and a 7 fold increase for the PPV/C₆₀ device. Compared to the devices without PEDOT:PSS, the dramatic improvement occurs in the V_{oc} , which reaches 780 mV for both the PPV/PCBM and PPV/C₆₀ devices, comparable with the value reported by Brabec et al [82]. PEDOT:PSS as an electron blocking layer not only effectively prevents devices from shorting due to pinholes but also enhance the charge extraction for PPV/PCBM device [82]. Furthermore, LiF has been proven to be a good buffer layer at the active/Al interface to reduce the series resistance [82], which is in accordance to the increase in the short circuit current from 0.09 to 0.25 mA/cm². However, LiF buffer layer seems to provide little improvement for PPV/C₆₀ device. It is found that although the short circuit current is increased from 0.52 to 0.69 mA/cm² for PPV/C₆₀ device, there is little change in the observed fill factor. In addition, the occurrence of an *S*-shape in the current-voltage measurement indicates that space-charge effects are starting dominate in the PPV/C₆₀ device [213]. In bilayer OPV devices, excitons separate most effectively at the electron donor/acceptor interface [214]. Although the PPV/C₆₀ structure generally provides a better electron donor/acceptor interface than that for PPV/PCBM structure, the low fill factor and high charge recombination may be due to poor transport across the active/electrode interfaces. It should be noted that the PEDOT:PSS layer has undergone an extensive annealing process during PPV preparation. Transformation from the precursor to PPV requires 14 hours of thermal conversion at 270°C, which may induce degradation and phase separation of PEDOT from PSS. Further work to replace PEDOT:PSS to a more thermally resistant material would be necessary.

A different buffer layer of calcium to replace LiF has also been investigated. Figure 5-36a and Figure 5-36b show the current voltage characteristics of the PPV/PCBM/Ca and PPV/C₆₀/Ca devices. A further improvement in V_{oc} is obtained for both devices. For PPV/PCBM device, the V_{oc} is increased from 780 to 1010 mV. For PPV/C₆₀ device, the V_{oc} is increased from 780 to 852 mV; the fill factor is increased from 0.25 to 0.36. However, the short circuit currents are also reduced for both devices, which also exhibit an *S*-shape in their IV measurements under illumination.

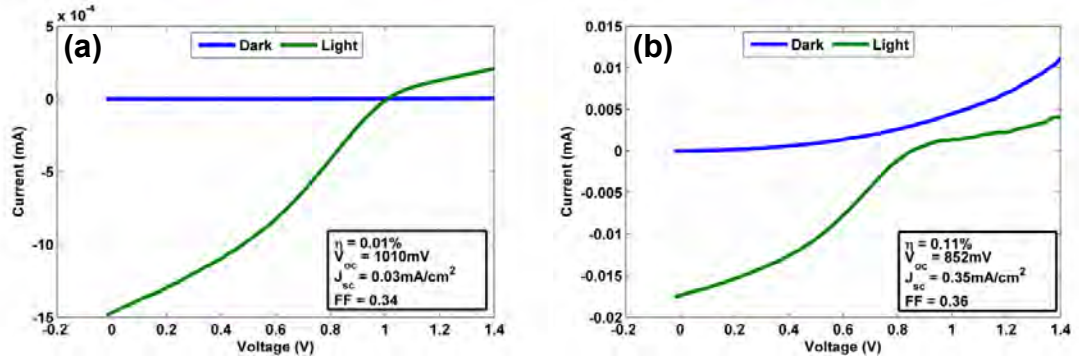


Figure 5-36: The current voltage characteristics of (a) ITO/PEDOT/PPV/PCBM/CaAl and (b) ITO/PEDOT/PPV/C₆₀/CaAl in the dark and under illumination of AM-1.5

The external quantum efficiency (EQE) of a bilayer OPV based on PPV/C₆₀/Ca structure has also been measured and shown in Figure 5-37. It shows that a large proportion of photocurrent is generated by photons in the range of 400 to 500 nm wavelengths, which is consistent with the PPV absorption profile. Interestingly, two extra shoulders at 620 and 675 nm have also been observed, which indicate very likely charge transfer states form at the PPV/C₆₀ interface [82]. The overall EQE is quite low (less than 5%). However, the observed low EQE cannot be due to insufficient absorption from a difference in active layer thickness because a device with 140 nm of PPV gives the same PCE as for PPV of 22 nm.

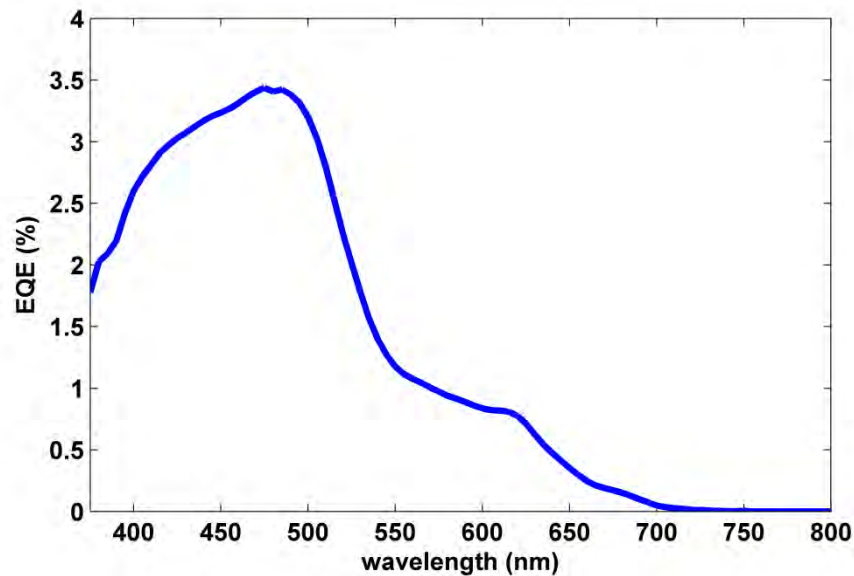


Figure 5-37: External Quantum Efficiency (EQE) spectrum of PPV/C₆₀

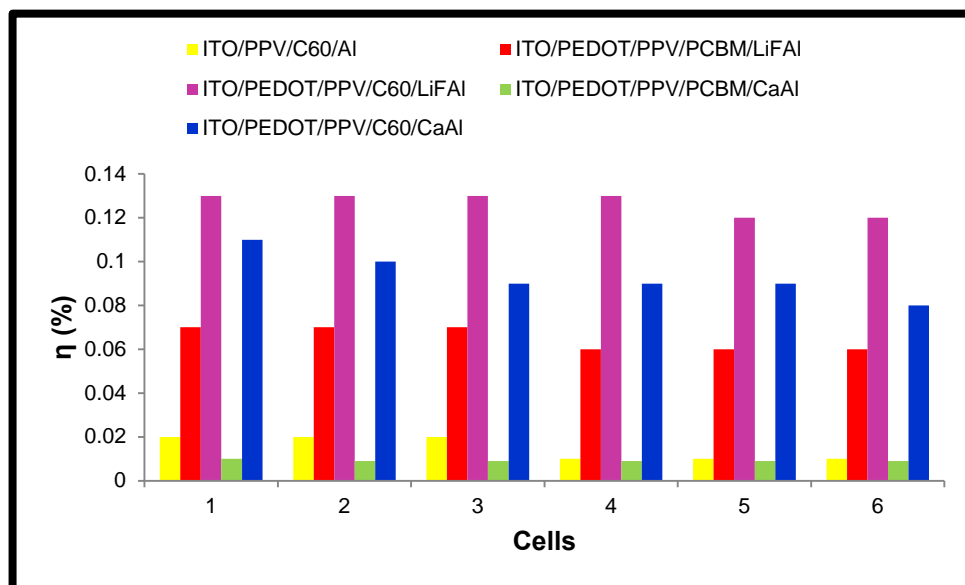


Figure 5-38: The efficiencies of cells produced by different device architectures

Figure 5-38 summarizes all the OPV devices using the CVD PPV polymer films, which show a high reproducibility in their device performance for the same architectures. The device efficiencies are also highly dependent on the device architecture. Devices using PEDOT:PSS as the electron block layer and LiF the cathode buffer layer give a consistently higher efficiency than all of the other architectures used in this investigation. The fact that the devices are highly sensitive to the preparation of the electron acceptor material and the device architecture indicates that charge separation and extraction are the limiting factor for these CVD PPV OPV devices. The limited bilayer structure constrains the area of electron donor/acceptor interface, therefore a better design of nanostructured PPV/PCBM or C₆₀ interfusion architecture would enlarge the interface, potentially improving the OPV device performance.

5.4 CONCLUSIONS

PPV films have been successfully deposited via CVD polymerisation. The chlorine precursor of α,α' -dichloro-p-xylene offers better PPV films over the brominated equivalent. The properties such as a smaller energy band gap and chemical structure composition, lead to the integration of CVD chlorinated PPV into a bilayer OPV structure. No other work to date has attempted to fabricate an OPV with the use of CVD. Since CVD does not require any solvent or additional chemicals and can generate conformal layers directly onto the device substrate, it is envisaged that this approach is a promising path to enhancing the efficiency of solvent-free based OPV.

Devices were fabricated using different: (i) electron acceptors (PCBM and C_{60}), (ii) metal cathodes (Al, Ca and LiF) and (iii) electron blocking layers (no blocking layer and PEDOT-PSS). The results show that the optimum devices are fabricated using the ITO/PEDOT-PSS/PPV/ C_{60} /LiF architecture and these devices exhibit device efficiencies that are comparable to similar non-CVD devices reported in the literature. Given that this is the first reported integration of CVD into OPV devices, this chapter provides valuable insights for the future work needed to optimise and improve device performance.

6 CHEMICAL VAPOUR DEPOSITION OF THE PPV NANOSTRUCTURES

6.1 INTRODUCTION

Synthesis of conjugated polymers in nanostructured shapes (eg: nanotube, nanorod, nanowire) can be achieved via CVD polymerisation [11, 70]. These morphologies can offer materials that are useful for nanoelectronic devices and sensors. For example, a PPV and perylene heterojunction has demonstrated the photovoltaic effect [81], and devices fabricated with PPV nanostructures may provide benefits in solar cell applications [179]. Production of nanostructured PPV is complicated by its insolubility [70]. Consequently, a synthetic method that proceeds via soluble precursor routes prior to the thermal conversion to the final polymer composition is required. Alternatively, CVD polymerisation of PPV precursors is a promising method for nanostructure fabrication.

There are many reports on the fabrication of conducting polymers nanostructures by soluble polymer precursors. However, there is only one report on the CVD polymerisation of PPV nanotubes and nanorods (Figure 6-1) [70]. Alumina and polycarbonate membrane filters, with pore diameter of 200 nm and 100 nm, were used for the polymer nanostructure fabrication in this work.

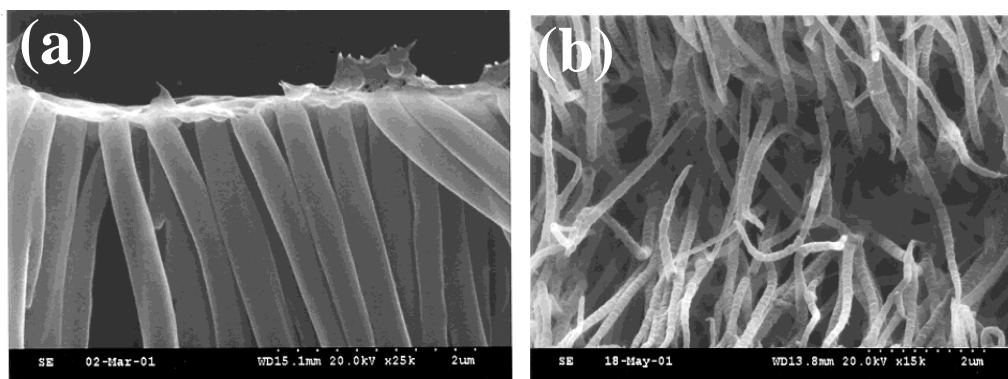


Figure 6-1: SEM images of PPV (a) nanotubes prepared in alumina filter membrane & (b) nanorods prepared in polycarbonate filter membrane [70]

Another insoluble conjugated polymer that has been synthesised via CVD polymerisation in an alumina membrane template is poly (2,5-thienylene vinylene) (PTV) [11]. The simple synthetic route of CVD has produced various shapes of PTV nanostructures (Figure 6-2). In addition, these nanostructured conjugated polymers can be doped with species such as I_2 or $FeCl_3$ at room temperature to boost their electrical conductivity properties.

PPV is a conjugated polymer the inherent conductivity of which is close to that of an insulator. The conductivity can however be easily improved via vapour phase doping [198]. The CVD technique not only results in the nanostructure formation, but also offers excellent dopant diffusion into the polymer matrix [198].

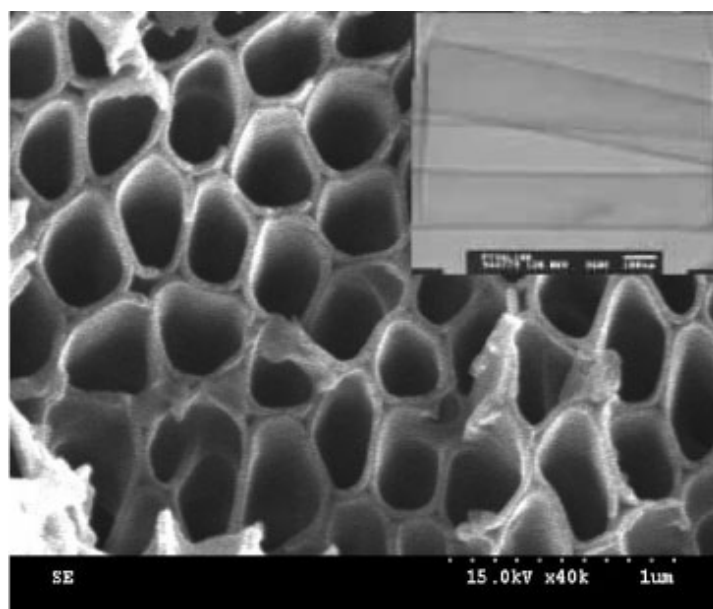


Figure 6-2: SEM images of PTV nanotubes prepared by alumina filter membrane [11]

In this work, we focus on the growth of PPV nanostructures. We have grown PPV nanostructures on a porous alumina template with nominal diameter of 100 nm. In order to glean more understanding as to how the vaporised monomer is deposited onto the template surface, five different angles of template with respect to the substrate holder were employed. The vaporised monomer flux is directed towards the tilted template where deposition occurs on the template facing towards substrate holder. Deposition of PPV was implemented at 0° (horizontal), 30° , 45° , 60° and 90° (vertical) of template angles. Templates with different angles were positioned side by side at spot 5 in the

CVD system (Figure 5-14) which was assessed to be the best spot for precursor collection. Other than the different substrate angle, all deposition parameters remained the same.

6.2 EXPERIMENTAL DETAILS

The experimental details of PPV nanostructure fabrication is described in Section 2.2. The porous alumina templates were first cleaned with acetone in order to remove impurities that might accumulate on the template surface. Templates were positioned in the deposition zone at the optimum position determined by the procedure described in Section 5.3.1. The angle between template and planar surface within the deposition zone was varied while keeping the other synthesis conditions constant. As shown in Figure 6-3, one template was positioned in a horizontal configuration (0°), whereas the other templates were positioned at angles of 30° , 45° , 60° and 90° . These templates were attached to the standing substrate of the desired angle.

After deposition, the alumina template was dissolved in 3M sodium hydroxide (NaOH) and the PPV film was rinsed in water before being characterised via SEM. In order to minimise the distortion of the PPV nanostructure prior to drying at room temperature, PPV isolated from the template was rinsed with a low surface-tension solvent such as methanol. To facilitate SEM characterisation, a thin gold coating was evaporated on the PPV to avoid charging. Photoluminescence measurements were taken for PPV deposited on the alumina template under excitation at 350 nm.

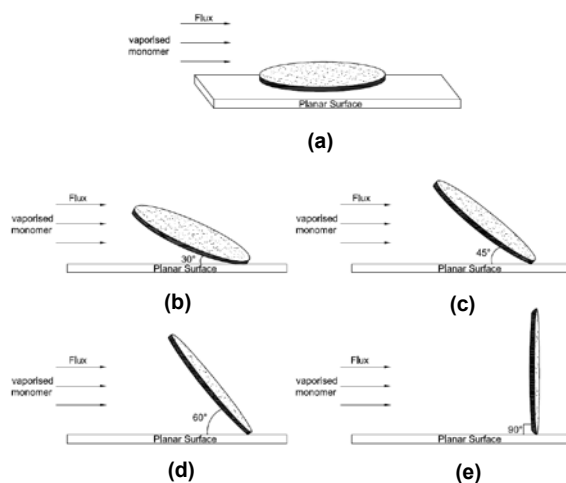


Figure 6-3: Schematic diagram of template positioned at (a) horizontal (0°) (b) 30° (c) 45° (d) 60° & (e) vertical (90°) respect to the planar surface

6.3 RESULTS AND DISCUSSION

6.3.1 Photoluminescence

The photoluminescence (PL) of the PPV deposited onto alumina templates at different angles is shown in Figure 6-4. A broad PL feature is observed, which starts around 500 nm and consists of 3 different peaks whose relative magnitude changes at different template angles. The peaks are at 520 nm, 549 nm and 593 nm which we label peak 1, 2 and 3, respectively. The strongest emission occurs at 549 nm for all angles. At 30° and 45°, peaks 1 and 2 are blue-shifted by 6 nm and 2 nm, respectively. Peak 3 starts to quench at angles of 45° and greater quenching occurs with increasing angle.

Figure 6-5 shows the PL intensity ratio of peak 1 (0-0 transition) to peak 2 (0-1 transition) [215, 216] at different deposition angles. The relative intensity of peak 2 is reduced as the template reaches the vertical position. However, no pronounced intensity enhancement is observed at peak 1 as the template is directed towards the vertical position. The quantitative summary of angle effects can be interpreted from Figure 6-5 by giving the percentage of relative intensity of peak 2 with respect to peak 1. PPV nanostructure deposited at 0° exhibits the lowest percentage of 9%, and a significant red shift of peak 1. The relative intensity (peak 1/peak 2) increases as the angle is directed towards the vertical position with respect to the deposition surface.

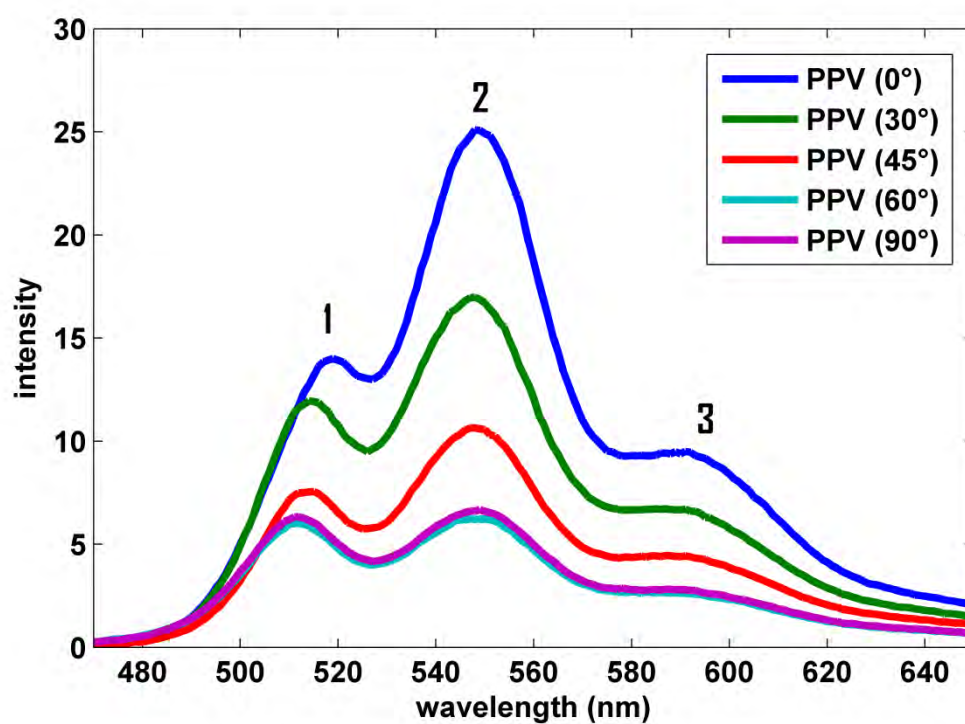


Figure 6-4: Photoluminescence spectra (excitation at 350 nm) of PPV deposited on alumina template of different angles

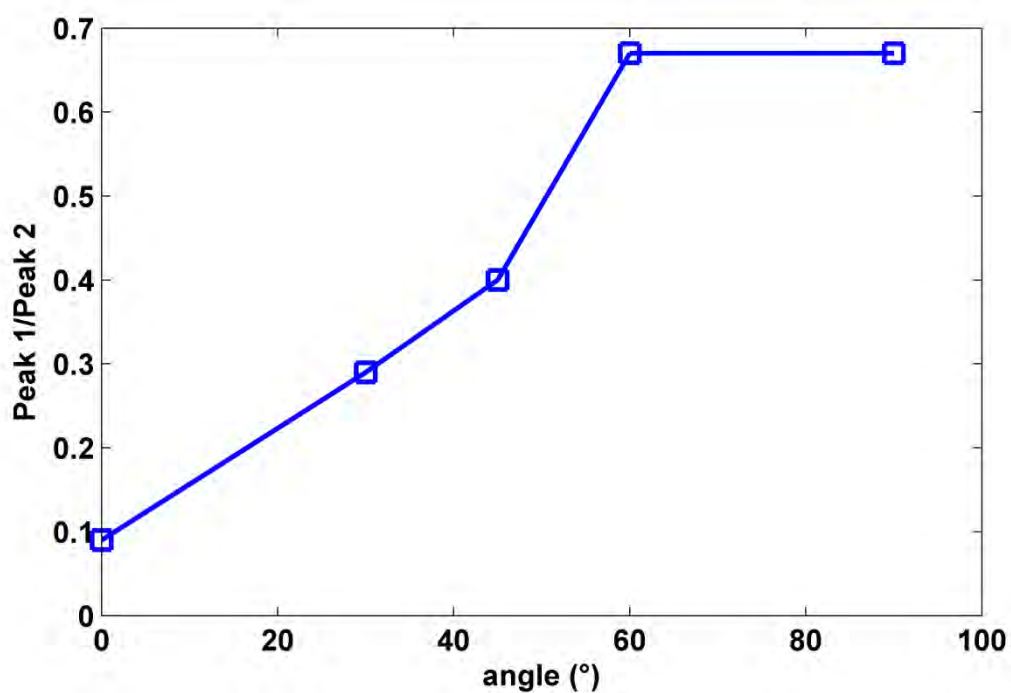


Figure 6-5: Photoluminescence intensity ratio of peak 1 to peak 2 of different deposition angles

6.3.2 Surface morphology of PPV as a function of deposition angle

6.3.2.1 Horizontal (0°)

PPV precursor was deposited on the high aspect ratio porous alumina template before being converted to PPV via thermal conversion treatment. Four SEM images are shown in Figure 6-6, Figure 6-7, Figure 6-8 and Figure 6-10, which correspond to the top surface of the PPV on the template, the bottom surface of template, a cross-section of PPV on the template, and PPV nanostructures after being isolated from template, respectively. Clear differences can be seen between the templates before PPV deposition (Figure 2-4) and template after PPV deposition (Figure 6-6), due to deposition of PPV on the template surface.

As shown on the top surface (Figure 6-6), the polymer has grown as a nanostructured material, with evidence of fibre formation. The template pores with a nominal diameter of 100 nm are completely covered by these fibrous PPV nanostructures, with no unfilled pores visible in this image. The diameter of the fibrous-like PPV nanostructures is in range between 50 to 250 nm, with some exhibiting cactus-like nanostructures where they are attached on top of each other. Thus, CVD polymerisation can not only be used for PPV thin film growth [71] but, as observed in this work, it also can be applied to the growth of PPV nanostructures.

In order to investigate whether PPV was deposited inside the porous template, an SEM image from the bottom surface of template was taken. It is clearly shown in Figure 6-7 that numerous template pores were unfilled. As such, the vaporised monomer did not diffuse all the way through the 60 μm pore long during the deposition time. This hypothesis is supported by SEM images (Figure 6-8) taken from a cross-section view of template. No PPV structure has been deposited through the pore and no layer of PPV can be seen infiltrating more than a few 10's of nm's inside the pore.

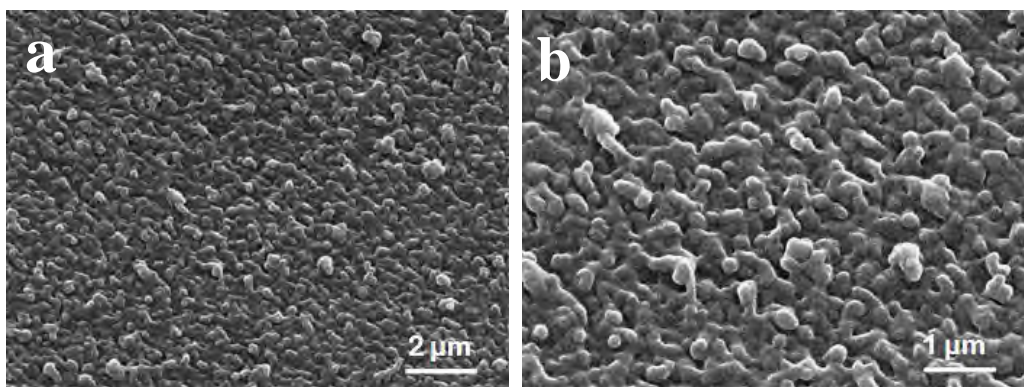


Figure 6-6: SEM image of PPV deposited on horizontal alumina template of (a) lower magnification & (b) higher magnification

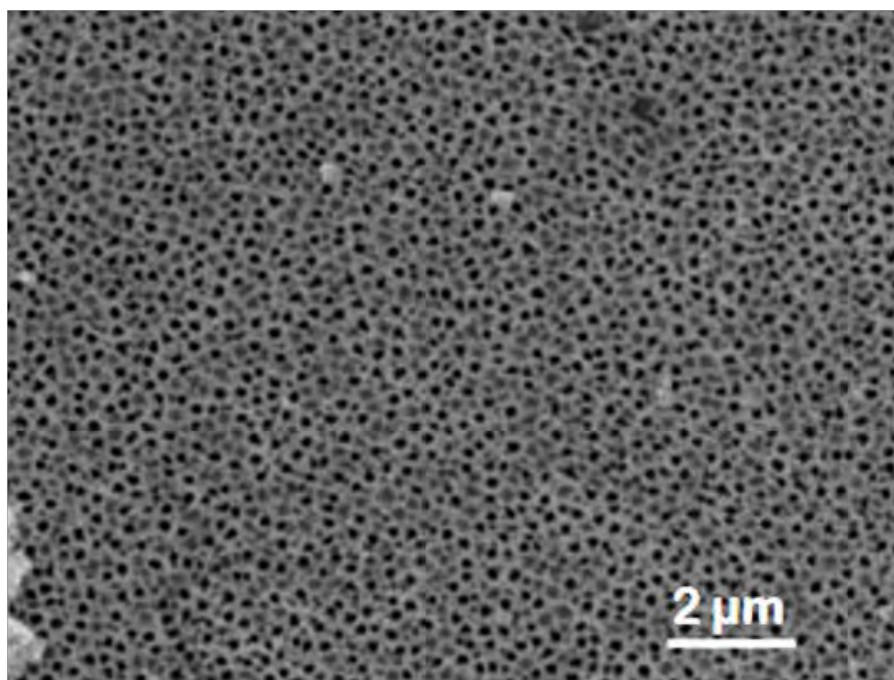


Figure 6-7: SEM image (Top view) of PPV deposited on alumina porous template taken from the bottom surface

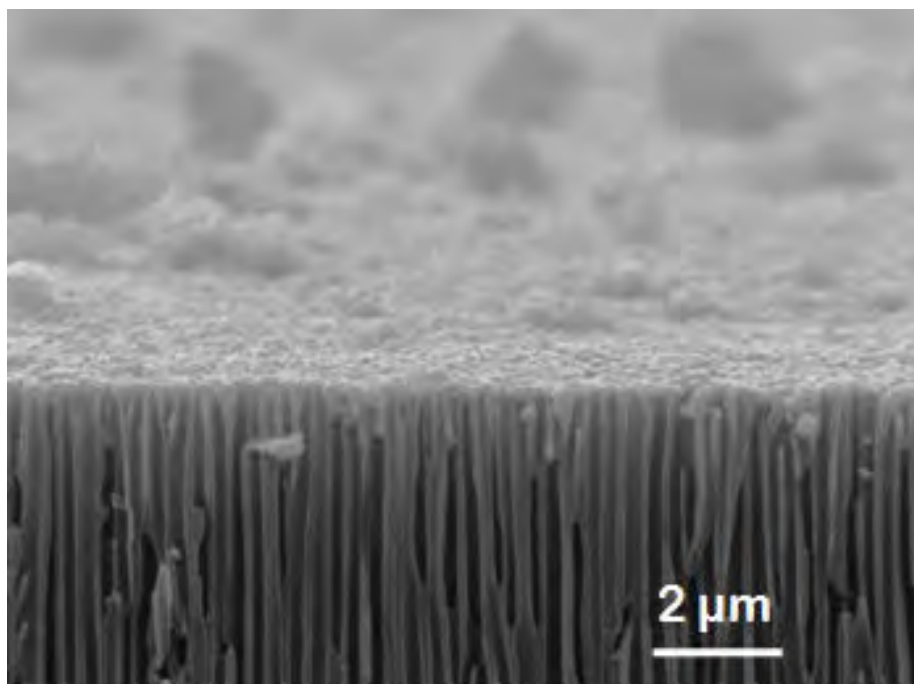


Figure 6-8: Cross-section SEM image of PPV deposited on horizontal alumina template

It should be noted that, although the bottom surface of the template shows that a number of pores are covered, this does not appear to be due to PPV deposition. The cross-section image has shown the pore structure of the alumina is branched, in other words, the pores exhibit a discontinuous connected structure. Vaporised monomer could be blocked by the alumina branches before it can reach the bottom surface of template. Despite that, PPV might have been deposited on the edge of the alumina branches [11].

The PPV nanostructures are originally deposited as monomer or chlorinated xylylene [71] upon condensation and polymerisation onto substrate. Therefore, chlorinated xylylene must be deposited in the pores prior to the dehydrochlorination process. According to Cetinkaya et al [217], nanostructured thin films of poly(*p*-xylylene) derivatives can be deposited by vapour deposition method. This work [217] is in agreement with the growth of PPV nanostructures observed here, as shown from the top view and cross-section view of SEM image.

The emissive characteristics of PPV nanostructures observed on alumina template are investigated via their PL spectra. Figure 6-9 compares the PL spectra between PPV nanostructures and a PPV thin film at $\lambda_{\text{exc}} = 350$ nm. Each PL spectrum exhibits three peaks; 1, 2 and 3 at increasing wavelength. However, a significant red-shift (~ 7 nm) occurred at peak 1 of the PPV nanostructure. In addition, a reduced intensity is recorded for the PL spectrum of the PPV thin film which indicates the different thicknesses between the two samples [218, 219]. As reported by Qi et al [215], the isolation of polymer chains on the alumina porous surface can induce blue shifts of PL spectrum. Apparently, cactus-like PPV nanostructures grown on the alumina template have a red-shift which implies that the polymer chains of PPV nanostructures have not been isolated or interacted within the alumina porous surface.

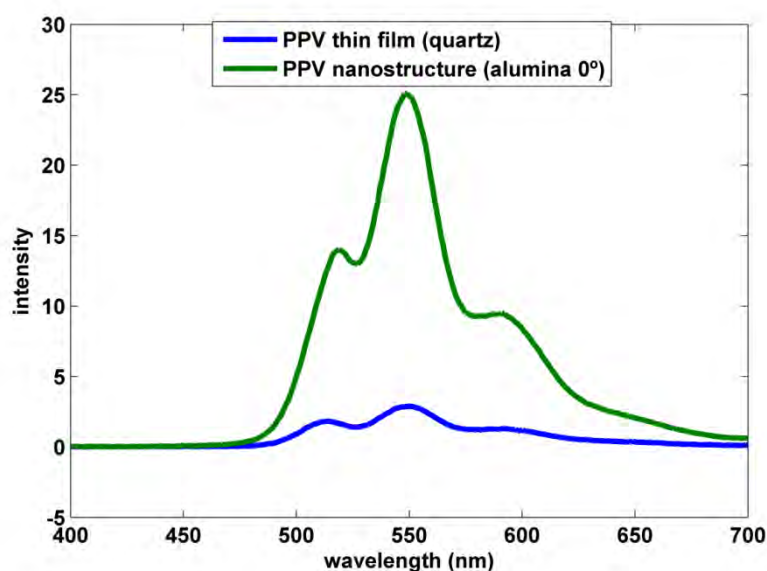


Figure 6-9: Photoluminescence spectra (excitation at 350 nm) of PPV thin film deposited on quartz and PPV nanostructure deposited on alumina template at 0°

Interestingly, based on the red shifts observed at 520 nm, PPV nanostructures grown on alumina template in the horizontal position have a longer conjugation segment length than PPV thin film deposited on quartz [220]. The enhancement of interchain interaction between polymer chains is pronounced in PPV nanostructures due to the restricted intrusion into the nanopores. The polymer chains of PPV nanostructures deposited onto the alumina porous surface would be expected to be segregated and thus experience weak interchain interactions [215].

PPV nanostructures that have been removed from the porous template exhibit considerable surface tension and clump together. Indeed, the PPV nanostructured layers can be seen to be lying on top of each other instead of forming one smooth layer. As reported by Kong et al [221], self-organized nanofibre micropatterns are mostly dependent on the dilation stress and interaction between nanofibres during the template removal. Therefore, the web-like pattern exhibited by PPV nanostructures occurs during template removal whereas these features are not observed whilst they are on the template.

Despite having an irregular PPV nanostructure film, the fibrous nanostructure of the PPV is preserved. The structure obtained in this work is similar to that reported by Kim and Jin [70], where the presence of multibranches is well observed. These multibranches have indicated that the pores inside the template are well interconnected. The only difference between PPV nanostructures grown in our work and the work of these authors [70] is the density of the PPV nanostructure branches. In our study, the branches are so dense that the gap between fibres is hard to distinguish. It appears that the PPV nanostructures are relatively well ordered, with a dendritic structure which replicates the structure of initial PPV nanostructure before being removed from the alumina template. The diameter of PPV nanostructures formed in the branches has a variation in size which ranges between 30 to 60 nm.

Different SEM images taken between 10000X to 80000X magnification are shown in Figure 6-10(a-d). Based on the observed SEM images, the genuine structure of PPV after being isolated from template is proposed and displayed in Figure 6-11. It exhibits a similar shape to a nanobud structure, in which a round head sits atop a small neck [10].

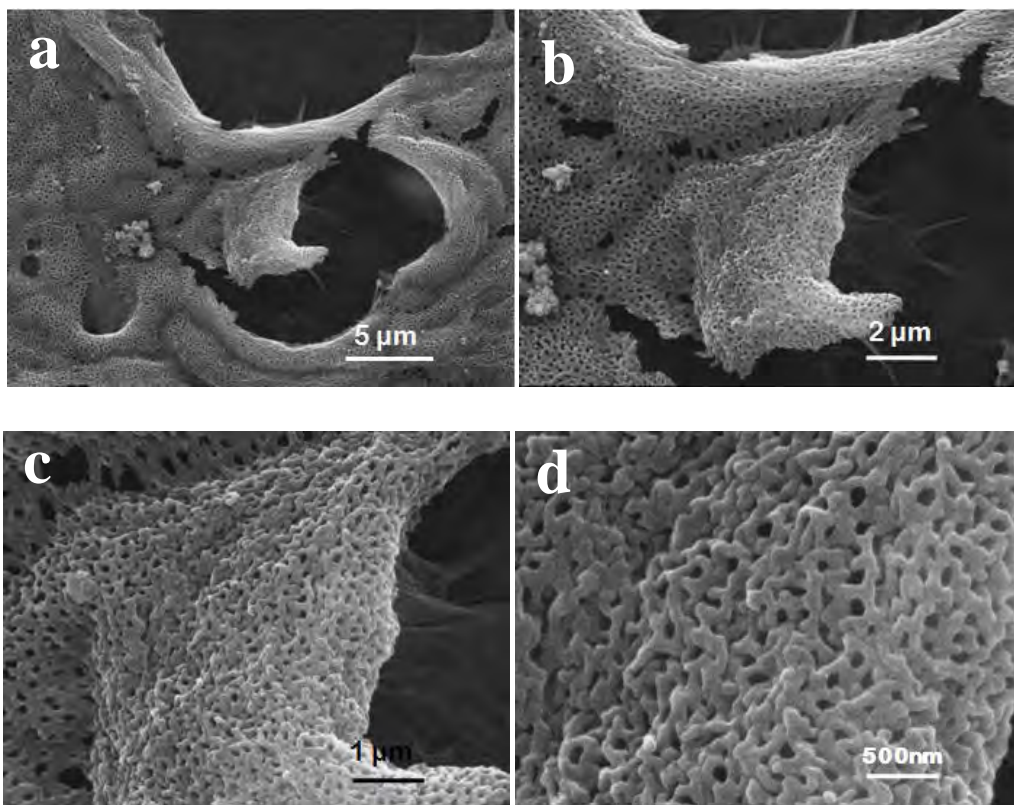


Figure 6-10(a-d): SEM image of PPV deposited on horizontal alumina template after being isolated from template

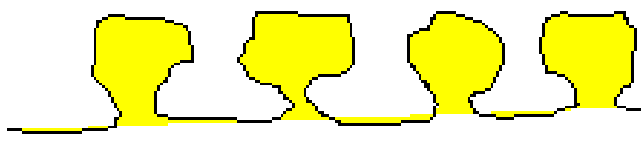


Figure 6-11: Schematic diagram of proposed nanostructure of fibrous-like PPV

6.3.2.2 Angle at 30°

Figure 6-12 and Figure 6-13 show the top view and cross-section view of PPV deposited at a 30° template angle. Significant differences in surface morphology of deposited PPV can be seen between the two different angles of 0° and 30°. At higher SEM magnification, a small area of porous alumina template that is not covered by PPV is seen. Inclination of the alumina template towards planar surface has reduced the amount of vaporised monomer getting onto the template.

The thickness of the PPV layer is affected by the amount of vaporised monomer deposited. PL spectra in Figure 6-4 show the intensity depletion at peak 2 and blue-shift to shorter wavelengths at peak 1 compared to the PL spectrum at 0°. The blue-shift observed at peak 1 of angle 30° is accompanied by the increment of ratio peak 1: peak 2. As reported elsewhere [215], the accumulated conjugated polymer inside the alumina template has a tendency to induce a blue shift in the PL due to the isolation of the polymer chains. Unlike the PPV cactus-like nanostructure exhibited by horizontal template, PPV deposited at a 30° angle does not exhibit nanostructure formation for thicker layers.

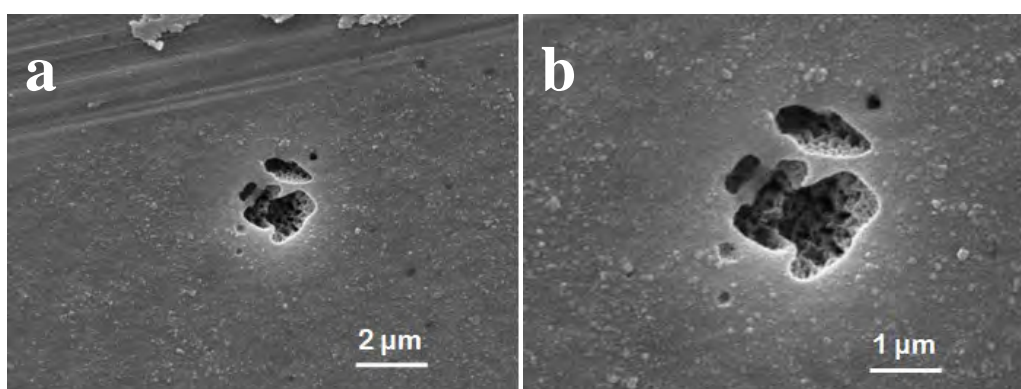


Figure 6-12: SEM image of PPV deposited at 30° of alumina template angle of (a) lower magnification & (b) higher magnification

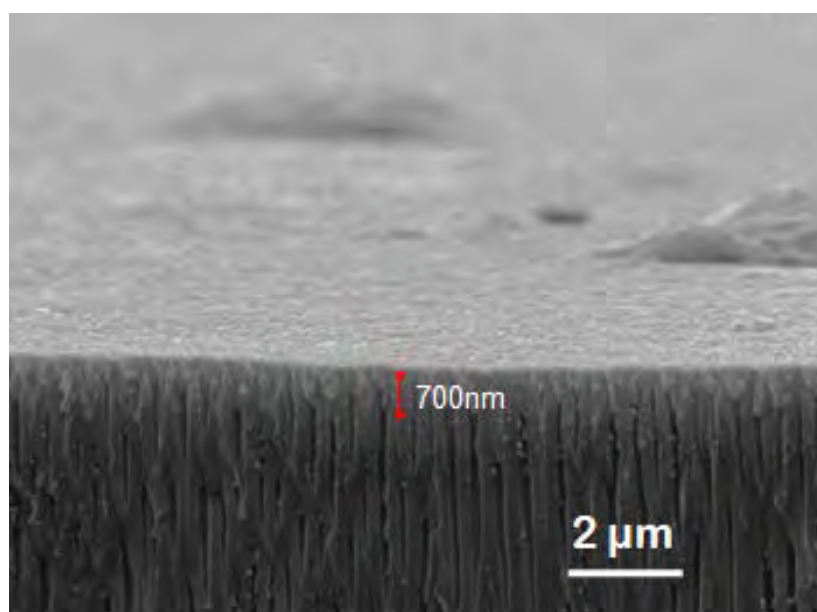


Figure 6-13: Cross-section SEM image of PPV deposited at 30° of alumina template angle

Furthermore, the cross-section SEM images of both angles display quite different diffusion behavior of the vaporised monomer. PPV deposited at 30° apparently diffuses deeper into the template pores compared with PPV deposited on a horizontal template, in which the layer of PPV nanostructure appears to be just deposited on top of the template. For the tilted template, vaporised monomer is seen to infiltrate into the nanoporous structure and generate approximately 700 nm of PPV thickness.

Figure 6-14(a-c) shows that CVD polymerisation of PPV has taken place in the inner surface of the pores with two types of morphologies. These two morphologies are; PPV that has been deposited up to ~700 nm to the pores and PPV that has diffused through the pores and subsequent deposited at the pores' edge. This observation is in agreement with previous studies on the CVD polymerisation of poly(2,5-thienylene vinylene) (PTV), which showed that after the dissolution of alumina template, PTV nanotubes were observed with the wall thickness of 35 nm which is due to the deposition of vaporised monomer at the pores' edge [11].

Previously, three types of nominal pore diameter (10 nm, 100 nm and 200 nm) of template have been used for preparation of PPV nanotubes and nanorods [70]. PPV nanorods have been successfully deposited in 10 nm pores [70] indicating that the vaporised monomer has a size less than 10 nm. A schematic illustration of the proposed formation of PPV nanotubes grown from the tilted template is presented in Figure 6-15. At a template angle of 30°, a small amount of vaporised monomer diffuses up to 3 µm into the pore. The total thickness of the porous alumina template is about 60 µm. Due to the limited extent of diffusion; the PPV nanotubes exhibit an irregular shape. This hypothesis is supported by Figure 6-14, where it can be seen that the bottom structure of the nanotube is very irregular and different to the top.

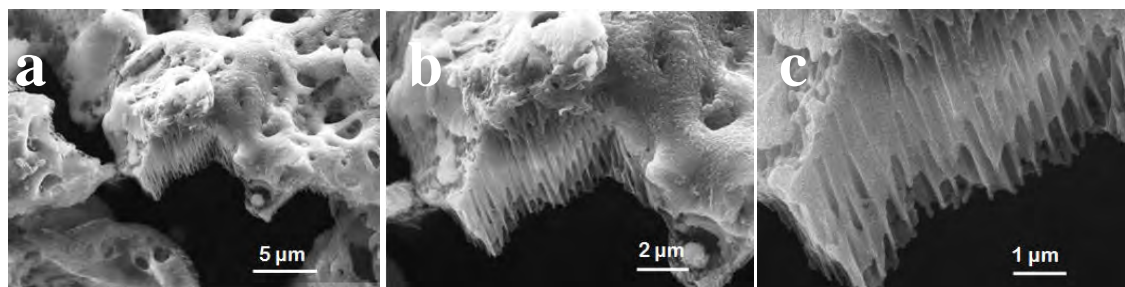


Figure 6-14: SEM image of PPV (a-c) deposited at 30° of alumina template angle after being isolated from template

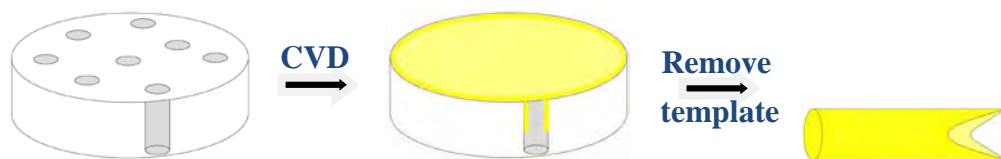


Figure 6-15: Schematic illustration of the proposed formation of PPV nanotubes synthesis at deposition template angle of 30° Angle at 45°

6.3.2.3 Angle of 45°

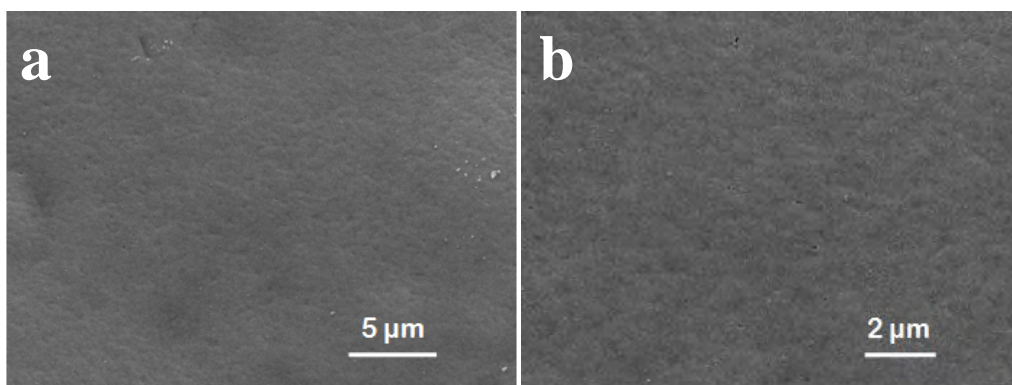


Figure 6-16: SEM image of PPV deposited at 45° of alumina template angle of (a) lower magnification & (b) higher magnification

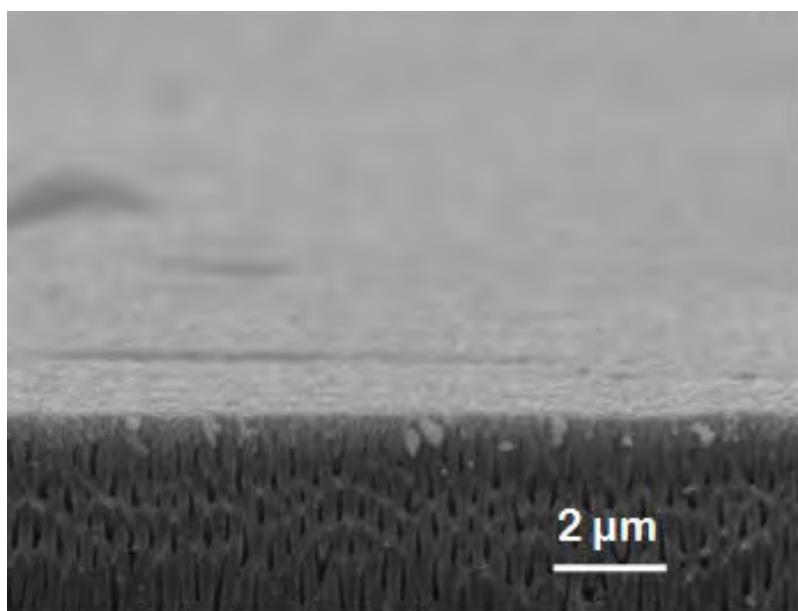


Figure 6-17: Cross-section SEM image of PPV deposited at 45° of alumina template angle

Figure 6-16 shows a slightly different surface morphology of PPV to that displayed in Figure 6-6 and Figure 6-12. The absence of any cactus-like PPV nanostructures in the top view SEM image indicates that the vaporised monomer has a similar behavior to 30° at the new tilted angle. Further evidence of similar behavior is supported by the diffusion of reactive monomer into nanopores (Figure 6-17). In addition, the identical peak intensity in PL spectrum indicates that the polymer chains are of a shorter length and are contacted with alumina surface of the tilted template [215].

Unlike the surface morphology observed at 30° , the template tilted at 45° has smoother film coverage. The latter comprises a wave-like surface pattern which may be attributable to a shadowing effect [21] resulting in isolated regions of the template surface being unreachable by the vaporised monomer. Moreover, since the template is tilted, some of the template areas which are facing towards the substrate holder will be impinged by the monomer flux at different times.

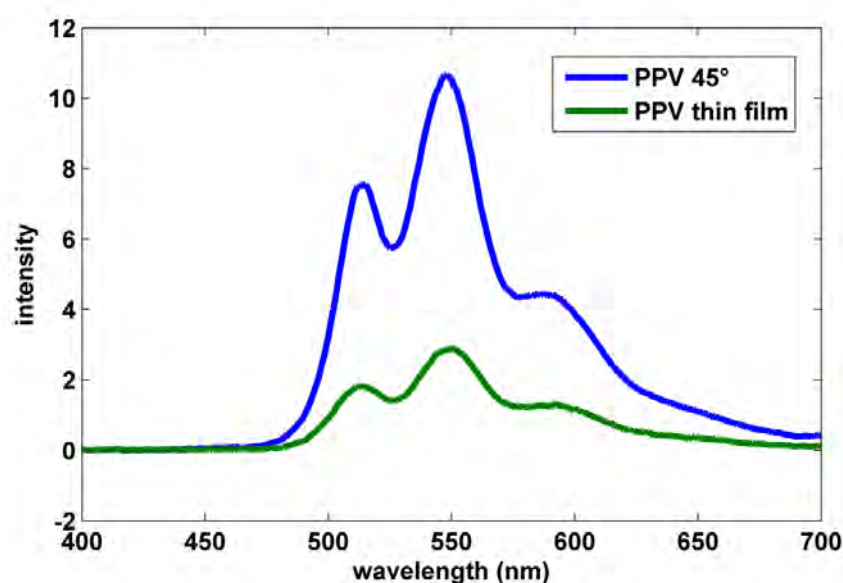


Figure 6-18: Photoluminescence spectra (excitation at 350nm) of PPV thin film deposited on quartz and PPV deposited on alumina template at 45°

Figure 6-18 shows the PL spectra of a PPV film deposited at a 45° template angle and a PPV thin film that has been deposited on quartz. Both spectra have identical peak positions, due to the similarity in the PL spectra, it appears that PPV deposited at a 45° template angle exhibits a similar morphology to that of a PPV thin film on quartz.

However, the thickness of both PPV films is different, as can be distinguished from the peak intensity [218, 219].

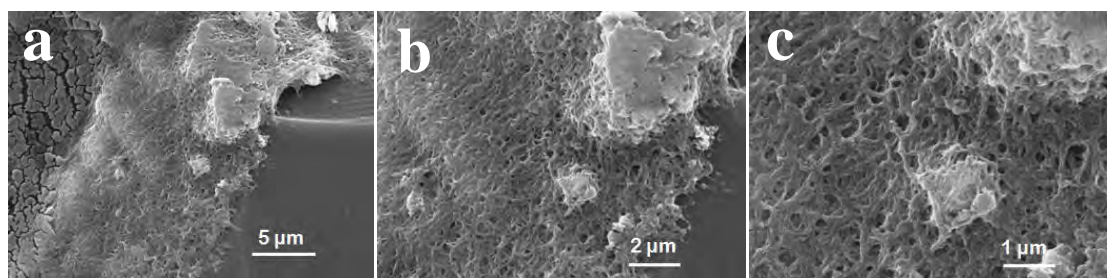


Figure 6-19: SEM image of PPV (a-c) deposited at 45° of alumina template angle after being isolated from template

The structure of PPV after the dissolution of alumina template is shown in Figure 6-19(a-c). Interestingly, PPV nanotubes were not observed in this film, but rather, bulk PPV with a web-like structure is seen. Therefore, it would appear that the vaporised monomer has deposited as a bulk PPV layers of low uniformity. Generally, a bulk PPV film will form with high uniformity if a solid structure without any web-like pattern is obtained. However, in this case, PPV with an undesired structure was formed from the non-ideal angle of deposition.

6.3.2.4 Angle at 60°

Figure 6-20 shows that, for the template aligned at 60°, a rougher surface morphology with a lack of uniform coverage is obtained. It is possible that a rougher polymer film is expected as a result of deposition via the vapor deposition polymerisation technique. It is well known that polymer chains comprise of two active ends. Instability of polymer during the deposition process can occur if monomer reaches both active ends of polymer chains, which leads to a roughening of the surface [222]. At this larger angle, the wave-like pattern observed from the top view SEM image is more marked with not of all template surfaces being perfectly coated.

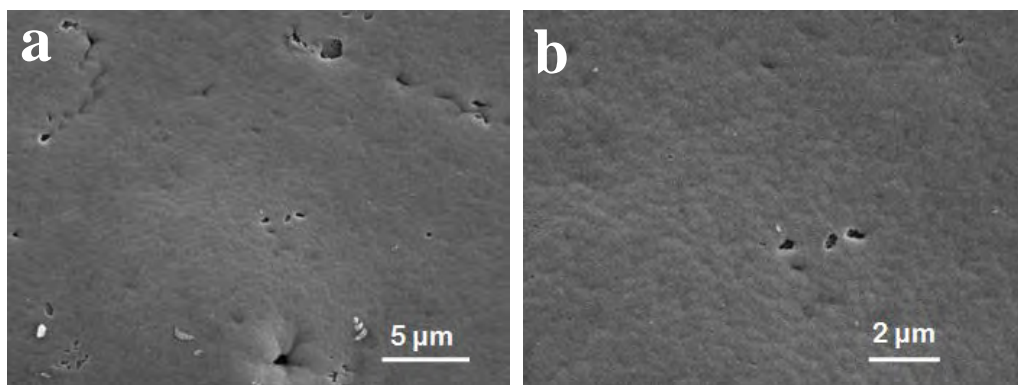


Figure 6-20: SEM image of PPV deposited at 60° of alumina template angle of (a) lower magnification & (b) higher magnification

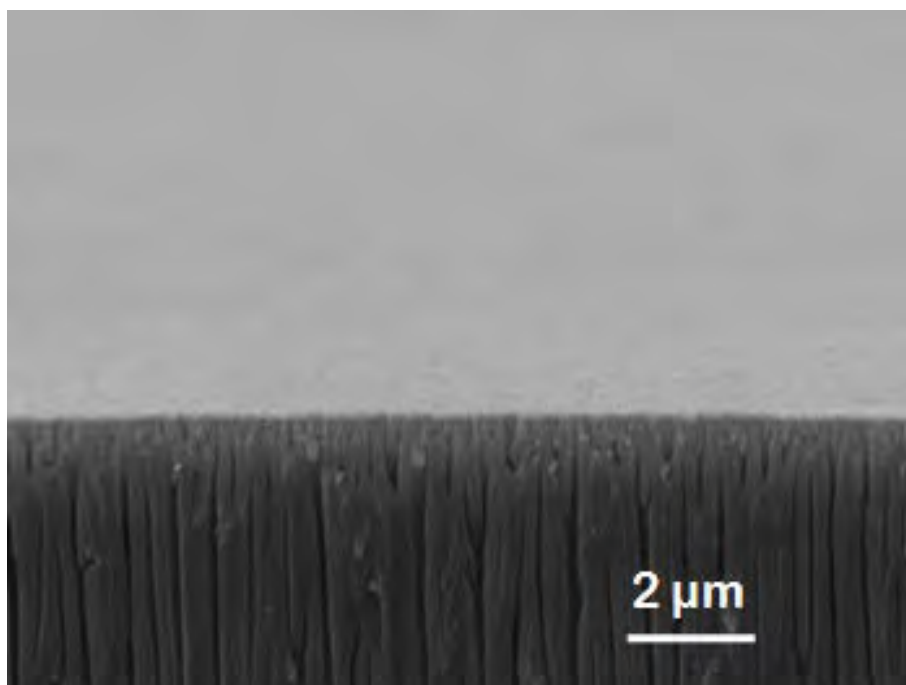


Figure 6-21: Cross-section SEM image of PPV deposited at 60° of alumina template angle

Figure 6-21 shows the cross-section SEM image of PPV deposited at 60°. A similar structure of PPV deposition is seen to that observed at other angles. The vaporised monomer has obviously deposited on top of the template rather than into the pores. A thinner layer deposited at 60° is indicated by the SEM images of the PPV isolated from the template shown in Figure 6-22(a-c). Compared to that shown in Figure 6-19, less vaporised monomer has impinged on the template surface at 60° which is supported by the reduced magnitude of the PL measurements. At this angle, no PPV nanostructures

such as shown in Figure 6-10 and Figure 6-14 are observed. In addition, the PL spectrum of PPV deposited at 60° of template angle shows the same characteristic peaks as the PPV thin film deposited on quartz except the peak 1/peak 2 ratio is different (Figure 6-23).

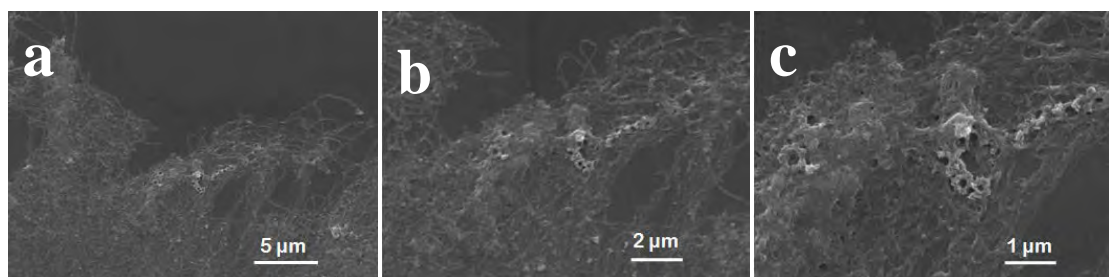


Figure 6-22: SEM image of PPV (a-c) deposited at 60° of alumina template angle after being isolated from template

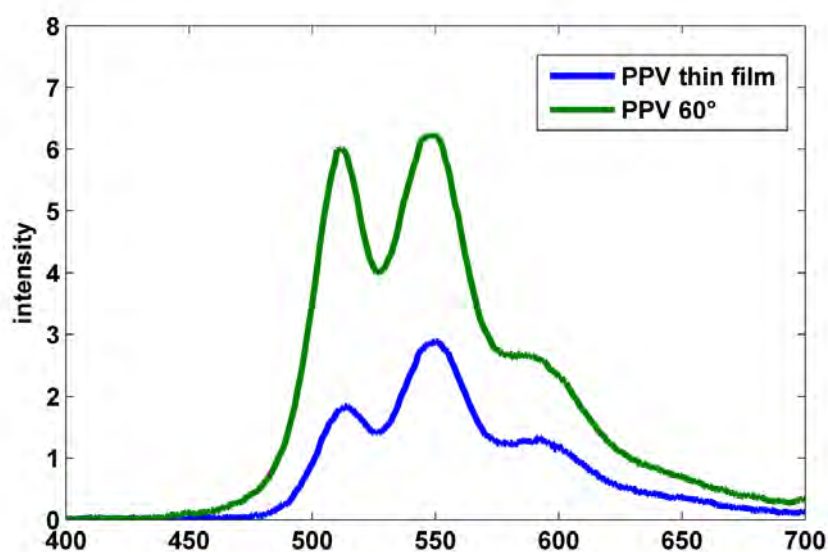


Figure 6-23: Photoluminescence spectra (excitation at 350 nm) of PPV thin film deposited on quartz and PPV deposited on alumina template at 60°

6.3.2.5 Vertical angle (90°)

Figure 6-4 shows a similarity of in both the intensity and PL emission peak between the template that tilted at 60° and 90°. This indicates that a similar PPV layer thickness has been deposited when the template is being tilted between 60° and 90°. However, the

surface morphology of the PPV shows distinctly different structure. The creation of additional PPV layer on the top of the pores is observed when tilting the template at 60° , this does not happen for template tilted at 90° . Demirel et al [21] has reported on the formation of an extra polymer layer deposited outside of the pores for similar depositions.

In contrast with the other tilted angles, none of the fibrous cactus-like nanostructures or wave-like pattern was observed on the vertical template. As shown in Figure 6-24 the porous structure of template can still be seen after PPV deposition. From the top view SEM image, the surface morphology of the porous template with PPV deposited in the vertical position is comparable to that without PPV (Figure 2-4). However, the only feature that differentiates both templates after and prior to PPV deposition is the size of the pores, with a smaller pore size seen after PPV deposition. This observation suggests that vaporised monomer has diffused through the pores [21] when the vapour flux is perpendicular to the template. Polymerisation has been initiated on the pore walls which leads to the formation of porous nanostructures [21].

However, patches of unknown material can also be seen lying on the top of template surface. It seems reasonable to speculate that these features arise from the deposition of residual impurities upon thermal conversion. Residues in the CVD polymer can be incorporated into the surface film due to fragmentation and dimerization of by-products during pyrolysis [200]. A template that is in the vertical position is more likely to collect the high concentration of vaporised monomer as well as the residue of side reactions during pyrolysis which might be contained in the vaporised monomer stream.

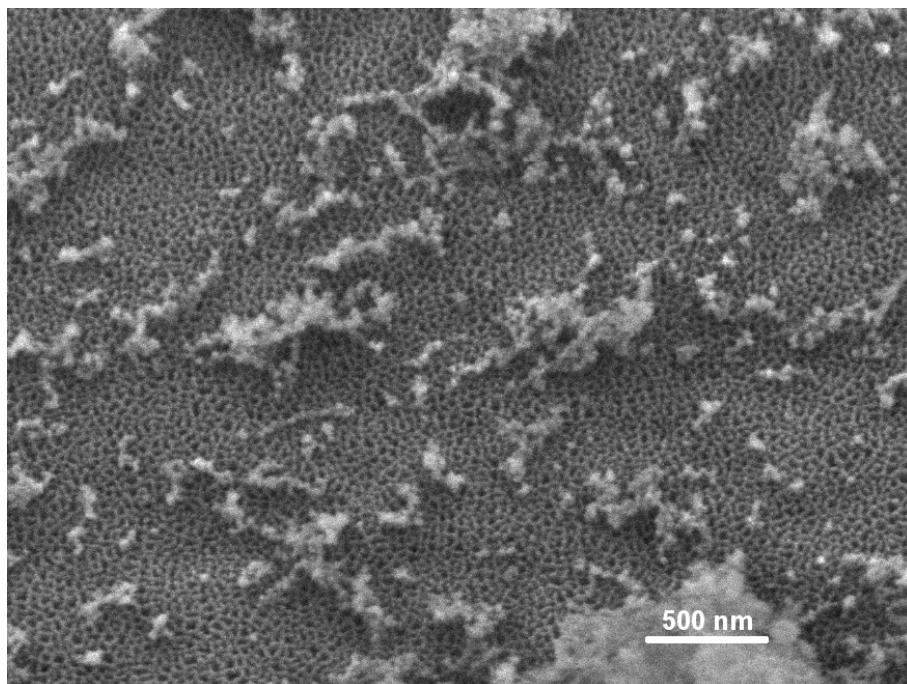


Figure 6-24: SEM image of PPV deposited on vertical alumina

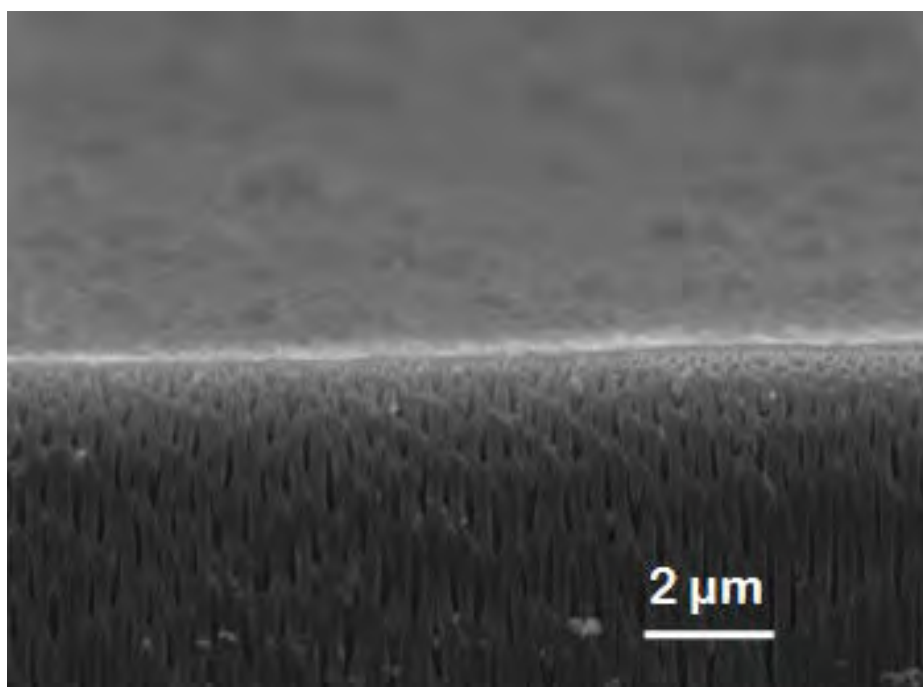


Figure 6-25: Cross-section SEM images of PPV deposited on vertical alumina template

Distinct colour differences between the two templates (0° and 90°) were observed after thermal conversion. PPV on the template with the vapour flux parallel to the template (0°) has an intense yellowish colour compared to that with the vapour flux flowing perpendicular to the template (90°). This observation is consistent with the yellow film colour observed for PPV by Vaeth et al [71]. They found that the transparent and colourless precursor polymer film changed to yellow upon thermal conversion. The less intense yellow colour obtained from template at 90° might be due to deposition of PPV inside the pores rather than on the top surface.

As the vaporised monomer flows from the vaporisation zone to the deposition zone, only a surface with temperature less than 95°C [71] within the deposition zone is suitable for condensation and polymerisation. Vaporised monomer that does not meet this desired temperature will leave the deposition zone and be trapped in the cold trap. Indeed a white or light yellow powder is always seen inside the cold trap. On the other hand, a template that has been positioned horizontal to the flow collect only the desired precursor polymer since vaporised monomer can flow parallel to the template without any obstacles. As such, only vaporised monomer that satisfies the strict deposition temperature criterion will accumulate on the template surface.

A template in the vertical position is more likely to be in contact with all of the vapour that flows within the deposition zone. Residuals that should be carried to the cold trap can be blocked by the template since the vapour flux is perpendicular to the template. This is likely leads to the accumulation of the unknown impurities shown in Figure 6-25. However, a template that has been positioned in the vertical position is more suited for PPV nanotube formation. Indeed, PPV nanotubes are observed in the film after being isolated from the alumina template, as shown in Figure 6-26(a-d).

PPV nanotubes of varying diameter and wall thickness were obtained. These nanotubes have created a hexagonal structure with diameter and wall thickness ranges from 125 to 250 nm and 25 to 75 nm, respectively. Interestingly, this result shows that the PPV nanotubes have a larger diameter than the original template pore diameter, and thus the hexagonal structure of the nanotubes has expanded during the template removal process. Clearly a template that is perpendicular to the vapour flux collects precursor in the inner surface of pores [11] rather than lying as a bulk film on the top surface of the template.

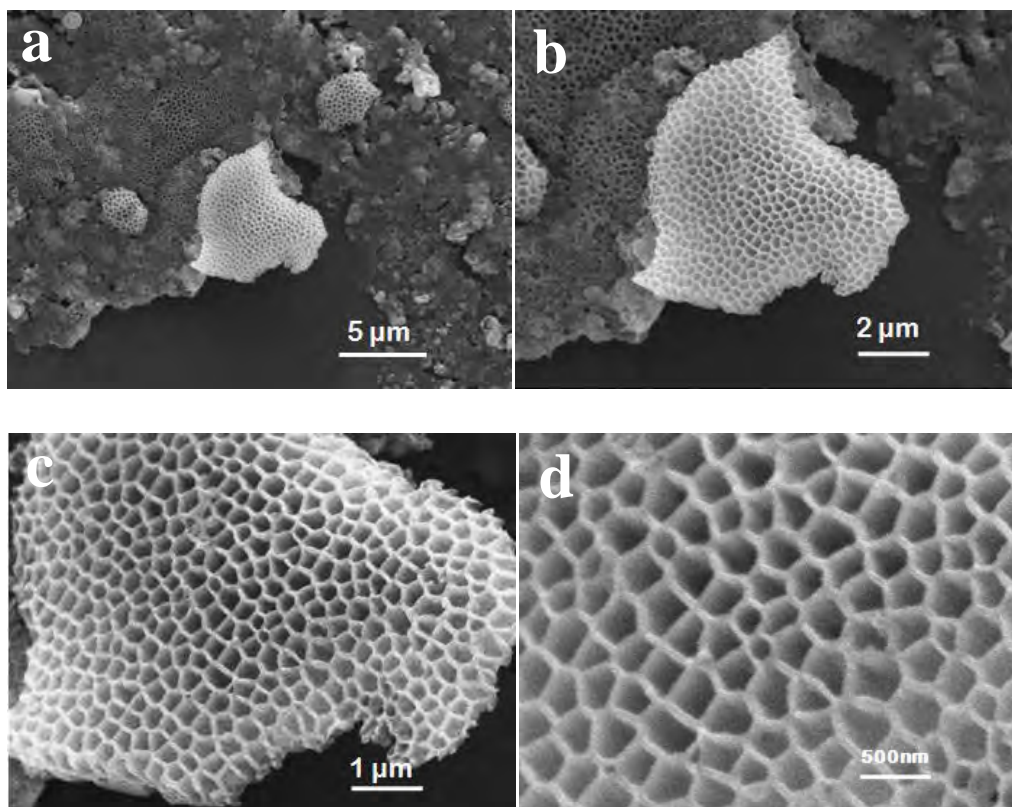


Figure 6-26: SEM image of PPV (a-d) deposited at 90° of alumina template angle after being isolated from template

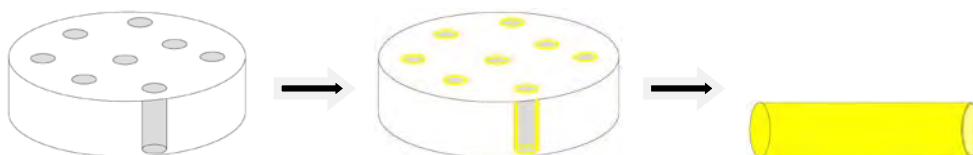


Figure 6-27: Schematic illustration of the proposed formation of PPV nanotubes synthesis at deposition template angle of 90°

The proposed formation of PPV nanotube grown from the vertical standing template which is perpendicular to the flux monomer is displayed in Figure 6-27. Precursor PPV is first accumulated around the pores without blocking them and diffuses deeper into the inner surface of pores. Compared to the polymer nanotube (Figure 6-2) prepared by Lee et al [11], the PPV nanotubes obtained in our work have a denser structure distribution with no gap between walls seen between one tube to another. Indeed, the close proximity exhibited by these nanotubes most likely drives the formation of the observed dense hexagonal structure.

6.3.3 Effect of nanostructures on optical emission

It is well known that photoinduced increasing and decreasing PL behaviour is dependent on the polymer film thickness and on the existence of crosslinking in the polymer network structure [219]. As shown in Figure 6-28, significant differences are seen between the emission characteristics of PPV nanostructures deposited in horizontal alumina template and the PPV thin film. At peak 1 of the emission peak (which is assigned to the 0-0 transition), the photoinduced signal is improved as the PPV is changed from a film to nanostructure. The intensity of PPV's thin film emission peak is reduced which may attributed to the increasing formation of nonemissive inter-chain excimers [219].

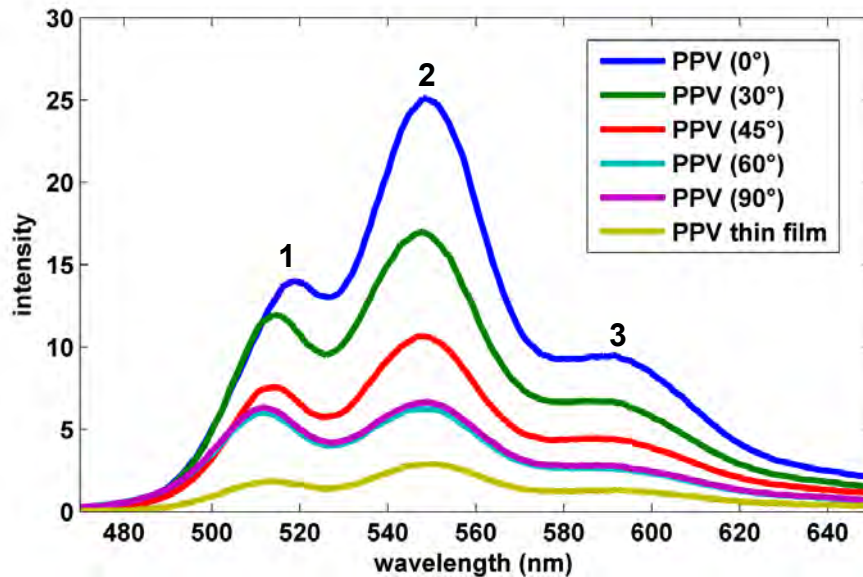


Figure 6-28: Photoluminescence spectra (excitation at 350 nm) of PPV thin film deposited on quartz and PPV deposited at different alumina template angles

The red shift of the emission peak of the PPV nanostructure also indicates that it has an increase conjugation length, and optimum bandgap and density of states [7]. The conformation of the PPV chains in the nanostructured formation is in the form of a bunch of polymer chains. PPV nanostructure that was observed on horizontal alumina template has shown no isolation of the conjugated polymer chains. This claim is supported by the work reported by Qi et al [215] which has observed on the blue shift of emission peak due to the isolation of polymer chain and interaction to the alumina surface.

The interaction between polymer and the alumina surface was reported to occur during the deposition of (poly(2-methoxy-5-(2'-ethyl-hexyloxy)-*p*-phenylene vinylene) (MEH-PPV) on alumina template [215]. The possible interaction is likely to occur because the polymer and alumina comprise Lewis base aromatic rings and Lewis acid aluminum and Bronstead acid surface hydroxyl groups, respectively. However, in the present work, the PPV nanostructures have shown no interaction with the alumina surface. Given the red shift to longer wavelength, it would appear that the conjugated polymer chains only build their structure laterally on the alumina surface rather than being diffuse or infiltrate into the pores [220].

The position of alumina template respective to incoming vaporised monomer has contributed to the extent of diffusion into nanopores and hence, the initiation of polymerisation in the nanoporous template. As reported by Demirel et al [21], parylene nanofibres were grown via template by adjusting the direction of vapour flux to the surface of the template. The height of nanofibre can be controlled which is depend on the deposition angle (α). In conjunction, the optical emission of different PPV structures obtained from different deposition angles helps to clarify the deposition. Better, or more desired, photoluminescence properties of nanostructures made of conjugated polymers can be tuned through the deposition angle between vaporised monomer flux and template (or deposition surface).

6.4 CONCLUSIONS

In conclusion, CVD polymerisation of PPV has been successfully implemented on a porous alumina template. Differences in surface morphology are observed for the different template angles. In particular, for a template that has been positioned horizontally with respect to the substrate holder surface, fibre-like PPV nanostructures with diameters ranging from 50 nm to 250 nm are observed. An optimum optical emission is exhibited from the fibrous PPV nanostructures, shown by the occurrence of a red shift in their PL spectra. After being isolated from the alumina porous template, the morphology of the fibrous PPV nanostructures is preserved. The unique PPV structure obtained from the horizontal alumina template before and after the dissolution of template has the potential to be beneficial for electronic applications due their height and diameter dimension.

In addition, PPV nanotubes were synthesised at 30° and 90° of template angle after the dissolution of template. Two types of nanotubes were observed at two different angles, with 90° producing new perfect nanotube morphology. However, shorter PPV nanotubes can be achieved by tilting the angle to 30° as the small amount of vaporised monomer diffuses into the template pores. This angle could be of beneficial in controlling nanotube height, which is crucial in device fabrication. Therefore, the production of desired polymer nanostructures is possible simply by tilting a template to an angle α with respect to a monomer flux.

7 SUMMARY AND FURTHER WORK

7.1 SUMMARY

The chemical vapour deposition (CVD) technique has the potential to synthesise nanostructures which would benefit optoelectronic devices and organic photovoltaics (OPVs). In this work, three different nanostructures (namely multiwalled carbon nanotube (MWCNT), indium oxide encapsulated by carbon layer and PPV nanostructures) have been realised via CVD. The work presented in this thesis has shown that the fabrication of such nanostructures through the technique of CVD has potential applications for the solvent-less fabrication of OPV devices by demonstrating a photovoltaic response from PPV nanofilms deposited in this way.

We have shown that system pressure is the key to controlling the different morphology of nanostructures grown by CVD. Indium, which originates in the indium tin oxide (ITO) substrate, is capable of diffusing into the nanostructure at 400 Torr and 450°C, resulting in the growth of indium oxide nanowires. In addition, a thicker interface layer of amorphous carbon is deposited at higher pressure of 400 Torr. H₂ plasma treatment applied to the amorphous carbon layer causes the depletion of both the interface and nanostructured layers.

The thickness of the amorphous carbon and MWCNT layers can be controlled by varying the pressure. At 100 Torr, a thinner amorphous carbon layer of 200 nm is deposited, compared to the one at 400 Torr which was 2 µm in thickness. On top of that, at 100 Torr, MWCNT with the average length of 400 nm is sparsely grown. Increasing the pressure to 300 Torr also results in MWCNTs but of different length. The length of individual nanotubes can reach a few microns. This length is too long for OPV fabrication, where film thicknesses of a few 100 nm are used to provide high absorbance and adequate charge transport [8].

In addition to carbon and metal oxide nanostructure growth, we have also used CVD to synthesise polymer nanostructures. A PPV nanofilm has been incorporated as an electron donor layer into the bilayer OPV. In spite of the low efficiency, the integration of chemically vapour deposited PPV into OPV is shown as a proof-of-principle demonstration of a photovoltaic response.

In addition to pressure, the growth of a CVD deposit also depends on transport in the tube flow. To examine this, PPV nanostructures were synthesised by placing the porous alumina template at different angles to the flow. The PPV nanostructure morphology, tube diameter and length have been found to vary with angle.

Consequently, the work presented here represents a step forward in the knowledge of the CVD of nanostructures; which has in turn allowed an extension in understanding of the process of producing carbon, metal oxide and polymer nanostructures.

7.2 FURTHER WORK

The integration of carbon and polymer nanostructures into OPV synthesised on ITO and alumina porous template, respectively, would be particularly worthwhile as future work. High optical transparency of carbon nanostructures grown onto ITO has already been reported [8] for a thickness of less than 200 nm. The work presented here used a total thickness of 600 nm which accounted for both the interface and nanostructured layer. However, the controlling pressure is an essential parameter in producing the desired thickness. Pressures lower than 100 Torr would be likely to deposit carbon nanostructures which would lie within an acceptable thickness.

Indium and tin particles have been observed on the surface of ITO upon heating above 400°C. It has also been observed that at these temperatures indium can incorporate into the carbon nanostructures grown via CVD. As such, it would be interesting to try to use these metal nanoparticles directly as the catalyst for nanotube growth.

PPV nanofilms synthesised via CVD were incorporated into an OPV. A low power conversion efficiency was recorded but this work acts as a proof that PPV formed via CVD can be used in this fashion. Since various types of PPV nanostructures can be grown in a porous alumina template by varying the angle of the template, future work might consider the integration of PPV nanostructures isolated from these templates into OPVs. It is worth trying to study the effect of different PPV nanostructures obtained at different angles upon the performance of OPV.

Additionally, the subsequent step to develop a synthesis of an electron acceptor via CVD may be warranted. At the moment, an electron acceptor layer is spin-coated on the PPV layer, which requires the use of solvent. An electron acceptor such as PCBM has not been synthesised via CVD. The advantage of CVD in depositing of the conformal layer (with less contamination) would lead to a fully CVD based OPV fabrication.

REFERENCES

1. Andre', J.A. and W.J. Blau, *Enhanced device performance using different carbon nanotube types in polymer photovoltaic devices*. Carbon, 2008. **46**: p. 2067-2075.
2. Chen, K.C., et al., *Low-temperature CVD growth of carbon nanotubes for field emission application*. Diamond & Related Materials, 2007. **16**: p. 566-569.
3. Fan, S., et al., *Self-oriented regular arrays of carbon nanotubes and their field emission properties*. Science, 1999. **283**(512).
4. Hsieh, C.T., et al., *Formation and field-emission properties of carbon nanofibers by a simplified thermal growth* Rev. Adv. Mater. Sci, 2003. **5**: p. 459-463.
5. Jang, H.S., et al., *Field emission from cone-like single crystalline indium tin oxide nanorods*. Materials Letters, 2005. **59**: p. 1526-1529.
6. Ma, W., et al., *Thermally stable, efficient polymer solar cells with nanoscale control of the interpenetrating network morphology*. Adv. Funct. Mater., 2005. **15**: p. 1617-1622.
7. Massuyeau, F., et al., *Elaboration of conjugated polymer nanowires and nanotubes for tunable photoluminescence properties*. Nanotechnology, 2009. **20**.
8. Miller, A.J., et al., *Carbon nanotubes grown on $\text{In}_2\text{O}_3\text{:Sn}$ glass as large area electrodes for organic photovoltaics*. Applied Physics Letters, 2007. **90**.
9. Wei, J., et al., *Double-walled carbon nanotube solar cells*. Nano Letters, 2007. **7**(8): p. 2317 - 2321.
10. Das, I. and S.A. Ansari, *Nanomaterials in science and nanotechnology*. Journal of Scientific & Industrial Research, 2009. **68**: p. 657-667.
11. Lee, K.R., et al., *Poly(2,5-thienylene vinylene) in Nano Shapes by CVD Polymerisation*. Macromol. Rapid Commun., 2007. **28**: p. 1057-1061.
12. Rao, R., K.G. Eyink, and B. Maruyama, *Single-walled carbon nanotube growth from liquid gallium and indium*. Carbon, 2010. **48**: p. 3964-3973.
13. Turano, S.P., J.D. Flicker, and W.J. Ready, *Nanoscale coaxial cables produced from vertically aligned carbon nanotube arrays grown via chemical vapor deposition and coated with indium tin oxide via ion assisted deposition*. Carbon, 2008. **46**: p. 723-728.
14. Valentini, L. and J. M Kenny, *Novel approaches to developing carbon nanotube based polymer composites: Fundamental studies and nanotech applications*. Polymer, 2005. **46**: p. 6715-6718.

15. Wang, X., et al., *A novel route to multiwalled carbon nanotubes and carbon nanorods at low temperature*. J. Phys. Chem. B, 2002. **106**(5): p. 933-937.
16. Wang, Y., L. Lu, and F. Wu, *Indium tin oxide@carbon core-shell nanowire and jagged indium tin oxide nanowire*. Nanoscale Res Letter, 2010. **5**: p. 1682-1685.
17. Xiang, Y., et al., *Single crystalline and core-shell indium-catalyzed germanium nanowires - a systematic thermal CVD growth study*. Nanotechnology, 2009. **20**.
18. Alet, P.J., et al., *In situ generation of indium catalysts to grow crystalline silicon nanowires at low temperature on ITO*. Journal of Materials Chemistry, 2008. **18**: p. 5187-5189.
19. Chen, G., et al., *Growth of In₂O₃ nanowires catalyzed by Cu via a solid-liquid-solid mechanism*. Nanoscale Res Letter, 2010. **5**: p. 898-903.
20. Cuong, P.H., et al., *About the octopus-like growth mechanism of carbon nanofibers over graphite supported nickel catalyst*. Journal of Catalysis, 2006. **240**: p. 194-202.
21. Demirel, G., N. Malvadkar, and M.C. Demirel, *Template-based and template-free preparation of nanostructured parylene via oblique angle polymerization*. Thin Solid Films, 2010. **518**: p. 4252-4255.
22. Li, R., et al., *Aligned heterostructures of single-crystalline tin nanowires encapsulated in amorphous carbon nanotubes*. J. Phys. Chem. C, 2007. **111**: p. 9130-9135.
23. International Energy Agency, *Technology Roadmap - Solar Photovoltaic Energy*. 2010.
24. Chapin, D.M., C.S. Fuller, and G.L. Pearson, *A new silicon P-N junction photocell for converting solar radiation into electrical power*. Journal of Applied Physics, 1954. **25**: p. 676-677.
25. Kallmann, H. and M.Pope, *Photovoltaic effect in organic crystals*. J. Chem. Phys., 1959. **30**: p. 585-586.
26. Tang, C.W., *Two-layer organic photovoltaic cell*. Appl. Phys. Lett., 1986. **48**: p. 183.
27. Ayzner, A.L., et al., *Reappraising the need for bulk heterojunctions in polymer-fullerene photovoltaics: The role of carrier transport in all-solution-processed P3HT/PCBM bilayer solar cells*. J. Phys. Chem. C, 2009. **113**: p. 20050-20060.
28. Markov, D.E., *Excitonic processes in polymer-based optoelectronic devices*. PhD Thesis, 2006.
29. Blom, P.W.M., et al., *Device physics of polymer:fullerene bulk heterojunction solar cells*. Adv. Mater., 2007. **19**: p. 1551-1566.

30. Haugeneder, A., et al., *Exciton diffusion and dissociation in conjugated polymer/fullerene blends and heterostructures*. The American Physical Society, 1999. **59**(23).
31. *Intergovernmental Panel on Climate Changes*, in *Third assessment report - climate changes*. 2001.
32. Yu, G. and A.J. Heeger, *Charge separation and photovoltaic conversion in polymer composites with internal donor/acceptor heterojunctions*. J. Appl. Phys., 1995. **78**: p. 4510.
33. Shaheen, S.E., C.J. Brabec, and N.S. Sariciftci, *2.5% efficient organic plastic solar cells*. Applied Physics Letters, 2001. **78**(6).
34. Li, G., et al., *High-efficiency solution processable polymer photovoltaic cells by self-organization of polymer blends*. Nature Mater., 2005. **4**: p. 864-868.
35. Kim, Y., et al., *Device annealing effect in organic solar cells with blends of regioregular poly(3-hexylthiophene) and soluble fullerene*. Appl. Phys. Lett., 2005. **86**.
36. Liang, Y., et al., *For the bright future - Bulk heterojunction polymer solar cells with power conversion efficiency of 7.4%*. Adv. Mater., 2010. **22**: p. 1-4.
37. Al-Ibrahim, M., et al., Sol. Energy Mater. & Solar Cells, 2005. **85**(13).
38. Bundgaard, E. and F.C. Krebs, *Low band gap polymers for organic photovoltaics*. Solar Energy Materials & Solar Cells, 2007. **91**: p. 954-985.
39. Park, S.H., et al., *Bulk heterojunction solar cells with internal quantum efficiency approaching 100%*. Nature Photonics., 2009. **3**.
40. Vanlaeke, P., et al., *Polythiophene based bulk heterojunction solar cells: Morphology and its implications*. Thin Solid Films, 2006. **511-512**: p. 358-361.
41. Forrest, S.R., *The limits to organic photovoltaic cell efficiency*. MRS Bulletin, 2005. **30**.
42. Marsh, R.A., C. Groves, and N.C. Greenham, *A microscopic model for the behaviour of nanostructured organic photovoltaic devices*. Journal of Applied Physics, 2007. **101**.
43. Yang, F. and S.R. Forrest, *Photocurrent generation in nanostructured organic solar cells*. American Chemical Society, 2008. **2**(5).
44. Lock, J.P., et al., *Electrochemical investigation of PEDOT films deposited via CVD for electrochromic applications*. Synthetic Metals, 2007. **157**: p. 894-898.

45. Amama, P.B., et al., *XPS and Raman characterization of single-walled carbon nanotubes grown from pretreated Fe₂O₃ nanoparticles*. J. Phys. D: Appl. Phys., 2008. **41**: p. 165306.
46. Deck, C.P. and K. Vecchio, *Growth mechanism of vapor phase CVD-grown multi-walled carbon nanotubes*. Carbon, 2005. **43**: p. 2608-2617.
47. Gohel, A., et al., *Field emission properties of N₂ and Ar plasma-treated multi-wall carbon nanotubes*. Carbon, 2005. **43**: p. 2530-2535.
48. Gohier, A., et al., *Carbon nanotube growth mechanism switches from tip- to base-growth with decreasing catalyst particle size*. Carbon, 2008. **46**: p. 1331 - 1338.
49. Gupta, M. and K.K. Gleason, *Large-scale initiated chemical vapor deposition of poly (glycidyl methacrylate) thin films*. Thin Solid Films, 2006. **515**: p. 1579-1584.
50. Holloway, C., et al., *Morphology study of vertically aligned carbon nanotubes*. Canadian Undergraduate Physics Journal, 2007.
51. Je, H.L. and J. Kanicki, *ITO surface ball formation induced by atomic hydrogen in PECVD and HW-CVD tools*. Thin Solid Films, 1997. **304**: p. 123-129.
52. Konya, Z., et al., *XPS study of multiwall carbon nanotube synthesis on Ni-, V-, and Ni, V-ZSM-5 catalysts*. Applied Catalysis A: General, 2004. **260**: p. 55-61.
53. Lau, K.K.S., et al., *Polymeric nanocoatings by hot-wire chemical vapor deposition (HWCVD)*. Thin Solid Films, 2006. **501**: p. 211 - 215.
54. Martin, T.P., et al., *Initiated chemical vapor deposition (iCVD) of polymeric nanocoatings*. Surface & Coatings Technology, 2007. **201**: p. 9400-9405.
55. McKee, G.S.B., C.P. Deck, and K.S. Vecchio, *Dimensional control of multi-walled carbon nanotubes in floating-catalyst CVD synthesis*. Carbon, 2009. **47**: p. 2085-2094.
56. Okazaki, N., et al., *Synthesis of carbon tubule nanocoils using Fe-In-Sn-O fine particles as catalysts*. J. Phys. Chem. B, 2005. **109**: p. 17366-17371.
57. Oncel, C. and Y. Yurum, *Carbon nanotube synthesis via the catalytic CVD method: A review on the effect of reaction parameters*. Fullerenes, Nanotubes, and Carbon Nanostructures, 2006. **14**: p. 17-37.
58. O'Shaughnessy, W.S., et al., *Stable biopassive insulation synthesized by initiated chemical vapor deposition of poly(1,3,5-trivinyltrimethylcyclotrisiloxane)*. Biomacromolecules, 2007. **8**(8): p. 2564-2570.

59. Tenhaeff, W.E. and K.K. Gleason, *Initiated and Oxidative Chemical Vapor Deposition of Polymeric Thin Films: iCVD and oCVD*. Adv. Funct. Mater., 2008. **18**: p. 979.
60. Yang, G., et al., *Two types of carbon nanocomposite: Graphite encapsulated iron nanoparticles and thin carbon nanotubes supported on thick carbon nanotubes, synthesized using PECVD*. Journal of Solid State Chemistry, 2009. **182**: p. 966-972.
61. Yun, Y.H., et al., *Growth mechanism of long aligned multiwall carbon nanotube arrays by water-assisted chemical vapor deposition*. J. Phys. Chem. B, 2006. **110**(47): p. 23920-23925.
62. Paradise, M. and T. Goswami, *Carbon nanotubes - Production and industrial applications*. Materials and Design, 2007. **28**: p. 1477-1489
63. Kaempgen, M. and S. Roth, *Transparent and flexible carbon nanotube/polyaniline pH sensors*. Journal of Electroanalytical Chemistry, 2006. **586**: p. 72-76.
64. Park, S.Y., et al., *Effect of hybrid carbon nanotubes-bimetallic composite particles on the performance of polymer solar cells*. Solar Energy Materials & Solar Cells, 2010. **94**: p. 750-754.
65. Agrawal, S., et al., *Directed growth and electrical-transport properties of carbon nanotube architectures on indium tin oxide films on silicon-based substrates*. Adv. Funct. Mater., 2005. **15**(12): p. 1922-1926.
66. Tadatsugu, M., *Transparent conducting oxide semiconductors for transparent electrodes*. Semicond. Sci. Technol., 2005. **20**(4): p. S35-S44.
67. Berne'de, J.C., et al., *Ultra-thin metal layer passivation of the transparent conductive anode in organic solar cells*. Solar Energy Materials & Solar Cells, 2008. **92**: p. 1508-1515.
68. Ulbricht, R., et al., *Polymeric solar cells with oriented and strong transparent carbon nanotube anode*. phys. stat. sol. (b), 2006. **243**(13): p. 3528-3532.
69. Senkevich, J.J. and S.B. Desu, *Poly_chloro-p-xylylene/rSiO multilayer thin films deposited near-room temperature by thermal CVD*. Thin Solid Films, 1998. **322**: p. 148-157.
70. Kim, K. and J.I. Jin, *Preparation of PPV nanotubes and nanorods and carbonized products derived therefrom*. Nano Letters, 2001. **1**(11): p. 631-636.
71. Vaeth, K.M. and K.F. Jensen, *Chemical vapor deposition of thin polymer films used in polymer-based light emitting diodes*. Advance Materials, 1997. **9**(6).

72. Iwatsuki, S., M. Kubo, and T. Kumeuchi, *New method for preparation of poly (phenylene-vinylene) film*. Chem. Lett., 1991. **20**: p. 1071.
73. Staring, E.G.J., et al., *Chemical vapour deposition of poly(1,4-phenylenevinylene) films*. Synth. Met., 1994. **67**(71).
74. Schafer, O., et al., *Poly(p-phenylenevinylene) by chemical vapor deposition: synthesis, structural evaluation, glass transition, electroluminescence and photoluminescence*. Synth. Met., 1996. **82**.
75. Limb, *Growth of fluorocarbon polymer thin films with high CF_{sub}.2 fractions and low dangling bond concentrations by thermal chemical vapor deposition*. Appl. Phys. Lett., 1996. **68**(20): p. 2810-2812.
76. Chen, X. and M. Anthamattan, *Multicomponent vapor deposition polymerization of poly (methyl methacrylate) in an axisymmetric vacuum reactor*. Polymer, 2008. **49**: p. 1823-1830.
77. Jarzabek, B., et al., *Optical properties of amorphous polyazomethine thin films*. Journal of Non-Crystalline Solids, 2006. **352**: p. 1660-1662.
78. Holt, L., J.M. Leger, and S.A. Carter, *Solid-state electrochromic devices based on poly phenylene vinylene polymers*. Applied Physics Letters, 2005. **86**: p. 123504.
79. Moses, D., et al., *Singlet exciton binding energy in poly(phenylene vinylene)*. 2001.
80. Wang, M. and X. Wang, *PPV/TiO₂ hybrid composites prepared from PPV precursor reaction in aqueous media and their application in solar cells*. Polymer, 2008. **49**: p. 1587-1593.
81. Halls, J.J.M. and R.H. Friend, *The photovoltaic effect in a poly(p-phenylenevinylene) / perylene heterojunction*. Synthetic Metals, 1997. **85**: p. 1307-1308.
82. Brabec, C.J., et al., *Photoactive blends of PPV with methanofullerenes from a novel precursor: Photophysics and device performance*. J. Phys. Chem. B, 2001. **105**: p. 1528-1536.
83. Klinke, C., J.M. Bonard, and K. Kern, *Comparative study of the catalytic growth of patterned carbon nanotube films*. Surface Science, 2001. **492**: p. 195-201.
84. Ruban, A., et al., *Surface electronic structure and reactivity of transition and noble metals*. Journal of Molecular Catalysis A: Chemical 1997. **115**: p. 421-429.
85. Zielinski, R.E. and D.T. Grow, *An iron catalyst for CVD of methane on carbon fibers*. Carbon, 1992. **30**(2): p. 295-299.

86. Hernadi, K., et al., *Fe-catalyzed carbon nanotube formation*. Carbon, 1996. **34**(10): p. 1249-1257.
87. Li, W.Z., et al., *Large-scale synthesis of aligned carbon nanotubes*. Science, 1996. **274**.
88. Nikolaev, P., et al., *Gas-phase catalytic growth of single-walled carbon nanotubes from carbon monoxide*. Chemical Physics Letters, 1999. **313**: p. 91-97.
89. Cassell, A.M., et al., *Large scale CVD synthesis of single-walled carbon nanotubes*. J. Phys. Chem. B, 1999. **103**: p. 6484-6492.
90. Wessling, R.A. and R.G. Zimmerman, *U.S. Patent 3*. 1968. **401**(152).
91. Gilch, H.G. and W.L. Wheelwright, J. Polym. Sci. A-1, 1966. **4**: p. 1337.
92. Morosanu, C.E., *Thin Films by Chemical Vapor Deposition*. Vol. Chapter 5. 1990: Elsevier, New York.
93. Wang, Z.L., *Transmission electron microscopy of shape-controlled nanocrystals and their assemblies*. J. Phys. Chem. B, 2000. **104**: p. 1153-1175.
94. Topsoe, H. and eds. *Geometric factors in four point resistivity measurement* 2nd revised edition ed. 1968.
95. Prelipceanu, M., et al., *Study of thermal conversion and patterning of a new soluble poly (p-phenylenevinylene) (PPV) precursor*. Materials Science in Semiconductor Processing, 2007. **10**: p. 77-89.
96. Dharma, J. and A. Pisal, *Simple method of measuring the band gap energy value of TiO₂ in the powder from using a UV/Vis/NIR spectrometer*. Application Note, 2009.
97. Pichlert, K., et al., *Optical spectroscopy of highly ordered poly(p-phenylenevinylene)*. J. Phys. Condens. Matter., 1993. **5**: p. 7155-7172.
98. *Visible & UV spectroscopy*.
99. Toman, P., L. Skala, and J. Pospisil, *Conformational properties of poly(p-phenylenevinylene)*. Czechoslovak Journal of Physics, 1998. **48**(4).
100. Zyung, T. and J.J. Kim, *Photodegradation of poly(p-phenylenevinylene) by laser light at the peak wavelength of electroluminescence*. Appl. Phys. Lett., 1995. **67**(23).
101. Wang, Y., S. Serrano, and J.J.S. Aviles, *Raman characterization of carbon nanofibers prepared using electrospinning*. Synthetic Metals, 2003. **138**: p. 423-427.

102. Rothberg, L.J., et al., *Photophysics of phenylenevinylene polymers*. Synthetic Metals, 1996. **80**: p. 41-58.
103. Wakizaka, D., et al., *Hole transport in conducting ultrathin films of PEDOT/PSS prepared by layer-by-layer deposition technique*. Polymer, 2004. **45**: p. 8561-8565.
104. Huang, J., et al., *Influence of thermal treatment on the conductivity and morphology of PEDOT/PSS films*. Synthetic Metals, 2003. **139**: p. 569-572.
105. Ngamsinlapasathian, S., et al., *Doubled layered ITO/SnO₂ conducting glass for substrate of dye-sensitized solar cells*. Solar Energy Materials & Solar Cells, 2006. **90**: p. 2129-2140.
106. Sawada, M. and M. Higuchi, *Electrical properties of ITO films prepared by tin ion implantation in In₂O₃ film*. Thin Solid Films, 1998. **317**: p. 157-160.
107. Zhang, D.H. and H.L. ma, *Scattering mechanisms of charge carriers in transparent conducting oxide films*. Applied Physics A: Materials Science & Processing, 1996. **62**(5): p. 487-492.
108. Chong, M.K., K. Pita, and S.T.H. Silalahi, *Correlation between diffraction patterns and surface morphology to the model of oxygen diffusion into ITO films*. Materials Chemistry and Physics, 2009. **115**.
109. Guai, G.H., et al., *Effects of multiple heat treatment cycles on structure, optical and electrical properties of indium-tin-oxide thin films*. Surface & Coatings Technology, 2011. **205**: p. 2852-2856.
110. Tak, Y.H., et al., *Criteria for ITO (indium-tin-oxide) thin film as the bottom electrode of an organic light emitting diode*. Thin Solid Films, 2002. **411**: p. 12-16.
111. Park, S.K., et al., *Deposition of indium-tin-oxide films on polymer substrates for application in plastic-based flat panel displays*. Thin Solid Films, 2001. **397**(1-2): p. 49-55.
112. Zeng, L., C.W. Tang, and S.H. Chen, *Effects of active layer thickness and thermal annealing on polythiophene: Fullerene bulk heterojunction photovoltaic devices*. Applied Physics Letters, 2010. **97**.
113. Hu, Y., et al., *Effects of heat treatment on properties of ITO films prepared by rf magnetron sputtering*. Vacuum, 2004. **75**: p. 183-188.
114. Deng, W., et al., *Development of conductive transparent indium tin oxide (ITO) thin films deposited by direct current (DC) magnetron sputtering for photon-STM applications*. Appl. Phys. A, 2001. **72**: p. 595-601.
115. Hsu, W.L., et al., *Annealing induced refinement on optical transmission and electrical resistivity of indium tin oxide*. Chinese Optics Letters, 2009. **7**(3).

116. Kerkache, L., et al., *Physical properties of RF sputtered ITO thin films and annealing effect*. J. Phys. D: Appl. Phys., 2006. **39**: p. 184-189.
117. De, A., P.K. Biswas, and J. Manara, *Study of annealing time on sol-gel indium tin oxide films on glass*. Materials Characterization, 2007. **58**: p. 629-636.
118. Pokaipisit, A., M. Horprathum, and P. Limsuwan, *Influence of annealing temperature on the properties of ITO films prepared by electron beam evaporation and ion-assisted deposition*. Nat. Sci., 2008. **42**: p. 362-366.
119. Wang, R.X., et al., *The effect of thermal annealing on the properties of indium tin oxide thin films*. IEEE, 2005.
120. Yun, Y.H., et al., *Effects of sequential annealing processes on surface morphology and resistivity of Indium-Tin Oxide (ITO) thin films fabricated by chemical solution deposition*. Journal of Ceramic Processing Research 2005. **6**(3): p. 259-262.
121. Lin, T.C., S.C. Chang, and C.F. Chiu, *Annealing effect of ITO and ITO/Cu transparent conductive films in low pressure hydrogen atmosphere*. Materials Science and Engineering B, 2006. **129**: p. 39-42.
122. Castillo, S.J., et al., *Structural, optical and electrical characterization of In/CdS/glass thermally annealed system*. Thin Solid Films, 2000. **373**: p. 10-14.
123. Bayliss, S., *Nanostructured growth of carbon/ITO via Plasma Enhanced CVD for organic photovoltaics*. Honours Thesis 2009 (unpublished).
124. Chen, C.-M., Y.-C. Hsu, and S.-J. Cherng, *Effects of annealing conditions on the properties of TiO₂/ITO-based photoanode and the photovoltaic performance of dye-sensitized solar cells*. Journal of Alloys and Compounds, 2010.
125. Wang, Z. and X. Hu, *Structural and electrochemical characterization of 'open-structured' ITO films*. Thin Solid Films, 2001. **392**: p. 22-28.
126. Morales, A.E., M.H. Zaldivar, and U. Pal, *Indium doping in nanostructured ZnO through low-temperature hydrothermal process* Optical Materials, 2006. **29**: p. 100-104.
127. *ITO, tin-doped indium oxide for optical coating*. [cited 2010 2nd Nov]; Available from: <http://www.cerac.com/pubs/proddata/ito.htm>.
128. Wilden, J., et al., *Cladding of aluminum substrates with iron based wear resistant materials using controlled short arc technology*. Surface & Coatings Technology, 2008. **202**: p. 4509-4514.
129. Tahar, R.B.H., et al., *Electronic transport in tin-doped indium oxide thin films prepared by sol-gel technique*. Journal of Applied Physics, 1998. **83**(4): p. 2139-2141.

130. Pujilaksono, B., et al., *X-ray photoelectron spectroscopy studies of indium tin oxide nanocrystalline powder*. Materials Characterization, 2005. **54**: p. 1-7.
131. So, S.K., et al., *Surface preparation and characterization of indium tin oxide substrates for organic electroluminescent devices*. Applied Physics A, 1999. **68**: p. 447-450.
132. Stoev, M.D., J. Tousekova, and J. Tousek, *X-ray photoelectron spectroscopy, scanning electron microscopy and optical transmittance studies of indium tin oxide and cadmium sulphide thin films for solar cells*. Thin Solid Films, 1997. **299**: p. 67-71.
133. Lai, B., et al., *Synchrotron radiation photoelectron spectroscopy study of ITO surface*. Applied Surface Science, 2000. **157**: p. 35-38.
134. Jie, L. and X. Chao, *XPS examination of tin oxide on float glass surface*. Journal of Non-Crystalline Solids, 1990. **119**: p. 37-40.
135. McCaldin, S., et al., *The effect of processing conditions on carbon nanostructures formed on an iron-based catalyst*. Carbon, 2006. **44**: p. 2273-2280.
136. Khedr, M.H., K.S.A. Halim, and N.K. Soliman, *Effect of temperature on the kinetics of acetylene decomposition over reduced iron oxide catalyst for the production of carbon nanotubes*. Applied Surface Science, 2008. **255**: p. 2375-2381.
137. Escobar, M., et al., *Synthesis of carbon nanotubes by CVD: Effect of acetylene pressure on nanotubes characteristics*. Applied Surface Science, 2007. **254**: p. 251-256.
138. Venegoni, D., et al., *Parametric study for the growth of carbon nanotubes by catalytic chemical vapor deposition in a fluidized bed reactor*. Carbon, 2002. **40**: p. 1799-1807.
139. Sharma, R., et al., *In situ observation of the growth mechanisms of carbon nanotubes under diverse reaction conditions*. Journal of Electron Microscopy, 2005. **54**(3): p. 231-237.
140. Pan, L., M. Zhang, and Y. Nakayama, *Growth mechanism of carbon nanocoils*. Journal of Applied Physics, 2002. **91**(12): p. 10058-10061.
141. Yan, H.F., et al., *Growth of amorphous silicon nanowires via a solid-liquid-solid mechanism*. Chemical Physics Letters, 2000. **323**: p. 224-228.
142. Hsu, C.L., et al., *Indium-diffused ZnO nanowires synthesized on ITO-buffered Si substrate*. Nanotechnology, 2006. **17**: p. 516-519.

143. Lo, K.C., et al., *Synthesis of indium oxide nanorods on indium phosphide substrate using plasma immersion ion implantation*. Surface & Coatings Technology, 2007. **21**: p. 6816-6818.
144. Yan, C., T. Zhang, and P.S. Lee, *Single crystalline semi-nanotubes of indium germanate*. Crystal Growth & Design, 2008. **8**(9): p. 3144-3147.
145. Ying, X., et al., *Vacuum annealing effects on properties of ITO films prepared by reactive low voltage ion plating technique*. Proc. of SPIE, 2005. **28**: p. 6024.
146. Muller, C., et al., *Growth studies, TEM and XRD investigations of iron-filled carbon nanotubes*. Phys. stat. sol. (a), 2006. **203**(6): p. 1064-1068.
147. Zong, B., et al., *Synthesis of iron oxide nanostructures by annealing electrodeposited Fe-based films*. Chem. Mater., 2005. **17**: p. 1515-1520.
148. Horikoshi, M. and A. Hirata, *Vacuum arc deposition of homogeneous amorphous carbon films at high growth rates*. New Diamond and Frontier Carbon Technology, 2006. **16**: p. 267-277.
149. Park, S. and R.M. Walser, *Hydrogen plasma etching of pyromeritic carbon films*. Carbon, 1985. **23**(6): p. 701-706.
150. Kobayashi, K., et al., *Etching characteristics of carbon films by RF plasma*. Science and Technology of New Diamond, 1990.
151. Nakahara, M. and Y. Sanada, *Effect of argon plasma treatment on graphitic surface structure*. Letters to the Editor, 1995.
152. Huang, S. and L. Dai, *Plasma etching for purification and controlled opening of aligned carbon nanotubes*. J. Phys. Chem. B, 2002. **106**: p. 3543-3545.
153. Yu, K., et al., *Electron field emission from soluble carbon nanotube films treated by hydrogen plasma*. Chemical Physics Letters, 2003. **373**: p. 109-114.
154. Yu, K., et al., *Change of surface morphology and field emission property of carbon nanotube films treated using a hydrogen plasma*. Applied Surface Science, 2004. **225**: p. 380-388.
155. Liu, Y., et al., *Plasma etching carbon nanotube arrays and the field emission properties*. Diamond & Related Materials, 2004. **13**: p. 1609-1613.
156. Han, J.B., et al., *Effect of Ar plasma treatment on the photo-electrical properties of nanocrystal TiO₂ films*. Solar Energy Materials & Solar Cells, 2005. **88**: p. 293-299.
157. Hassanien, A., et al., *Selective etching of metallic single-wall carbon nanotubes with hydrogen plasma*. Nanotechnology, 2005. **16**: p. 278-281.

158. Katayama, K., et al., *Erosion of carbon deposition layer by hydrogen RF plasma*. Fusion Engineering and Design, 2006. **81**: p. 247-252.
159. Zeng, L., et al., *The changes of morphology, structure and optical properties from carbon nanotubes treated by hydrogen plasma*. Materials Chemistry and Physics, 2008. **108**: p. 82-87.
160. Shinohara, M., et al., *Interaction between hydrogen plasma and hydrogenated amorphous carbon film, investigated by infrared spectroscopy*. Thin Solid Films, 2008. **516**: p. 4379-4383.
161. Xie, W.G., et al., *Study on effect of hydrogen treatment on amorphous carbon film using scanning probe microscopy*. Ultramicroscopy, 2009. **109**: p. 451-456.
162. Xu, J., et al., *The effect of hydrogen plasma chemical annealing on electron field emission of amorphous carbon films*. Diamond and Related Materials, 2003. **12**: p. 2016-2019.
163. Zhu, J., et al., *Synthesis of multiwalled carbon nanotubes from bamboo charcoal and the roles of minerals on their growth*. Biomass and Bioenergy, 2012. **36**.
164. Toebes, M.L., et al., *Impact of the structure and reactivity of nickel particles on the catalytic growth of carbon nanofibers*. Catalysis Today, 2002. **76**: p. 33-42.
165. Nasibulin, A.G., et al., *Investigations of mechanism of carbon nanotube growth*. Phys. stat. sol. (b), 2006. **243**(13): p. 3095-3100.
166. Aguayo, N.A., et al., *Magnetic response of CVD and PECVD iron filled multi-walled carbon nanotubes*. Diamond & Related Materials, 2009. **18**.
167. Ermakova, M.A., et al., *Decomposition of Methane over Iron Catalysts at the Range of Moderate Temperatures: The Influence of Structure of the Catalytic Systems and the Reaction Conditions on the Yield of Carbon and Morphology of Carbon Filaments*. Journal of Catalysis, 2001. **201**: p. 183-197.
168. Kim, H. and W. Sigmund, *Iron nanoparticles in carbon nanotubes at various temperatures*. Journal of Crystal Growth, 2005. **276**: p. 594-605.
169. Lehman, J.H., et al., *Evaluating the characteristics of multiwall carbon nanotubes*. Carbon, 2011. **49**: p. 2581-2602.
170. Liu, G., *Synthesis, Characterization of In₂O₃ Nanocrystals and their photoluminescence property*. Int. J. Electrochem. Sci., 2011. **6**: p. 2162 - 2170.
171. Lin, K.C., et al., *Low Temperature Growth of Carbon Nanotubes by Thermal Chemical Vapor Deposition using Novel Catalyst*. TDC, 2006: p. 06-018.
172. Ferrari, A.C., *Raman spectroscopy of graphene and graphite: Disorder, electron-phonon coupling, doping and nonadiabatic effects*. Solid State Communications, 2007. **143**: p. 47-57.

173. Liu, Y., C. Pan, and J. Wang, *Raman spectra of carbon nanotubes and nanofibers prepared by ethanol flames*. Journal of Materials Science, 2004. **39**: p. 1091-1094.
174. Puech, P., et al., *Raman bands of double-wall carbon nanotubes: comparison with single- and triple-wall carbon nanotubes, and influence of annealing and electron irradiation*. J. Raman Spectrosc., 2007. **38**: p. 714-720.
175. Zhang, H.X. and P.X. Feng, *Properties of one-dimensional tilted carbon nanorod arrays synthesized by the catalyst-assisted oblique angle deposition technique*. J. Phys. D: Appl. Phys., 2009. **42**.
176. Rao, M.V., et al., *In situ lithium intercalation of carbon nanorods using flame synthesis*. Composite Science and Technology, 2010. **70**: p. 255-259.
177. Yudasaka, M., et al., *Pressure dependence of the structures of carbonaceous deposits formed by laser ablation on targets composed of carbon, nickel and cobalt*. J. Phys. Chem. B, 1998. **102**: p. 4892-4896.
178. Alvarez, L., et al., *Solar production of single-wall carbon nanotubes: growth mechanisms studied by electron microscopy and Raman spectroscopy*. Appl. Phys. A, 2000. **70**: p. 169-173.
179. Tung, N.T. and N.D. Nghia, *Preparation of nano-thin films from conducting polymer by chemical vapour deposition method and its application for light emitting diodes (LED) and organic solar cells*. Journal of Physics: Conference Series 187, 2009 **012006**.
180. Vaddiraju, S., K. Seneca, and K.K. Gleason, *Novel strategies for the deposition of -COOH functionalized conducting copolymer films and the assembly of inorganic nanoparticles on conducting polymer platforms*. Adv. Funct. Mater., 2008. **18**: p. 1929-1938.
181. Ueberreiter, K. and K. Yamaura, *Dependence of surface tension and polymer concentration in surface on solvent interaction of polystyrene solutions*. Colloid & Polymer Sci., 1977. **255**: p. 1178-1180.
182. Wiedemann, W., et al., *Nanostructured interfaces in polymer solar cells*. Applied Physics Letters, 2010. **96**.
183. McDonald, R.N. and T.W. Campbell, *The witting reaction as a polymerization method*. Journal of American Chemical Society, 1960. **82**.
184. Papadimitrakopoulos, F., et al., *The role of carbonyl groups in the photoluminescence of poly(p-phenylenevinylene)*. Chem. Mater., 1994. **6**: p. 1563-1568.
185. Wallace, G.G., et al., *Conjugated polymers: New Materials for Photovoltaics*. Chem. Inov. , 2000. **30**: p. 14-22.

186. Weinberger, B.R., M. Akhtar, and S.C. Gau, *Polyacetylene photovoltaic devices*. Synthetic Metals, 1982. **4**: p. 187-197.
187. Cha, M., et al., *Enhanced nonlinear absorption and optical limiting in semiconducting polymer/methanofullerene charge transfer films*. Appl. Phys. Lett., 1995. **67**.
188. Sariciftci, N.S., et al., *Photoinduced electron transfer from a conducting polymer to buckminsterfullerene*. Science, 1992. **258**.
189. Marks, R.N., et al., *The photovoltaic response in poly(p-phenylene vinylene) thin film devices*. J. Phys.: Condens. Matter, 1994. **6**: p. 1379-1394.
190. Halls, J.J.M., et al., *Exciton dissociation at a poly(p-phenylenevinylene) / C₆₀ heterojunction*. Synthetic Metals, 1996. **77**: p. 277-280.
191. Chambon, S., et al., *Aging of a Donor Conjugated Polymer: Photochemical Studies of the Degradation of Poly[2-methoxy-5-(3',7'-dimethyloctyloxy)-1,4-phenylenevinylene]*. Journal of Polymer Science, 2007. **45**: p. 317-331.
192. Morgado, J., R.H. Friend, and F. Cacialli, *Environmental aging of poly(p-phenylenevinylene) based light-emitting diodes*. Synthetic Metals, 2000. **114** p. 189-196.
193. Nguyen, T.P., et al., *Optical Spectroscopic Investigations of Phenylene Vinylene Oligomers*. Synth. Met., 1999. **101**: p. 633-634
194. Dermaut, W., et al., *Cold stretching of PPV with Water as a Plasticizer*. Macromolecules, 2000. **33**: p. 5634-5637.
195. Alimi, K., et al., *Synthesis and characterization of copolymer derived from poly-phenylene-vinylene potentially luminescent copolymers*. European Polymer Journal, 2001. **37**: p. 781-787.
196. Lefrant, S., E. Perrin, and J. P. Buisson, *Vibrational Studies of Polyparaphenylene-vinylene (PPV)*. Synthetic Metals, 1989. **29**: p. 91-96.
197. Lee, C.Y., et al., *Crosslinked structure of pristine poly(p-phenylene vinylene) thin-films synthesized by chemical vapour deposition polymerization*. Synthetic Metals, 2009.
198. Cirpan, A., Z. Kucukyavuz, and S. Kucukyavuz, *Synthesis, Characterization and Electrical Conductivity of Poly(p-phenylene vinylene)*. Turk J Chem, 2003. **27**: p. 135-143.
199. Heeger, A.J., et al., *Solitons in conducting polymers*. Reviews of Modern Physics, 1988. **60**(3): p. 781.
200. Vaeth, K.M. and K.F. Jensen, *Poly(p-phenylene vinylene) prepared by chemical vapour deposition: Influence of monomer selection and reaction conditions on*

- film composition and luminescence properties*. Macromolecules 1998. **31**: p. 6789-6793.
201. Saxena, A., B.P. Tripathi, and V.K. Shahi, *Sulfonated poly(styrene-co-maleic anhydride)-poly(ethylene glycol)-silica nanocomposite polyelectrolyte membranes for fuel cell applications*. J. Phys. Chem. B, 2007. **111**: p. 12454-12461.
 202. Son, S., et al., *Luminescence enhancement by the introduction of disorder into poly(p-phenylene vinylene)*. Science Vol., 1995. **269**.
 203. Kayashima, H., et al., *Poly(p-phenylenevinylene)-based field-effect transistors with platinum source-drain electrodes*. J. Phys. D: Appl. Phys. , 2007. **40**: p. 1646-1648.
 204. Gmeiner, J., et al., *Synthesis, electrical conductivity and electroluminescence of poly(p-phenylene vinylene) prepared by the precursor route*. Acta Polymer, 1993. **44**: p. 201-205.
 205. Janssen, F.J.J., et al., *Degradation effects in poly para-phenylene vinylene derivatives due to controlled oxygen exposure*. Synthetic Metals, 2002. **131**: p. 167-174.
 206. Cumpston, B.H. and K.F. Jensen, *Photo-oxidation of polymers used in electroluminescent devices*. Synthetic Metals, 1995. **73**: p. 195-199.
 207. Kumar, S., et al., *Application of spectroscopic ellipsometry to probe the environmental and photo-oxidative degradation of poly(p-phenylenevinylene) (PPV)*. Synthetic Metals, 2003. **139**: p. 751-753.
 208. Lee, H.C., et al., *Improved environmental stability in poly(p-phenylene vinylene)/layered silicate nanocomposite*. Applied Clay Science, 2002. **21**: p. 287-293.
 209. Pacios, R., et al., *Effects of photo-oxidation on the performance of poly[2-methoxy-5-(3',7'-dimethyloctyloxy)-1,4-phenylene vinylene]:[6,6]-phenyl C61-butyric acid methyl ester solar cells*. Adv. Funct. Mater., 2006. **16**: p. 2117-2126.
 210. Sarkas, H.W., et al., *Enhanced photooxidative stability of conjugated polymers via C60 Doping*. J. Phys. Chem. B, 1996. **100**: p. 5169-5171.
 211. Touihri, S., et al., *Towards anode with low indium content as effective anode in organic solar cells*. Applied Surface Science, 2012. **258**: p. 2844-2849.
 212. Yu, W., et al., *A two-step method combining electrodeposition and spin-coating for solar processing*. J Solid State Electrochem, 2010. **14**: p. 1051-1056.
 213. Kumar, A., S. Sista, and Y. Yang, *Dipole induced anomalous S-shape I-V curves in polymer solar cells*. Journal of Applied Physics, 2009. **105**.

214. Drees, M., et al., *Creation of a gradient polymer-fullerene interface in photovoltaic devices by thermally controlled interdiffusion*. Applied Physics Letters, 2002. **81**.
215. Qi, D., et al., *Optical emission of conjugated polymers adsorbed to nanoporous alumina*. Nano Letters, 2003. **3**(9): p. 1265-1268.
216. Guha, S., et al., *Temperature-dependent photoluminescence of organic semiconductors with varying backbone conformation*. Physical Review B, 2003. **67**.
217. Cetinkaya, M., S. Boduroglu, and M.C. Demirel, *Growth of nanostructured thin films of poly(p-xylene) derivatives by vapor deposition*. Polymer, 2007. **48**: p. 4130-4134.
218. Xu, Y.F., et al., *Thickness dependent behavior of photoluminescence of tris(8-hydroxyquinoline) aluminum film*. Chinese Journal of Chemical Physics, 2006. **19**(2).
219. Chang, I.H., et al., *Photoinduced increasing or decreasing behaviors of photoluminescence in phenylene vinylene polymer derivatives*. Journal of the Korean Physical Society, 2004. **45**: p. 505-508.
220. Kong, F., et al., *Optical emission from nano-poly[2-methoxy-5-(2'-ethyl-hexyloxy)-p-phenylene vinylene] arrays*. Journal of Applied Physics, 2005. **98**(074304).
221. Kong, J., et al., *Self-organized micropatterns of high aspect ratio polymer nanofibers by wetting of nanopores*. Journal of Polymer Science Part B: Polymer Physics, 2008. **46**(12): p. 1280-1289.
222. Son, S.W., M. Ha, and H. Jeong, *Anomalous scaling behavior in polymer thin film growth by vapor deposition*. Journal of Statistical Mechanics: Theory and Experiment, 2009.